Impact of order and disorder on phase formation in $(In_xGa_{1-x})_2O_3$ investigated by transmission electron microscopy

Dissertation

zur Erlangung des akademischen Grades

doctor rerum naturalium (Dr. rer. nat.)

im Fach Physik
Spezialisierung: Experimentalphysik

eingereicht an der
Mathematisch-Naturwissenschaftlichen Fakultät
der Humboldt-Universität zu Berlin

von

M.Sc. Charlotte Wouters

Präsidentin der Humboldt-Universität zu Berlin:
Prof. Dr.-Ing. Dr. Sabine Kunst

Dekan der Mathematisch-Naturwissenschaftlichen Fakultät
Prof. Dr. Elmar Kulke

Gutachter/innen: 1. Prof. Dr. Christoph Koch
2. Prof. Dr. Thomas Schröder
3. Prof. Dr. Sandra Van Aert

Tag der mündlichen Prüfung: 15.03.2021

Abstract

In this work, we study the impact of order and disorder on the phase formation in $(In_xGa_{1-x})_2O_3$ by means of transmission electron microscopy (TEM) and in-situ TEM. The studied thin film samples are grown epitaxially on crystalline substrates by pulsed laser deposition, molecular beam epitaxy and metalorganic vapor phase epitaxy, or deposited amorphously to be crystallized in-situ. Based on the experimental findings and ground-state energies of the various phases from cluster expansion, a phase diagram is developed. The last part of the thesis focuses on a computational study of high-angle annular dark field scanning TEM (HAADF-STEM) contrast in ordered materials.

We find strong ordering on the cation sublattices of $(In_xGa_{1-x})_2O_3$ in the case of epitaxial growth, which is energetically driven by the tendency of In and Ga to each assume their preferred coordination environment. The energetic stability of the ordered multi-coordinated monoclinic (β) and hexagonal (h) lattices requires a modification of the general assumption of ideal mixing in solid solutions to realistically estimate the configurational entropy. Based on these considerations, we construct the temperature dependent phase diagram, which was up to now not available in literature. While very narrow thermodynamically stable ranges exist for each phase, wide composition ranges of metastable compounds are predicted, which can be achieved at temperatures that are typical for epitaxy: the monoclinic phase is metastable in the composition range $x \leq 0.5$, the hexagonal phase for $0.55 \leq x \leq 0.7$, and the cubic bixbyite phase for $x \geq 0.91$. The predictions of the model are in excellent agreement with other experimental findings in literature.

When crystallizing $(In_xGa_{1-x})_2O_3$ from the amorphous phase, the solubility of Ga in the bixbyite phase extends to $x \geq 0.33$ and the miscibility gap between $0.7 < x < 0.91$ for thermodynamic equilibrium is closed. This is explained by the fact that a high configurational entropy thermodynamically favors the bixbyite lattice, in which the cations are all octahedrally coordinated compared to the phases with multiple coordination. The high amount of configurational entropy frozen in the amorphous phase is kinetically stabilized below a critical temperature. In the compositional range $x \leq 0.22$, we find in addition the formation of spinel γ-$(In_xGa_{1-x})_2O_3$. A model is developed that describes the γ-phase as a disordered β-phase and the detailed atomic mechanisms that mediate the $\gamma \rightarrow \beta$ phase transition observed at higher annealing temperatures, are described.

The last chapter shows that sublattice ordering in two-compound structures with relatively high and low Z components, such as β- and h-$(In_xGa_{1-x})_2O_3$, strongly affects compositional quantification by Z-contrast. Ordering reduces the HAADF-STEM intensity compared to that found for disordered lattices of the same composition. This is a consequence of the $2s$ Bloch state excitation for an electron probe traveling on an atom column with high atomic number Z. Similar to the $1s$ channeling oscillation, the $2s$ excitation creates an oscillation in the electron wave function due to beating with the unbound Bloch states, which influences the scattering to the HAADF detector. This effect on the other hand can be used to measure the order parameter in solid solutions with known composition.

Zusammenfassung

In dieser Arbeit untersuchen wir den Einfluss von Ordnung und Unordnung auf die Phasenbildung in $(In_xGa_{1-x})_2O_3$ mittels Transmissionselektronenmikroskopie (TEM) und in-situ TEM. Die untersuchten dünnen Filme werden epitaktisch auf kristallinen Substrate mittels gepulste Laserdeposition, Molekularstrahlepitaxie und metallorganische Gasphasenepitaxie gewachsen, oder amorph abgeschieden um in-situ kristallisiert zu werden. Auf der Basis unsere experimentellen Ergebnisse und auf Berechnungen mit der Clusterexpansionstechnik wird ein Phasendiagramm entwickelt. Der letzte Teil der Arbeit konzentriert sich auf Simulationen zum quantitativen Z-Kontrast (Kontrast durch Detektion von Elektronen, die in große Winkel gestreut werden) bei der Rastertransmissionselektronenmikroskopie (HAADF-STEM) geordneter Materialien.

Im Falle epitaktischem Wachstums, finden wir eine ausgeprägte Ordnung auf den Kationenuntergittern von $(In_xGa_{1-x})_2O_3$, die energetisch getrieben wird von der Tendenz von Indium und Gallium ihr jeweils bevorzugte Koordination zum Sauerstoff einzunehmen. Ausgehend von der experimentell beobachteten Stabilität der geordneten monoklinen (β) und hexagonalen (h) Phasen, modifizieren wir die allgemeinen Annahme des Modells der idealen Mischung der Konstituenten auf dem Untergitter um die Konfigurationsentropie realistisch zu berechnen. Basierend auf diesen überlegungen, konstruieren wir ein temperaturabhängige Phasendiagramm, das bisher in der Literatur nicht verfügbar war. Obwohl für jede der Phasen sehr enge thermodynamisch stabile Bereiche existieren, sagen unsere Berechnungen weite Zusammensetzungsbereiche vorher, in denen die Legierungen metastabil existieren für Temperaturen die typisch für epitaktisches Wachstum sind. Für die monokline Phase liegt dieser metastabile Zusammensetzungsbereich für $x \leq 0.5$ vor, für die hexagonale Phase zwischen $0.55 \leq x \leq 0.7$. Die Bixbyitphase ist für $x \geq 0.91$ metastabil. Die Vorhersagen des Modells stimmen ausgezeichnet mit unseren experimentellen Befunden und denen anderer Autoren in der Literatur überein.

Bei der Kristallisation von $(In_xGa_{1-x})_2O_3$ aus der amorphen Phase erstreckt sich die Löslichkeit von Ga in der Bixbyitphase bis zu $x \geq 0.33$ und die im Gleichgewichtsphasendiagramm bestehende Mischungslücke für $0.7 < x < 0.91$ wird geschlossen. Dies wird dadurch erklärt, dass die hohe Konfigurationsentropie das kubische Gitter, in dem die Kationen alle oktaedrisch koordiniert vorliegen, gegenüber den Phasen mit multiplem Koordinationen thermodynamisch begünstigt. Die bei der Deposition des amorphen Materials vorhandene hohe Konfigurationsentropie ist unterhalb einer kritischen Temperatur kinetisch stabilisiert. Im Konzentrationsbereich für $x \leq 0.22$ finden wir zusätzlich eine Spinell Phase, i.e. γ-$(In_xGa_{1-x})_2O_3$. Auf Basis eines Modells, welches die γ-Phase als eine fehlgeordnete β-Phase beschreibt, werden die atomaren Mechanismen bei höheren Temperaturen den $\gamma \rightarrow \beta$ Phasenübergang detailliert beschreiben.

Das letzte Kapitel zeigt dass Untergitterordnung in Zweistoff-Legierungen bestehend aus Elementen mit hoher und niedriger Kernladungszahl, wie β- und h-$(In_xGa_{1-x})_2O_3$, die Quantifizierung mittels Z-Kontrast stark beeinträchtigt. Geordnete Phasen weisen eine deutlich reduzierte STEM-Intensität im Vergleich zum ungeordneten Gittern der gleichen Zusammensetzung auf. Dies ist eine Folge der $2s$-Bloch-Zustandsanregung für

eine Elektronensonde, die sich entlang einer Atomsäule mit hoher Kernladungszahl Z bewegt. Ähnlich wie die 1s-Channeling-Oszillation, erzeugt die 2s-Anregung eine Oszillation in der Elektronenwellenfunktion aufgrund des Beating mit den ungebundenen Bloch-Zustanden, die die Streuung zum HAADF-Detektor beeinflusst. Dieser Effekt lässt sich dazu nutzen um den Ordnungsparameter bei bekannter Zusammensetzung zu quantifizieren.

Contents

List of Figures

List of Tables

List of Abbreviations

2D	two-dimensional
3D	three-dimensional
ASE	atomic simulation environment
BEP	beam equivalent pressure
BF	bright field
BOFM	Baliga's figure of merit
BSE	backscattered electrons
CCD	charge coupled device
CCS	continuous composition spread
CE	cluster expansion
CTF	contrast transfer function
CVD	chemical vapor deposition
DF	dark field
DFT	density functional theory
ECI	effective cluster interaction
ECN	effective coordination number
EDXS	energy dispersive X-ray spectroscopy
EXAFS	extended X-ray absorption fine structure
FFT	fast Fourier transform
FIB	focused ion beam
GGA	generalized gradient approximation
HAADF	high angle annular dark field
HRTEM	high resolution transmission electron microscopy
HVPE	halide vapor phase epitaxy
ICSD	inorganic crystal structure database
IR	infrared
ITO	indium tin oxide
LED	light emitting diode
MBE	molecular beam epitaxy
MEMS	micro-electro-mechanical system
MOCVD	metalorganic chemical vapor deposition
MOVPE	metalorganic vapor phase epitaxy
NCSI	negative spherical aberration imaging

PIPS	precision ion polishing system
PLD	pulsed laser deposition
SEM	scanning electron microscopy
STEM	scanning transmission electron microscopy
TCO	transparent conducting oxide
TDS	thermal diffuse scattering
TEM	transmission electron microscopy
TSO	transparent semiconducting oxide
UHV	ultra-high vacuum
UV	ultraviolet
WPOA	weak phase object approximation
YSZ	yttria-stabilized zirconia
XRD	X-ray diffraction

1

Introduction

1.1 Development of semiconductor solid solutions

An important aspect that strongly advanced the field of semiconductors over the last century is the formation of solid solutions. By forming a mixture of two crystalline solids that coexist, a new crystalline solid emerges, which typically has a relaxed lattice parameter somewhere in between those of the two original components. Thus, by varying the solid solution composition through chemical substitution, its bond length can be engineered and with that also the semiconductor's optical and electrical properties are modified to obtain the desired functionality. An extremely valuable use of solid solutions in thin film technologies is strain engineering through the formation of heterostructures. This comprises the coherent growth of an epitaxial layer, which is lattice mismatched with the underlying substrate, such that a compressively or tensily strained layer results. The induced strain can change the material's fundamental parameters such as the band gap, effective masses and mobilities of the charge carriers, refractive indices, electron energy spectrum, etc., to benefit certain applications. Devices such as the heterobipolar transistor, high electron mobility transistors, light emitting diodes (LEDs) and semiconductor lasers are made of such structures. The concepts trace back to the work by Shockley [1], Krömer [2] and Alferov [3, 4], the latter who has been awarded the Nobel prize in physics for the development of semiconductor heterostructures in high-speed- and optoelectronics [5]. Discoveries such as the quantum Hall effect by Klitzing [6] could not have been made without the realization of semiconductor heterostructures. To realize such structures, knowledge of the phase diagram of the particular solid solution in use is a key issue.

The evolution in the used materials for these semiconductor solutions and heterostructures built upon them, is characterized by the continuing search for materials with a wider band gap [7,8]. For optical devices, the interest lies in shifting the emission and absorption edge into the deep ultraviolet (UV) region of the wavelength spectrum for applications as light emitting devices and photodetectors. In case of electronic devices, the main interest is to increase the breakdown field for power electronic applications. In the mid-twentieth century, semiconductor technology was limited to the elemental diamond Si and Ge semiconductors and compound semiconductors based on III-V zincblende materials, which operate in the infrared (IR), as visible in Fig. 1.1. The available heterostructures were based on Si_xGe_{1-x} and $Al_xGa_{1-x}As$ solid solutions. Due to relatively small lattice mis-

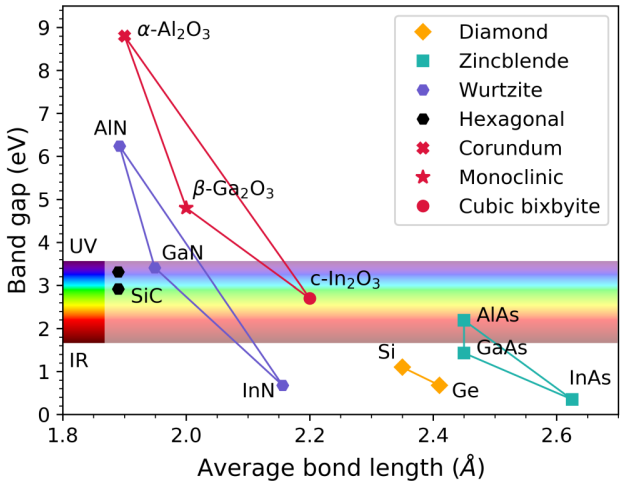

Figure 1.1: Band gap as a function of average bond length for the group-III sesquioxides in comparison to other important semiconductors. Based on Ref. [7].

matches in these systems, they are fully miscible over the whole composition range. This lead to easily tunable devices, such as $Al_xGa_{1-x}As$-based infrared photodetectors [9] and laser diodes [10] and high-mobility transistors based on strained Si_xGe_{1-x}/Si heterostructures [11]. By shifting the research focus to new hexagonal lattice structures, the next generation of semiconductors emerged in the 1980s, with materials like SiC, $In_xGa_{1-x}N$ and $Al_xGa_{1-x}N$. The absorption edge shifted into and beyond the visible spectral range, which opened new fields of advanced optoelectronics and electronic applications such as LEDs [12], laser diodes [13] and power devices [14], with outstanding thermal stability. The larger lattice mismatch, especially in $In_xGa_{1-x}N$ (Fig. 1.1), gives rise to a miscibility gap at low temperatures. However, because the binary components have identical lattice structures, in which all cations sites are equivalent and thus statistical mixing can be assumed, full miscibility can still be reached at elevated temperatures [15, 16]. This is the typical behavior of a conventional isostructural phase diagram, which is mostly driven by strain considerations.

Since the last decade, semiconductor development is taking the next step towards ultra-wide band gap materials to achieve extended functionality in the UV range. Here, the most promising candidates are found in oxides. Due to the higher electronegativity of oxygen compared to other semiconductor anions [8], oxides tend to have more ionic bonds which leads to wider band gaps. This is shown for our system of interest, the group-III oxides, in Fig. 1.1, where the band gap varies from 2.7 eV in In_2O_3 [17] to 4.8 eV in Ga_2O_3 [18–20] and 8.9 eV in Al_2O_3 [21]. Additionally, the flexibility of oxygen to compensate different charges leads to many different phases and stoichiometries that come into play in these oxide systems. Rocksalt and wurtzite crystal structures are observed for MgO and ZnO, respectively, where the coordination environment changes from six-fold to four-fold. Also in the group-III sesquioxides, a high structural diversity exists. Al_2O_3, Ga_2O_3 and In_2O_3 have different ground-state crystal structures: α-Al_2O_3 has corundum symmetry ($R\bar{3}c$) [22], β-Ga_2O_3 has monoclinic symmetry ($C2/m$) [23] and c-In_2O_3 has cubic bixbyite symmetry ($Ia\bar{3}$) [24]. Apart from different structures between oxide materials, also within one oxide different structures exist. The best example is Ga_2O_3, which appears as multiple metastable polymorphs (α, γ, ϵ/κ) in addition to the stable β-phase [25, 26]. The structural diversity provides a new incentive of solid

solution formation of structural modification as another way to modify the material's properties. On the other hand, it makes it much harder to make predictions on the phase stability as a function of composition. Another factor that plays a role here is the diversity of coordination environments of the cations with respect to the oxygen atoms, such as the case in monoclinic β-Ga_2O_3, which has four- and six-fold coordinated cation sites. The mixing of the different cation components on these lattice might be far from purely statistic. It has, for example, been shown by Maccioni *et al.* [27] that incorporating indium on a four-fold coordinated lattice site in β-Ga_2O_3 costs 1.1 eV more than on a six-fold coordinated site. Studying the physics of these solid solutions and developing a reliable phase diagram is therefore of utmost importance, in order to make predictions on which solid solution structures and compositions are achievable in thin film growth or other synthesis methods.

1.2 Technological relevance of Ga_2O_3-In_2O_3 system

Ga_2O_3, as well as the isovalent compounds, In_2O_3 and Al_2O_3, labeled as the group-III sesquioxides, are emerging as a new class of transparent (semi)conducting oxides (TSOs or TCOs). The direct band gap of cubic bixbyite In_2O_3 at 2.7 eV is optically forbidden [17] and strong absorption only sets in for photon energies above $\sim$ 3.7 eV [28, 29], which renders the material transparent. In_2O_3 is widely researched and in the past mainly applied as active material in gas sensing, as its conductivity strongly depends on the gas atmosphere it is in contact with [30, 31]. Doped with Sn, to form the TCO indium tin oxide (ITO), its electron concentration is highly increased (to 10^{20} cm^{-3}) [32] and it is widely applied in displays [33], LEDs [34] and as electrodes in solar cells [35]. More recently, In_2O_3 is rediscovered for its wide band gap semiconducting properties and high-quality bulk and thin film structures are pursued for it to act as active material in novel electronic devices. In view of electronics applications though, it is especially the monoclinic polymorph of Ga_2O_3, β-Ga_2O_3, that stands out. It has the advantage that it can be doped efficiently over a wide range of carrier concentrations from 10^{15} cm^{-3} – 10^{20} cm^{-3}. High free carrier concentrations can be reached without significant compensation despite the wide band gap of 4.8 eV. In addition, with its high estimated breakdown field of 8 MV/cm, it stands out in comparison to successfully industrialized older-generation semiconductors like Si or GaN. This is typically demonstrated by Baliga's figure of merit (BOFM)[1], which estimates a material's potential for power switching device performance based on properties like the dielectric constant, electron mobility and band gap. β-Ga_2O_3 is calculated to have a BOFM in the range of 2000 – 3400, which is at least four times larger than that of SiC or GaN [36]. In addition, high-quality bulk β-Ga_2O_3 substrates can be grown from the melt [37, 38], which is a big advantage for thin film technologies, especially in comparison to Al-based nitrides for which obtaining defect-free material is challenging. High-power electronic applications for β-Ga_2O_3 include power field effect transistors [39–42] and Schottky barrier diodes [43–46], topics which are booming in amount of publications. To fully exploit the sesquioxide TSOs properties, however, band gap engineering is desired, based on the formation of solid solutions of the binary compounds, as introduced earlier. In this way, the band gap could be engineered over the range from 2.7 eV for In_2O_3 to 8.9 eV for Al_2O_3 [21], as illustrated in Fig. 1.1. $(In_xGa_{1-x})_2O_3$ solid solutions are mostly

[1] Calculated as $\epsilon\mu E_b^3$, with ϵ the dielectric constant, μ the electron mobility, and E_b the band gap energy.

investigated for their high potential as active material in optoelectronic devices such as UV photodetectors [47–49]. Large band off-set heterostructures with $(In_xGa_{1-x})_2O_3$ or $(Al_xGa_{1-x})_2O_3$ [50, 51] are interesting for transistor devices to create 2D conductive channels by carrier confinement. To fully estimate the potential of the group-III oxide solid solutions for devices though, knowledge on the miscibility of the different crystal structures as a function of composition and temperature is required.

1.3 Miscibility in $(In_xGa_{1-x})_2O_3$ solid solutions

In this thesis, we will focus on the phase stability in the $(In_xGa_{1-x})_2O_3$ system. As described above, the properties of the binary structures are relatively well studied, while the ternary system is largely undiscovered, apart from very recent work mostly from the last few years. Theoretical predictions on the phase formation in $(In_xGa_{1-x})_2O_3$ are limited to two works based on density functional theory (DFT). The reliability of these studies, however, is affected by the required large supercells, which take a long process time to be calculated by DFT. As a consequence, also the sampling of different configurations is limited. Peelaers *et al.* [50] found a strong stability of the monoclinic phase at an indium concentration of $x = 0.5$, indicating the formation of an ordered structure. In their further analysis though, this interesting finding was completely ignored and the regular solution model was simply applied to find a lower bound for miscibility of the β-phase over the complete composition range at a temperature of 527°C, as shown in Fig. 1.2(a). Maccioni *et al.* [52] considered in their calculations apart from the binary stable phases, a hexagonal solid solution phase ($P6_3/mmc$) that has been experimentally observed as a high-pressure phase [53] at indium compositions close to $x = 0.5$. In agreement, Maccioni finds that this hexagonal phase is lower in energy than the monoclinic solid solution at $x = 0.5$ and stable in the range $0.4 \leq x \leq 0.6$. Additionally, they predict a stability of the monoclinic phase for $x \leq 0.18$ and of the bixbyite phase for $x \geq 0.9$. These solubility limits are claimed to be independent of temperature as shown in Fig. 1.2(b), and the miscibility gaps on both sides of the phase diagram are persistent for all relevant growth temperatures.

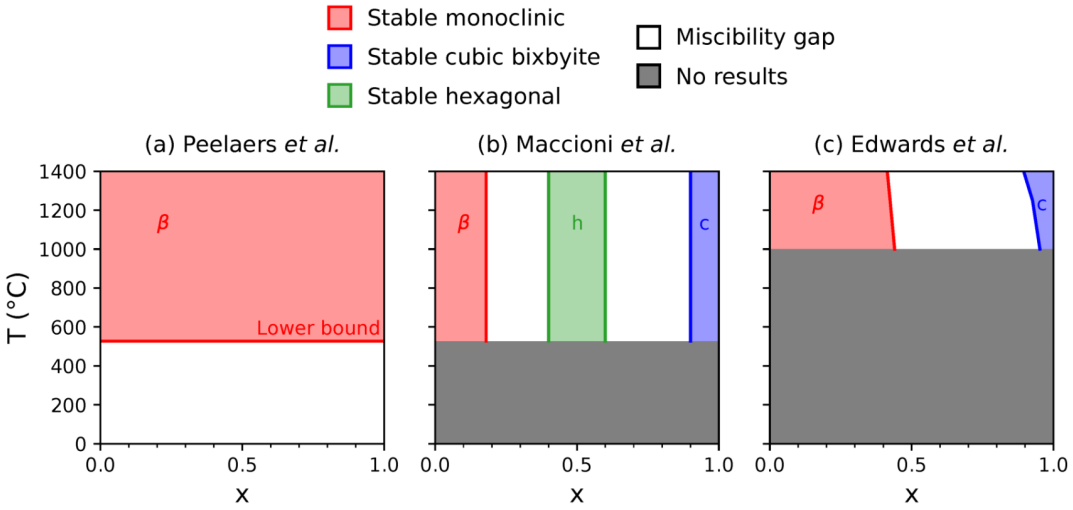

Figure 1.2: Current literature on the phase diagram of $(In_xGa_{1-x})_2O_3$. (a) and (b) are the result of theoretical DFT work by Peelaers *et al.* [50] and Maccioni *et al.* [52], respectively, while (c) is the result of powder sintering experiments by Edwards *et al.* [54].

The first experimental work on mixing of Ga_2O_3 and In_2O_3 has been done by Edwards *et al.* [54], who mechanically mixed, pressed and heated Ga_2O_3 and In_2O_3 powders to achieve equilibrated materials. They present a maximum indium solubility of $x = 0.44$ in monoclinic β-$(In_xGa_{1-x})_2O_3$ at 1000°C and a maximum Ga solubility of $1 - x = 0.11$ in cubic bixbyite c-$(In_xGa_{1-x})_2O_3$ at 1400°C, as illustrated in Fig. 1.2(c). Other bulk growth or sintered powder methods in a comparable temperature range find a solubility limit of the monoclinic phase in the range of $x = 0.2 - 0.4$ [53, 55–58]. Later, thin film growth approaches were explored to produce $(In_xGa_{1-x})_2O_3$ in a typically lower temperature range of $600 - 900$°C to investigate its technological promises. These investigations are up to now mostly focused on the heteroepitaxial growth of the gallium-rich monoclinic solid solution. Pioneering work on β-$(In_xGa_{1-x})_2O_3$ as a photodetector is done by Kokubun *et al.* [48] and von Wenckstern *et al.* [59], who grew thin films on c-sapphire substrates by the sol-gel method and pulsed laser deposition (PLD), respectively. They achieved respective indium concentrations up to $x = 0.40$ and $x = 0.15$ in the monoclinic phase without secondary phase formation and demonstrated a linear shift in the band gap and the photo response wavelength. Another PLD work by the same group [60] showed indium solubility limits of $x = 0.2$ on c-sapphire and $x = 0.3$ on MgO substrates. The growth of β-$(In_xGa_{1-x})_2O_3$ on sapphire by molecular beam epitaxy was reported for In compositions up to $x = 0.35$ before phase separation takes place [61]. There exists only one report on the epitaxial growth of In-rich bixbyite $(In_xGa_{1-x})_2O_3$, which was grown on quartz, and finds an incorporation of gallium into c-In_2O_3 up to 55% [62].

1.4 Objective of this thesis

From the above summary of data, which mostly rely on X-ray diffraction (XRD) for phase characterization, it is clear that a large variation in the observed solubility limits of $(In_xGa_{1-x})_2O_3$ solid solutions exists, which depend on the synthesis method and the used substrate. The limited theoretical work provides contradicting predictions for the stability and both are up too now not able to explain the experimental findings. Therefore, there is a need for an understanding of the underlying physics that is governing the phase formation in this system and the development of a reliable phase diagram. This will be the main objective of this thesis. Instead of XRD, we will rely on transmission electron microscopy (TEM) as the main characterization technique because of its sensitivity for phase detection. Our investigations will comprise the nanoscale analysis of the phase formation in thin $(In_xGa_{1-x})_2O_3$ films grown by three different high-temperature growth methods. Additionally, in-situ TEM to heat and crystallize amorphous $(In_xGa_{1-x})_2O_3$ films, in order to follow the phase evolution as a function of temperature, was performed. An equilibrium phase diagram is developed computationally based on cluster expansion calculations, which provides an efficient configurational sampling method of the different lattices. A comparison between experiment and theory will help us to understand the physics that are important in the different phase formation approaches.

1.5 Outline

Chapter 2 contains an overview of the theoretical background underlying this work and the experimental and computational methods that were used. The structural properties of the different group-III oxide polymorphs are summarized and the basic principles of

miscibility theory in solid solutions are presented. Following that, the computational procedure, based on density functional theory and cluster expansion, for the construction of the phase diagram of $(In_xGa_{1-x})_2O_3$ is laid out. The epitaxial growth methods used for the deposition of crystalline and amorphous $(In_xGa_{1-x})_2O_3$ thin film samples are described. Section 2.4 on transmission electron microscopy (TEM) contains the imaging principles of the different imaging modes used during TEM characterization and the theory underlying the Bloch wave and multislice calculations that are used for the scanning TEM (STEM) simulations of Chapter 5. The methodology that was used for the in-situ TEM annealing experiments of Chapter 3 is tackled, and additional characterization methods that were used are explained.

In the first part of Chapter 3, the experimental results obtained by TEM on the phase formation in $(In_xGa_{1-x})_2O_3$ thin films grown by pulsed laser deposition, molecular beam epitaxy and metalorganic vapor phase epitaxy are presented. This includes the phase stability in heteroepitaxial films grown on sapphire substrates that cover the full composition range, and indium and gallium solubility limits in monoclinic and bixbyite films on native substrates. In the second part, the computational equilibrium phase diagram is constructed. At the end of the chapter, the computational results are discussed in comparison to previous literature, and from a comparison of the experimental and computational results, the importance of ordering on the phase stability is acknowledged.

Chapter 4 presents the crystallization data obtained by annealing amorphous $(In_xGa_{1-x})_2O_3$ films in-situ in the TEM and the experimental phase diagram that can be constructed based on those data. The kinetics of the crystallization and annealing process are discussed to explain the formation of kinetically stabilized and highly disordered phases and the phase transitions that take place.

Chapter 5 is linked to the other parts of this thesis by dealing with the impact of ordering on quantitative high angle annular dark field (HAADF) STEM imaging based on a computational study. At first, it is shown that the expected relation between HAADF intensity and composition in β-$(In_xGa_{1-x})_2O_3$ is disrupted when the cations are ordered on distinct sublattices. This finding is generalized to other solid solution systems with relatively high Z elemental components. With the help of Bloch wave calculations, the cause of these unexpected findings is investigated and linked to the excitation of the $2s$ Bloch wave state in the propagating STEM electron beam under certain conditions.

Finally, in Chapter 6, the most important conclusions based on the presented results are drawn.

2

Theoretical background and methods

2.1 Properties of group-III sesquioxide polymorphs

In this section, the structural properties, stability and synthesis routes of the various group-III sesquioxide polymorphs will be summarized. The properties of the most relevant polymorphs are collected in Table 2.1 at the end of the section.

2.1.1 The ground-state polymorphs

Even though the three sesquioxides Al_2O_3, Ga_2O_3 and In_2O_3 are isovalent, they have different thermodynamically stable crystal structures. Later will be described what drives the phase stability in these systems. Here, we summarize the properties of the stable phases, which are hexagonal (corundum) α-Al_2O_3, monoclinic β-Ga_2O_3 and cubic bixbyite c-In_2O_3. The model structures of each of the phases are represented in Fig. 2.1 in a few relevant projection orientations.

β-Ga_2O_3

β-Ga_2O_3 is the most stable polymorph of Ga_2O_3. It has been shown by Roy *et al.* [25] and Playford *et al.* [26] that all other polymorphs (α, γ, δ, ϵ, κ) transform to the β-polymorph after heating to sufficiently high temperature. It has a monoclinic crystal structure with space group $C2/m$, lattice parameters $a = 12.214$Å, $b = 3.0371$Å, $c = 5.7981$Å and monoclinic angle $\beta = 103.83°$ between the a and c axis [23]. The structure contains two types of cation lattice sites, which differ in their coordination to the neighboring oxygen atoms. As illustrated in Fig. 2.1(a), the blue Ga sites are octahedrally (six-fold) coordinated and the green Ga sites are tetrahedrally (four-fold) coordinated and there is an equal amount of them. Similarly, the oxygen atoms occupy three inequivalent lattice sites. O(I) and O(III) have three-fold coordination to the Ga atoms, while O(II) has four-fold coordination. The $(\bar{2}01)$ planes consist solely of octahedrally or tetrahedrally coordinated Ga atoms. β-Ga_2O_3 is the only polymorph of Ga_2O_3 that can be grown from the melt, with a melting temperature of $T = 1793°$. The Czochralski method [38, 63] is used to grow 2-inch crystals that can be used as substrates for epitaxial growth in different orientations. Literature shows that both homo- and heteroepitaxial growth of β-Ga_2O_3 is possible by a variety of growth methods such as metalorganic vapor phase epitaxy (MOVPE) [64–67],

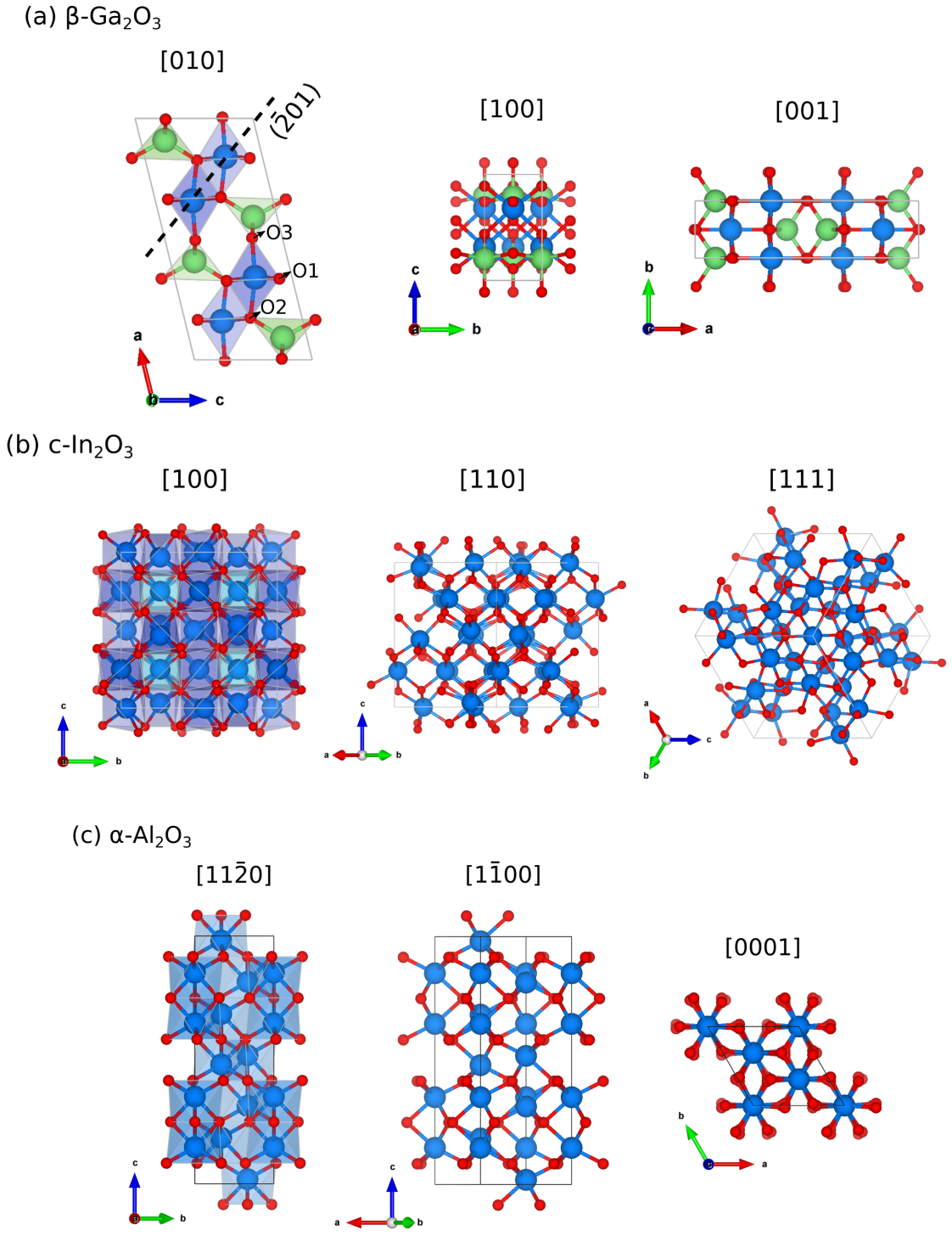

Figure 2.1: Model structures in relevant orientations of one unit cell of the (a) monoclinic $C2/m$, (b) cubic bixbyite $Ia\bar{3}$ and (c) hexagonal $R\bar{3}c$ lattices, which are the ground-state structures of β-Ga_2O_3, c-In_2O_3 and α-Al_2O_3, respectively. Green/blue balls and polyhedra represent tetrahedrally/octahedrally coordinated cations, red balls are oxygen. In the cubic bixbyite model in [100] projection (left) the difference between symmetric (dark blue) and distorted (light blue) octahedrons is highlighted.

halide vapor phase epitaxy (HVPE) [68, 69], chemical vapor deposition (CVD) [70, 71], molecular beam epitaxy (MBE) [72–74] and pulsed laser deposition [75–78] and the growth along different planes [(100), (010), (001) and $(\bar{2}01)$] is investigated.

c-In_2O_3

In_2O_3 crystallizes in the cubic bixbyite structure with space group $Ia\bar{3}$. This specific polymorph will be indicated in this work as c-In_2O_3. The structure is identical to that of the C-type rare-earth oxides (R_2O_3) [79]. The large body-centered cubic unit cell is formed of 80 atoms and has a lattice parameter of $a = 10.117$Å [24]. c-In_2O_3 can be regarded as a defective and distorted $2 \times 2 \times 2$ superstructure of the fluorite structure where 1/4th of the anions, i.e. oxygen atoms here, have been removed [80, 81]. All indium atoms are octahedrally coordinated with respect to oxygen and distributed over symmetrical and distorted octahedral lattice sites, as illustrated in Fig. 2.1(b). High quality indium oxide substrates were long not available and therefore c-In_2O_3 has been mainly grown by heteroepitaxy. Yttria-stabilized zirconia (YSZ) with the fluorite structure has been used as a substrate [82, 83], since its lattice constant ($a = 5.15$Å) fits to half that of In_2O_3. This results in a small effective misfit for 1×1 In_2O_3 growth on 2×2 YSZ. Since a few years, In_2O_3 crystals with high purity and low unintentional electron concentrations suitable for substrate preparation have been grown from the melt [84], which allow for homoepitaxy. Typical growth orientations are (001) and (111).

α-Al_2O_3

α-Al_2O_3, usually referred to as sapphire, has a hexagonal corundum crystal structure with space group $R\bar{3}c$. Its lattice parameters are $a = 4.760$Å, $c = 12.995$Å and $\gamma = 120°$ [22]. Oxygen atoms are arranged on a hexagonal close-packed sublattice, with aluminum atoms occupying 2/3 of the octahedral sites, as depicted in Fig. 2.1(c). Bulk growth of sapphire, which has a melting point of 2050°C, is achieved by a variety of methods [85–88]. α-Al_2O_3 is a hard and insulating material and is often used as a substrate for epitaxial growth.

2.1.2 Metastable and other polymorphs

Apart from the thermodynamically stable polymorphs, Al_2O_3, Ga_2O_3 and In_2O_3 also exist in the form of other metastable crystal structures.

The first investigations on the thermal stability of the different Ga_2O_3 polymorphs were done by Roy *et al.* [25] in 1952. They used gallia gels [1] and metallic gallium as starting materials to synthesize metastable α-, γ-, δ- and ϵ-Ga_2O_3 polymorphs, by applying a hydrothermal treatment (wet) or by heating in air in a platinum crucible (dry). Upon further heating to temperatures ranging from 300°C to 870°C, all phases underwent a phase transition to the thermodynamically stable β-modification. A more recent study by Playford *et al.* [26] presents in addition a detailed structural investigation of the up to then unknown γ-, δ- and ϵ-polymorphs. In this work, the different polymorphs are created by solvothermal oxidation, thermal decomposition or calcination followed by heating of metallic gallium or gallium nitrate. Fig. 2.2, adapted from Ref. [26], summarizes the chemical synthesis routes and phase transformations of the different polymorphs that

[1] Formed from an aqueous solution of gallium nitrate by adding ammonia and heating in the range of 0 – 50°C.

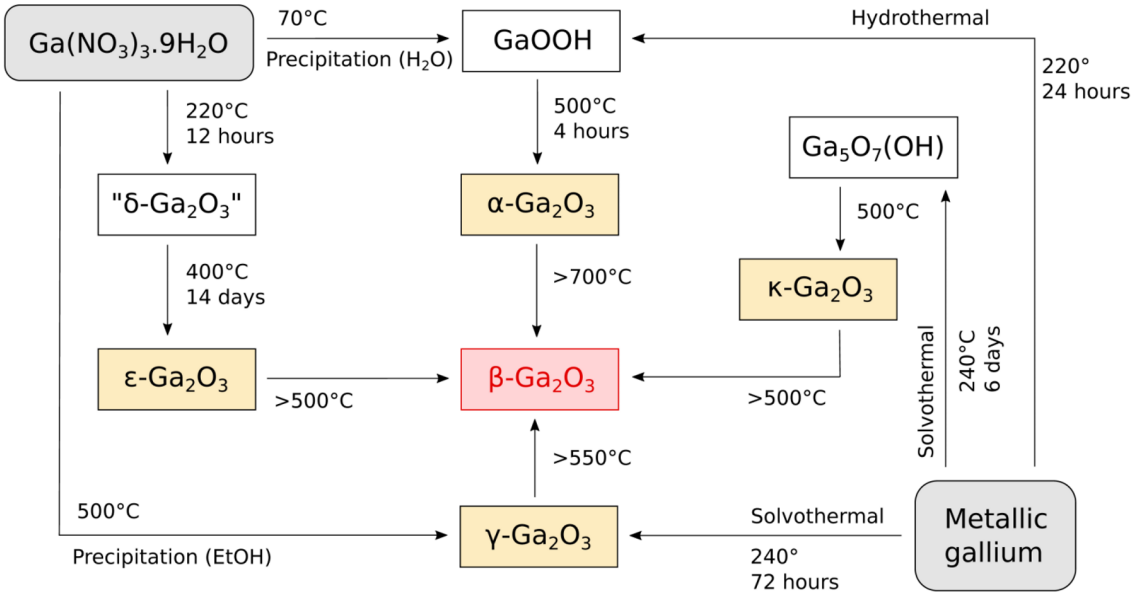

Figure 2.2: Schematic overview of the conversions of the different polymorphs of Ga_2O_3 as described by Playford *et al.* [26].

result from these processes. The details on the structure, synthesis/growth and stability of each polymorph will be summarized in the following sections.

In_2O_3 and Al_2O_3 exhibit polymorphism as well. The following metastable polymorphs have been experimentally established for In_2O_3: rhombohedral corundum-type rh-In_2O_3 ($R\bar{3}c$) [89,90], orthorhombic Rh_2O_3(II)-type o'-In_2O_3 ($Pbcn$) [91] and orthorhombic α-Gd_2S_3-type o''-In_2O_3 ($Pnma$) [92]. Al_2O_3 metastable polymorphs are monoclinic θ-Al_2O_3 ($C/2m$) [93] (same structure as β-Ga_2O_3), tetragonal γ-Al_2O_3 ($I4_1/amd$) [94] and orthorhombic κ-Al_2O_3 ($Pna2_1$) [95]. Since these polymorphs will not be of importance in this thesis, the structures will not be discussed in detail here.

α-Ga_2O_3

α-Ga_2O_3 ($R\bar{3}c$) has the same hexagonal symmetry and atomic positions as α-Al_2O_3 [shown in Fig. 2.1(c)], but with lattice parameters of $a = 4.983$Å and $c = 13.433$Å [96]. This results in a misfit of 4.7% and 3.4% along the a- and c-axes of sapphire, respectively. Due to the peculiarities of the glide system, α-Ga_2O_3 grows epitaxially on sapphire substrates with a critical thickness depending on the substrate orientation. Most investigations have been done on c-sapphire, where it is observed that three monolayers of α-Ga_2O_3 can be pseudomorphically stabilized before the layer transforms to β-Ga_2O_3 [97]. This observation is independent on the growth method used, i.e. MBE, MOVPE or PLD. Another study of MBE grown films, however, shows that relaxed α-Ga_2O_3 with a critical thickness of approximately 33 nm can be obtained on c-sapphire [96]. Also, on a- and m-plane sapphire substrates, the growth of single-phase α-Ga_2O_3 has been demonstrated [96, 98, 99]. In Playford's work [26], α-Ga_2O_3 is synthesized by heating of gallium oxyhydroxide GaOOH[2] for 4 hours at 500°C. A transformation from α- to β-phase is observed for temperatures higher than 700°C. For epitaxial layers grown by mist CVD [100], α-Ga_2O_3

[2]To produce GaOOH, gallium nitrate hydrate was dissolved in distilled water and diluted with concentrated aqueous ammonia. The solution was left to stand overnight, and then the fine white precipitate produced was collected by vacuum filtration and dried at 70°C overnight to leave GaOOH as the product.

starts to be unstable at 550°C and a full transition to β-phase was observed at 700°C. The reverse transition from β- to α-phase is possible under high pressure due to the higher density of the latter [101].

γ-Ga_2O_3

The γ-polymorph, which exists also for Al_2O_3 [102], is the defective cubic spinel structure of space group $Fd\bar{3}m$, with a lattice constant of $a = 8.224$Å. The structure has been studied in detail by Playford *et al.* [26, 103] by Rietveld refinement using neutron diffraction data. It is found that gallium is distributed over four different lattice sites with partial occupancy: two tetrahedral (8a and 48f) and two octahedral sites (16d and 16c). The ratio of octahedral to tetrahedral occupancy is 1.35:1. A complete statistical distribution of the gallium atoms on each site is excluded due to unphysically short Ga-Ga distances[3] (< 2.4Å) that might occur in that case. An average structure of one unit cell in which each cation position is assigned a statistical occupancy from Rietveld refinement is presented in Fig. 2.3(a). Almost all γ-Ga_2O_3 presented in literature has been produced by solution methods [25, 104, 105] with gallia gel, metallic gallium or gallium nitrate hydrate [$Ga(NO_3)_3 \cdot 9\ H_2O$] as starting product; epitaxy has been very rarely reported [106, 107]. The γ-phase easily collapses to β-phase under heat treatment at a temperature of 550°C, as reported by Playford *et al* [26], or 650°C, as reported by Roy *et al* [25].

ϵ-Ga_2O_3

ϵ-Ga_2O_3, as shown in Fig. 2.3(b), was first reported by Roy *et al.* [25] and exhibits the hexagonal $P6_3mc$ space group. The gallium atoms are distributed with partial occupancy over two octahedral and one tetrahedral lattice site with an occupation ratio of octahedral to tetrahedral of 2.2:1. The oxygen atoms are arranged on a close-packed hexagonal lattice according to ABAC stacking. The lattice parameters are $a = 2.9036$Å and $c = 9.2554$Å. Playford *et al.* [26] prepared ϵ-Ga_2O_3 by the prolonged heating of gallium nitrate hydrate at 400°C. At temperatures higher than 500°C, the ϵ-phase becomes unstable and transforms into the β-phase. Based on structural data form X-ray diffraction, several authors claimed to have grown ϵ-Ga_2O_3 on c-sapphire substrates by metalorganic chemical vapor deposition (MOCVD) [108, 109], atomic layer deposition [108] and HVPE [109]. A detailed TEM study by Cora *et al.* [110], however, shows that these layers consist of nm-sized rotational domains of the orthorhombic κ-phase (discussed below). In case of characterization techniques that integrate over a number of these rotational domains (such as X-ray diffraction), the structure effectively mimics the higher symmetry of $P6_3mc$, which is the reason for the confusion.

κ-Ga_2O_3

The κ-polymorph has the orthorhombic symmetry and space group $Pna2_1$, with lattice parameters $a = 5.0463$Å, $b = 8.70209$Å and $c = 9.2833$Å [110]. The ratio of cations that are octahedrally coordinated to those that are tetrahedrally coordinated is 3:1. The structure, as depicted in Fig. 2.3(c), is the gallium analogue of κ-Al_2O_3 [95]. It was first reported

[3] The distance between two atoms becomes unphysically short when their wave functions (more specifically the inner shells of the atoms) start to overlap. Since Pauli's principle forbids two electron to be in the same state, the energy costs to occupy higher energy shells results in a repulsive interaction.

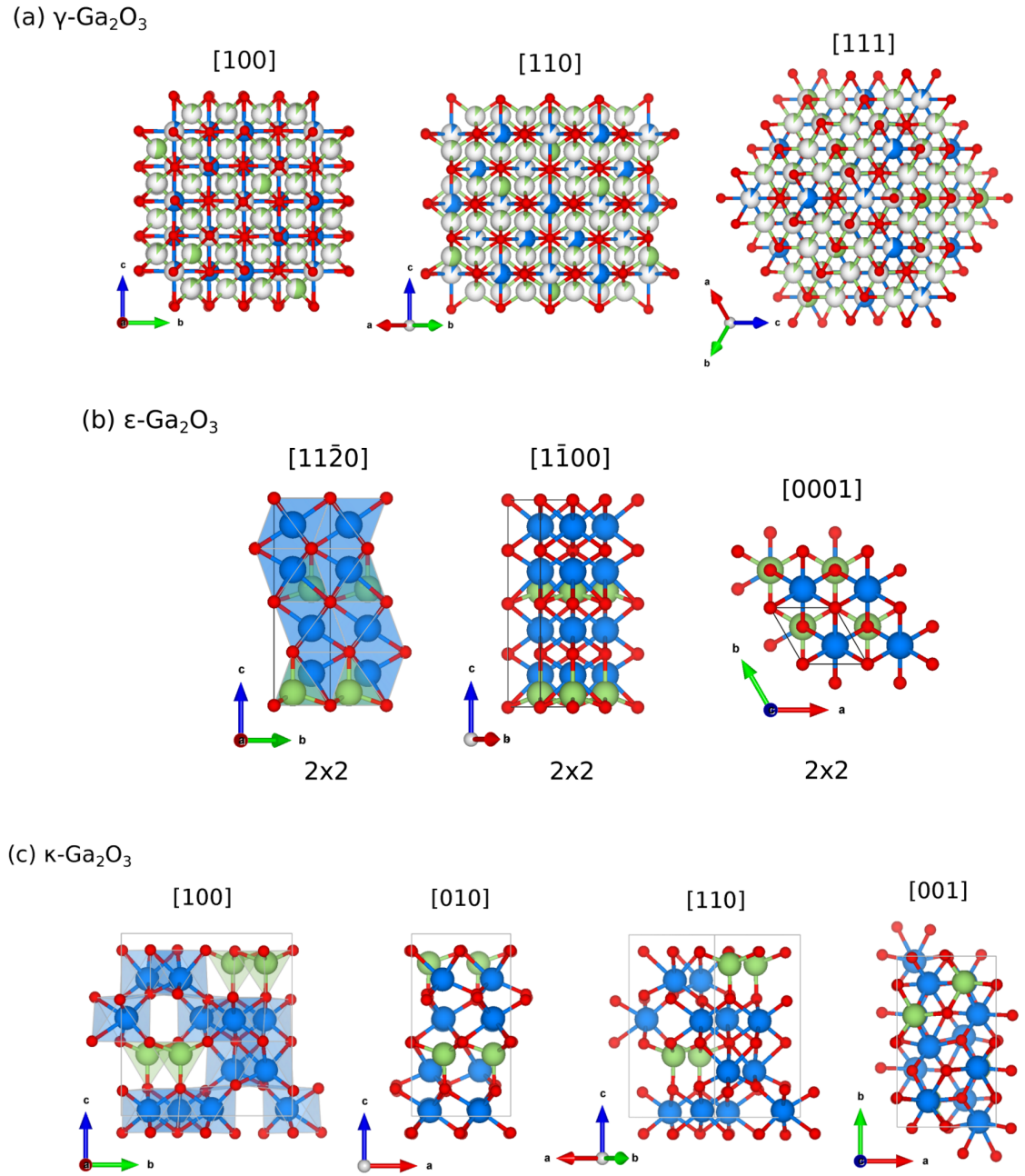

Figure 2.3: Model structures in relevant orientations of one (or multiple) unit cell(s) of the (a) cubic spinel $Fd\bar{3}m$, (b) hexagonal $P6_3mc$ and (c) orthorhombic $Pna2_1$ lattices of $\gamma-$, ϵ- and κ-Ga_2O_3, respectively. Green/blue balls and polyhedra represent tetrahedrally/octahedrally coordinated cations, red balls are oxygen.

by Playford *et al.* [26], who synthesized it by the thermal decomposition of Ga-tohdite [$Ga_5O_7(OH)$], the product of a solvothermal treatment of metallic gallium, at 240°C. They observed the transition from κ- to β-phase at a temperature of 500°C. A detailed structural investigation of the κ-polymorph by Cora *et al.* [110] showed that it corresponds to a derivative of ϵ-Ga_2O_3 with the gallium vacancies being ordered instead of being statistically distributed. Up to now the κ-phase has been observed to consist of small rotational domains (< 10 nm in width) and therefore is easily mistaken for ϵ-Ga_2O_3, when analyzed by spatially integrating methods. Epitaxial κ-Ga_2O_3 films have been grown mainly by PLD [111] and MOCVD [108] and a transition to the β-phase is observed by Fornari *et al.* [112] at a temperature in the range of 880°C–920°C.

δ-Ga_2O_3

Originally, Roy *et al.* [25] presented first results on δ-Ga_2O_3, which they identified as Ga_2O_3 with cubic bixbyite structure with the same space group ($Ia\bar{3}$) as In_2O_3 [see Fig. 2.1(b)] and a lattice constant of 10Å. These authors synthesized it as the initial product of thermal decomposition of gallium nitrate [$Ga(NO_3)_3$] at 250°C. The material consisted of particles with sizes ranging from 20 – 50 nm. Later, Playford *et al.* [26], following the same synthesis route, could prove that the poorly crystalline material 'δ-Ga_2O_3' was wrongly classified as a distinct polymorph. Their neutron diffraction data showed that it is rather a nanocrystalline two-phase mixture of hexagonal ϵ-Ga_2O_3 and β-Ga_2O_3. Prolonged heating of this material at 400°C results in ϵ-Ga_2O_3; further heating to temperatures higher than 500°C results finally in β-Ga_2O_3.

h-$InGaO_3$

A hexagonal polymorph of the $(In_xGa_{1-x})_2O_3$ solid solution with space group $P6_3mmc$, of which the lattice is shown in Fig. 2.4, has been experimentally reported by Shannon and Prewitt [53]. It is the first structure reported that contains Ga^{3+} in five-fold coordination. The lattice parameters of the hexagonal unit cell are a = 3.310Å and c = 12.039Å. It contains an equal amount of five- and six-fold coordinated cation positions, which are stacked in form of alternating layers on the < 0001 > planes as can be seen in the [$11\bar{2}0$] and [$1\bar{1}00$] projections in Fig. 2.4. According to Shannon and Prewitt [53], h-$InGaO_3$

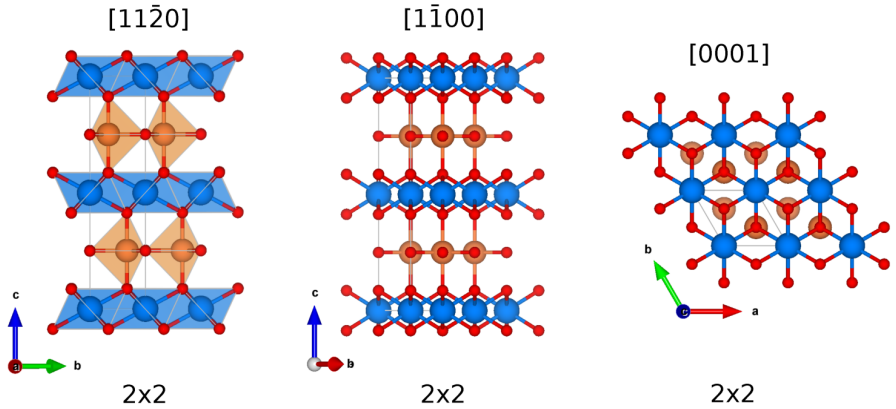

Figure 2.4: Hexagonal $P6_3/mmc$ model structure of one unit cell of h-$InGaO_3$. Orange/blue balls and polyhedra represent five-fold/six-fold (octahedrally) coordinated cations, red balls are oxygen.

(they labeled it as $InGaO_3$ II) is a high-pressure phase. They synthesized it by mixing Ga_2O_3 and In_2O_3 in a 1:1 ratio and applying high pressure (15-65 kbar) and high temperature (T=1200°C). This resulted in h-$InGaO_3$ [i.e. $(In_xGa_{1-x})_2O_3$ with $x = 0.5$] with indium atoms occupying the six-fold positions and gallium atoms occupying the five-fold positions. The h-phase shows remarkable stability up to temperatures of 1020°C under ambient conditions. Epitaxial growth of this phase has been reported by von Wenckstern *et al.* [49], using pulsed laser deposition at a temperature of 650°C. It is interesting to note that this polymorph has not been observed for the binary compounds Ga_2O_3 and In_2O_3.

2.1.3 Origin of the structural diversity in group-III sesquioxides

The observed structural diversity of the ground-state crystal structures of Al_2O_3, Ga_2O_3 and In_2O_3 is unlike other well-known semiconductor compounds such as arsenides (MAs) and nitrides (MN) that for M = Al, Ga, In all adopt the same crystal structure: zincblende and wurtzite, respectively. These structures both have only tetrahedral coordination of the cations and the stability of the one over the other for bonding to N ($Z = 7$) or As ($Z = 33$) can be fully attributed to the atomic radius of the anion and the resulting ionicity of the bonding [113].[4] Due to the different stoichiometry in group-III oxides, other lattice structures come into play, which possess different types of coordination environments, which plays an important role in the stability. Two separate DFT-based investigations by Sabino *et al.* [114] and Ma and Wei [115] found out that it is the interplay of the cation radius and the orbital interaction between the cat- and anions in the corundum, monoclinic and cubic bixbyite structures that controls the stable phase, although different arguments are discussed.

In Sabino's work, it is argued, based on a space-filling consideration previously reported in Ref. [116], that oxides with smaller cations crystallize in the corundum structure, while oxides with larger cations crystallize in the bixbyite structure. This is contradicted by Ma and Wei, who show that the Coulomb interaction stabilizes the monoclinic structure for small cations. In the monoclinic structure, tetrahedral sites exist at which the cation-anion bond length is the shortest among all bonds in the three structures. Therefore, the energy gained by the Coulomb interaction, which increases for smaller bond lengths and thus for smaller cation sizes, increases most significantly in the monoclinic structure for small cations like Al and Ga, and decreases the most for a large cation like In. Comparing the corundum and bixbyite structures, which both have only octahedral cation sites, the average cation-anion bond length in the bixbyite structure is the highest. Therefore, for larger cations like In, the bixbyite phase is found to have the lowest Coulomb energy.

A second factor determining the relative stability is the energy separation of the cation valence electrons and the oxygen $2p$ states, which determines the ionicity of the bonding. Ga atoms have the highest valence electron energies, and thus are the most covalently bonded, while Al and In have lower valence electron energies, such that electrons are more easily attracted by the neighboring O, resulting in more ionic bonds. Since covalent materials can gain more orbital interaction energy from tetrahedral bonds, the monoclinic lattice is preferred for Ga_2O_3 in this regard as well. The more ionic Al and In oxides on the other hand, give a stronger preference to the corundum or cubic bixbyite structure.

[4] Nitrogen, with its smaller atomic radius, pulls harder on the electrons (because they sit closer to the nucleus) than arsenic, and thus the bonding type with nitrogen is more ionic. Since the Madelung constant, which is a measure for the ionicity of the bonding, for wurtzite is slightly larger than for zincblende, the more ionic the compound, the more it will prefer the wurtzite lattice.

Table 2.1: Structural properties and stability of relevant group-III sesquioxide polymorphs.

Phase	Space group	a (Å)	b (Å)	c (Å)	α	β	γ	Cation coordination	Stability	References
α-Al_2O_3	$R\bar{3}c$	4.760	4.760	12.995	90°	90°	120°	6-fold only	Stable	[22]
α-Ga_2O_3	$R\bar{3}c$	4.983	4.983	13.433	90°	90°	120°	6-fold only	>700°C $\rightarrow \beta$	[25, 26, 96, 117] [97, 100]
β-Ga_2O_3	$C2/m$	12.214	3.0371	5.7981	90°	103.83°	90°	4:6-fold 1:1	Stable	[23, 25, 26, 36, 118]
γ-Ga_2O_3	$Fd\bar{3}m$	8.224	8.224	8.224	90°	90°	90°	4:6-fold 1.35:1	$>550/650$°C $\rightarrow \beta$	[25, 26, 103, 104]
ϵ-Ga_2O_3	$P6_3mc$	2.9036	2.9036	9.2554	90°	90°	120°	4:6-fold 2.2:1	>500°C $\rightarrow \beta$	[25, 26, 108, 109]
κ-Ga_2O_3	$Pna2_1$	5.0463	8.7021	9.2833	90°	90°	90°	4:6-fold 3:1	>500°C $\rightarrow \beta$	[26, 110–112]
h-$InGaO_3$	$P6_3mmc$	3.310	3.310	12.039	90°	90°	120°	5:6-fold 1:1	Stable up to 1020°C	[49, 53, 119]
c-In_2O_3	$Ia\bar{3}$	10.117	10.117	10.117	90°	90°	90°	6-fold only	Stable	[24]

Additionally, it is stated by Sabino *et al.* [114] that energy gained from the hybridization due to the energy overlap between the cation valence *d* states (which are absent in Al) and the oxygen *s* states, is maximized for cations in a four-fold coordination environment.

From this overview, it is clear that the stability is the result of a complex interplay of different Coulomb and orbital interaction energy contributions. Taking all of them into account results, in the end, in an agreement with the experimentally observed stabilities of corundum Al_2O_3, monoclinic Ga_2O_3 and cubic bixbyite In_2O_3.

2.2 Miscibility theory in solid solutions

2.2.1 Basic thermodynamic considerations

The system we are studying, $(In_xGa_{1-x})_2O_3$, is a mixture of two crystalline solids, Ga_2O_3 and In_2O_3, that coexist and form a new crystalline solid of composition x. To understand the miscibility and solubility limits in our system, we must define the thermodynamics of such a solid solution. The total energy of the mixture is defined by the Gibbs free energy as

$$G_m = H_m - TS_m \tag{2.1}$$

where H_m is the mixing enthalpy, S_m is the mixing entropy and T is the temperature. Let's start with the discussion for an ideal isostructural solid solution system, where the two components have exactly the same crystal structure. In that case, by applying the regular solution model [120], the mixing enthalpy at $T = 0$ can simply be defined as

$$H_m = \Omega x(1-x) \tag{2.2}$$

with Ω the so-called interaction parameter that is specific to each system. Plotting H_m versus x will show a concave parabola with a maximum at $x = 0.5$ and minima at the binary compositions. An example of such a case is $In_xGa_{1-x}N$, as described by Ho and Stringfellow [15], where both GaN and InN adopt the same zincblende crystal structure. The mixing entropy is independent of temperature and in the regular/ideal solid solution model defined as

$$S_m = -k_B[x\ln(x) + (1-x)\ln(1-x)] \tag{2.3}$$

with k_B the Boltzmann constant. The entropy term is maximized at $x = 0.5$, where the highest amount of disorder is present in the mixture. With both contributions to the free energy defined, we can understand its behavior as a function of composition and temperature as plotted in Fig. 2.5 for a model system. As the temperature increases, the free energy decreases due to the entropy term and the shape transforms from concave to convex for all x.

The miscibility in isostructural systems is typically limited by binodal and spinodal decomposition, which correspond to the limits of thermodynamic solubility and stability against composition fluctuations, respectively. From thermodynamics, the binodal and spinodal limits are determined by the zero points of the first and second derivative of G with respect to x, respectively. For $\frac{d^2G}{dx^2} < 0$, i.e. inside the spinodal line, the mixture is unstable and will phase separate into two coexisting phases, which add up to the lowest G. This process of spinodal decomposition happens spontaneously because small composition fluctuations immediately lower the free energy. The decomposition typically

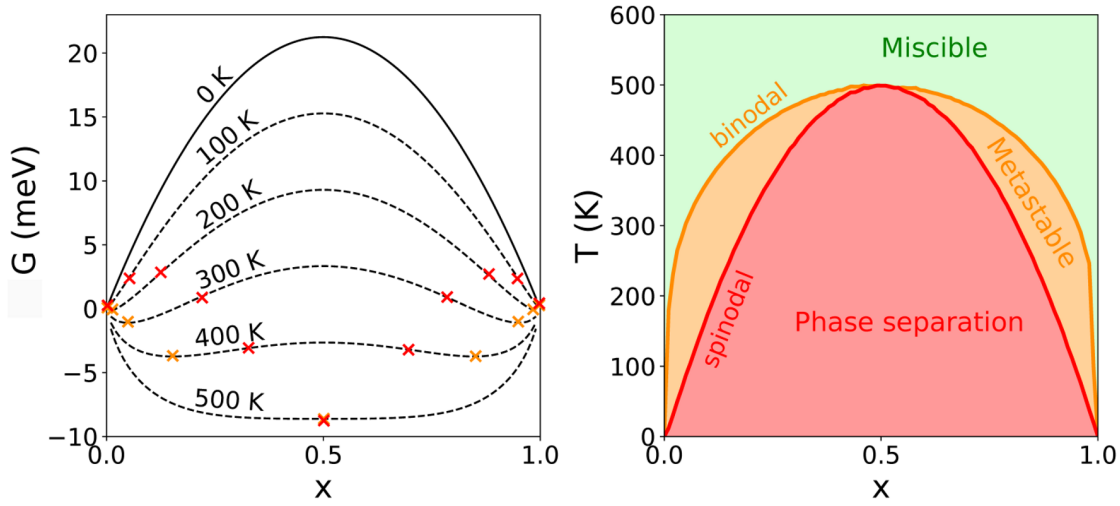

Figure 2.5: Left: Free energy of mixing according to the regular solution model as a function of composition for different temperatures, with binodal (orange) and spinodal (red) limits indicated for each temperature. Right: The corresponding phase diagram constructed using the binodal and spinodal lines.

takes place on a small length scale so that nanoscale regions of phases with different compositions can be expected. The separation can be kinetically forbidden if diffusion in the system is not possible. For the small region in between the binodal $\left(\frac{dG}{dx} = 0\right)$ and spinodal $\left(\frac{d^2G}{dx^2} = 0\right)$ lines, the system is metastable. This means that the mixture is stable against small composition fluctuations, but for a larger disturbance or on a large time scale also phase separation should be expected. This process of binodal decomposition happens via nucleation and growth. Only by overcoming a nucleation barrier, a nucleus of a large enough size of the low-energy phase is created and can start to grow freely. The other compositions for which $\frac{d^2G}{dx^2} > 0$ are stable. For temperatures above the critical point in the phase diagram, which is the point where the binodal and spinodal come together, the system is fully miscible. For the example of $In_xGa_{1-x}N$ mentioned above, the phase diagram looks similar to the one of the isostructural model system we depict here in Fig. 2.5 and the interaction parameter is found to be $\Omega = 5.98$ kcal/mole, which results in a critical temperature for miscibility of 1250°C [15]. At the maximum growth temperature used for $In_xGa_{1-x}N$ of 800°C, the InN solubility in GaN is calculated to be less than 6% [15].

2.2.2 Computational methodology for $(In_xGa_{1-x})_2O_3$ phase diagram

In the case of a heterostructural solid solution, like $(In_xGa_{1-x})_2O_3$, the picture described above becomes more complicated. Due to the different stable structures of both compounds, multiple free energy curves have to be considered and a phase transition has to take place at a certain composition. A computational study by Holder *et al.* [121] of heterostructural solid solutions (e.g. $Mn_{1-x}Zn_xO$, $Sn_{1-x}Ca_xS$) showed that this leads to phase diagrams that look markedly different from the isostructural phase diagram in Fig. 2.5. They exhibit large metastable composition regions and no critical temperature can be defined.

With respect to the computational method of choice, other difficulties, which are more

specific to our system, must be taken into account. In contrast to the rather simple crystal symmetries (wurtzite and zincblende) in arsenides or nitrides, the crystal structures in oxides have lower symmetry and large unit cells, e.g. the bixbyite lattice with a 80-atom unit cell. Additionally, as seen in the previous section, different types of coordination environments of the cations with respect to oxygen exist within and between the different oxide structures. Therefore, the stability of these various phases is determined by the relative energy of the specific arrangement of the individual atoms on the given lattice type and it is important to consider the different lattice configuration possibilities at each composition. For a substitutional solid solution involving the mixture of two atoms, there are approximately 2^N possible configurational states (without considering the possibility of duplicate configurations because of symmetry), where N is the number of atoms in the unit cell. Density functional theory methods, for which the computational time scales as $N^3 - N^4$, are very limited to examine such a large combinatorial space. Instead, first-principles based cluster expansion models offer a computationally efficient protocol to examine the vast configurational space of substitutional solid solutions.

In the following, we describe the computational procedure used to construct the phase diagram for $(In_xGa_{1-x})_2O_3$, which was done as a joint effort with Christopher Sutton, Dr. Luca Ghiringhelli and Prof. Dr. Matthias Scheffler from the Fritz Haber Institute in Berlin in the framework of our collaboration within GraFOx. First, the basic principles of density functional theory and the cluster expansion method will be described. These methods were combined to scan the large configurational space of the $(In_xGa_{1-x})_2O_3$ lattices and to determine the lowest energy configurations. Next, the calculated quantities needed to construct the temperature dependent phase diagram will be explained.

Density functional theory

Density functional theory (DFT) [122] is a computational method that derives ground-state properties of many-body systems, such as atoms, molecules and condensed phases. The complexity of solving the N-body Schrödinger equation to find the system's wave function is circumvented by assuming that the total energy of the system is a unique functional of the electron density. Since the electron density is a function of only three variables, the x-, y-, and z-position of the electrons, this simplifies the original ($3N$-dimensional) many-body problem significantly. Different approximations for the density functional exist, such as the local density approximation (LDA), which assumes a uniform electron density throughout the system, or the improved generalized gradient approximation (GGA), which additionally includes a dependence on the local density gradient. DFT allows to optimize an input lattice geometry by an energy optimization, from which structure properties such as the optimal atom positions and the relaxed lattice parameters can be deducted.

The DFT calculations in this work, were carried out using FHI-aims [123], an all-electron full potential electronic structure code with numeric atom-centered basis functions. Tight numerical settings were used and a k-grid density of 3 k-points/Å was set using the ASE[5] package [124] based on the convergence of the total energy. We compared two GGA functionals, PBE [125] and PBEsol [126], and selected PBEsol for this study because it gives the best accuracy for predicting lattice parameters in group-III oxide systems. The average absolute difference between the volume (normalized by the number

[5] Atomic simulation environment.

of cations) of the DFT-optimized structures and the ICSD[6] [127] reported structures (cards #34243, #27431, #187791, #425685 and #187792) of five experimentally reported Ga_2O_3 and In_2O_3 polymorphs is a factor of 3 lower for PBEsol compared to PBE. The PBEsol calculations are performed using the 80-atom supercell of the β-phase ($2 \times 2 \times 1$) and h-phase ($2 \times 2 \times 2$) and the 80-atom conventional unit cell of the c-phase.

Cluster expansion method

In the cluster expansion (CE) method, the total energy of the system for a certain configuration is expressed in terms of the occupation of each known atomic position in the crystal by the different chemical species. In the case of a crystal with M positions and two species A and B, the distinct configurations can be represented by a vector $\overrightarrow{\sigma}$ of size M with values +1 (i.e. occupied by A) or −1 (i.e. occupied by B) assigned to each lattice site. The energy of each configuration is then simply expressed as a function of this vector:

$$E_{conf} \equiv E(\sigma_1, \ldots, \sigma_M). \tag{2.4}$$

To compute $E(\overrightarrow{\sigma})$, a basis set of inequivalent interactions or 'clusters' should be defined that consist of a particular combination of atomic lattice sites (e.g. pairs, triplets, many-body interactions). In terms of such a basis of clusters α, the cluster expansion of the energy per lattice site can be written as

$$E_{CE}(\overrightarrow{\sigma}) = \sum_{\alpha} m_\alpha J_\alpha \overline{\Pi}_\alpha(\overrightarrow{\sigma}), \tag{2.5}$$

where each term is the product of the multiplicity m_α, the correlation matrix element $\overline{\Pi}_\alpha(\overrightarrow{\sigma})$[7] and the 'effective cluster interaction' (ECI) J_α (in units of eV) of cluster α. To find the best set of clusters and corresponding ECIs for a certain lattice, the energies of a few configurations are calculated at the DFT level. For a certain cluster set, the ECIs that minimize the error between the DFT calculated energies and the predicted energies from the CE model are computed. Also the predictability of the cluster set and corresponding ECIs can be tested by comparing the predicted energies of 'unknown' configurations to the DFT calculated energies. By the method of compressed sensing [128], the cluster set with the best accuracy and predictability can be found. A more detailed overview of the CE method and its application to computational materials science can be found in Ref. [129].

Constructing the phase diagram

For our problem, separate CE models were trained (as described above) for the β- (monoclinic), h- (hexagonal) and c- (cubic bixbyite) lattices, until a sufficient accuracy is obtained. Using the obtained ideal basis sets of clusters in Eq. 2.5, the CE energies of various lattice configurations at each composition, i.e. for different distributions of gallium and indium on the different lattice sites, are compared. The ground-state configurations at each composition x for each lattice type l are determined and re-computed by DFT using PBEsol.

[6] Inorganic crystal structure database.

[7] The correlation matrix $\overline{\Pi}_\alpha(\overrightarrow{\sigma})$ is a matrix with the configurations as rows and the clusters as columns, in which the value of each element is related to the probability of finding the cluster or 'pattern' α in the configuration $\overrightarrow{\sigma}$.

The mixing enthalpy relative to the stable binary phases for all lowest-energy structures is calculated by

$$\Delta H_l(x) = E\left[(\mathrm{In}_x\mathrm{Ga}_{1-x})_2\mathrm{O}_3\right]_l - xE\left[\mathrm{In}_2\mathrm{O}_3\right]_c - (1-x)E\left[\mathrm{Ga}_2\mathrm{O}_3\right]_\beta \tag{2.6}$$

where $E\left[\mathrm{In}_2\mathrm{O}_3\right]_c$, $E\left[\mathrm{Ga}_2\mathrm{O}_3\right]_\beta$ and $E\left[(\mathrm{In}_x\mathrm{Ga}_{1-x})_2\mathrm{O}_3\right]_l$ are the total energies per cation of the cubic (c) and monoclinic (β) binary systems and the mixed system in phase l, as determined by DFT. The entropy contribution to the free energy, consists of a configurational and a vibrational part. The configurational entropy $S_{\mathrm{config},l}$ is calculated using the equation for the entropy of mixing of an ideal mixture

$$S_{\mathrm{config},l}(x) = -N_l k_B\left[x\ln x + (1-x)\ln(1-x)\right] \tag{2.7}$$

where N_l is the number of sites available for mixing in lattice type l and k_B is the Boltzmann constant. We will see though, in Chapter 3, that this assumption has to be modified for the monoclinic and hexagonal lattices due to ordering on the cation sublattice. To calculate the vibrational entropy S_{vib} (independent of the lattice type) each atom (total N) is considered as a single-Debye-frequency oscillator and the mixture's Debye temperature $\Theta(x)$ is interpolated between those of the binary compounds, which are ≈ 730 K for $\mathrm{Ga}_2\mathrm{O}_3$ [130, 131] and ≈ 700 K for $\mathrm{In}_2\mathrm{O}_3$ [132]. In that case, we can apply [133]

$$S_{\mathrm{vib}}(x,T) = 3Nk_B\left[(1+n)\ln(1+n) - n\ln(n)\right] \tag{2.8}$$

with $n(x,T) = (\exp[(\Theta(x)/T) - 1])^{-1}$ as Planck's distribution. The Gibbs free energy for lattice l with composition x at temperature T is then calculated relative to the stable binary phases by

$$\Delta G_l(x,T) = G\left[(\mathrm{In}_x\mathrm{Ga}_{1-x})_2\mathrm{O}_3\right]_l - xG\left[\mathrm{In}_2\mathrm{O}_3\right]_c - (1-x)G\left[\mathrm{Ga}_2\mathrm{O}_3\right]_\beta \tag{2.9}$$

$$= \Delta H_l(x) - T[\Delta S_{\mathrm{config},l}(x) + \Delta S_{\mathrm{vib}}(x,T)]. \tag{2.10}$$

All quantities will be normalized to the number of cations.

To find the stable compounds at a certain temperature, the Gibbs free energy curves of the different lattices have to be considered together. It is not sufficient to define the binodal limits for each lattice separately by the condition $\frac{d\Delta G}{dx} = 0$ as in Fig. 2.5 for isostructural solid solutions. Instead, the stable compounds are found by identifying the set of compositions that form the global convex hull, which is the convex boundary of the two-dimensional plane of $\Delta G_l(x)$ and compositions x, as illustrated in Fig. 2.6 in the case of two lattices. If a given structure at a specific composition lies on the convex hull, then the material is considered thermodynamically stable. The limiting compositions on the convex hull versus temperature define the binodal line in the phase diagram, which is constructed for each phase separately.

Next to the thermodynamically stable compositions, we can define the metastable ranges in the phase diagram by the area between the binodals and the spinodals. The spinodal limits are defined as the points where the second derivative of the Gibbs free energy changes from positive to negative. Only the spinodal limits for the lowest energy phases are considered in the phase diagram.

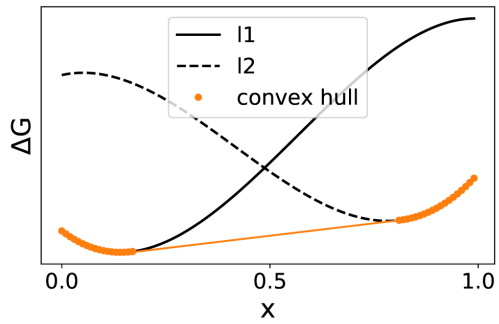

Figure 2.6: Convex hull construction to find the thermodynamically stable compositions in case of two lattices $l1$ and $l2$.

2.3 Growth methods

This section will give an overview of the epitaxial growth methods that were used to produce the studied samples. In our case, heteroepitaxy, i.e. growth of a crystalline layer on a foreign substrate, is done by pulsed laser deposition and molecular beam epitaxy. Samples labeled as pseudohomoepitaxial samples, in the sense that the crystal layer is grown on a substrate with the same crystal structure [e.g. β-$(In_xGa_{1-x})_2O_3$ on β-Ga_2O_3], are grown by molecular beam epitaxy and metalorganic vapor phase epitaxy.

2.3.1 Pulsed laser deposition

Pulsed laser deposition (PLD) is a physical vapor deposition growth technique that allows to prepare thin films of a variety of materials, and most commonly of oxides. The general set-up of a PLD chamber is shown in Fig. 2.7(a). A short pulse laser beam is focused on a ceramic target consisting of the material to be deposited. The photon energy of the laser heats up the surface of the target until it starts to melt and eventually to vaporize. Due to ionization of the vaporized material, the material is expelled from the surface as a plasma plume at high velocity. The plasma plume has a conical shape and consists of a mix of atoms, ions, molecules, and electrons. A big advantage of PLD is that the ablation of the target typically happens in a stoichiometric way (congruent ablation), though the stoichiometry of the resulting film may depend in detail on various parameters. When the plasma plume reaches the substrate surface, the material is deposited on the substrate as a thin film. Due to the high kinetic energy of the arriving particles, the growth can be performed at relatively low temperatures but the incoming ions may also cause some structural damage. In this work, samples having a continuous composition spread (CCS) [59] along a lateral direction are grown by PLD. In this approach, a two-fold segmented (A/B) ceramic target is rotating synchronously with the substrate. The point of incidence of the laser radiation on the target and the substrate center are positioned off-axis, such that a lateral shift ϵ exists between them, as illustrated in Fig. 2.7(b). In this way, the composition distribution of the film will mimic that of the target and continuously vary laterally across the sample. The target is also moved such that the circular race track of the laser has different radii to ensure an efficient and homogeneous ablation of the target surface. The process can be done in ultra high vacuum or in the presence of a gas with a controlled pressure. This can be a reactive gas such as oxygen for growing oxides, or a non-reacting gas such as argon or a mixture of them. Parameters such as laser fluence,

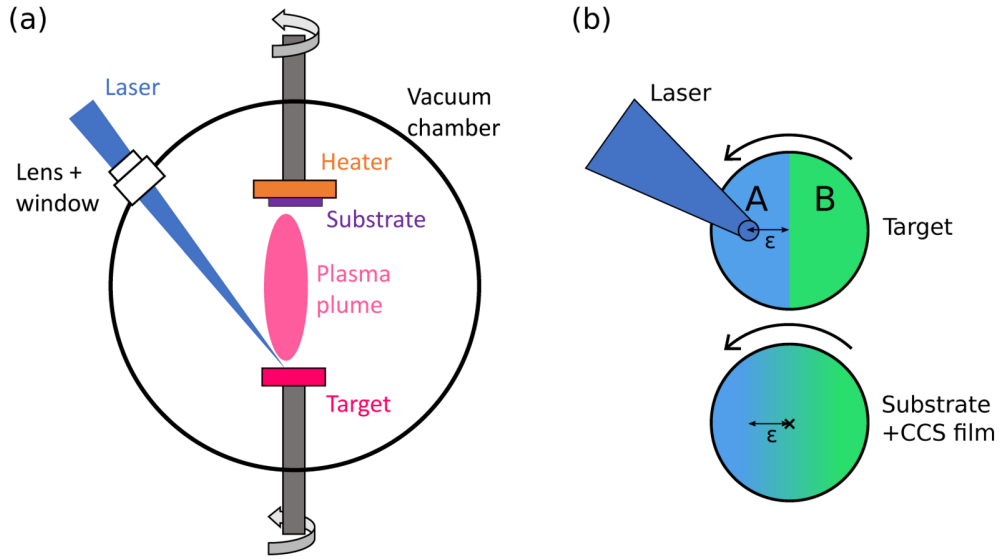

Figure 2.7: Schematic overview of (a) the basic elements of a PLD growth chamber, and (b) the continuous composition spread (CCS) approach to obtain films with a continuously laterally varying composition of two components A and B.

background pressure and substrate temperature will influence the properties of the grown film. To add dopants to the deposited film, the dopant element is admixed in the target with the desired composition.

The $(In_xGa_{1-x})_2O_3$ samples studied in this work are grown in the group of Dr. Holger von Wenckstern at the Felix Bloch Institute for Solid State Physics at the University of Leipzig. A two-fold segmented $(In_2O_3)/(Ga_2O_3)$ ceramic target is used, and the films are deposited on c-oriented sapphire substrates in an oxygen atmosphere. The growth temperatures are in the range $T_g = 640°C–680°C$ and the oxygen background pressure is set to $p(O_2) = 3 \cdot 10^{-4}$ mbar. Prior to deposition, the substrate is heated for about 45 minutes at the growth temperature. The CCS growth technique described above was employed to grow $(In_xGa_{1-x})_2O_3$ films with a continuously varying indium content with x-values in between $x = 0$ and $x = 0.87$. One film was grown with a cation share of 0.6 at% SnO_2 admixed to the $(In_2O_3)/(Ga_2O_3)$ target.

2.3.2 Molecular beam epitaxy

Similar to PLD, molecular beam epitaxy (MBE) is a physical vapor deposition technique. The deposition takes place in a ultra-high vacuum (UHV) chamber (10^{-8} - 10^{-12} mbar) and happens due to the interaction of a single or multiple molecular/atomic beam(s) with a heated substrate. The molecular beams are created by effusion cells, which consist of a radiatively heated crucible, the temperature of which is controlled by a close coupled thermocouple. In this way, the effusion cell acts as a stable and reproducible evaporation or sublimation source of a liquid or solid source material. The beam fluxes are measured as beam equivalent pressures (BEP) prior to deposition, by a nude ion gauge filament placed in the beam path. Due to the UHV environment, the beams will only interact with each other once they reach the substrate, which is positioned on a substrate heater that controls the growth temperature. On the substrate surface, the growth takes place atomic layer by layer. Since the growth is governed by surface kinetics at relatively low substrate

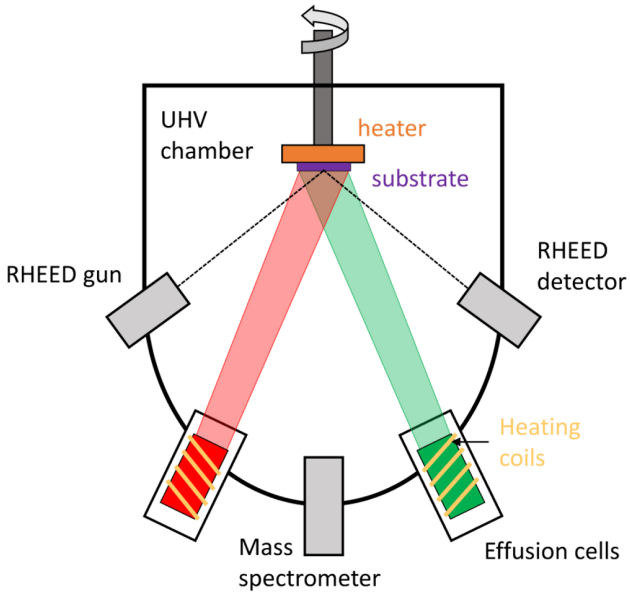

Figure 2.8: Schematic overview of the basic elements of a MBE growth chamber.

temperatures, the interdiffusion of the source materials or impurities can be kept to a minimum. Therefore, MBE is capable of producing extremely high purity and highly crystalline thin-film heterostructures with uniform compositions and sharp interfaces. On the other hand, growth rates are typically low in comparison to other growth techniques. An advantage of the high vacuum inside the growth chamber is that the growth can easily be monitored and controlled by in-situ measuring techniques like mass spectroscopy or reflection high energy electron diffraction.

The MBE samples investigated in this work have all been grown at the Paul-Drude-Institut für Festkörperelektronik in Berlin in the group of Dr. Oliver Bierwagen. For the growth of $(In_xGa_{1-x})_2O_3$ in the high-x bixbyite phase end, (111)-oriented yttria-stabilized zirconia (ZrO_2:Y or YSZ) kept at 600°C was used as substrate. A buffer layer of pure In_2O_3 with a thickness of approximately 40 nm has been grown between the substrate and the $(In_xGa_{1-x})_2O_3$ film. c-oriented sapphire has been used as a substrate for the growth of amorphous $(In_xGa_{1-x})_2O_3$ films at a substrate temperature of 100°C. The composition of the deposited films was tuned by varying the Ga and In BEP fluxes, which are controlled by the effusion cell temperatures. For the supply of mono-atomic oxygen, a radio-frequency plasma source run at 300 W was used.

2.3.3 Metalorganic vapor phase epitaxy

In contrast to PLD and MBE, which are physical deposition techniques, metalorganic vapor phase epitaxy (MOVPE)[8] is a chemical vapor deposition method. Precursor gases containing the desired species are transported into a reactor chamber through gas inlets, usually with the help of a non-reactive carrier gas. In there, they are guided to a heated substrate where a chemical reaction between the different molecules takes place. This results in the incorporation of the elements into a new epitaxial layer of the desired compound on the substrate surface. The substrate wafer is typically rotating slowly

[8] Also known as metalorganic chemical vapor deposition (MOCVD).

during the deposition process, such that a uniform distribution of the materials across the wafer is ensured. While the vapor to solid phase transition of the deposited species is driven by the thermodynamics of the reaction, the actual crystal growth is also governed by the kinetic processes of the ad-atoms or molecules on the growth surface. These processes involve adsorption, desorption, and diffusion of ad-atoms on the growth surface. It is important to tune these processes through an optimization of the MOVPE parameters to obtain the highest growth rate and the best crystalline quality of the films. In literature, many studies can be found on the optimization of homoepitaxy of β-Ga_2O_3 to obtain step-flow growth and defect-free layers [66, 67, 134–137].

$(In_xGa_{1-x})_2O_3$ MOVPE films studied in this work were grown by Dr. Saud Bin Anooz at the Leibniz-Institüt für Kristallzüchtung. Highly pure O_2 gas, triethylgallium and triethylindium were used as oxygen, gallium, and indium precursors, respectively, and highly pure Ar was used as carrier gas. The layers that were studied were grown on (100)-oriented β-Ga_2O_3 substrates with a miscut angle of 2° and were prepared from 2-inch diameter bulk crystals obtained by the Czochralski method [37]. The growth temperature and chamber pressure were set to 825°C and 5 mbar, as these conditions resulted in the highest crystalline quality and the highest amount of indium incorporation in the film [138].

2.4 Transmission electron microscopy

The main characterization technique employed in this work is transmission electron microscopy (TEM). The TEM is a very versatile instrument that offers a broad range of characterization techniques with high spatial and analytical resolution that can be applied to basically any type of material. In this section, we describe the basic set-up of a TEM and the basic principles of image and contrast formation for the different imaging techniques that will be applied to obtain the results. For a more in-depth description of TEM, we refer to the following textbooks by Williams and Carter [139], Fultz and Howe [140], Bethge and Heydenreich [141] and Pennycook and Nellist [142].

2.4.1 Basic principles of imaging

The basic principle of operation, i.e. magnifying the image of a small object using lenses, of a TEM is similar to that of a light microscope, although photons and optical lenses are replaced by electrons and electromagnetic lenses. In the TEM, high-energetic electrons are generated by an electron source and accelerated in an electric field. The electron beam is imposed on and transmitted through a thin specimen and shaped by electromagnetic lenses to produce an image on a detection screen. The path of the electron rays from source to screen is illustrated in Fig. 2.9. The spatial resolution of a microscope is determined by the focal length f and diameter D of the image forming lens and the wavelength λ of the radiation as given by Rayleigh's criterion

$$R = 1.22\frac{f\lambda}{D}, \tag{2.11}$$

and is thus inversely proportional to the energy of the radiation. While photons in the visible part of the spectrum have a limited and fixed energy range (1.65 – 3.26 eV), charged electrons can be accelerated to much higher energies such that a better resolution can

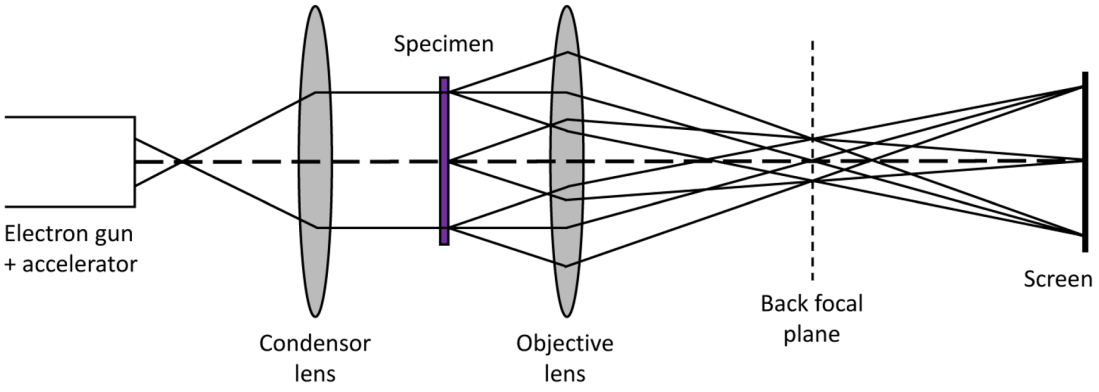

Figure 2.9: Schematic overview of the basic working principle of a TEM showing the paths of the electron rays. The horizontal dashed line denotes the optical axis of the microscope.

be obtained. The wavelength λ of a particle with momentum p is determined by the following relation according to de Broglie [143]:

$$\lambda = \frac{h}{p} \tag{2.12}$$

with h ($= 6.626 \cdot 10^{-34}$ J·s) being Planck's constant. In case of a typical electron microscope, the relativistic approximation for the momentum p should be used in the above formula, which results in [139]

$$\lambda_r = \frac{h}{\sqrt{\left[2m_0 eU\left(1 + \frac{eU}{2m_0 c^2}\right)\right]}} \tag{2.13}$$

with m_0 ($= 9.109 \cdot 10^{-31}$ kg) and e ($= 1.602 \cdot 10^{-19}$ C) the electron rest mass and elementary charge, respectively, and U the accelerating voltage of the microscope. In our case, an acceleration voltage of 300 kV was used, which results in a wavelength of 1.97 pm ($= 0.0197$Å).

As illustrated in Fig. 2.9, the condensor lens shapes the electron beam to get parallel illumination of the sample specimen. The parallel electron beam can be described as a plane wave Ψ_0:

$$\Psi_0(\vec{r}) = A_0 \exp\left[2\pi i \vec{k}_0 \cdot \vec{r}\right] \tag{2.14}$$

where A_0 is the wave amplitude and $\vec{k}_0$ the wave vector for which $|\vec{k}_0| = 1/\lambda$. The wave is then transmitted through the electron transparent sample. The interaction of the beam with the sample consists of multiple processes like coherent elastic scattering, incoherent quasi-elastic scattering and inelastic scattering of the beam electrons. Inelastically scattered electrons have lost part of their energy to the specimen through e.g. atom ionization, phonon or plasmon excitation. The spectroscopic detection of the energy loss of the inelastically scattered electrons (electron energy loss spectroscopy) or the characteristic x-rays emitted following the excitation of atoms (energy dispersive x-ray spectroscopy, EDXS) can give useful information on the composition of the sample material. Elastically scattered electrons, on the other hand, for which the energy and thus the wavelength is unchanged, will mainly contribute to structural imaging. The amplitude and the phase of the incident electron wave are modified, and the resulting object wave contains the

full information on the specimens projected potential. The incoming electron wave is diffracted by the periodic potential of the crystalline specimen into different waves, each with a specific wave vector $\vec{k}_g$. Therefore, considering only elastic scattering, the exit wave can be described as a sum of Fourier waves, according to [141]

$$\Psi_{\text{exit}}(\vec{r}) = \sum_g \Psi_{k_g}(\vec{r}) = \sum_g A_g \exp\left[2\pi i\left(\vec{k}_g \cdot \vec{r} + \phi_g\right)\right] \tag{2.15}$$

with A_g and ϕ_g the amplitude and phase offset of each diffracted wave, respectively. Each diffracted wave vector $\vec{k}_g$ is connected to the initial wave vector $\vec{k}_0$ by a reciprocal lattice vector $\vec{g}$ of the crystalline specimen, following the Laue condition:

$$\vec{k}_g = \vec{k}_0 + \vec{g}. \tag{2.16}$$

Since for elastic scattering $|\vec{k}_g| = |\vec{k}_0|$, all $\vec{k}_g$ can be found by the points were the so-called Ewald sphere[9] intersects a lattice point in reciprocal space. This relation in reciprocal space is equivalent to the well-known Bragg's equation

$$2d\sin(\theta) = n\lambda, \tag{2.17}$$

which describes diffraction from a set of lattice planes (defined by specific hkl Miller indices) in real space. In this equation, θ is the scattering angle, n is an integer and d ($= 1/|\vec{g}|$) is the lattice spacing of the diffracting lattice planes. Both Bragg's law and the Laue condition with the 2D projected Ewald sphere construction are illustrated in Fig. 2.10.

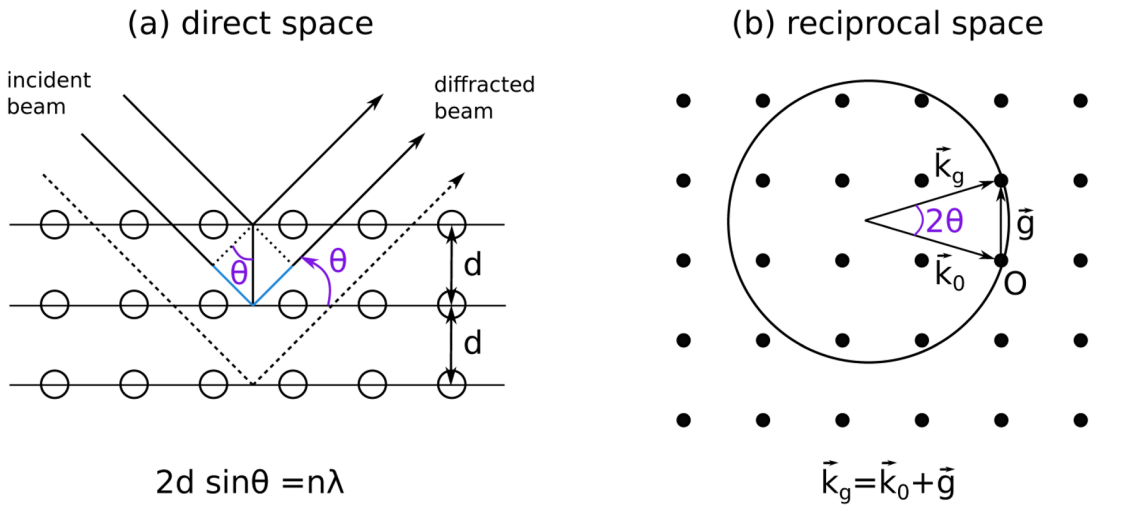

Figure 2.10: Schematic representation of plane wave diffraction on a crystal. (a) In real space, the scattering follows Bragg's law (Eq. 2.17), which states that the path length difference (in blue) of waves scattering on a set of parallel planes should equal a multiple of the wavelength of the rays. (b) This is equivalent to Laue's condition (Eq. 2.16) in reciprocal space, which is visualized using the (2D projected) Ewald sphere construction. O represents the origin of the lattice.

[9] Ewald's sphere is constructed in reciprocal space with a radius equal to $|\vec{k}_0|$ and with the origin of the reciprocal lattice placed at the tip of $\vec{k}_0$.

Behind the sample, the direct and diffracted waves are focused by the objective lens. Electrons scattered in the same direction are focused in the back focal plane, forming the diffraction pattern, and electrons coming from the same point in the sample are focused on the image plane (see Fig. 2.9). In the back focal plane, the electron wave can be expressed by [141]

$$\Psi'(q) = \mathscr{F}\{\Psi_{\text{exit}}(\vec{r})\} \cdot T(q) \tag{2.18}$$

as the product of the Fourier transform of the exit wave function and the contrast transfer function $T(q)$ as a function of the spatial frequency q, which is for small scattering angles equal to θ/λ. The contrast transfer function describes the influence of the objective lens on the exit wave function, to which we will go in more detail in the next section. Using an aperture in the back focal plane, one can select the diffracted waves wanted to contribute to the image formation. The waves then fall onto the fluorescent detection screen or the CCD (charge couple device) camera where they interfere with each other to produce the final image. The wave function at the image plane is given by the inverse Fourier transformation of Eq. 2.18

$$\Psi_{\text{image}}(x, y) = \mathscr{F}^{-1}\{\Psi'(q)\}, \tag{2.19}$$

which inverts the coordinates back to real space. What we finally observe in the image is then the intensity which is equal to the modulus squared of the wave function:

$$I_{\text{image}}(x, y) = |\Psi_{\text{image}}|^2. \tag{2.20}$$

Contrast transfer function

The form of the electron wave function - and thus the information it carries - when it reaches the detection screen is not the same as the one just after exiting the specimen. By passing through the objective lens, it gets modified due to unavoidable lens aberrations. This alteration is mathematically comprised in the contrast transfer function (CTF) that was introduced in Eq. 2.18, and has a contribution of three terms as follows [139]

$$T(q) = A(q) \cdot E(q) \cdot \exp(i\chi(q)). \tag{2.21}$$

$A(q)$ is the aperture function, $E(q)$ is the envelope function and $\chi(q)$ the aberration function. The first modification comes from the aperture function, which cuts off all spatial frequencies q above a certain value. The reason for this is that waves with high scattering angles, and thus correspondingly high q, are focused outside of the imaging screen by the objective lens. The envelope function accounts for the attenuation of the electron wave due to limited coherence. By assuming no spatial decoherence (illuminating beam is parallel) and neglecting the influence of specimen drift and vibrations, the main contribution to the attenuation is the result of temporal decoherence. This in turn is a consequence of the chromatic aberration[10] of the lens in combination with the energy distribution (ΔE) of the emitted electrons and instabilities in the acceleration voltage (ΔV) and the lens currents (ΔI). The envelope function is then defined as [139]

$$E(q) = \exp\left[-\left(\pi\lambda\frac{\Delta}{2}\right)^2 q^4\right], \text{ with} \tag{2.22}$$

[10]Chromatic aberration of the lens causes electrons coming from the same point in the sample but with different energy to not be focused again in the same point.

$$\Delta = C_c \sqrt{\left(\frac{\Delta E}{E}\right)^2 + \left(\frac{\Delta V}{V}\right)^2 + 4\left(\frac{\Delta I}{I}\right)^2}, \tag{2.23}$$

where Δ is called the focal spread and C_c is the chromatic aberration parameter of the lens. Lastly, the aberration function $\chi(q)$ combines the effect of lens aberrations that cause a phase shift of the electron wave depending on q. The most important ones are the spherical aberration[11] and the defocus, and thus is $\chi(q)$ typically defined as [139]

$$\chi(q) = \pi\lambda q^2 \Delta f + \frac{\pi}{2}\lambda^3 q^4 C_s, \tag{2.24}$$

where Δf is the defocus and C_s the spherical aberration parameter of the objective lens. From equations 2.22 and 2.24, it is obvious that the largest attenuation and modification takes place for high q values, i.e. electron waves scattered to high angles. Therefore, both functions limit the achievable resolution of the electron microscope. The so-called 'information limit' of the microscope is typically defined as the spatial frequency where the envelope function has dropped to $1/e^2$. For our TEM, this value amounts approximately 12.5 nm^{-1}, which gives a minimum resolvable spacing of 0.8Å.

2.4.2 High resolution transmission electron microscopy

When the electron wave passes through the sample, both its amplitude and phase get modified. In the case of high resolution transmission electron microscopy (HRTEM), however, where one typically investigates thin samples, the amplitude is assumed constant and there is only a small change in the phase of the electron wave. The phase change varies spatially with the (x, y)-position in the sample and is proportional to the atomic potential of the crystal at this position. The exit wave can be written as [139]

$$\Psi_{\mathrm{exit}}(x, y) = \Psi_0 \exp(-i\sigma V_t(x, y)). \tag{2.25}$$

Here, $\sigma = \frac{\pi}{\lambda E}$ is called the interaction constant and

$$V_t(x, y) = \int_0^t V(x, y, z) dz \tag{2.26}$$

is the projected atomic potential for a specimen of thickness t. For very thin samples, the phase shift is so small that we can assume $\sigma V_t(x, y) \ll 1$. In that case, the exit wave function can be approximated by (also normalizing $\Psi_0 = 1$)

$$\Psi_{\mathrm{exit}}(x, y) \approx 1 - i\sigma V_t(x, y), \tag{2.27}$$

which is called the weak phase object approximation (WPOA) [139]. Ψ_{exit} now carries all the position dependent information about the atomic structure of the sample. On its way to the detection screen, where it interferes with itself to produce the phase contrast image, it passes through the objective lens where it gets modified by the CTF (Eq. 2.21) due to the lens aberrations, as discussed in the previous section. Thus, the image wave function has an additional q dependent phase modulation that 'blurs' the sample information. This

[11] Spherical aberration of the lens means that parallel rays or monochromatic rays coming from the same point are focused at different points depending on the position where they passed the lens. When the lens has negative(/positive) spherical aberrations, rays that pass through the center of the lens are focused more(/less) strongly than rays passing through the outer part of the lens.

makes that HRTEM images are typically not straightforward to interpret, e.g. maxima or minima in intensity do not always correspond to positions of atomic columns. Therefore, image simulations are required for a correct and quantitative analysis. When the weak phase object approximation applies and non-linear contributions to the HRTEM image formation process are neglected, the CTF that describes the phase modulation can be simplified to [139]

$$T_{\mathrm{WPOA}}(q) = A(q) \cdot E(q) \cdot 2\sin[\chi(q)]. \tag{2.28}$$

Ideally, the transfer function would be a constant up to a cut-off value of q. However, the equation above is a function of q that in addition strongly depends on the defocus Δf and the spherical aberration C_s through the aberration function $\chi(q)$ (Eq. 2.24).

For a 300 kV TEM operated at the optimal defocus, i.e. the focus at which the maximum of spatial frequencies is transmitted with a constant phase shift, which is called Scherzer defocus [144]

$$\Delta f_{\mathrm{Sch}} = -1.2\sqrt{C_s \lambda}, \tag{2.29}$$

and a C_s value of 1.2 mm, which is typical for a conventional TEM, the transfer function is plotted in blue in Fig. 2.11 on the left. We recognize the oscillating behavior caused by the $\sin[\chi(q)]$ term and the attenuation for increasing q due to the envelope function, which is also plotted separately in red. For spatial frequencies up to 5 nm^{-1}, the CTF doesn't change rapidly and has a value close to -1 for a broad range of frequencies. This means that over this range the wave function experiences an almost constant phase shift of $-\frac{\pi}{2}$, which results in a dark atom intensity contrast for thin samples (in the WPOA). For higher frequencies, the transfer function oscillates rapidly and the phase shift of the waves transferred through the objective lens quickly changes between positive and negative values. This gives rise to image artifacts which don't allow a direct interpretation of the image. Those image artifacts due to spherical aberration are most pronounced in HRTEM images of objects involving a large number of different spatial frequencies, like disordered materials or complex crystalline structures. The point where the CTF first crosses zero defines the minimal interpretable spacing and is commonly defined as the point resolution. Thus, for a conventional 300 kV microscope with $C_s = 1.2$ mm, the point resolution amounts 2Å, which is found by the inverse of the first zero-crossing at 5 nm^{-1}, indicated by the orange line in Fig. 2.11.

Additionally, the effect of contrast delocalization is limiting the available resolution in HRTEM imaging. It arises because of the bending of the isophase front emitted from a specific point in the sample due to the q-dependent phase shift obtained in the objective lens. As a result, the wave emitted by a single point in the specimen forms a delocalized wave at the image plane with a radius of delocalization given by [145]

$$R = \max\left|\frac{1}{2\pi}\frac{\partial\chi(q)}{\partial q}\right|, \text{ with } q \in [0, q_{\max}], \tag{2.30}$$

with $q_{\max}$ the information limit of the microscope. R is dependent on the change of the aberration function with q and amounts typically a few ångström for a conventional TEM.

Aberration corrected HRTEM

As we have just seen, the imaging resolution in HRTEM is limited by the aberrations of the lens system and especially by the strong spherical aberration of the objective lens.

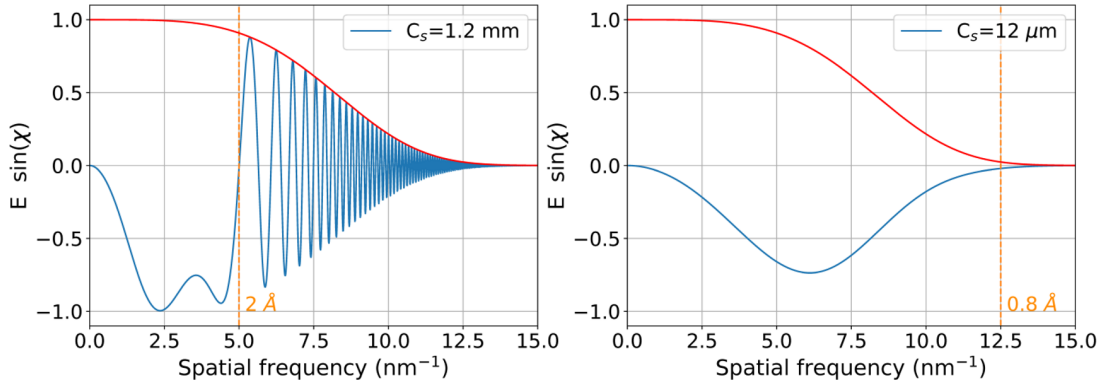

Figure 2.11: Contrast transfer function (in blue) as a function of spatial frequency q for TEMs with spherical aberration constants of C_s = 1.2 mm and C_s = 12 μm (aberration corrected) and operated at Scherzer defocus. The envelope function, for which a focal spread (Δ) of 4 nm is assumed, is plotted in red and the resolution limit (= $1/q$) in both cases is indicated in orange.

In optical microscopy, where the same type of lens aberrations exists, this problem is simply solved by the use of non-spherical dispersing lenses. For electromagnetic lenses, however, the solution is not so straightforward, as Otto Scherzer derived in 1936 [146] that "*Spherical and chromatic aberrations are unavoidable for static rotationally symmetric charged-particle lenses free of space charges*", known as Scherzer theorem. Therefore, Rose [147, 148] proposed the insertion of a multipole system in the optical path behind the objective lens that allows for correction of the spherical aberration. Such a corrector system can strongly reduce the spherical aberration coefficient and even tune it to negative values, which results in a more favorable contrast transfer. Moreover, it doesn't only correct the spherical aberrations but also higher order lens aberrations like axial coma, 3-fold and 4-fold astigmatism and star aberration. The corrector allows to reduce the resolution limit of the microscope to the sub-ångström regime as shown in Figure 2.11 on the left, where the transfer function is plotted for a 300 kV aberration corrected microscope with a spherical aberration of C_s = 12 μm and again operated at Scherzer defocus. There are no strong oscillations as were observed for an uncorrected microscope with high C_s values and the first zero-crossing is only reached at approximately q = 12.5 nm^{-1}, which equals the information limit. This gives a resolution limit of 0.8Å. Also the delocalization radius (defined in Eq. 2.30) is strongly reduced due to the aberration correction to an approximate value of 0.6Å.

The improvement in resolution due to aberration correction is illustrated in Fig. 2.12. The left and middle images show simulated HRTEM images of a 7 nm thick α-Al_2O_3 structure at Scherzer defocus in case of an uncorrected and corrected TEM with C_s = 1.2 mm and C_s = 12 μm, respectively. These cases correspond to the transfer functions as in Fig. 2.11 left and right, respectively. In the uncorrected image, the contrast features appear blurry and the Al dumbbell arrangement with a separation of about 1.5Å in the [11$\bar{2}$0] projection for example is not resolved. In the corrected microscope image, more detailed contrast features can be seen due to an improved resolution. For this positive corrected C_s value, (most) atomic columns appear with a reduced intensity (relatively dark). By a comparison with the atomic model structure, we can distinguish closely-spaced aluminum and oxygen columns from each other through their difference in contrast. Using the

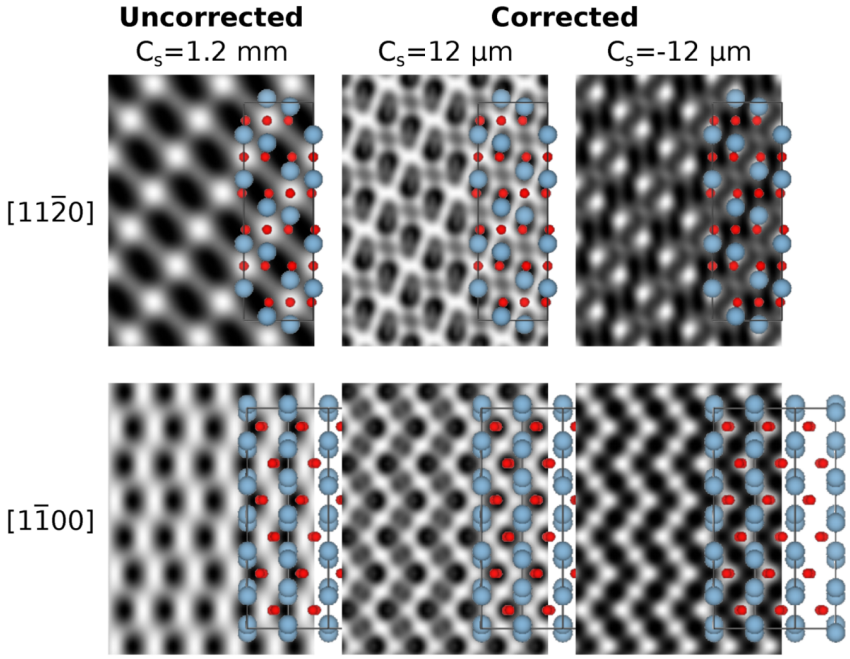

Figure 2.12: Multislice simulated HRTEM images of α-Al_2O_3 (7 nm thick) along the [1$\bar{1}$00] and [11$\bar{2}$0] zone axis orientations at Scherzer defocus, comparing the cases of uncorrected spherical aberration to positive and negative corrected values of C_s. Ball models of the α-Al_2O_3 lattice are superimposed, with Al atoms in blue and O atoms in red.

corrector, the C_s value can also be tuned to negative values to reach negative spherical aberration corrected imaging conditions (NCSI) [149]. The main advantage of these conditions is an inversion and a strong enhancement of the atomic column contrast, such that atomic columns appear bright instead of dark, as can be seen in Fig. 2.12 on the right. This strongly enhanced atomic contrast makes the NCSI conditions [149] optimal for imaging. In particular, for our TEM which has $C_s = -12$ μm, maximum phase contrast and minimum delocalization is obtained for a small positive defocus value of about 5 – 6 nm.

Apart from the spherical aberration, the HRTEM image contrast can also strongly depend on the defocus of the microscope (through Eq. 2.24) and the sample thickness. Inverting the defocus from positive to negative will cause an inversion of the contrast, and variations in the sample thickness can also cause changes in the contrast. For these reasons, it is in many cases necessary to perform image simulations to correctly interpret the HRTEM intensity contrast, for which in this work the multislice method is used as explained in Section 2.4.5.

2.4.3 Diffraction contrast imaging

Another imaging mode in the TEM is diffraction contrast imaging. Here, an objective aperture is placed in the back focal plane, where the diffraction pattern is formed, to select certain diffracted beams to contribute to the image, as illustrated in Fig. 2.13. Different sizes of apertures can be employed to select a single or multiple electron beams. The smaller the aperture, the higher the contrast will be in the image. When selecting only the direct beam ($\vec{k}_0$), i.e. electrons that have not scattered inside the sample, a bright field

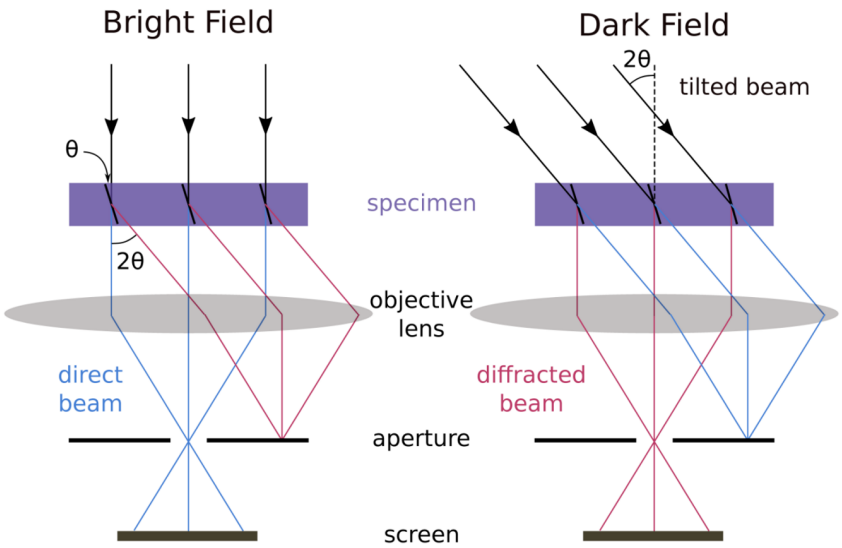

Figure 2.13: Schematic overview of bright field and dark field imaging (with tilted beam) conditions in the TEM. The objective aperture selects either the direct or diffracted beam in the back focal plane of the objective lens.

(BF) image is formed. Areas in the sample that scatter more will appear dark in the image, while the vacuum background appears bright. When only one of the diffracted beams ($\vec{k}_g$) is selected by the aperture, a dark field (DF) image is formed on the screen. In that case, areas that scatter stronger in this direction will appear bright on a dark background. DF imaging can be done either by mechanically shifting the objective aperture or by tilting the incident beam such that the direction of the diffracted beam becomes parallel to the optical axis, as illustrated in Fig. 2.13. To increase the intensity in the image, diffraction contrast imaging is usually done in so-called 'two-beam' conditions. To achieve this, the sample is tilted out of zone axis such that only a few diffraction spots are in Bragg condition.

The intensity in diffraction contrast images can be influenced by different structural properties of the sample under study. First, there will be a contribution from mass/thickness contrast. The thicker or heavier the sample, the more electrons will scatter and therefore, the diffracted beams will carry more intensity at the expense of intensity in the direct beam. Another thickness effect is the appearance of thickness fringes (oscillating intensity), typically at sample edges where the thickness of the specimen increases continuously. This effect follows from the following equation for the intensity of the diffracted (I_g) and direct beam (I_0) in the case of two-beam conditions,

$$I_g = \left(\frac{\pi t^2}{e_g}\right)^2 \frac{\sin^2(\pi t s_{\text{eff}})}{(\pi t s_{\text{eff}})^2} = 1 - I_0, \tag{2.31}$$

which is derived from the Howie-Whelan equations for transmission and diffraction [139]. It is clear form Eq. 2.31 that the diffracted intensity has a periodic behavior with thickness t, which is complemented by the direct beam intensity and causes the thickness fringes. For polycrystalline samples, diffraction contrast can be used to distinguish differently oriented grains or grains with different crystal structure. The diffracted beam selected by the aperture corresponds to scattering from a certain plane specific to the crystal

symmetry with a certain orientation. Differently oriented grains or areas with different crystal structure will most likely not have a diffraction beam at the same position in the back focal plane and will consequently produce different intensities. Lastly, structural defects of the lattice such as dislocations or planar defects can also be imaged using diffraction contrast. The local lattice distortions around such defects will change the diffraction conditions locally. The resulting change in intensity of the diffracted beam will create contrast around the defect in the image.

2.4.4 Scanning transmission electron microscopy - HAADF

In contrast to plane wave illumination in conventional TEM modes, scanning transmission electron microscopy (STEM) employs a convergent beam probe. The electron beam, with a semi-convergence angle α, is focused on the sample surface into a point and scans a certain area by moving across the surface in the x and y direction. At each scanning point, forwardly scattered electrons to low (BF STEM) or high (DF STEM) angles are collected by an appropriate detector, as illustrated in Fig. 2.14, and a structure image is built from the recorded intensities. At the same time, a secondary signal emerging from the beam-sample interaction such as characteristic X-rays (EDXS) or lower-energetic photons (cathodoluminescence) may be detected for additional information.

A BF STEM image results from collecting electrons scattered to low angles using a disk-shaped detector placed in the optical axis. This method is used to obtain high-resolution images of atomic columns of light elements such as oxygen, which don't produce scattering to high angles. A more common method is high-angle annular dark-field (HAADF) imaging, in which electrons scattered to relatively high angles are collected by an annular detector. The inner- and outer-acceptance angle of detection can be changed by varying the camera length, i.e. the sample-detector distance, but typical values are $\theta_{\text{in}} = 35$ mrad and $\theta_{\text{out}} = 300$ mrad. It was shown by Howie [150] that for such high scattering angles the contribution from elastic Bragg-scattering becomes small and that the intensity is dominated by thermal diffuse scattering (TDS). In TDS, the electrons scatter inelastically from atoms vibrating around their equilibrium position (known as phonons). This means that diffraction contrast is suppressed in HAADF-STEM images and the intensity becomes highly sensitive to the atomic number Z of the sample material, as shown below. Hall and Hirsch [151] calculated the TDS scattering intensity as a function of the scattering parameter $s = \frac{\sin(\theta/2)}{\lambda}$ to be

$$I_{\text{TDS}}(s) = [f^e(s)]^2 \{1 - \exp[-2M(s)]\}. \tag{2.32}$$

Here, $M(s)$ is the Debye-Waller factor given by

$$M(s) = 2\pi^2 s^2 \bar{u}^2, \tag{2.33}$$

with $\bar{u}^2$ the temperature-dependent mean-square displacement of the specific atom. $f^e(s)$ is the atomic scattering factor for electrons, which is equal to [152]

$$f^e(s) = \frac{m_0 e^2}{8\pi\epsilon_0 h^2} \frac{Z - f^x(s)}{s^2} \approx \frac{m_0 e^2}{8\pi\epsilon_0 h^2} \frac{Z}{s^2} \text{ for large } s, \tag{2.34}$$

where m_0 is the electron mass, e is the elementary charge, ϵ_0 is the vacuum permittivity, h is the Planck constant and $f^x(s)$ the atomic scattering factor for X-rays. Combining

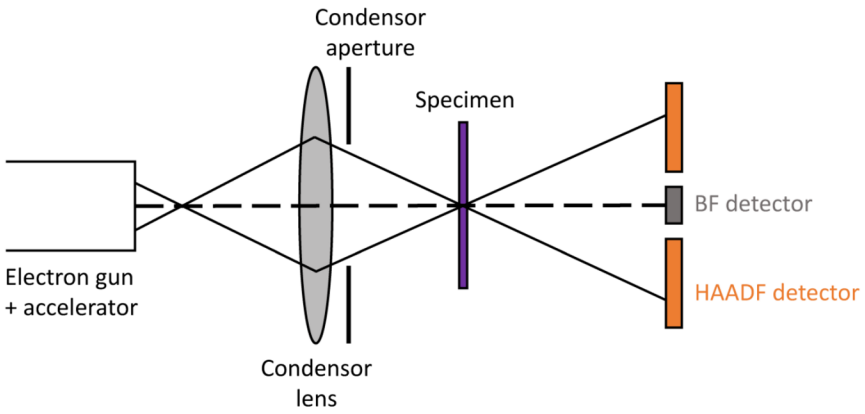

Figure 2.14: Schematic overview of the image formation in STEM.

Eqs. 2.32 and 2.34, the Z-dependency of the scattering intensity becomes evident and information about the chemical composition can be obtained from it. HAADF-STEM of crystalline materials is typically performed along a low-order zone axis such that atoms line up as columns parallel to the beam direction. Therefore, the higher the mean atomic number of an atomic column, the brighter it will appear in the image. Low Z atoms such as oxygen will produce negligible intensity.

A big advantage of HAADF-STEM imaging compared to HRTEM is the incoherent nature of the image formation. This means that the image intensity I at a position $\vec{r}$ is simply given by the convolution [153]

$$I_{\mathrm{HAADF}}(\vec{r}) = P(\vec{r}) \otimes O(\vec{r}) \tag{2.35}$$

of the probe function $P(\vec{r})$ and the object function $O(\vec{r})$. As a result, the object appears as 'self-illuminating' and intensity can directly be linked to the presence of atoms, making the image interpretation very straightforward. There is no contrast reversal with changing defocus or sample thickness and the image intensity increases monotonically with thickness. These two properties are illustrated in Fig. 2.15 which shows the result of a multislice HAADF-STEM simulation of a β-Ga_2O_3 supercell in the [010] projection. In the image on the left, which shows the simulated HAADF-STEM image at a thickness of 10 nm, the Ga columns appear as bright dots on a dark background. The oxygen columns produce negligible contrast. The mean intensity as a function of thickness displays a monotonically increasing behavior. The incoherent nature of the HAADF images stems from the incoherence of the thermal diffuse scattering process itself, where each atom in considered as an independent incoherent scattering center. However, TDS is not a necessary requirement for incoherence. Even for a stationary lattice (i.e. no vibrations and no TDS), it was shown by Nellist and Pennycook [154] that HAADF-STEM images keep their incoherent nature due to the integration of the intensity over a large area on the detector. In this way, the intensity of multiple Bragg spots is summed up and the coherent interference effects are destroyed. This can also be explained by the principle of reciprocity [142, 154], which states that the annular DF detector in STEM is equivalent to using a large convergent incoherent illuminating source in a conventional TEM configuration.

As a consequence of Eq. 2.35, the spatial resolution in HAADF images is largely

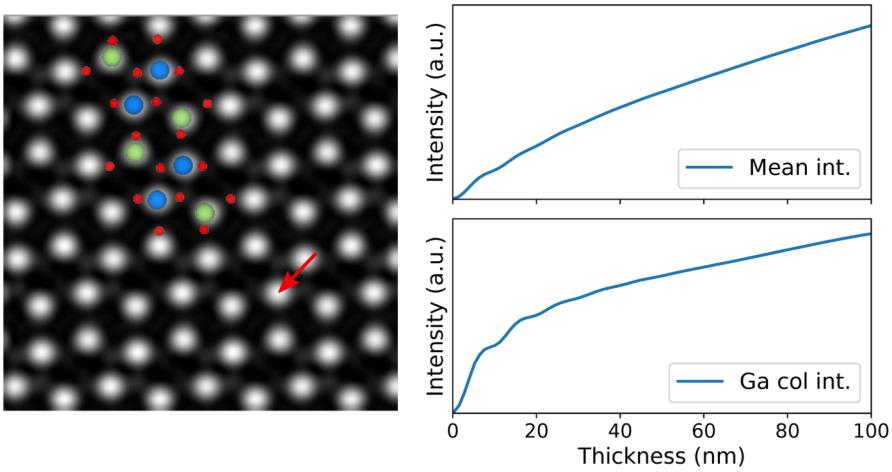

Figure 2.15: Multislice simulated HAADF-STEM image of a β-Ga_2O_3 supercell along the [010] projection at a thickness of 10 nm, with the ball model of one unit cell superimposed. The mean intensity and a single Ga column (indicated by the red arrow) intensity are plotted as a function of sample thickness.

determined by the probe size on the sample surface. The sharply peaked object function is blurred by the point-spread function that is $P(\vec{r})$. Since the convergent electron beam probe is obtained by focusing through a forming lens, it is also subject to the typical lens aberrations with spherical aberration as the most important one, which limit the minimum probe radius. The full width at half maximum of the STEM probe intensity profile is a good measure for the eventual resolution and is determined by (at optimal defocus) [153]

$$d = 0.4\lambda^{3/4}C_s^{1/4}. \tag{2.36}$$

In case of a 300 kV microscope with a spherical aberration coefficient C_s of 1.2 mm of the forming lens (value for the TEM used in this work), this gives a resolution of 1.2 Å. This implies that atomic columns with a separation larger than 1.2 Å perpendicular to the beam are resolvable.

The strong Z-dependence of the scattering amplitude at high angles that was already discussed is not the only determining factor for the image intensity. As can be seen from Eq 2.32, the intensity also depends on the strength of the atomic vibrations through the Debye-Waller factor M. Additionally, an important effect to consider is the so-called 'channeling' [155] of the electron beam on atomic columns, which is especially strong when imaging along a low-order zone axis. Due to the positive electrostatic potential of the atom column, it acts as a guide or channel for the electrons, as illustrated in Fig. 2.16. This results in an oscillating HAADF intensity as a function of sample thickness, as can be seen in Fig. 2.15 for the intensity of a single Ga column for thicknesses lower than $\approx$ 40 nm. This phenomenon will be explained more thoroughly in the next section in terms of Bloch states. On average, channeling will increase the scattered intensity since the electrons stay in the vicinity of the atoms which are scattering centers. Thus, off-axis imaging typically results in lower intensities. Lattice distortions that cause a disruption of the periodicity of the crystal might, on the one hand, give rise to additional diffuse scattering [156], but, on the other hand, can cause 'dechanneling' which reduces the scattering probability [157]. As a consequence, for the quantitative analysis of HAADF-STEM images, a comparison with image simulations is still required.

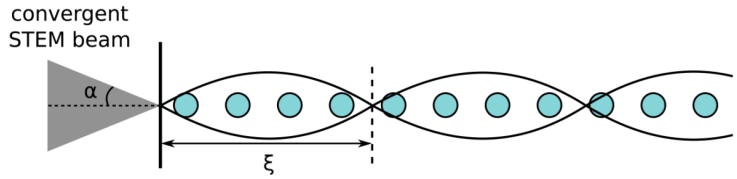

Figure 2.16: Schematic representation of channeling of the STEM electron beam on an atomic column inside the sample. ξ is called the extinction length and is equal to the period of the channeling oscillation.

STEM in terms of Bloch states

A more detailed and mathematically founded description of the propagation of a convergent STEM beam inside a crystal will be given in this section. This will give us insight into the physics of electron wave propagation that will be needed to understand the calculation results of Chapter 5.

The electron wave function $\Psi(\vec{r})$ inside a crystalline specimen is given by the solution of the Schrödinger equation

$$\left[-\frac{h^2}{8\pi^2 m_e}\nabla^2 + V(\vec{r})\right]\Psi(\vec{r}) = E\Psi(\vec{r}) \tag{2.37}$$

with a periodic crystal potential $V(\vec{r})$. According to Bloch's theorem, the solution for the wave function in a periodic potential can be written as a sum of Bloch waves $b^j(\vec{r},\vec{k}^j)$

$$\Psi(\vec{r}) = \sum_j \epsilon^j b^j(\vec{r},\vec{k}^j), \tag{2.38}$$

with ϵ^j the excitation strength of the jth Bloch wave. Each Bloch wave has an associated wave vector $\vec{k}^j$ and can be expanded as a Fourier series over the reciprocal lattice vectors $\vec{g}$ as follows

$$b^j(\vec{r},\vec{k}^j) = \sum_{\vec{g}} C^j_{\vec{g}} \exp\left[2\pi i(\vec{k}^j + \vec{g})\cdot\vec{r}\right]. \tag{2.39}$$

Combining Eqs. 2.38 and 2.39, we can formulate the Bloch wave expression for the electron wave function for plane wave illumination of a incident wave with a transverse component $\vec{k}_t$

$$\Psi(\vec{r}_t, z, \vec{k}_t) = \sum_j \epsilon^j b^j(\vec{r}_t, \vec{k}^j_t)\exp\left[2\pi i k^j_z z\right], \tag{2.40}$$

where the jth wave vector $\vec{k}^j = \vec{k}_t + k^j_z\vec{e}_z$ and the position vector $\vec{r} = \vec{r}_t + z\vec{e}_z$ have been splitted in transverse and longitudinal (i.e. along the propagation direction) components. In the case of a convergent STEM probe, the incident cone of illumination consists of many different plane waves with different transverse components $\vec{k}_t$. Each partial plane wave will excite its own set of Bloch states. The total wave function is then obtained by integrating Eq. 2.40 over all $\vec{k}_t$ contained in the incident cone as defined by the top-hat aperture function $A(\vec{k}_t)$

$$\Psi_{\text{STEM}}(\vec{r}_t, z) = \int \sum_j A(\vec{k}_t)\epsilon^j b^j(\vec{r}_t, \vec{k}^j_t)\exp\left[2\pi i k^j_z z\right] d\vec{k}_t. \tag{2.41}$$

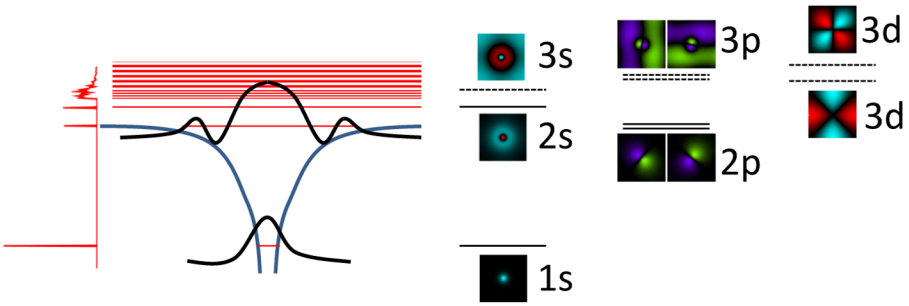

Figure 2.17: Right: representation of the 2D projected potential of an atomic column in a crystal with bound (localized) and unbound (dispersive) energy eigenstates. Left: nomenclature of the columnar Bloch wave eigenstates with their spatial electron density amplitude distribution.

The wave function is thus a sum of many Bloch states each propagating at different velocities and interfering with each other constructively or destructively depending on depth. After leaving the specimen, the wave function is diffracted onto the HAADF detector and the measured intensity is obtained by integrating $|\Psi_{\mathrm{STEM}}|^2$ over the detector geometry.

Each excited Bloch state in Eq. 2.41 is an eigenstate of the Schrödinger equation with an energy eigenvalue E (see Eq. 2.37). In the following, we will rather associate each Bloch state with its so-called 'transverse energy' E_T. E_T is defined as the difference between the z component of the kinetic energy of the Bloch wave in the sample and that of the incident wave ($\vec{k_i}$) in the vacuum

$$E_T^j = \frac{\hbar}{2m_e}\left(k_z^{j2} - k_{i,z}^2\right). \tag{2.42}$$

Fig. 2.17 shows the 2D projected potential of an atomic column in a crystal, with each energy eigenstate represented by a red line. These Bloch wave eigenstates can be described as atomic orbitals $1s$, $2p$, $2s$, etc. with a radial and angular quantum number, according to Ref. [158]. The electron density amplitude of the s states is strongly localized on the center of the atomic column, with a single maximum for $1s$, a second radially symmetric maximum for $2s$ and so on. p states on the other hand, have an asymmetric electron density amplitude distribution.

An important distinction is made between bound and unbound eigenstates. Bound Bloch states (positive E_T) are localized by the potential on the atomic column and form sharp lines in the energy spectrum. The unbound states (negative E_T) are delocalized/dispersive plane waves and they are grouped together in the energy spectrum as a continuum of energies. The lowest energy $1s$ Bloch state is typically bound, but the stronger the potential, the more Bloch states will be confined by it. Due to beating between the bound (B) states and the continuum of unbound (UB) states, oscillations in the wave function amplitude along the propagation direction arise with a frequency equal to $f = |k_z^B - k_z^{UB}|$. For the continuum of unbound states, the wave vector is determined by the median of the distribution. Beating of the $1s$ state with the unbound states produces the short wavelength intensity oscillation with thickness, as shown in Fig. 2.15 for a single Ga column. The earlier explanation for channeling behavior in the classical particle picture finds here a quantum analogue. The period of the channeling oscillation, as

illustrated in Fig. 2.16, is called the extinction length ξ, and is strongly dependent on the atomic number of the atoms inside the column: the heavier the atom, the smaller the extinction length. The beating oscillation is damped due to the dephasing of the continuum of unbound states [159]. In the classical particle picture, we can explain this as the result of the dechanneling of the beam electrons from the column at a certain depth in the specimen. From there on, the STEM intensity is believed to increase monotonically proportional to the average atomic number. In Fig. 2.15, we see indeed how the oscillating behavior in the intensity of the Ga column dies out around a thickness 40 nm, after which it increases monotonically with thickness.

Details of the Bloch wave calculations

Bloch wave calculations and their spectral description are performed using the custom software B_WISE [159], developed in the group of Dr. Vincenzo Grillo at CNR-NANO in Modena, Italy. Since Bloch wave algorithms only work for plane wave illumination conditions, the software samples a number of points within the probe: the spectra reported in here have been calculated sampling a STEM probe obtained for a semi-convergence angle of 9 mrad and acceleration voltage of 300 kV into 2445 individual points. For each one of these points, a Bloch wave calculation is performed following the original algorithm proposed by Metherell [160], and the resulting Bloch coefficients are summed up taking into account the appropriate aberration phase. Thermal vibrations of the atoms are accounted for by considering a thermally averaged potential. The potential has no imaginary part, which means inelastic scattering and absorption effects are not included. A Debye-Waller factor of 0.2Å^2 was used in all calculations. For calculating the propagation of the STEM probe on an atomic column, a superstructure formed by repeating a simple cubic unit cell with lattice parameter $a = 3\text{Å}$ and a single atom in the unit cell in all directions is considered and the probe is placed exactly centered on a column.

2.4.5 Multislice simulation method

The multislice method of Cowley and Moodie [161] is a numerical iteration approach to calculate the exit wave function and can be applied to HRTEM and STEM imaging conditions. Its starting point is the Schödinger equation and it takes into account the full dynamical scattering interaction of the electron beam with the specimen, which is not necessarily crystalline.

In the multislice method, the sample is divided into thin slices of thickness Δz perpendicular to the beam direction. At each slice, the interaction of the electron wave with the 2D projected atomic potential $V(x,y)$ of the atom slice is calculated and the resulting wave function is propagated to the next slice. For such a thin slice, the interaction results only in a phase change of the wave function which is proportional to the projected potential and is described by the so-called transmission function

$$t(x,y) = \exp[iV(x,y)]. \tag{2.43}$$

The propagation of the wave between the individual slices follows the Huygens-Fresnel principle. The wave function at the entrance of the n^{th} slice is given by the coherent superposition of spherical waves emanating from all point sources at the exit of the $n-1^{\text{th}}$

slice. This process is accounted for by convolution of the wave function with the Fresnel propagator $p(x,y)$. Combining this two-step process, the wave function exiting slice n is given by

$$\Psi_n(x,y) = t_n(x,y)[\Psi_{n-1}(x,y) \otimes p_n(x,y)]. \tag{2.44}$$

The convolution operation of $\Psi_{n-1}(x,y)$ with $p_n(x,y)$ in real space (x,y) can be replaced by an easy multiplication in Fourier space (u,v), in which case the Fresnel propagator is equal to $p_n(u,v) = \exp\left[2\pi i \Delta z(u^2+v^2)\right]$. Then, with $\mathscr{F}$ the 2D Fourier transform and $\mathscr{F}^{-1}$ its inverse, the complete recursive multislice operation to calculate the electron wave function at a thickness $n\Delta z$ is given by

$$\Psi_n(x,y) = t_n(x,y)\mathscr{F}^{-1}\{\mathscr{F}\{\Psi_{n-1}(x,y)\}p_n(u,v)\}. \tag{2.45}$$

The simulated image for this thickness is then simply obtained by calculating the wave function intensity on the detector plane according to Eq. 2.20. In this way, the multislice method is very computationally efficient, especially in the case of HRTEM, where the incident probe is a simple plane wave. Another advantage is that large unit cells can be used and that the calculation also works for non-periodic structures (in contrast to Bloch wave calculations).

In the case of STEM, the method requires significantly higher computational effort since the multislice simulation has to be repeated for each probe position with a focused probe wave function for the incident wave as described in Ref. [162]. The STEM image is then reconstructed by integrating the calculated exit wave function intensity over the simulated detector for each probe position. Thus, the amount of scanning points $N_x N_y$ will be equal to the number of pixels in the simulated image. To account for thermal vibrations of the atoms, the simulation is performed using the 'frozen phonon' approximation according to Loane *et al.* [163]. In this approximation, the passing of the electron beam through the specimen is assumed much more rapid than the vibration speed of the atoms. The electron beam then basically interacts with a stationary lattice, of which the atoms are frozen in place in mid-vibration. Therefore, in the simulated crystal structure, the atoms are randomly displaced from their ideal position by some distance in accordance to their vibration amplitude. The simulation is then repeated for a set of different frozen phonon configurations and in the end the results of all simulations are averaged.

Details of the multislice simulations

The details of the STEM multislice simulations that are performed to obtain the results of Chapter 5 are summarized here. The same semi-convergence angle of the beam of 9 mrad, acceleration voltage of 300 kV of the beam and respective inner- and outer-acceptance angles of the HAADF detector of 35 mrad and 270 mrad are chosen for all simulations, to match typical experimental conditions. In all simulations, between 20 and 40 frozen phonon configurations are averaged over. The supercells for the simulations extend minimally 3×3 nm^2 perpendicular to the beam direction (to ensure a small enough sampling in k-space) and are constructed with periodic boundary conditions in the x, y, and z directions. The slice thickness for each structure is defined as the shortest inter-atomic spacing along the beam direction, such that each slice contains only one atom per column. Typical values range in between 3 – 5Å. When disordered lattices are

simulated, the supercell thickness extends over approximately 30 nm along the beam direction and is repeated multiple times to reach the final thickness. In this way, statistical incorporation of the different constituent atoms along the columns creates a sample that represents a completely random configuration without producing any periodicity effects, as shown in Appendix A. For the $(In_xGa_{1-x})_2O_3$ and $(Al_xGa_{1-x})_2O_3$ supercells with varying In/Al concentrations, the a, b and c lattice parameters are adapted according to the linear relations found by Kranert *et al.* [60, 164] based on ceramic samples. The 3×3 nm^2 supercells of the 'isolated' columns are mostly empty with just a single atomic column at the center with inter-atomic spacing of 3Å. The same is true for the two-column structures, but with two columns with an inter-column spacing of 3Å placed at the center of the supercell. Therefore, due to the repetition of the cell in x and y directions, we are actually simulating a very loose lattice in both cases. However, the distance between those columns is large enough for them not to influence each other. The same Debye-Waller factor of 0.06Å^2 is adopted for all elements. The supercells are not relaxed and static displacements of the atoms are not taken into account in our simulations. Visualizations of the (projected) supercells and more detailed information on the cell dimensions can be found in Appendix A.

2.4.6 Experimental details

TEM set-up

The transmission electron microscope used in this work is a TEM/STEM FEI Titan 80-300 operated at an acceleration voltage of 300 kV (λ = 1.97 pm). The electron source is a high-brightness field electron gun (FEG), in which a high electric field causes high-energy electrons to be emitted from a filament. The vacuum inside the TEM column is typically close to $7 \cdot 10^{-7}$ mbar. TEM images are recorded with a Ceta2 $4k \times 4k$ camera, which has a maximum frame rate of 400 images/s. In addition, the microscope is equipped with a Fischione model 3000 annular detector to perform HAADF-STEM measurements. The objective lens of the microscope is aberration corrected and for HRTEM imaging, the spherical aberration is typically tuned to a small negative value of approximately $C_s \approx -12$ μm. This results in NCSI conditions and an improvement of the point resolution towards the information limit of about 12.5 nm^{-1}, which allows atoms with a spacing of 0.8Å to be resolved. In TEM mode, the parallel beam has a semi-convergence angle smaller than approximately $\alpha \leq 0.4$ mrad and the beam current ranges from 0.1 to 1 nA. In the case of STEM imaging, we use a focused convergent probe with a semi-convergence angle of $\alpha = 9$ mrad. The probe forming lens is not corrected and has a spherical aberration coefficient of approximately $C_s \approx 1.2$ mm, which limits the spatial resolution in STEM to 1.2 Å.

Sample preparation

The following procedure is used to prepare electron transparent cross-sectional samples for TEM. First, the in-plane low order zone axis orientations of the substrate are determined by X-ray diffraction. Since the tilting capability of the TEM sample holder is limited, it is important to prepare the TEM surface perpendicular to the desired crystallographic orientation. Therefore, small sample pieces ($\sim 2 \times 1$ mm^2) are cut using a wire saw with the long side perpendicular to the desired direction. For c-oriented sapphire substrates, we use the $< 1\bar{1}00 >$ and $< 11\bar{2}0 >$ in-plane orientations, which are highlighted in Fig.

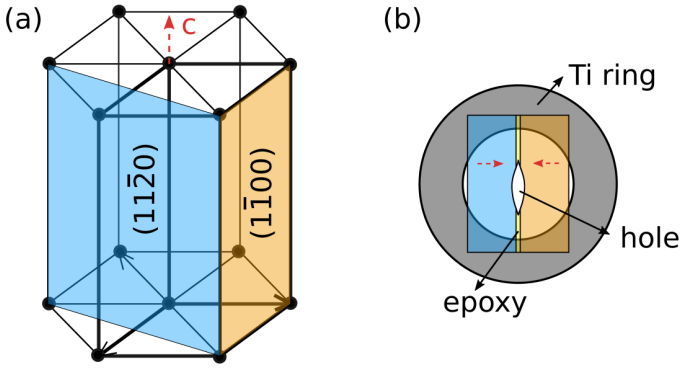

Figure 2.18: (a) Hexagonal unit cell of the sapphire substrate. The (1$\bar{1}$00) and (11$\bar{2}$0) planes used for TEM preparation and the out-of-plane c-direction are highlighted. (b) Schematic of a cross-section TEM sample glued on a titanium ring with the PIPS hole on the interface.

2.18(a) in the hexagonal unit cell. Two sample pieces, one for each orientation, are glued together layer to layer using GATAN G1 two-component epoxy resin and heated to 150°C, creating a thin interface glue line between the two layers in cross-section view [see Fig. 2.18(b)]. This structure is glued onto a titanium support ring and is thinned down to $5-10$ μm by plan-parallel mechanical polishing of the cross-section plane (perpendicular to the desired crystallographic orientation) from both sides. For the polishing of each side, a series of diamond lapping foils are used, decreasing in grain size from 35 μm to 0.1 μm. In the last step, the sample is inserted in a Gatan precision ion polishing system (PIPS) for ion milling to electron transparency. The milling is done using Ar^+ ions at an energy of 3.5 kV and at an angle of incidence of 4° until a hole is obtained along the interface. The sample is cooled to liquid nitrogen temperature during the milling procedure to minimize ion beam damage to the sample. Finally, a cleaning process is applied by a step-wise lowering of the beam energy to 0.2 kV and by increasing of the angle to 7° to remove amorphidized material.

2.5 Methodology of the in-situ annealing TEM experiments

By in-situ TEM experiments, changes in the structure or the properties of the sample are observed as the result of an external stimulus or a changing environment. Such a stimulus can be e.g. the application of heat, strain or an electrical impulse to the sample. The big advantage of in-situ microscopy is that it allows for a continuous observation of a process in a single experiment, rather than studying multiple samples that were first altered ex-situ. In-situ TEM is performed using a specially designed sample holder, equipped with e.g. a heater or electrical contacts, depending on the type of experiment that is to be performed. Some holders also allow the sample to be exposed to a background gas by enclosing the sample and its environment in a small volume between two electron transparent membranes.

In this work, we will do in-situ annealing experiments by heating and for this purpose two dedicated TEM holders from the Protochips, Inc. company are used, which are trademarked as Fusion[TM,12] and Atmosphere [TM,13]. Both holders can hold an Environmental

[12]Trademark for Protochips Inc.'s in-situ system for heating, electrical and electrothermal analysis.
[13]Trademark for Protochips Inc.'s TEM environmental gas cell system.

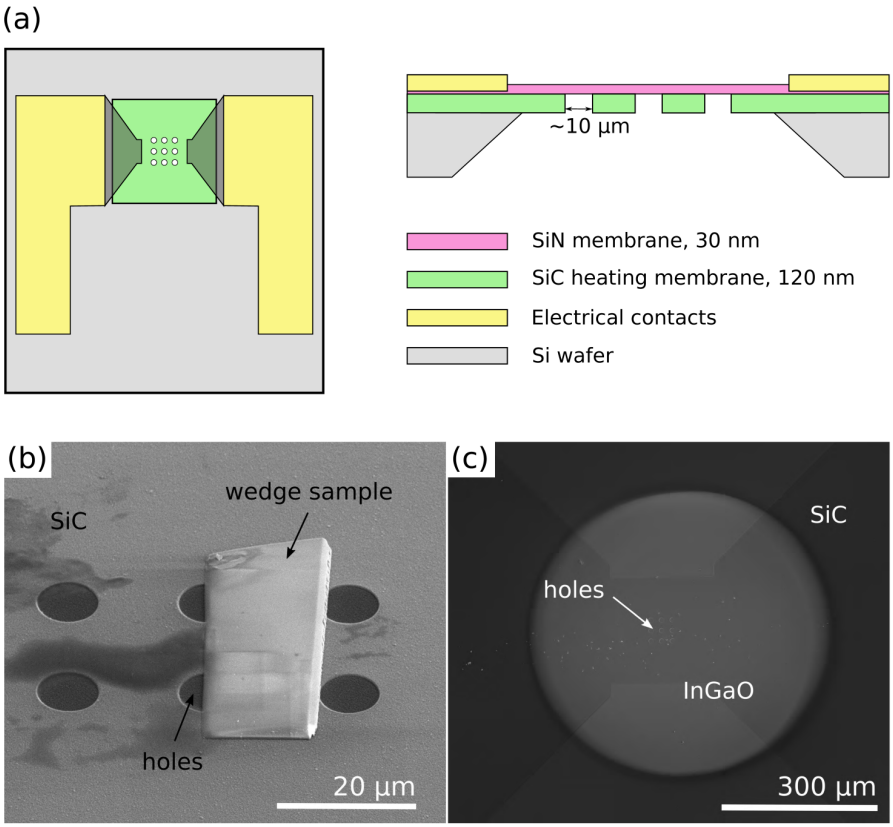

Figure 2.19: (a) shows plan-view and cross-section schematics of the design of a heating chip for in-situ TEM. Below scanning electron microscopy images of (b) a wedge polished $(In_xGa_{1-x})_2O_3/Al_2O_3$ lamella on the SiC-membrane (method 1) and (c) the circular area of amorphous $(In_xGa_{1-x})_2O_3$ deposition on the E-chip (method 2) are presented.

chip (E-chip), which is manufactured using MEMS[14] technology and provides the heating stimulus to the sample attached to it. The general design of the heater E-chip is illustrated in Fig. 2.19(a). The chip is made of silicon with a thin 500 μm^2 SiC heating membrane in the middle. A current to heat the SiC membrane is provided by electrical leads which stand in contact with the holder. The electron-transparent sample should be deposited on/attached to the SiC membrane. TEM imaging is then possible through micrometer-sized holes which are only coated with a 30 nm thick amorphous SiN membrane for support. Each chip is calibrated by the manufacturer using an optical pyrometer, and a table of current versus temperature is provided such that the membrane and sample temperature can be determined during an experiment. The rapid response of the MEMS device to changes in current, allows the membrane to be heated to temperatures of 1000°C or higher in only 1 ms. The maximum heating temperature that we can achieve is around 1100°C.

With the Fusion TEM holder, the chip is simply clamped into place on the holder and the sample is exposed to the vacuum of the TEM chamber. With the Atmosphere holder, a second smaller chip with a similar electron transparent window is placed on top of the first one such that the sample is confined between the two. The two chips are then sealed

[14]Micro-electro-mechanical systems.

together by a O-ring[15], such that the sample is hermetically sealed from the vacuum. In this way, a small 'reaction chamber' is created inside the TEM connected to a gas inlet and outlet on the holder. This allows the heating experiment to be performed under different atmospheres and pressures up to 1 bar.

2.5.1 Sample deposition and preparation

In this work, we use two different ways to get our sample material on the E-chip ready for an in-situ experiment. In each case the starting material is amorphous (a) $(In_xGa_{1-x})_2O_3$.

For the first approach, an amorphous $(In_xGa_{1-x})_2O_3$ thin film with a thickness in the range of 100 – 150 nm is grown on a c-oriented sapphire substrate by molecular beam epitaxy (see Section 2.3.2) with a substrate temperature of $T = 100°C$. Higher deposition temperatures result in (partially) crystalline samples. First, a sample piece is mechanically and chemically plan-view polished from the substrate side under a small angle of $\approx 4°$, until an electron transparent area is obtained at the thinnest edge. At the very edge, the substrate is completely polished away and we end up with a small part of just 'free-standing' layer. The polished sample is then inserted into the scanning electron microscope (SEM, see Section 2.6.1), where the rest of the procedure is carried out under vacuum. The focused ion beam is used to cut out a small lamella of approximately 30 μm in width at the thin edge of the wedge sample. Using a micromanipulator, the lamella is transferred to the chip such that the thin edge (which is the region of interest) is right above one of the electron transparent holes in the membrane, exactly as in the SEM image in Fig. 2.19(b). As a last step, the lamella is fixed to the membrane by applying platinum deposition under the electron beam on the thicker sides.

Because this process requires a number of steps that might cause contamination or loss of the sample at some point, a second method was developed where the heating chip is inserted in the MBE chamber, and using a boron nitride mask with a 600 μm diameter hole, amorphous $(In_xGa_{1-x})_2O_3$ is directly deposited on the dedicated area of the chip, again at a temperature of $T = 100°C$. This results in a circular area of deposited material centered on the membrane holes with a diameter of approximately 500 μm, as shown in the SEM image in Fig. 2.19(c). The deposition time was set to 16 minutes to obtain a film with a thickness of approximately 100 nm. The deposition time was determined by a previous deposition on c-plane sapphire substrates in which the thickness could be determined by infrared reflectometry.

2.5.2 Influence of the experimental conditions

Table 2.2 contains a summary of the important experimental parameters and some crystallization characteristics of all investigated samples, which cover the full composition range $0 \leq x \leq 1$. As one can see, most annealing experiments are performed under so-defined 'standard annealing conditions': in-situ in the TEM, under vacuum, at a slow heating rate ($\leq 1°C/s$) and by direct deposition of the film on the heating chip. To investigate the influence of

- the exposure to the high energy electron beam,

[15] An O-ring is a mechanical gasket in the shape of a torus typically made of synthetic rubber. It is designed to be seated in a groove and compressed during assembly between two or more parts, creating a seal at the interface.

Table 2.2: Summary of the experimental parameters and crystallization characteristics of all annealed $(In_xGa_{1-x})_2O_3$ samples. x_i and x_f are the indium contents of the as-deposited films and after annealing to T_{max}, respectively.

x_i	Experiment type	Sample type	Atmosphere	Heating rate (°C/s)	T_{cryst} (°C)	T_{max} (°C)	Phase evolution	x_f	Series in Fig. 2.20
0.0	in-situ	MBE on chip	vacuum	0.5	470	1000	a → γ → β	0.0	
0.0	in-situ	wedge on sapphire	O_2	0.5	500	1000	a → γ → β	0.0	
0.22	in-situ	MBE on chip	vacuum	1	675	1000	a → γ → β	0.15	
0.33	ex-situ	wedge on sapphire	O_2	–	≤ 800	800	a → c	0.33	5
0.4	in-situ	MBE on chip	vacuum	0.2 – 0.5	685	1000	a → c → β	0.35	
0.4	in-situ	MBE on chip	vacuum	fast pulse	–	1100	a → c → β	0.34	
0.44	in-situ	MBE on chip	vacuum	1.0	670	1080	a → c → β	0.0	1
0.44	in-situ	MBE on chip	O_2	0.2	700	800	a → c	0.43	
0.44	in-situ	MBE on chip	O_2	1.0	725	1100	a → c → β	0.0	2
0.55	in-situ	wedge on sapphire	vacuum	0.5	680	1050	a → c → β	0.55	3
0.55	in-situ	wedge on sapphire	O_2	0.5	770	1050	a → c	–	
0.55	ex-situ	wedge on sapphire	O_2	–	≤ 800	800	a → c	0.55	4
0.6	in-situ	MBE on chip	vacuum	1.0	650	1000	a → c	–	
0.78	in-situ	MBE on chip	vacuum	0.5	430	1000	a → c	0.55	
1.0	in-situ	MBE on chip	vacuum	0.5	< 100	1000	c	1.0	

- the presence of an oxygen atmosphere,
- the presence of a crystalline (sapphire) substrate, and
- the heating rate,

annealing of samples with the same composition is repeated for different experimental conditions. Some annealing experiments are performed in an oxygen atmosphere using the Atmosphere TEM holder; films are deposited on a sapphire substrate and annealed both in-situ and ex-situ in an oven; and a fast heating pulse was applied instead of a slow ramp rate, as a comparison to the 'standard' conditions, described above.

In general, we see that for any two samples with the same initial composition but annealed under different experimental conditions, the phase evolution is not changing. For the samples highlighted in grey, which all have intermediate indium concentrations close to $x = 0.5$, the evolution of the electron diffraction data with temperature are shown in Fig. 2.20 as a demonstration of the phase evolution. The first image series represents the standard annealing conditions for a film with indium content $x = 0.44$, and shows a phase transformation from amorphous to cubic bixbyite at 670°C and in a later stage from bixbyite to monoclinic at 870°C. Applying an oxygen atmosphere during the annealing (series 2), results in the same crystallization pathway. The only difference is that the a $\rightarrow$ c and c $\rightarrow \beta$ phase transition temperatures are increased by 55°C and 40°C, respectively. In a similar comparison of vacuum versus oxygen atmosphere for the crystallization of Ga_2O_3 ($x = 0$), also the only observed difference is a slight increase in the crystallization temperature, as indicated in Table 2.2. The oxygen gas that flows through the Atmosphere gasket is possibly providing a cooling effect to the sample. Annealing of a film of indium content $x = 0.55$, which was deposited on a sapphire substrate instead of directly on the amorphous chip membrane (series 3), also presents the same phase evolution. The higher c $\rightarrow \beta$ transition temperature can here be attributed to the higher indium content in the sample compared to the previous series, as will be discussed in Chapter 4. Series 4 and 5 are examples of samples on sapphire substrates that were annealed ex-situ in an oven under oxygen atmosphere. The annealing was performed at a single temperature of 800°C for 30 minutes and also in this case the material crystallized in bixbyite phase. This means an exposure of the 300 kV electron beam is not significantly influencing the phase formation.

Based on these findings, we can conclude that the experimental conditions do not play a role in the phase formation other than shifting the transition temperatures and the determining factor for phase stability is simply the ratio of indium to gallium in the material. Therefore, the presented results in Chapter 4 will mostly be limited to films annealed in-situ in vacuum and both films deposited directly on the chip and wedge samples on sapphire will be considered in the analysis.

2.5.3 Desorption at high temperatures

Table 2.2 contains the initial composition x_i of the samples, as well as the composition (in the central area of the deposition where TEM was performed) after annealing to the maximum temperature x_f, both of which are determined by EDXS in the scanning electron microscope (see Section 2.6.1) using an electron voltage of 7 keV. The spectra of the EDXS measurements are added in Appendix B. For most samples, the composition is not conserved, especially when heated at temperatures higher than 1000°C. The change is

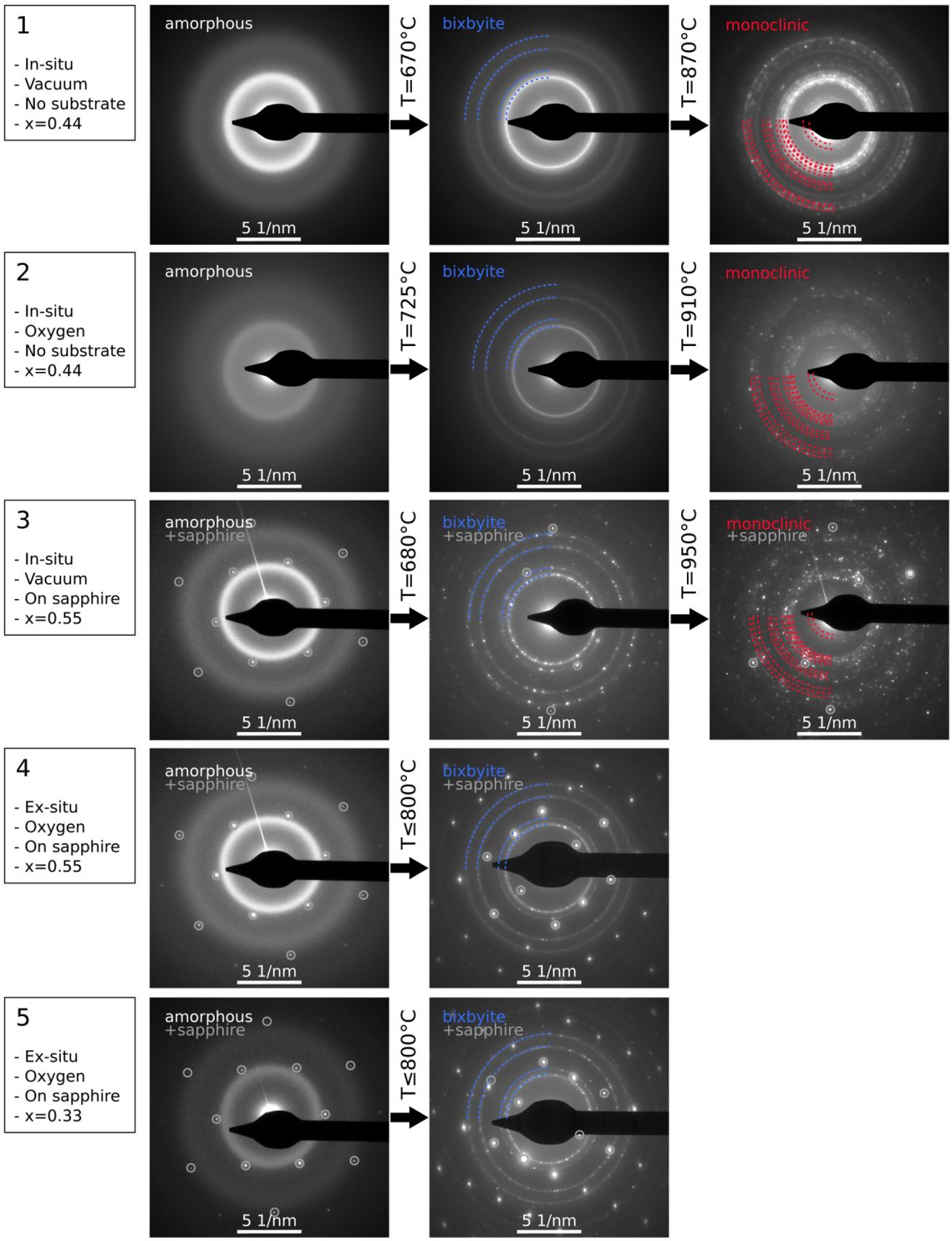

Figure 2.20: Comparison of the phase evolution in $(In_xGa_{1-x})_2O_3$ upon annealing by electron diffraction images for different sets of experimental conditions, which correspond to the grey-colored samples in Table 2.2.

characterized by a (partial) loss of indium, while the M_2O_3 stoichiometry of the film is conserved. For annealing temperatures close to 1000°C, the electron diffraction pattern of the film typically starts changing very quickly, with both existing spots that are disappearing and new ones that are appearing. The Debye-Scherrer rings completely disappear and diffraction spots seem almost randomly distributed. In Appendix C, a HRTEM image series in time shows how a Ga_2O_3 film is disappearing quickly under the intensity of the highly magnified electron beam at a temperature of 1000°C. The changes in chemical composition of the complete sample area before and after annealing in vacuum to 1080°C are visualized using SEM and EDXS in Fig. 2.21 for the film with initial indium content of $x_i = 0.44$. After annealing, the holes in the membrane underlying the deposited sample are much more visible in the SEM image, indicating a decrease in thickness of the film. The removal of material is stronger in the center than closer to the edges. The EDXS maps of each individual element confirm this observation: no indium at all is left in the central region and also the amount of gallium is more strongly reduced there. In contrast, closer to the edges of the deposition, the average composition is conserved. Our suggestion is that the combination of heating the sample and the impact of the high-energy electron beam is strongly damaging the sample and causing decomposition and desorption. Electron stimulated desorption [165] due to ionization has been observed during in-situ experiments in the TEM as described in literature [166,167]. The effect is less strong at the edges of the sample which are farther away from the electron beam position. Additionally, the heat distribution over the membrane might not be uniform, but peaked exactly in the central region located in between the edges of the electrodes, where desorption is the strongest. The reason why indium is desorbing more strongly than gallium and oxygen is not entirely clear. One aspect that might play a role in this process is that due to the weaker In-O bond compared to Ga-O [168], the former one is more easily broken by the combined effect of heat and electron beam energy leading to a stronger indium desorption. One in-situ sample with $x_i = 0.44$ and two ex-situ samples with $x_i = 0.33$ and $x_i = 0.55$ were heated only up to 800°C and there the composition of the film is still unaffected (see Table 2.2 and Appendix B).

Following the observation that for temperatures above 1000°C the $(In_xGa_{1-x})_2O_3$ material is not stable anymore and the composition starts to change, which will influence

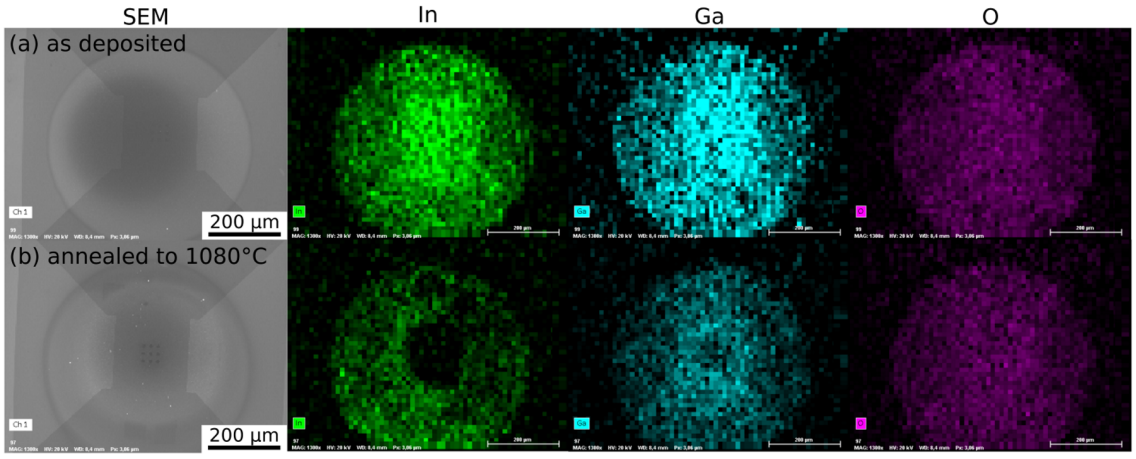

Figure 2.21: SEM images and EDXS signals of In, Ga and O elements of the $x_i = 0.44$ $(In_xGa_{1-x})_2O_3$ sample on the heating chip, (a) as deposited at 100°C and (b) after in-situ TEM annealing in vacuum to 1080°C.

the phase stability, these high temperature data will not be considered to build the phase diagram. It must be noticed that for the more indium-rich films, the degradation process already commences for temperatures slightly below 1000°C, and thus the phase diagram will be cut off at the corresponding temperatures.

2.6 Other characterization methods

2.6.1 Scanning electron microscopy and energy dispersive X-ray spectroscopy

The scanning electron microscope (SEM) functions similar to the STEM, as described in Section 2.4.4, but is operated at lower voltages (1 – 30 kV) and doesn't require a thin sample. The electron beam is focused on the sample surface and scans an area in (x, y)-space in a vacuum chamber. At each scanning point, the beam interacts with the sample material, producing different types of secondary radiation that are observed by different detectors:

- Secondary electrons: The beam electrons knock out secondary electrons from their atomic shell inside the specimen. They typically have a low energy (< 50 eV) and thus only secondary electrons created close to the surface will be able to escape the sample and reach the detector, which is placed at an asymmetric position with respect to the sample. This means the signal is very surface sensitive and a topographical image will be obtained from the detected electron intensities.

- Backscattered electrons (BSE): Elastically scattered electrons at high angles are detected by the back-scatter detector, which is positioned above the sample in a 'doughnut' type arrangement, concentric with the electron beam. Since heavy elements backscatter electrons more strongly than light elements, the BSE image has atomic number contrast and areas with different chemical compositions appear with different intensities. Using a segmented BSE detector, topography contrast can also be obtained by only counting electrons from one side of the detector.

- Characteristic X-rays: To fill the electron hole left behind by the secondary electron, an electron from a higher energy shell jumps into the empty position and the energy difference between the two shells is emitted in the form of an X-ray photon. Since the X-ray energy is specific to each element, detection of the X-ray energy spectrum by a semiconductor detector allows to identify the elements present in the sample and to quantify its relative composition. This elemental analysis method is called energy dispersive X-ray spectroscopy (EDXS).

The spatial resolution of the SEM depends on the energy of the electrons, the size of the electron probe when it hits the sample surface, and additionally for each type of signal individually on the size of the interaction volume, i.e. the volume of specimen material that interacts with the electron beam, as illustrated in Fig. 2.22. The resolution will typically fall somewhere between less than 1 nm and 20 nm, which is not high enough to image individual atoms as in TEM. Advantages of SEM are the possibility to investigate relatively larger sample areas, and to use bulk and unprepared material.

The SEM used in this work is an FEI Nova 600 equipped with a focused ion beam (FIB), which is tilted with respect to the electron beam by 52°. It can be used to sputter material from the sample in a desired way. The beam consists of Ga^+ ions with energies in the range of 5 – 30 kV and a minimum spot size of 5 nm.

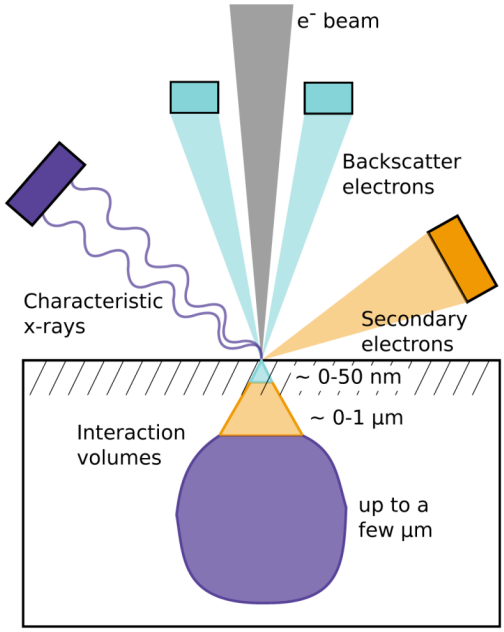

Figure 2.22: Schematic overview of the different secondary radiations produced in the SEM and their interaction volume within the specimen.

In this work, SEM-EDXS is used to quantify the indium content in our $(In_xGa_{1-x})_2O_3$ samples. The spectroscopic analysis of the EDXS spectra and calculation of the at% composition is done standardless by the software (EDAX Genesis) using the ZAF correction method. This method takes into account the influence of the atomic number (Z), the absorption effect (A) and the fluorescence excitation effect (F) on the intensity of the emitted X-rays. The FIB is used for the preparation of TEM lamellae for in-situ, as described in Section 2.5.1.

STEM-EDXS

Similar to EDXS in the SEM, we can apply EDXS in the STEM to get chemical composition information of our TEM sample with a high spatial resolution. The convergent STEM probe is scanned over the sample and the characteristic X-rays resulting from electron excitations in the specimen are detected. For quantification of the data, we use the Cliff-Lorimer method [169], also called the thin-film approximation method. The concentration ratio of element A to element B (C_A/C_B) is obtained from the equation $C_A/C_B = k_{A,B} \cdot I_A/I_B$, where I_A and I_B are the measured X-ray peak intensities and $k_{A,B}$ is a proportionality factor, which is determined by the ionization cross sections and fluorescent yields of the elements and some TEM specific parameters. In the case of our $(In_xGa_{1-x})_2O_3$ samples, $k_{In,Ga}$ is determined from a calibration measurement on a sample with known In/Ga ratio. Because of the high voltage in TEM and a sample thickness on the order of nm, it is justified to neglect the effects of atomic number, absorption and fluorescence excitation. In principle, atomic resolution EDXS is possible in the STEM, however, sample drift and instabilities of the stage may limit the spatial resolution of the measurement.

The STEM-EDXS measurements for this work are performed using a JEOL JEM2200FS operated at 200 kV microscope and equipped with a LN2 free energy dispersive X-ray SD detector (Bruker).

2.6.2 X-ray diffraction

X-ray diffraction (XRD) is a characterization tool to determine the crystalline structure, strain state and crystal orientation of materials. X-rays with a wavelength on the order of the atomic distances in the crystal are incident on the sample and the diffracted beams are detected by scintillation detector. The diffraction follows Bragg's law (Eq. 2.17) and the detected intensity, dependent on sample orientation and diffraction angle, gives information on the lattice spacing inside the crystal. The general set-up is depicted in Fig. 2.23. The specimen is mounted on a goniometer stage which allows movement in every direction and a ω-, ϕ- and ψ- tilt. A copper anode is used as X-ray source and a monochromator is placed in the beam line to select the Cu $K_{\alpha 1}$ radiation with a wavelength equal to 1.54056Å.

An $\omega - 2\theta$ measurement registers the diffracted X-ray intensity as a function of the diffraction angle 2θ. While the source is fixed, the detector scans the 2θ angle with a simultaneous sample tilt of $\omega = \theta$. At the angles where Bragg's law is satisfied, a peak in the X-ray intensity will be recorded that can be linked to a certain d_{hkl}. When the scattering vector[16] $\vec{s}$ (see Fig. 2.23) is normal to the sample surface, this measurement probes the out-of-plane lattice spacing. In case of an initial sample tilt off-set (along ω and/or ψ), also planes in other directions can be measured. For single-crystalline samples, only one family of peaks should be produced. For polycrystalline samples, typically an $\omega - 2\theta$ scan with Bragg-Brentano geometry is applied. Here, the incident beam is diverging on the sample and refocused at the detector, and $\vec{s}$ is always normal to the sample surface. In this way, a larger sample area is probed including thousands of polycrystallites. The many differently oriented polycrystals will have different sets of lattice planes normal to $\vec{s}$, and thus all possible diffraction peaks should be observed.

Once the orientation of the crystal is known, the presence of a certain hkl plane can be checked by a ϕ-scan. In this measurement, the diffraction angle 2θ is fixed to the corresponding d value and ω is set to the in-plane angle of the plane you are looking for. Then the XRD intensity is recorded while rotating ϕ over 360°. This will produce a peak for every orientation where the lattice spacing matches the preset value of d and provides information on the symmetry inside the crystalline sample.

In this work, XRD will be used as a primary investigation tool to distinguish amor-

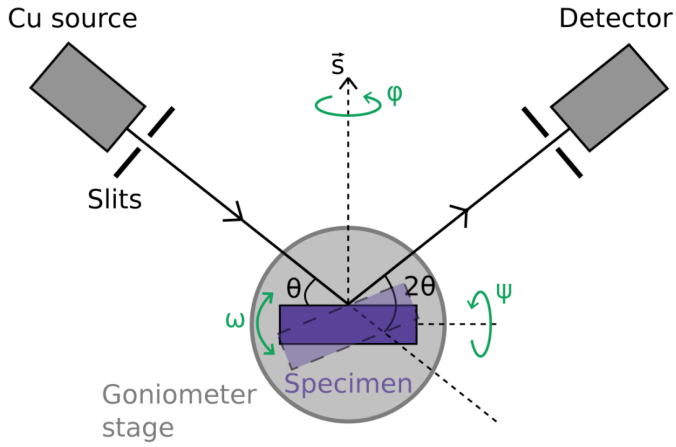

Figure 2.23: Schematic overview of the X-ray diffraction set-up.

[16] The vector that bisects the angle between the incident and scattered beam.

phous from single- and polycrystalline samples and to identify the crystalline phases present in the samples. It is also used to determine the desired in-plane orientation of the samples needed for TEM preparation.

3

Phase stability in epitaxial $(In_xGa_{1-x})_2O_3$ thin films

In this chapter, the crystalline phase formation in thin $(In_xGa_{1-x})_2O_3$ films grown at high temperatures is investigated on the nanoscale by cross-sectional TEM. Both heteroepitaxial films on c-sapphire substrates and pseudohomoepitaxial films on β-Ga_2O_3 and In_2O_3/YSZ substrate templates, that are obtained by three different growth methods (PLD, MBE and MOVPE), are studied. The experimental phase stabilities will be compared to the equilibrium phase diagram that will be constructed computationally on the basis of cluster expansion method and DFT. The epitaxial relations of the different observed phases with respect to the sapphire substrate will be reported throughout this chapter, and a summary of it is attached in Appendix D.

Partial results of the presented work in this chapter are published in: C. Wouters *et al.*, Phys. Rev. Materials 4, 125001 (2020) [119] and S. Bin Anooz *et al.* J. Appl. Phys. 125, 195702 (2019) [138].

3.1 Heteroepitaxy on c-sapphire by PLD/MBE

In this section, we describe the phase formation in heteroepitaxial $(In_xGa_{1-x})_2O_3$ thin films grown on c-sapphire substrates. We will focus mostly on results of a sample grown at $T_g = 680$°C and $p(O_2) = 3 \cdot 10^{-4}$ mbar with a continuous composition spread (CCS) ranging from $0 \leq x \leq 0.87$. Previously obtained XRD and EDXS results on this sample were published by H. von Wenckstern and C. Kranert in Refs. [49, 60]. These data will be presented first. Additionally, results from a CCS PLD sample grown at a comparable but slightly lower temperature of 640°C and with the introduction of Sn atoms during growth, and of a MBE film grown at 800°C and a mean indium content of $x = 0.67$ are discussed.

The EDXS and XRD data of the continuous CCS sample grown at $T_g = 680$°C and $p(O_2) = 3 \cdot 10^{-4}$ mbar are shown in Fig. 3.1. The wafer is 50 mm in diameter and the indium content changes from $x = 0$ to $x = 0.87$ across the wafer. Up to an indium content of $x \approx 0.15$, x increases slowly by 0.003/mm, while the increase from $x \approx 0.15$ to $x = 0.87$ occurs much more abruptly over a distance of only ≈ 10 mm, as visualized in the EDXS line scan in the lower panel of Fig. 3.1(a). To identify the crystallographic properties of

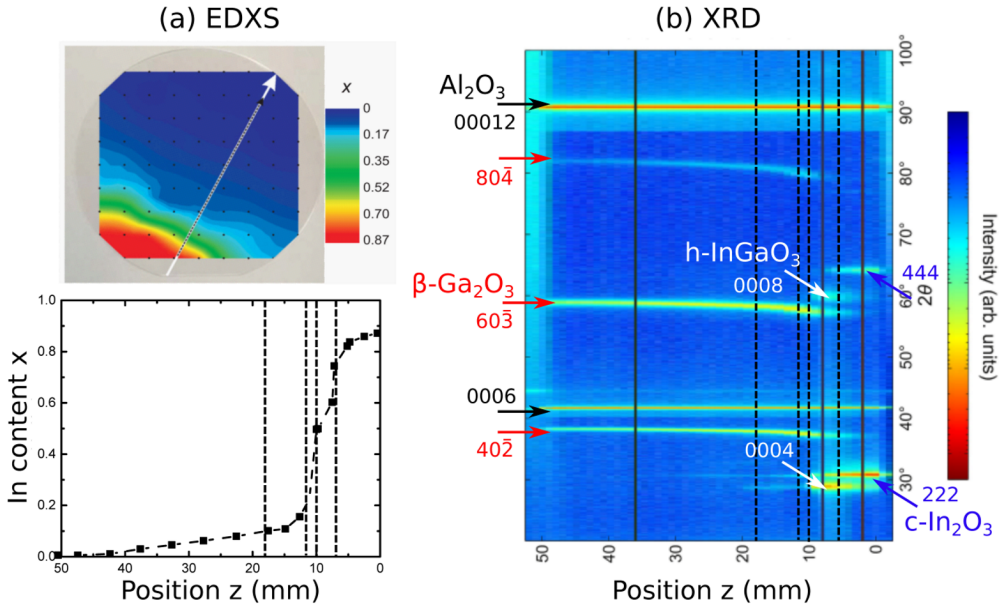

Figure 3.1: (a) EDXS map (up) and line scan along the compositional gradient (down) of the CCS wafer grown by PLD at $T_g = 680°C$ and $p(O_2) = 3 \cdot 10^{-4}$ mbar. (b) XRD $\omega - 2\theta$ scan along the compositional gradient of the thin film wafer. The positions on the sample were TEM is done are indicated by the dashed black lines. Data from von Wenckstern *et al.* [49].

the film as dependent on the composition, an XRD $\omega - 2\theta$ scan is performed along the compositional gradient, as shown in Fig. 3.1(b). The (0006) and (00012) reflections of the Al_2O_3 substrate are indicated and may serve as a reference. The other reflections are attributed to the $(In_xGa_{1-x})_2O_3$ layer. For indium contents $0 \leq x \leq 0.5$ ($50 \geq z \geq 10$ mm), the dominating peak positions can be assigned to the $(\bar{2}01)_n$ family of planes of the monoclinic β-Ga_2O_3 phase (red arrows). A shift in the $(\bar{2}01)_n$ peak positions to lower 2θ angles with increasing indium content is observed. This corresponds to an increase in the lattice parameter, indicating that indium is incorporated in the monoclinic phase. Beyond an In content of $x = 0.5$, the angular position of the β-peaks stays constant, i.e. at a constant indium incorporation, up to a mean In content of the layer of $x \approx 0.8$. For indium contents $0.5 < x \leq 0.87$, multiple phases are present in the layer. Peaks that can be assigned to the $(0004)_n$ family of reflections of the hexagonal $InGaO_3$ phase (white arrows) are dominating for $0.5 < x \leq 0.75$ ($10 > z \geq 5$ mm), while for $0.75 < x \leq 0.87$ ($5 > z \geq 0$ mm) the dominating peaks correspond to the $(222)_n$ family of reflections of the cubic bixbyite c-In_2O_3 phase (blue arrows).

The XRD measurement may give us a good estimate of the phases that are present at a given indium composition and their crystallographic orientation. However, the measured quantities are averaged over μm^2-sized areas both laterally and perpendicular to the surface. Thus, spinodal decomposition or phase separation on a shorter length scale, especially of the monoclinic phase in the composition range $0 < x \leq 0.5$, cannot be excluded. For nanoscale characterization of the phases and their distribution inside the layer in cross-section view, we therefore apply TEM. For the TEM results, we will distinguish between the 'mean' indium content $\tilde{x}$ as determined by SEM-EDXS in the scanning electron microscope (presented in Fig. 3.1) and the 'local' indium content x as determined by STEM-EDXS in the scanning transmission electron microscope. The

SEM-EDXS is performed in plan-view geometry and averages over μm-sized areas and the entire thickness of the film. Therefore, possible local variations in indium content due to nanoscale phase separation are not registered in the measurement of the global indium content $\tilde{x}$. Determination of the 'local' indium content x is carried out in cross-section on the film by STEM-EDXS with nanoscale resolution and will be important to determine the limits of indium/gallium incorporation in the separated phases.

3.1.1 Monoclinic phase at low indium content

At the positions indicated by black dashed lines in Fig. 3.1, which correspond to mean indium contents of $\tilde{x} = 0.1$, 0.25, 0.45 and 0.75, sample pieces are cut out and prepared for cross-sectional TEM characterization. For the three samples with the lowest indium concentrations, the TEM measurements show that the layers crystallize exclusively in the monoclinic β-phase. Since bright field, electron diffraction and STEM data of these three samples are similar, we present here some exemplary experimental results of the samples

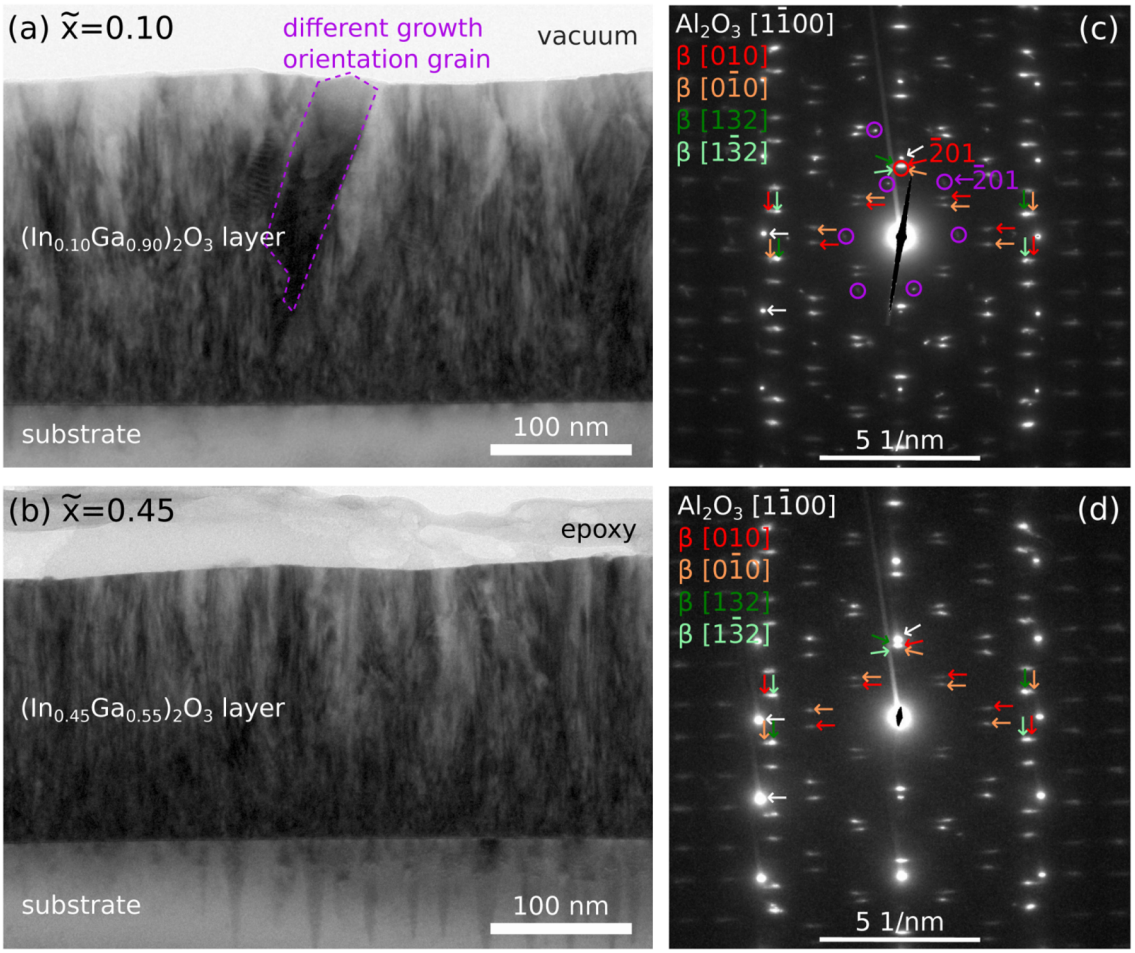

Figure 3.2: TEM bright field image of the monoclinic single-phase (a) $(In_{0.10}Ga_{0.90})_2O_3$ and (b) $(In_{0.45}Ga_{0.55})_2O_3$ films on sapphire grown by PLD. (b) and (d) show the respective electron diffraction patterns of a sample area containing both the substrate and the layer along the $[1\bar{1}00]$ zone axis of the sapphire substrate. In both layers, four different in-plane orientations with the same $(\bar{2}01)$ growth orientation of the β-phase are identified. In the film in (a), one β-phase grain with a different growth orientation is found of which the corresponding diffraction spots are assigned in purple in (c).

with $\tilde{x} = 0.10$ and $\tilde{x} = 0.45$. Fig. 3.2 shows typical bright field images of both samples in (a) and (b), respectively, which exhibit a similar grainy morphology, typical for these layers. The corresponding electron diffraction patterns taken in the $[1\bar{1}00]$ zone axis orientation of the sapphire substrate are presented in images (c) and (d). In the diffraction patterns of both samples, four different in-plane orientations of the β-phase can be identified, namely [010], [132] and the twinned orientations $[0\bar{1}0]$ and $[1\bar{3}2]$. This is confirmed in the STEM image of the film with $\tilde{x} = 0.45$ shown in Fig. 3.3, taken also along the $[1\bar{1}00]$ zone axis of the sapphire. In high magnification images of different grains, at the positions indicated by the rectangle shapes, the atomic pattern of the four different orientations is resolved and matched to the projected model structures. All grains have the same growth orientation with the $(\bar{2}01)_\beta$ planes parallel to the (0001) planes of the sapphire substrate, but are rotated in-plane by 60° with respect to each other. This is due to the symmetry mismatch between the monoclinic $(In,Ga)_2O_3$ layer and the hexagonal symmetry of the sapphire substrate, as described in [170]. In the film with an indium content of $\tilde{x} = 0.10$, rare monoclinic grains with a different growth orientation can be identified, such as the one indicated in purple in Fig. 3.2(a). From the electron diffraction spots produced by this grain, which are the ones circled in purple, the projection orientation can be identified as [010] but the $(\bar{2}01)$ planes are rotated by approximately 40° with respect to the other grains.

The TEM identification of the β-phase for the areas of the layer that exhibit an indium content of $\tilde{x} \leq 0.45$ is consistent with the findings of the XRD data shown in Fig. 3.1, i.e.

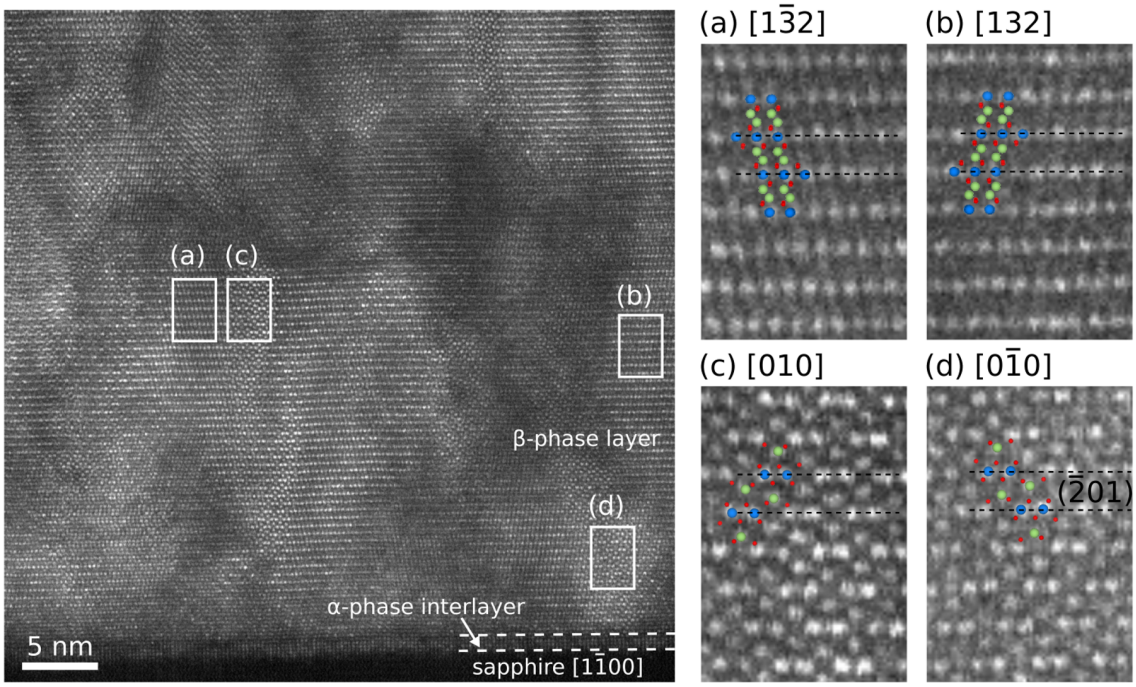

Figure 3.3: HAADF-STEM image of the monoclinic $\tilde{x} = 0.45$ sample, taken close to the interface with the sapphire substrate in $[1\bar{1}00]$ orientation. On the right, the indicated areas, which correspond to domains with four different in-plane orientations of the monoclinic phase, are enlarged to resolve the atomic pattern in each domain and fit it to the structure model in the corresponding projection orientation. All domains have the same growth orientation along the $(\bar{2}01)$ planes. The formation of 3 – 4 monolayers of α-$(In_xGa_{1-x})_2O_3$ phase at the sapphire substrate interface is indicated.

that the β-phase forms the predominant phase for compositions $0.0 \leq \tilde{x} \leq 0.5$ with $(\bar{2}01)$ as the main out-of-plane orientation of the layer. The XRD spectrum also indicates faint lines belonging to the hexagonal and cubic phase for $\tilde{x} \geq 0.1$. However, these phases are not observed in our TEM studies. Since the grain size of the crystallites ranges from 2 to 50 nm, an unambiguous identification of the phase requires a sample area that is thin enough for high resolution. Since this area is rather small ($\sim 1\,\mu$m laterally), it is possible that due to statistics we were unable to detect these grains and therefore the layer appeared single-phase monoclinic. However, X-ray diffraction might also find some residual grains that have crystallized on the surface.

In the STEM image in Fig. 3.3, the formation of $3-4$ monolayers of α-$(In,Ga)_2O_3$ on the α-Al_2O_3 substrate can be observed, before the layer growth continues in β-phase. This is a common phenomenon that is present for all $(In_xGa_{1-x})_2O_3$ layers grown on sapphire studied in this work and independent of the growth method used, the respective growth conditions or the In/Ga composition. This observation was already demonstrated in the epitaxial growth (PLD, MBE and MOVPE) of Ga_2O_3 on c-oriented sapphire by Schewski *et al.* [97]. Since the thin α-interlayer forms as a strain-stabilized phase in all heteroepitaxial films, it will not be considered in the phase diagram.

3.1.2 Hexagonal phase at intermediate indium content

For the CCS film discussed above, the XRD data in Fig. 3.1 showed that for $x > 0.50$ always a mixture of phases is present, as will be investigated in more detail in the next section. In contrary, for a CCS sample grown at a comparable but slightly lower temperature of 640°, the same oxygen pressure of $p(O_2) = 3 \cdot 10^{-4}$ mbar and with SnO_2 admixed in the PLD target, a single-phase hexagonal layer is obtained at a mean indium content of $\tilde{x} = 0.55$, as shown in Fig. 3.4(a). The electron diffraction pattern shows the epitaxial out-of-plane relationship $(0004)_\mathrm{h} \parallel (0006)_\mathrm{sapph}$ and in-plane relationship $[1\bar{1}00]_\mathrm{h} \parallel [11\bar{2}0]_\mathrm{sapph}$ (which implies $[11\bar{2}0]_\mathrm{h} \parallel [1\bar{1}00]_\mathrm{sapph}$) between the hexagonal phase of the layer and the corundum sapphire substrate. Similar to the monoclinic single phase layer in Fig. 3.2, the layer is not single-crystalline but the hexagonal phase consists of small grains with an average

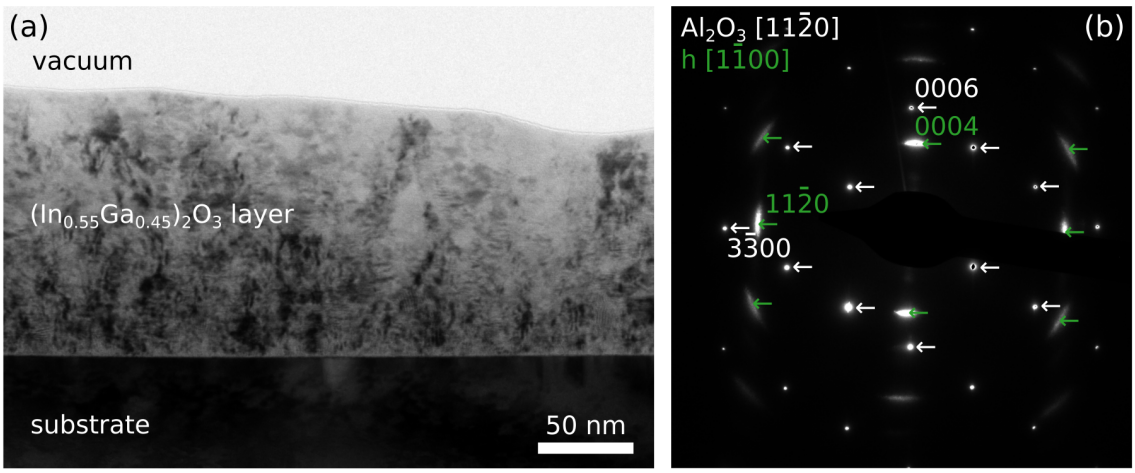

Figure 3.4: (a) TEM bright field image of a hexagonal single-phase $(In_{0.55}Ga_{0.45})_2O_3$ layer on sapphire grown by PLD at $T_g = 640°$ and $p(O_2) = 3 \cdot 10^{-4}$ mbar and (b) the diffraction pattern of an area containing both the substrate and the layer along the $[11\bar{2}0]$ zone axis of the sapphire substrate.

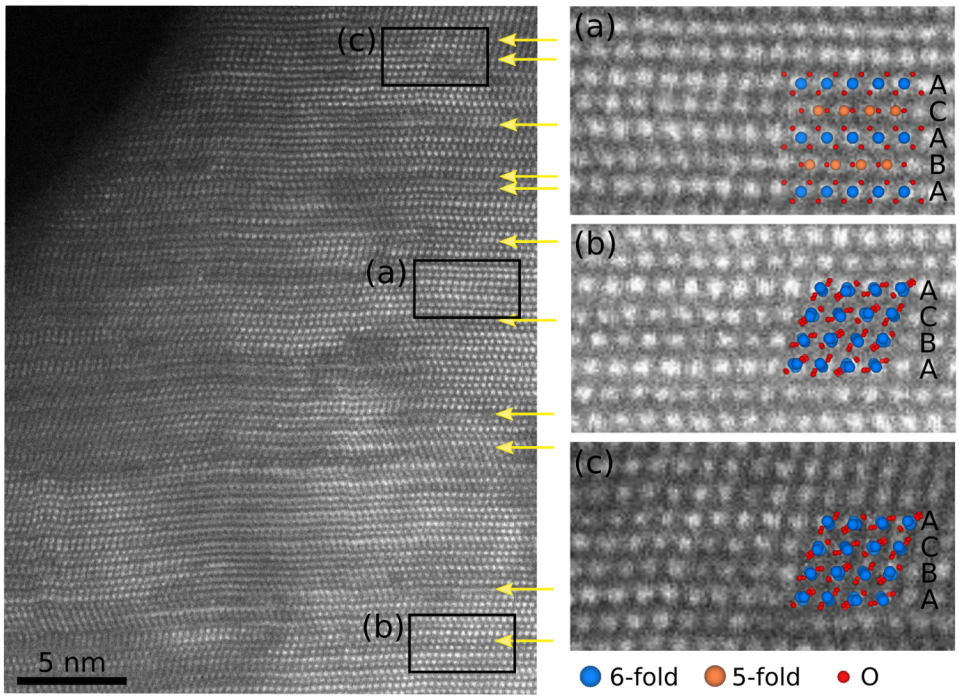

Figure 3.5: HAADF-STEM image of the hexagonal $(In_xGa_{1-x})_2O_3$ phase, showing its defective structure. The highlighted area in (a) fits to the ideal ABAC stacking of the hexagonal lattice in the $[11\bar{2}0]$ projection, while for the areas in (b) and (c) stacking faults transform the structure so it resembles more the ABC stacking of cubic bixbyite In_2O_3 in the $[1\bar{1}0]$ orientation. All such stacking faults are indicated by yellow arrows.

size of 7 ± 4 nm, as apparent from the short-range contrast variations in the bright field image of the layer. The grains all have the same epitaxial relationship to the substrate but are slightly off-orientated with respect to each other, which explains the streaky behavior of the diffraction spots.

A striking observation is the high amount of stacking faults present in the hexagonal phase, as illustrated in the STEM image in Fig. 3.5. The ideal ABAC stacking, which consists of alternating five-fold (orange) and six-fold (blue) cations layers in the hexagonal lattice, is observed in the highlighted area in (a) by overlaying the ball model structure. However, throughout the layer, many disruptions of this ideal stacking, as denoted by the yellow arrows, are revealed. Two such areas are shown at higher magnification in images (b) and (c). In those areas, we recognize an ABC stacking pattern that resembles that of cubic In_2O_3 of which the model structure is overlaid. This would mean that the five-fold coordinated cation layer is replaced by two consecutive six-fold coordinated cation layers. However, since the oxygen atoms are not visible in the HAADF-STEM images, we can not assign the coordination of these layers with certainty.

3.1.3 Phase separation at high indium content

Let us start here by focusing again on the CCS PLD sample grown at $T_g = 680°$ and $p(O_2) = 3 \cdot 10^{-4}$ mbar. TEM investigations of an area of the film with a mean indium content of $\tilde{x} = 0.75$, for which XRD clearly indicated the presence of both β, h- and c-phase, reveals a layered structure indicative of phase separation. In the bright field image in Fig. 3.6(a), three regions of different contrast can be observed which are identified by means of selected area electron diffraction and STEM. We find that the β-phase is observed

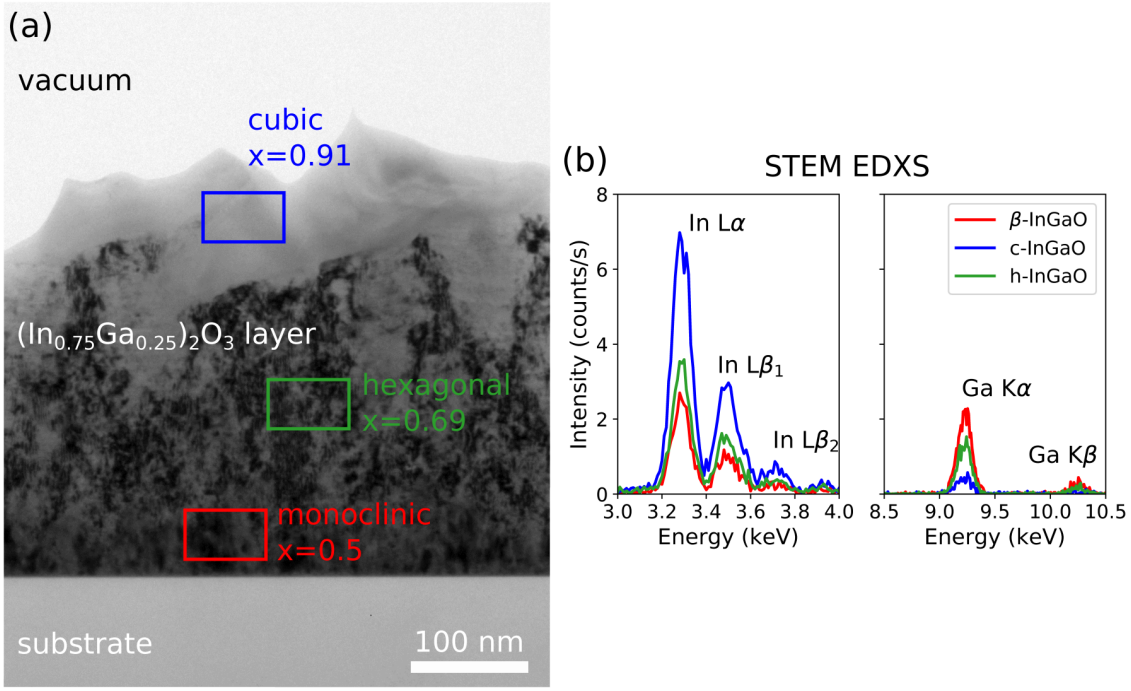

Figure 3.6: (a) TEM bright field image of a phase separated $(In_{0.75}Ga_{0.25})_2O_3$ thin film on sapphire substrate grown by PLD at $T_g = 680°$ and $p(O_2) = 3 \cdot 10^{-4}$ mbar. The local indium content x in the monoclinic, the hexagonal and the cubic regions is determined by the STEM-EDXS measurement shown in (b).

close to the interface with the substrate, followed by the h-phase, and the c-phase forming at the surface. For this phase separated sample, indium contents of $x = 0.50 \pm 0.02$ for the β-phase, $x = 0.69 \pm 0.03$ for the h-phase, and $x = 0.91 \pm 0.05$ for the c-phase are determined by EDXS. Two details of the STEM-EDXS spectra presented in Fig. 3.6(b) show how the relative height of the In L and Ga K X-ray peaks varies for the different phases due to the different amount of In/Ga incorporation. The β- and h-phase consist of small grains with average sizes of 6 ± 3 nm and 10 ± 5 nm, respectively, while the cubic phase is almost single-crystalline, as apparent by the more homogeneous intensity in the bright field image. Therefore, we note that for the β- and h-phase, the STEM-EDXS measurement is averaged over different few nanometer sized grains along the projection direction. This is not an issue for the c-phase because of the larger single-crystallites ($250 - 600$ nm).

Fig. 3.7 shows a layer with a mean indium content of $\tilde{x} = 0.8$, which was grown by PLD at $T_g = 680°$ and $p(O_2) 3 \cdot 10^{-8}$ mbar and with the presence of Sn atoms during growth. From electron diffraction and STEM-EDXS studies, we find the layer to exhibit a layered structure indicative of phase separation. Close to the interface with the substrate, the layer is composed of fine hexagonal grains, with an average indium content of $x = 0.70 \pm 0.03$. The hexagonal phase exhibits a similar morphology and orientation relationship to the substrate as the single-phase hexagonal layer. On top of the hexagonal phase, cubic $(In_xGa_{1-x})_2O_3$ crystals form with an indium content of $x = 0.91 \pm 0.03$. Just like the phase separated sample in Fig. 3.6, the cubic phase shows larger grains with sizes in the range of 35 to 285 nm (130 ± 80 nm). In contrast to the previous sample that shows phase separation, we find no evidence for presence of the monoclinic phase in the TEM measurements. This follows from the fact that this film was grown with tin in the PLD target which induces a catalyzed growth process under metal-rich conditions in which the

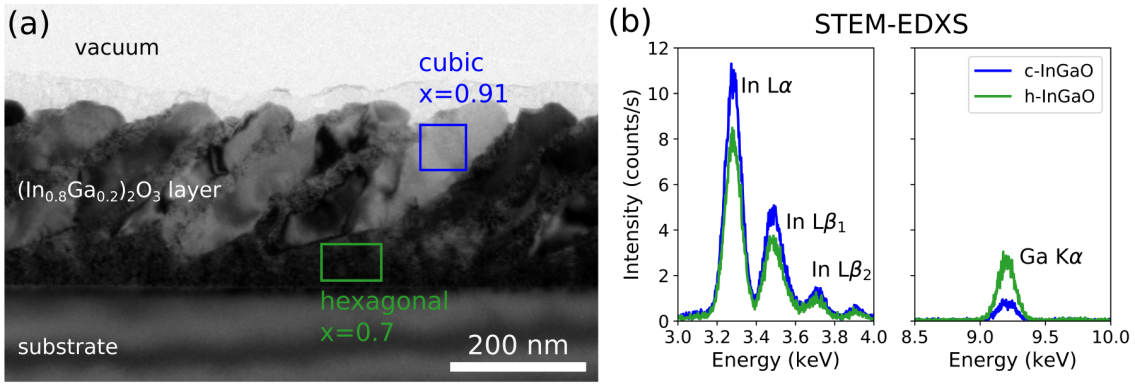

Figure 3.7: (a) TEM bright field image of a phase separated $(In_{0.80}Ga_{0.20})_2O_3$ layer on sapphire grown by PLD, with a local indium content of $x = 0.7$ in the hexagonal phase and $x = 0.91$ in the cubic phase, as determined by the STEM-EDXS measurement shown in (b).

orthorhombic κ-phase is stabilized over the β-phase [111, 171, 172].

Phase separation was also observed in a high indium content $(In_xGa_{1-x})_2O_3$ thin film with a mean indium content of $\tilde{x} = 0.67$ which was grown by MBE at a substrate temperature of $T_s = 800°C$. In HAADF-STEM images of the layer taken along the $[1\bar{1}00]$ zone axis of the sapphire substrate, presented in Fig. 3.8, large domains of brighter and darker intensity can be observed. Although STEM-EDXS was not performed on this sample, which means we don't have an estimate of the local indium content in the different intensity regions, the bright appearing regions can be assigned to indium-rich phase-domains while the darker grey regions are In-poor. The phase separated domains have sizes which range between 20 and 200 nm in size. From a high magnification STEM study, the lower indium content regions are identified as hexagonal $(In_xGa_{1-x})_2O_3$ in the $[11\bar{2}0]$ projection with the growth orientation along the (0001) planes. The atomic lattice consists of alternating layers of high intensity columns, i.e. containing more indium, and low intensity columns, i.e. containing more gallium. Similarly to the hexagonal $(In_xGa_{1-x})_2O_3$ in the PLD samples (see Fig. 3.5), the hexagonal lattice is not perfect but stacking faults transforming the stacking from ABAC to ABC are frequently observed, as indicated by the yellow arrows in Fig. 3.8(a). The short-scale average intensity variations in the hexagonal phase regions can be attributed to different grains, some of which are in perfect zone axis orientation, which give higher intensity, and others which are slightly off-oriented, resulting in reduced intensity. The bright indium-rich domains can be identified as cubic bixbyite $(In_xGa_{1-x})_2O_3$ in the $[1\bar{1}0]$ projection with the growth orientation along the (222) planes. As apparent in the magnified area in Fig. 3.8(b), the cubic structure perfectly follows the model structure and contains a low concentration of structural defects. The described out-of-plane and in-plane epitaxial relations with respect to the sapphire of both phases are the same as they are in the PLD layers. Together with the outcome of both PLD films, we can say that phase separation seems rather consistent in the $\tilde{x} = 0.67 - 0.91$ regime, independent of growth conditions or growth method.

3.1.4 Occupation sites of gallium and indium

High-resolution HAADF-STEM (Z-contrast) imaging in the TEM is used to determine the lattice site occupations of the gallium and indium atoms in β-, h-, and c-$(In_xGa_{1-x})_2O_3$. The analysis is based on the HAADF images presented in Fig. 3.9, which are taken along

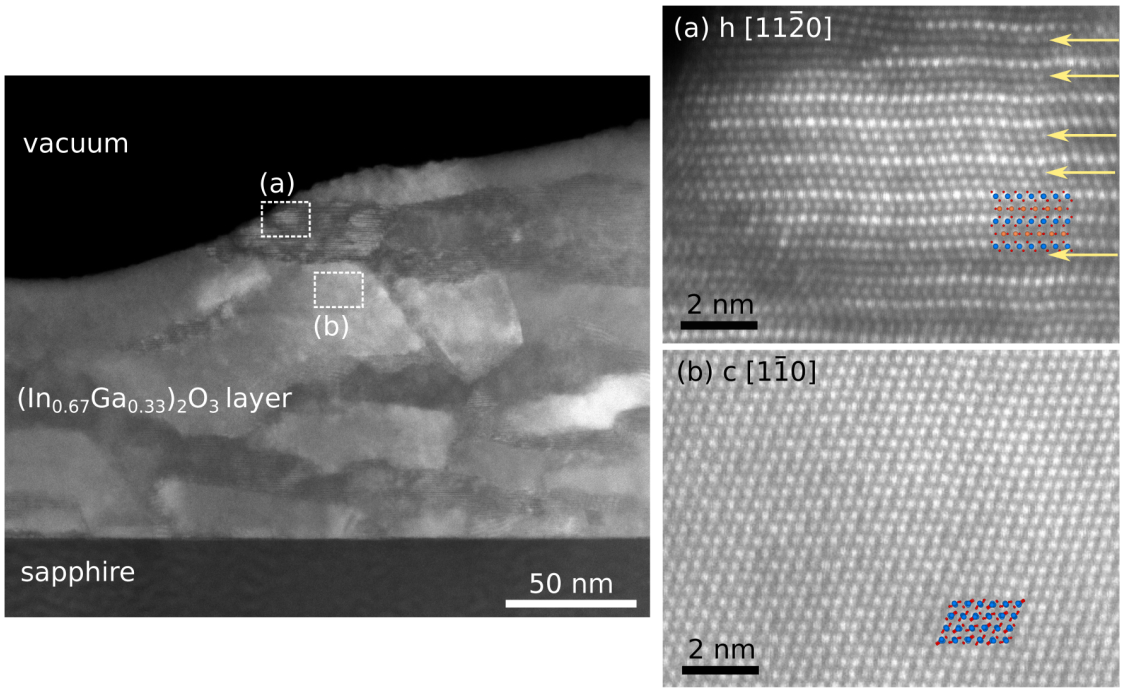

Figure 3.8: HAADF-STEM images taken along the [1$\bar{1}$00] zone axis of the sapphire substrate of a phase separated $(In_{0.67}Ga_{0.33})_2O_3$ layer grown by MBE at 800°C. Areas in the grainy hexagonal regions and in the bright cubic domains are magnified in (a) and (b), respectively, and the model structures are fitted to the experimental pattern in the [1$\bar{1}$0] and [11$\bar{2}$0] projections. Similar stacking faults, indicated by yellow arrows, as described in Fig. 3.5 for PLD layers, are found in the hexagonal structure.

the [010], [11$\bar{2}$0] and [1$\bar{1}$0] zone axis orientations of the respective lattices and have indium contents of $x = 0.45$, 0.55 and 0.91, respectively. In these specific lattice orientations, cations of the same coordination environment are aligned along columns. Thus, by matching the experimental high-resolution image pattern to the projected ball models of the structures (without oxygen), a unique coordination environment can be assigned to each intensity spot. In the monoclinic and hexagonal lattices, this distinguishes four-fold or five-fold coordinated columns from six-fold coordinated columns, respectively, while in the bixbyite lattice all columns are six-fold coordinated.

The black intensity line profiles shown at the bottom of Fig. 3.9 are averages of multiple line scans extracted along two different cation columns for each of the phases, as indicated by the white arrow in the structural images. The higher HAADF intensity on the six-fold lattice positions compared to the four- and five-fold lattice positions for the β- and h-phase, respectively, indicates in both cases a preference of the heavier indium atoms for the six-fold coordination environment. To quantify this, HAADF-STEM multislice simulations of the corresponding structures were performed. In the monoclinic simulated structure with $x = 0.45$, all indium atoms are randomly distributed on octahedral sites only; in the hexagonal simulated structure with $x = 0.55$, all octahedral sites are occupied by indium atoms and the remaining 5% of indium is randomly distributed on the five-fold sites. The simulated images are shown as insets on the experimental HAADF images and a good agreement is found. Similar intensity line profiles along two differently coordinated atom columns are extracted from the simulated HAADF-STEM images and added as red curves in the graphs. For the hexagonal phase, a perfect agreement is found

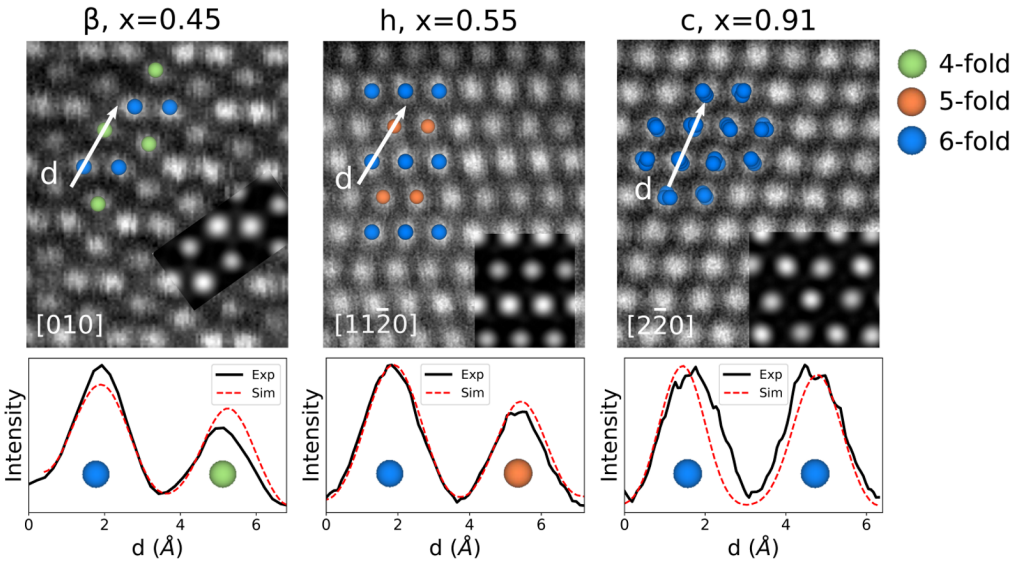

Figure 3.9: Experimental high-magnification HAADF-STEM images (several images summed to enhance contrast) of β-, h-, and c-$(In_xGa_{1-x})_2O_3$ with overlay of the ball models of each structure without oxygen atoms. The insets in the lower right corners show simulated HAADF-STEM images by the multislice method. The lower plots show experimental (black) and simulated (red) HAADF intensity line profiles (multiple averaged) along two different atom columns, as indicated by the white arrow in each of the structural images. The coordination environment of the atoms in the projected columns is indicated by the colored balls.

between experiment and simulation, while for the monoclinic phase the trend is similar but the intensity difference is slightly higher for the experimental structure. A possible explanation for this small discrepancy could be a locally higher indium content with all extra indium atoms incorporated on the octahedral sites as well. In contrast to the β- and h-phases, only slight variations in intensity of the different columns are observed in the HAADF-STEM image of the cubic bixbyite phase. Since all cation lattice sites have the same six-fold environment, gallium atoms have no preference for a specific site and they are statistically incorporated in the lattice. This is proven as well, by a comparison to a simulated bixbyite lattice with $x = 0.91$ in which indium and gallium atoms are randomly distributed in the supercell. These results provide experimental evidence for the strong preference of In^{3+} for an octahedral coordination environment and indicate that the occupation of the lattice sites by indium and gallium is consistent between the various phases across all examined compositions.

3.2 Pseudohomoepitaxy on β-Ga_2O_3 and c-In_2O_3

3.2.1 In solubility in β-Ga_2O_3 by MOVPE

Two samples, which are part of a series of β-$(In_xGa_{1-x})_2O_3$ thin films grown by MOVPE on β-Ga_2O_3 (100) substrates with increasing indium flow rate over the range 0 to 0.26 μmol/min, are investigated in cross-section view by TEM. Bin Anooz *et al.* [138] showed by $\omega - 2\theta$ XRD measurements that the (100) out-of-plane lattice parameter of the films increases up to an indium flow rate of 0.13 μmol/min, at which point it starts to decrease again upon a further increase of the indium flow rate.

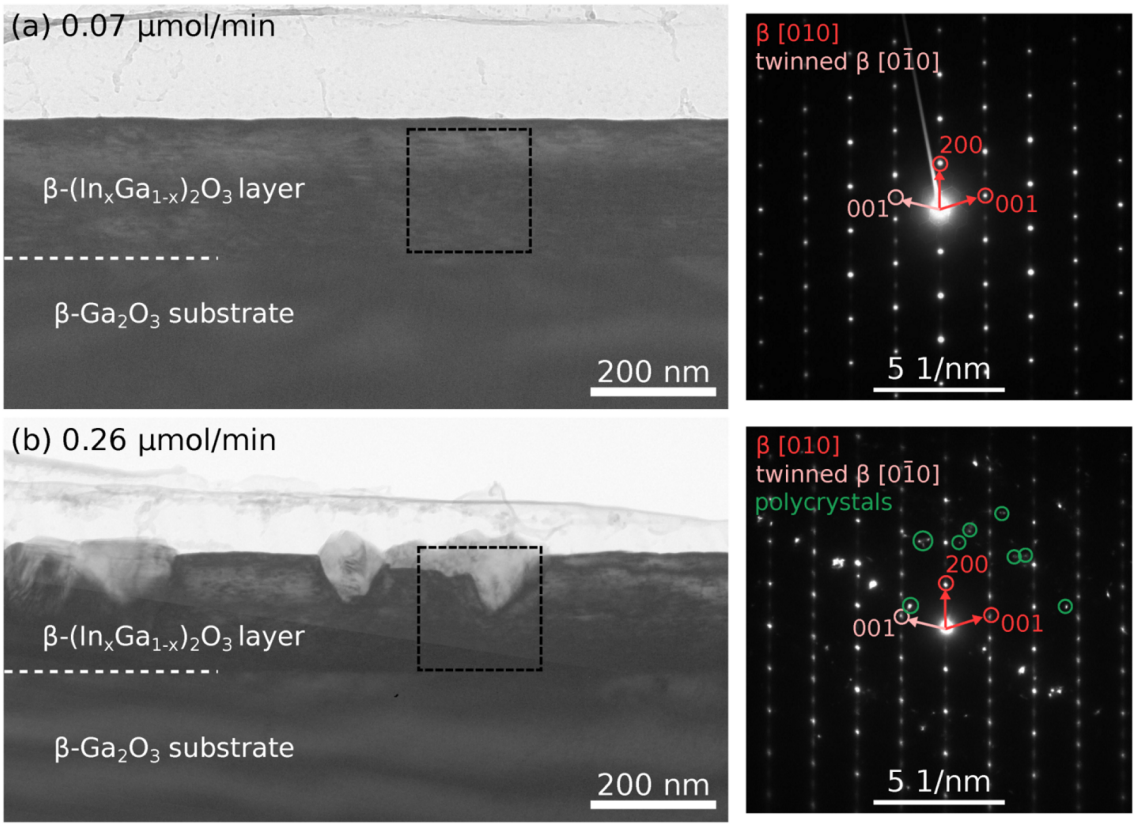

Figure 3.10: Bright field TEM images of MOVPE grown β-$(In_xGa_{1-x})_2O_3$ thin films grown at (a) 0.07 μmol/min and (b) 0.26 μmol/min indium flow rate on β-Ga_2O_3 (100) substrates, with on the right the respective diffraction patterns of the areas indicated by the dashed rectangles. Redrawn from Bin Anooz *et al.* [138].

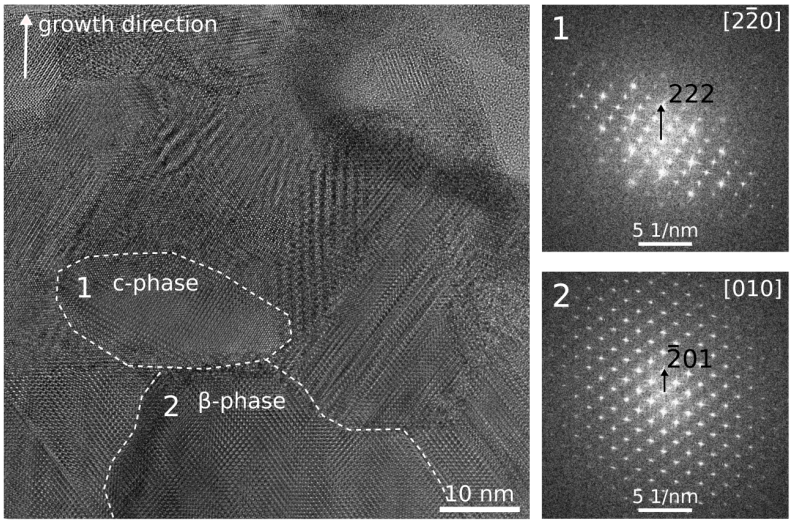

Figure 3.11: High resolution TEM image of a polycrystalline, phase separated 'island' in the MOVPE sample grown with an indium flow rate of 0.26 μmol/min. A cubic $(In_xGa_{1-x})_2O_3$ and a β-$(In_xGa_{1-x})_2O_3$ grain are indicated with their respective fast Fourier transforms, which show the (222) and ($\bar{2}$01) growth orientations, respectively. Redrawn from Bin Anooz *et al.* [138].

The bright field TEM image of the film grown at an indium flow rate of 0.07 μmol/min, shown in Fig. 3.10(a), exhibits no contrast variations that would indicate the formation of additional phases. The indium is thus completely incorporated in the β-phase layer. The only contrast variations in the layer come from planar defects that lie parallel to the (100) growth surface and can be attributed to the formation of twin lamellae and twinned domains, frequently observed in homoepitaxial (100) β-Ga_2O_3 films as described in the works of R. Schewski *et al.* [135,136]. This becomes obvious from the diffraction pattern of the layer [Fig. 3.10(a)], in which the dominant reflections can be assigned to the [010] orientation, i.e. equal to the substrate, while the less intense spots can be identified as the twinned $[0\bar{1}0]$ orientation. These twin lamellae form easily when the diffusion length of the gas species is shorter than the average terrace length on the growth surface, which is the case here for a relatively small miscut angle of the substrate of 2°. For the film grown at 0.26 μmol/min, of which a bright field image is presented in 3.10(b), the presence of islands that appear at higher intensity in bright field contrast can be observed. They typically start to form mid-way in the layer and extend up to the surface where they stick out by a few tens of nm compared to the flat plateau parts of the layer surface. Laterally, they extend up to a few 100 nm in size, which is consistent with the AFM observations in Ref. [138]. In the diffraction pattern of the indicated area of the film, again the [010] and $[0\bar{1}0]$ orientations of the monoclinic matrix can be identified. Additional spots can be observed, which are due to the island, that indicate polycrystalline behavior. A high resolution TEM image of such an island in Fig. 3.11 shows that they consist of a polycrystalline mixture of cubic $(In_xGa_{1-x})_2O_3$ grains and monoclinic β-$(In_xGa_{1-x})_2O_3$ grains. The cubic grains show two preferential orientations, namely perpendicular to the (222) or (200) planes. The monoclinic polycrystalline grains are $(\bar{2}01)$ oriented, which differs from the (100) orientation of the rest of the β-$(In_xGa_{1-x})_2O_3$ layer. From the maximum shift in the β-$(In_xGa_{1-x})_2O_3$ (100) lattice parameter measured by XRD and taking into account the biaxial strain induced by the substrate, the maximum amount of indium that can be incorporated in the monoclinic lattice before phase separation with the formation of a bixbyite phase takes place, is estimated to be 4%, for the growth at 825°C [138].

3.2.2 Ga solubility in c-In_2O_3 by MBE

c-$(In_xGa_{1-x})_2O_3$ films grown by MBE on (111) YSZ substrates covered by a c-In_2O_3 buffer layer at a substrate temperature of T_s = 600°C are investigated by TEM to check how the phase formation develops for increasing Ga contents. Fig. 3.12(a) and (b) present cross-section HAADF-STEM images of c-$(In_xGa_{1-x})_2O_3$ films with $x = 0.91$, i.e. 9 % Ga, and $x = 0.86$, i.e. 14 % Ga, as determined by SEM-EDXS. Areas with reduced intensity areas at the interface between the substrate and the In_2O_3 buffer are regularly observed in the sample with 9% Ga. These could be identified as voids in the In_2O_3 buffer layer. A possible hypothesis for the void formation, is that In_2O_3 grows in the form of 3D islands on the YSZ substrate [173,174]. When such islands coalesce, certain areas might become overgrown and leave voids behind. Nevertheless, the final growth surface, as imaged in Fig. 3.12(c), appears flat and smooth due to the high stability of the (222) plane of the bixbyite phase [174], which could suggest a transition from 3D to 2D growth with increasing thickness. In the rest of the In_2O_3 and $(In_{0.91}Ga_{0.09})_2O_3$ layers, less significant HAADF intensity variations can be observed, the origin of which is investigated later

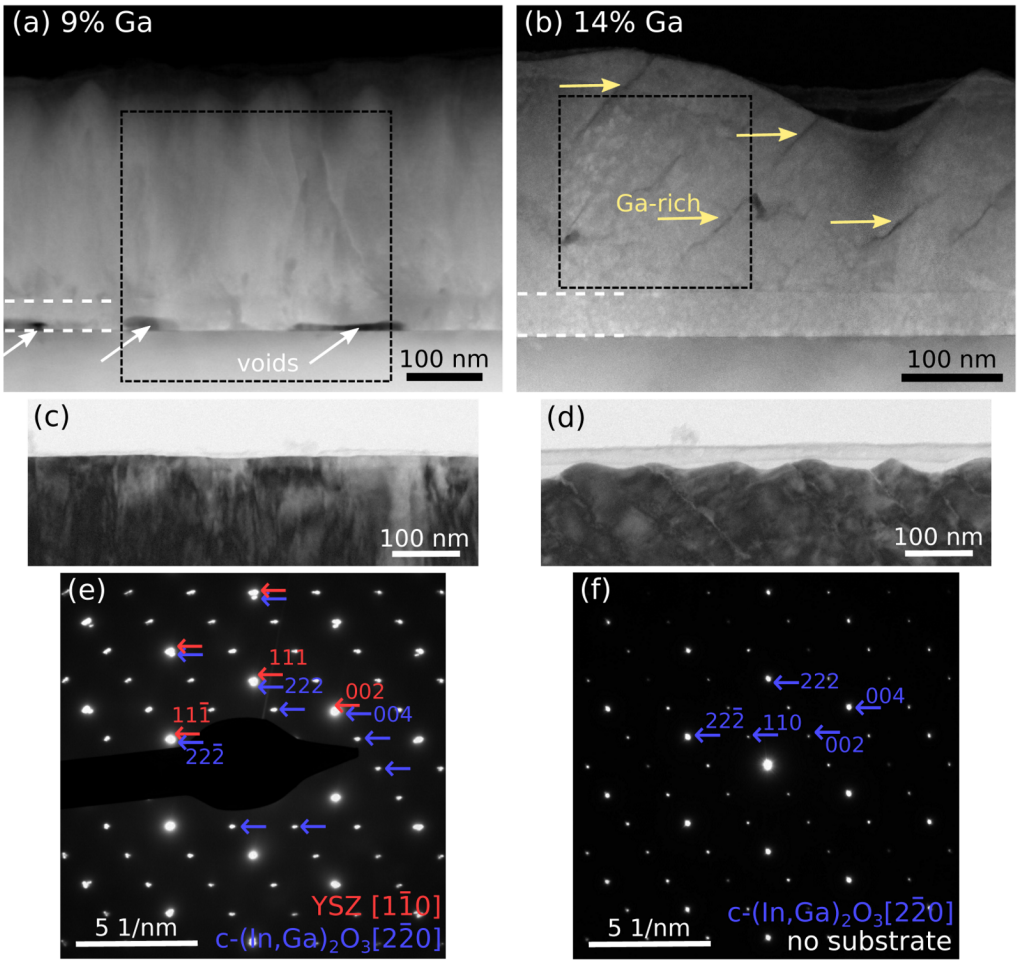

Figure 3.12: HAADF-STEM cross-section images of MBE grown $(In_xGa_{1-x})_2O_3$ films with (b) 9% Ga ($x = 0.91$) and (c) 14% Ga ($x = 0.86$), grown at a substrate temperature of $T_s = 600°C$. The white dashed lines indicate the interfaces between the YSZ substrate, the In_2O_3 buffer and the $(In_xGa_{1-x})_2O_3$ film. (c)&(d) are bright field images which show the as-grown film surfaces of both samples. (e)&(f) are electron diffraction patterns taken from the corresponding area indicated by the black dashed squares in (a)&(b), with spots belonging to the substrate and the film indexed in red and blue, respectively.

by STEM-EDXS. The film with a Ga content of 14% doesn't show voids at the interface, while the surface, as shown in Fig. 3.12(d), appears rougher with an average peak to valley distance of 17 ± 6 nm. This seems to suggest that the addition of more gallium to the growth process, induces a different growth mode along facets due to destabilization of the (222) plane. The most important feature here are dark HAADF intensity stripes traveling diagonally upward at a fixed angle through the layer, which will be identified as regions of increased gallium incorporation by the EDXS analysis shown below. Electron diffraction patterns [Fig. 3.12(e)&(f)] are recorded along the [1$\bar{1}$0] zone axis orientation from the areas in the samples indicated by the black dashed squares in images (a) and (b). These include a part of the substrate for the sample with 9% Ga, while for the sample with 14% Ga only the $(In_xGa_{1-x})_2O_3$ film is included. Because of the same symmetry of the substrate and the film and because $2a_{YSZ} \approx a_{In_2O_3}$, the diffraction spots of YSZ coincide closely with some $(In_xGa_{1-x})_2O_3$ spots. The coinciding spots appear brighter in Fig. 3.12(e) and are doubly indexed. In both cases only spots that correspond to the cubic bixbyite phase can

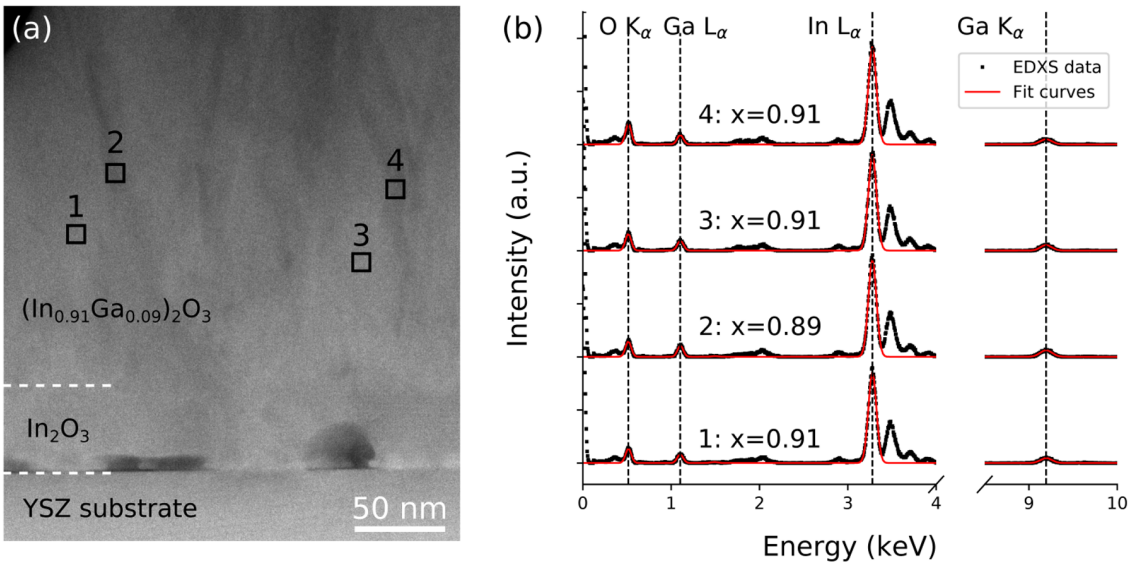

Figure 3.13: (a) HAADF-STEM image of the $(In_{0.91}Ga_{0.09})_2O_3$ film on In_2O_3/YSZ template. (b) STEM-EDXS spectra recorded as point scans at the positions indicated 1-4 in (a), with fit curves in red, which fit the O K_α, Ga L_α, In L_α and Ga K_α peaks as Gaussians.

be identified for the layer, and no additional phase is observed.

The sample with a Ga content of 9% was studied by EDXS in the STEM. Measurements were performed for points in areas that appeared with reduced (points 2 & 4) and increased (points 1 & 3) HAADF intensity, as shown in Fig. 3.13. The relevant spectrum peaks are fitted as Gaussians and the gallium content in the layer is quantified from the Ga K_α and In L_α peak intensities. The average x are determined to be $x = 0.91 \pm 0.01$ and $x = 0.90 \pm 0.01$ in the bright and dark HAADF regions, respectively. These values are equal within error bars and thus no correlation is found between lower STEM intensity and the Ga content in the film. This means that the gallium atoms are homogeneously incorporated in the cubic bixbyite lattice. Due to the low crystalline quality of the film as a consequence of island growth, the contrast variations can probably be attributed to void formation and different kinds of defects instead.

EDXS line scans crossing the dark stripe features of the sample with a mean Ga content of 14% (measured by EDXS in the SEM), were performed in a few different areas, to determine the Ga content as a function of position as shown in Fig. 3.14. We find increased Ga contents varying from 20 up to 50%, compared to the surrounding matrix in which an average Ga incorporation of 8% was measured. One of such dark stripes is imaged by HAADF-STEM at high magnification in Fig. 3.14(a) in the $[2\bar{2}0]$ zone axis orientation of the lattice. Bright spots correspond to projected atomic (In,Ga) columns, and the observed pattern fits to the bixbyite model structure. The bixbyite structure is preserved throughout the dark stripe without the formation of an additional phase or any lattice defects, which confirms the conclusion from the electron diffraction data that the layer is single-phase. The rough surface and the defined orientation of the Ga-rich stripes suggests a faceted 3D island growth, with phase separation resulting from the preferential incorporation of gallium at edges of voids and on well-defined facets. The edge of preferential incorporation seems to correspond to the $(22\bar{2})$ plane (equivalent to 222), as indicated in Fig. 3.14(a), and the edge travels both laterally and vertically (in the direction of the green arrow) through the layer. Similar Ga-rich features are observed in

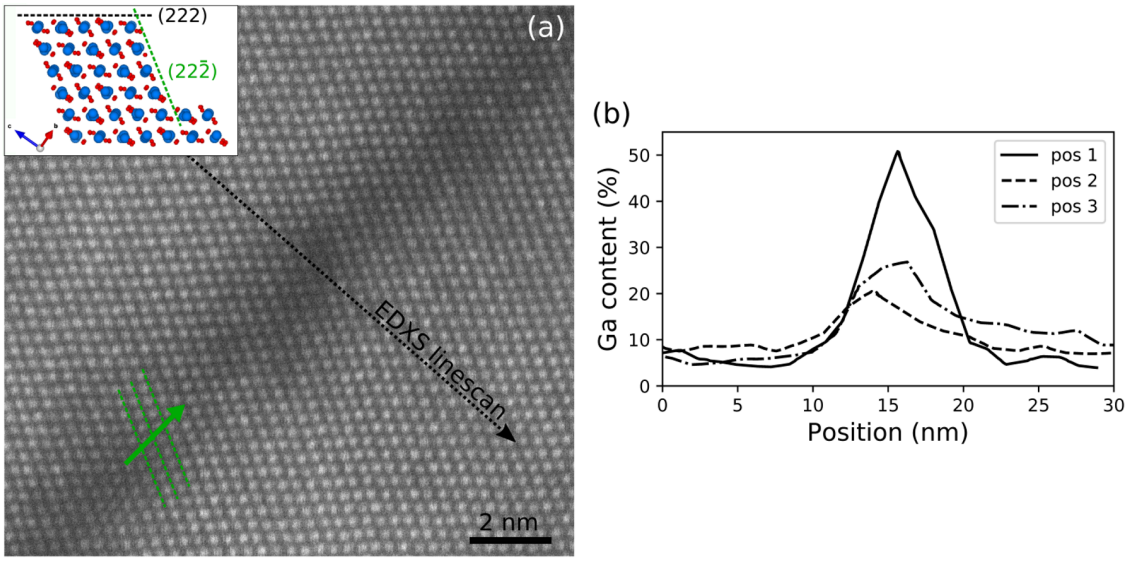

Figure 3.14: (a) High magnification HAADF-STEM image capturing one of the dark stripes traveling through the c-$(In_xGa_{1-x})_2O_3$ layer with $x = 0.86$ (14% Ga). The atomic pattern is resolved and fits to the model structure of cubic bixbyite phase in $[2\bar{2}0]$ orientation. (b) EDXS line scans across three different dark stripes showing an increased Ga incorporation in these areas.

the MBE growth of AlGaN, where enhanced Ga incorporation is observed on step edges due to a higher Ga desorption rate on the terraces [175].

3.3 Short summary of the experimental results

Heteroepitaxy. From the study of heteroepitaxial $(In_xGa_{1-x})_2O_3$ films on c-sapphire substrates with a continuously varying indium content in the range $0 \leq x \leq 0.87$ and grown in the temperature range 640°C–680°C using PLD, we obtained the following main results:

- For In contents up to $x = 0.5$, monoclinic single-phase films are observed.
- For In contents $0.55 \leq x \leq 0.7$, single-phase hexagonal $(In_xGa_{1-x})_2O_3$ can be achieved.
- For In contents $0.7 < x \leq 0.91$, we find phase separation into the cubic ($x = 0.91$), monoclinic ($x = 0.5$) and hexagonal phase ($x = 0.7$).
- For In contents beyond $x > 0.91$, we find single phase material in the cubic bixbyite structure.
- The monoclinic and hexagonal lattices show a pronounced ordering on the cation sublattice, were indium is preferentially occupying the six-fold lattice sites, while gallium is mostly incorporated on the four- or five-fold lattice sites, in β- and h-$(In_xGa_{1-x})_2O_3$, respectively.

These results are supported by the analysis of an indium-rich layer of $\tilde{x} = 0.67$ grown by MBE at 800°C on c-sapphire, which exhibits phase separation as well, with relatively In-poor hexagonal and In-rich cubic domains.

Pseudohomoepitaxy. The solubility limit of indium in the monoclinic phase was investigated for β-$(In_xGa_{1-x})_2O_3$ films grown on β-Ga_2O_3 (100) substrates by MOVPE. At the optimized growth temperature of 825°C, only 4% of indium could be incorporated before phase separated island including In-rich bixbyite grains formed on the surface. The solubility limit of gallium in the cubic bixbyite phase was determined for MBE c-$(In_xGa_{1-x})_2O_3$ films grown on YSZ substrates with an In_2O_3 buffer layer at 600°C. Up to 9% of gallium could be homogeneously incorporated in the film, while for a mean gallium content of 14% the gallium atoms clustered together to form confined Ga-rich bixbyite areas containing up to 50% Ga.

3.4 Computational phase diagram

In this section, the equilibrium phase diagram of $(In_xGa_{1-x})_2O_3$ is constructed, following the computational methodology described in Section 2.2.2. First, the minimum energy configurations of the different phases at 0 K are identified by cluster expansion and recomputed by DFT. This step of the procedure was carried out by Dr. Christopher Sutton from the Fritz Haber Institute. Next, the free energies at elevated temperatures are calculated by adding the configurational entropy, which considers the ordering on the cation sublattice found in experiment, and vibrational entropy of the solid solution. Finally, the convex hull and curvature of the free energy curves are analyzed to construct the temperature dependent phase diagram with binodal and spinodal lines.

3.4.1 $T = 0$ mixing enthalpies

Figure 3.15 shows the PBEsol-computed mixing enthalpy (ΔH) values (in eV/cation) of the lowest-energy structures of the β-, h- and c-phases at $T = 0$, as identified by the cluster expansion protocol, over the composition range $0 \leq x \leq 1$.

The ΔH curve of the cubic phase displays a concave parabolic shape over the whole composition range with a maximum close to $x = 0.5$. This energy surface is reminiscent of the regular solution energy of mixing in a crystal phase with only one type of lattice site, e.g. $(In_xGa_{1-x})N$ in the zincblende structure [15, 121] as described in Section 2.2. Indeed, in the c-phase all cation sites have equal six-fold coordination with respect to oxygen, which means all sites have equal probability to be occupied by either gallium or indium. In contrast, the evolution of ΔH for the β- and h-phase differs qualitatively from the classical behavior of the c-phase. This can be attributed to the fact that these structures contain an equal amount of mixed four-/six-fold and mixed five-/six-fold coordinated cation sites, respectively. For both phases, the lowest energy configurations in the range $0 \leq x \leq 0.5$ correspond to those where indium is incorporated only into the six-fold coordinated lattice sites. For the β-phase, this results in a rather flat evolution in the mixing enthalpy in this composition range, reaching a local maximum of $\Delta H = 0.035$ eV/cation around $x = 0.34$, followed by a decreases to $\Delta H = 0.024$ eV/cation at $x = 0.5$. At this concentration, all gallium atoms occupy the four-fold coordinated positions, and all indium atoms occupy the six-fold positions, creating a long-range ordered structure where all indium and gallium atoms are in their preferred coordination environment. For β-$(In_xGa_{1-x})_2O_3$ with $x > 0.5$, extra indium atoms can only be incorporated into the four-fold coordinated cation sites, which is energetically destabilizing and leads to the observed steep increase in energy. The h-phase is very unstable for the binary systems

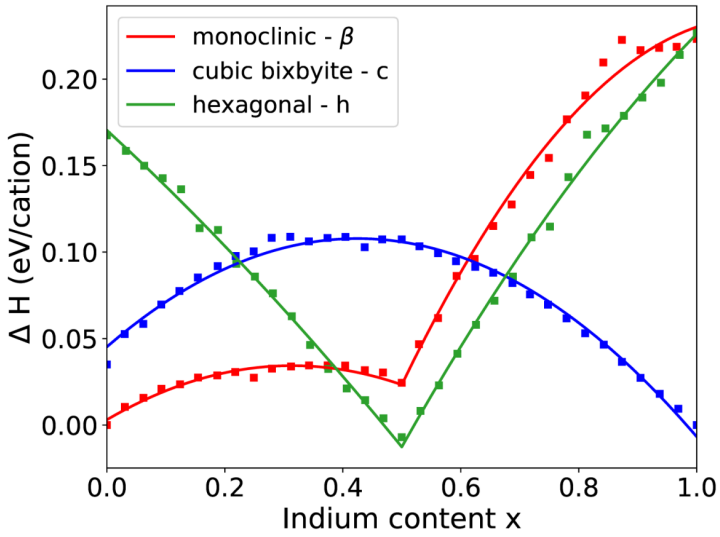

Figure 3.15: Mixing enthalpies (ΔH) for the lowest energy configurations of the β-, h- and c-lattices calculated by DFT using the PBEsol functional with fit lines to the data.

at $x = 0$ ($\Delta H = 0.167$ eV/cation) and $x = 1$ ($\Delta H = 0.23$ eV/cation), but displays a concave energy evolution and reaches a minimum at $x = 0.5$ ($\Delta H = -0.008$ eV/cation). At this concentration, the lowest-energy structure corresponds to one with all gallium atoms on the five-fold sites and all indium atoms on the six-fold sites. Similar to the monoclinic lattice at $x = 0.5$, this results in a long-range ordered h-structure, where the cation sites in consecutive lattice planes are either fully occupied by gallium atoms or by indium atoms. Deviating from the ideal composition $x = 0.5$ to either higher gallium or higher indium concentrations, disrupts this perfect order and requires to place In or Ga atoms into unfavorable bonding configurations, which causes a strong increase in the mixing enthalpy on either side of $x = 0.5$.

The sampled ΔH data points are fitted to a single parabola for the cubic phase and two distinct parabolas for $x \leq 0.5$ and $x > 0.5$ for the β- and h-phase to reproduce the sharp edges at $x = 0.5$. The fitted curves, depicted as full lines in Fig. 3.15, will be used for the calculation of the Gibbs free energies ΔG.

3.4.2 Ordered low-energy β- and h-configurations

The strong influence of the coordination environment of gallium and indium on ΔH is highlighted in Fig. 3.16(a), where mixing enthalpies are calculated for about 100 random configurations of all three lattice structures at $x = 0.5$. The mean effective coordination numbers (ECN)[1] [176] of the indium and gallium atoms are determined for each configuration and plotted as a function of ΔH. See Appendix E for a description of how the ECN is calculated. Clear trends can be observed for the β- and h-phase of respective decreasing and increasing ECN for indium and gallium with increasing mixing enthalpy. The lowest energy configurations in both phases are the one with all indium

[1] The ECN of an atom h is obtained through a weighted sum of its nearest neighbor atoms i, with the weight inversely proportional to the bond distance to atom h. For example, if atom h has six nearest neighbors at equivalent distances, then the ECN = 6. In the case that one of the six nearest neighbors has a slightly longer bond distance, 5 < ECN < 6 depending on how large the elongation of the bond distance is compared with the other five bond distances.

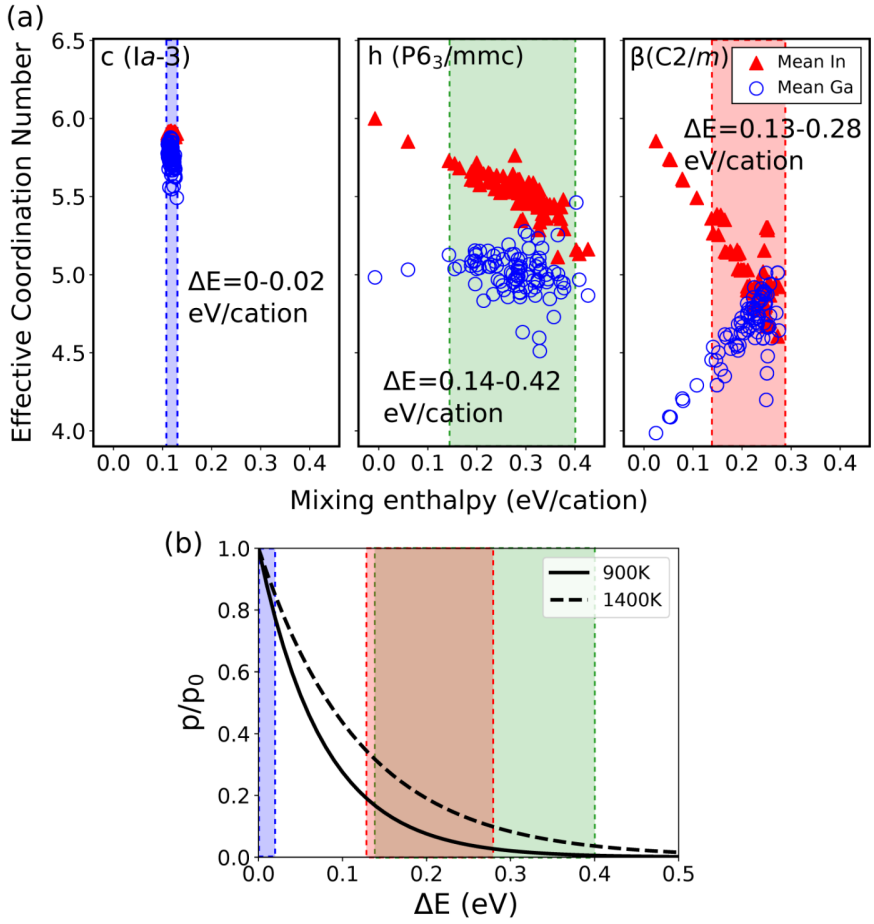

Figure 3.16: (a) Mean effective coordination number of indium and gallium in about 100 randomly generated structures for c-$InGaO_3$ (left), h-$InGaO_3$ (middle), and β-$InGaO_3$ (right), i.e. $x = 0.5$, plotted as a function of ΔH. In (b) the relative Boltzmann probability to occupy a configuration with an energy ΔE above the ground-state is plotted for two temperatures of 900 K and 1400 K. In both (a) and (b), the ΔE window where most configurations are distributed is indicated by the blue, green and red areas for the cubic, hexagonal and monoclinic phase, respectively.

atoms on six-fold sites and all gallium atoms on four- or five-fold sites, respectively. Disturbing these ordered structures by displacing indium and gallium atoms to the other coordination environment causes a strong increase in the mixing enthalpy. This is in sharp contrast to the situation for the c-phase, where the spread in mixing enthalpies is much smaller. Because the c-phase has only one type of coordination site, the only spread in the mixing enthalpies is caused by nearest-neighbor interactions. This result shows the strong energetic preference of indium for incorporation into six-fold coordinated lattice sites in the sesquioxide systems. This finding from theory is in excellent agreement with our experimental observation of the occupation sites of gallium and indium, that was presented in Fig. 3.9.

For the β- and h-lattices, there is an 'energy gap' between the ordered ground-state configuration and the majority of configurations, where very little configurations exist. This is because because misplacing indium atoms on the wrong coordination site, immediately causes a strong increase in mixing enthalpy. The relative probability p_i/p_0 to occupy configurations at an energy ΔE above the ground-state configuration is given according to

the Boltzmann distribution as

$$\frac{p_i}{p_0} \sim \exp\left[\frac{-\Delta E}{k_B T}\right], \tag{3.1}$$

resulting in the probability distribution shown in Fig. 3.16(b) for temperatures of 900 K and 1400 K. The energy windows where the majority of configurations are distributed for each phase are indicated by the colored rectangles in Figs. 3.16(a) and (b). For the hexagonal (green) and monoclinic (red) phase, the probability to occupy higher energy configurations at least 0.13 eV above the ground-state is rather low at realistic growth temperatures around 900 K (< 0.2). Even at the maximal temperature considered in this work of 1400 K, the probability is still only < 0.34. It is clear that the ordered β- and h-configurations are very hard to disturb. For the cubic (blue) phase, all configurations lie within an energy window of 0 – 0.02 eV above the ground-state and thus have almost equal probability to be occupied at these temperatures.

3.4.3 Temperature dependent phase diagram

A common approach to account for the configurational entropy is the ideal solution model (see Eq. 2.7), which starts from the assumption that all cation sites are energetically equal. Therefore, a random distribution of the two components on the cation sites is assumed. Being already in conventional solid solutions a simplified model, it holds in our case only for the cubic phase where the unit cell contains solely six-coordinate cation sites. Thus indium and gallium mix on all sites with approximately equal probability. The corresponding result for ΔS_{config} as a function of In concentration, with N_l taken to be the number of cation sites, is displayed as the blue curve in Fig. 3.17. However, based on the results of Fig. 3.16 and the experimental results showing a strong preference of indium for the six-fold sites, mixing in the monoclinic and hexagonal phase cannot be considered ideal and a different entropy term has to be applied. Configurational entropy is a measure for the configurational disorder, which in our case is proportional to the amount of different configurations of a lattice that are occupied. In the previous section, we showed that for the β- and h-lattices with In concentration $x = 0.5$, the probability to occupy other states than the ordered ground-state configuration is very small for the temperatures considered. Therefore, at $x = 0.5$ we can approximate the configurational entropy as zero. Further, we assume that for $x < 0.5$ indium and gallium are mixing only on the six-fold sites, while for $x > 0.5$ indium and gallium are mixing only on the four-/five-fold sites in β- and h-$(In_xGa_{1-x})_2O_3$, respectively. This means Eq. 2.7 has to be modified such that $N_l \to 1/2N_l$ and $x \to 2x$ for $x < 0.5$ and $x \to 2(1-x)$ for $x > 0.5$, which gives the red curve for the entropy in Fig 3.17.

The vibrational entropy, which ranges in between $10^{-7} - 10^{-9}$ eV/cation depending on T and x, is negligible compared to the configurational entropy and the mixing enthalpy. Thus it will not significantly influence the free energy.

Using the total entropy, the Gibbs free energies are calculated as a function of indium content for each phase for various temperatures. The free energy curves are plotted for $T = 0$ K, $T = 600$ K, $T = 1000$ K and $T = 1400$ K in Fig. 3.18. The thermodynamically stable phases and compositions can now be identified through the construction of the convex hull, which is represented by black lines and crosses in Fig. 3.18. The convex hull at $T = 0$ K (i.e., without any entropic contributions) includes only three stable structures at $x = 0$ (β-phase), $x = 0.5$ (h-phase), and $x = 1$ (c-phase). The unstable mixtures in the range

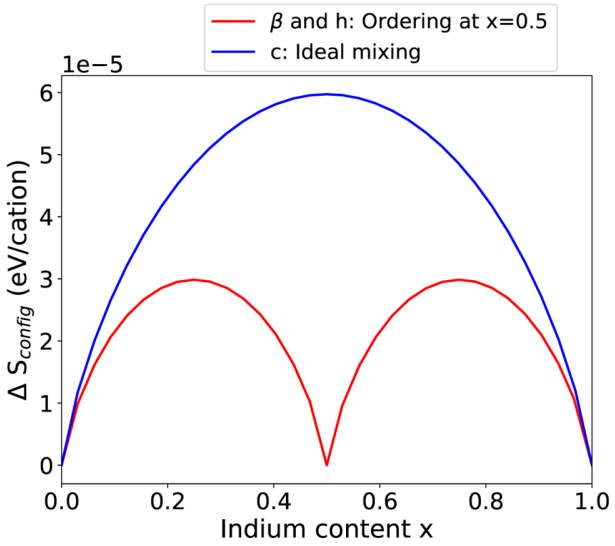

Figure 3.17: Configurational entropy as a function of indium content x. The cubic phase follows ideal mixing behavior, while for the β- and h-phase, the preferential incorporation of indium on the six-fold coordinated lattice sites alters the behavior of the configurational entropy.

$0 < x < 0.5$ will phase separate into β-Ga_2O_3 and h-$InGaO_3$ ($x = 0.5$). For the indium-rich regime ($0.5 < x < 1$), the negative curvature indicates phase separation into h-$InGaO_3$ ($x = 0.5$) and c-In_2O_3 ($x = 1$). At higher temperatures, the free energy curves become more convex due to the $-T\Delta S$ term, and more compositions will become stable, as can be seen by the appearance of more black crosses especially for $T = 1000$ K and $T = 1400$ K in Fig. 3.18. The limiting compositions for stability of each phase form the binodals and they are plotted for temperatures up to 1400 K in Fig. 3.19 by the dotted lines. The red, green and blue filled regions define the thermodynamic stable ranges for the β-, h- and c-phase, respectively. The stable range is rather narrow, especially for the h-phase which is practically only stable at $x = 0.5$ for all temperatures. The monoclinic phase is stable for a larger compositional window compared with the cubic one due to the rather flat ΔH curve of the β-phase for $x \leq 0.5$.

Since epitaxial growth methods (like PLD e.g.) do not always operate at thermodynamic equilibrium, it is also interesting to define metastable ranges in the $(In_xGa_{1-x})_2O_3$ phase diagram. To do this, we follow the work of Holder *et al.* [121], who have constructed phase diagrams including metastable regions for heterostructural material systems, like e.g. MgZnO. Compounds are labeled as metastable, meaning stable against small composition fluctuations, when the second derivative of the free energy curve is convex, i.e. $d^2G/dx^2 > 0$. The zero-crossings of d^2G/dx^2 at the four illustrated temperatures in Fig. 3.18 are indicated by crosses that match the curve color for each phase. These limiting compositions form the spinodals in the phase diagram, which are plotted by the squared colored lines in Fig. 3.19 for each phase. Metastable compounds are found in the region in the phase diagram between the binodal and the spinodal lines, which is colored grey. The black lines in the phase diagram define the 'critical' compositions for a phase transition, i.e. where the lowest energy structure changes from (1) monoclinic to hexagonal and from (2) hexagonal to cubic. They additionally limit the metastable region for each phase sepa-

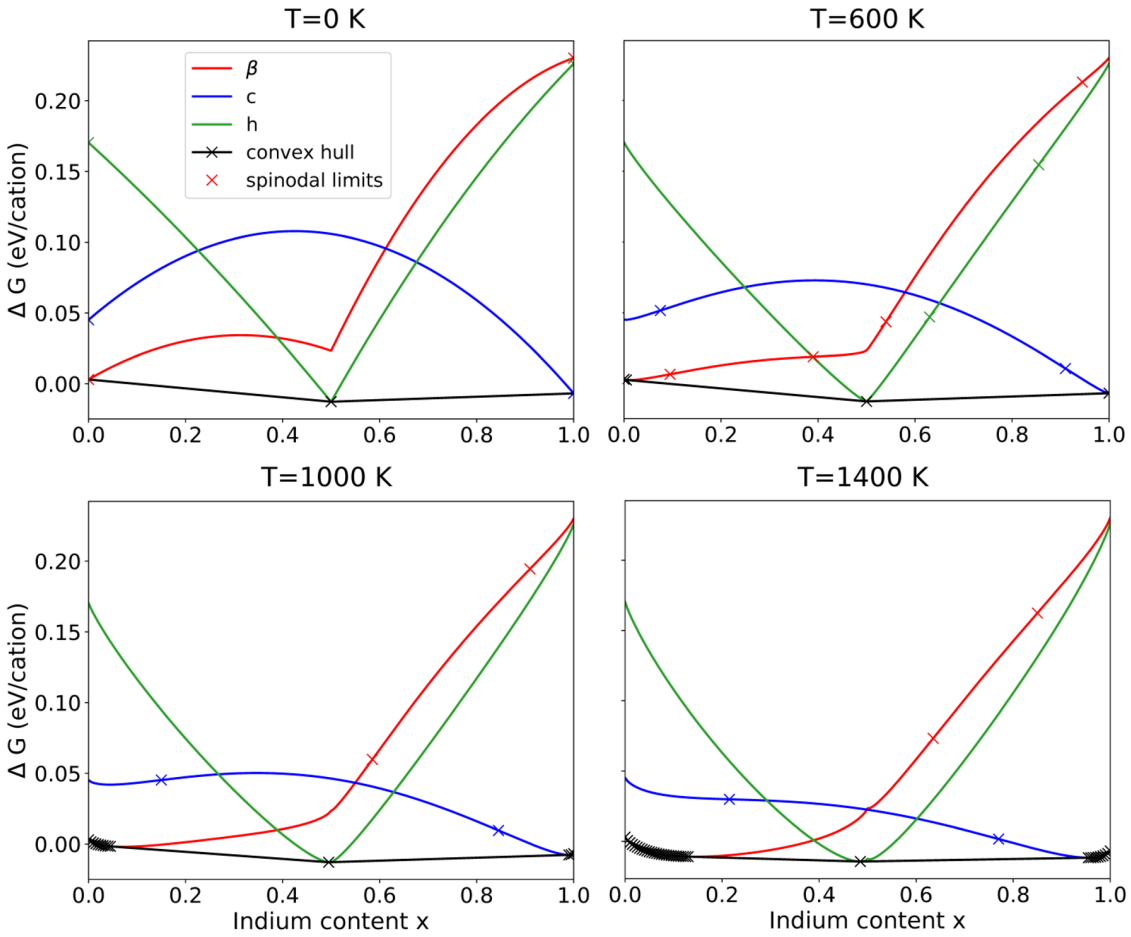

Figure 3.18: Gibbs free energies at $T = 0$ K, $T = 600$ K, $T = 1000$ K and $T = 1400$ K as a function of indium content for the β-, h- and c-phase. The global convex hull is indicated by the black crosses and line, the spinodal limits are indicated by the crosses matching the curve colors.

rately. At these critical compositions, the two touching phases have the same free energy. However, since the different phases have crystal symmetries that are related through a reconstructive transformation, bond-breaking is required (to change the coordination environments) for the phase transition. This imposes an additional (free) energy barrier for the phase transformations and thus an external energy input is required to accomplish these lattice changes.

At $T = 0$ K, binodal and spinodal limits coincide and no stable or metastable compounds exist. As the temperature increases, metastable regions start to open up for all three phases. For growth temperatures above 900 K (627°C), a large metastable region on the gallium rich side extends up to indium contents around $x = 0.6$, containing the monoclinic compound up to $x = 0.385$ and the hexagonal compound for $0.385 < x \leq 0.6$. For the monoclinic phase, this large metastable window is a result of the flat behavior of its ΔH curve in the range $0 \leq x \leq 0.5$ (see Fig. 3.15). This in turn follows from the fact that indium can be accommodated in its preferred six-fold coordinated environment for this composition range. As a result of this, for increasing temperatures, the free energy curve relatively quickly converts to a convex shape due to the entropy contribution. While for ideal mixtures, the spinodal is concave parabolic with a maximum at $x = 0.5$ where disorder is maximum, the monoclinic spinodal presents this behavior over the range

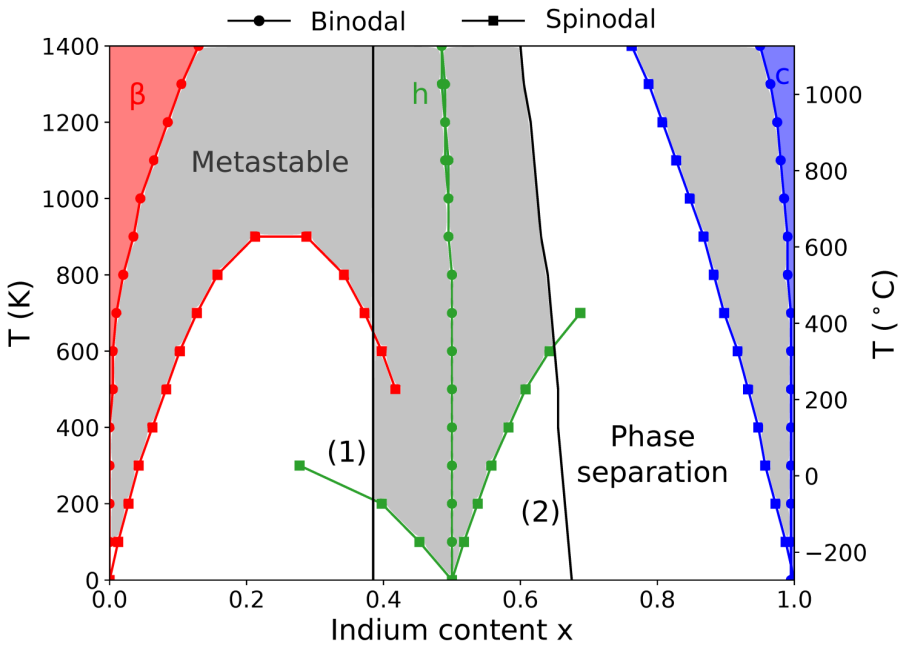

Figure 3.19: Computed temperature dependent phase diagram for $(In_xGa_{1-x})_2O_3$ including binodal and spinodal lines for the monoclinic (red), hexagonal (green) and cubic bixbyite (blue) phases. Thermodynamic stable composition ranges are color-filled, metastable ranges are grey, and for the white area below the spinodal lines phase separation is expected. The black vertical lines indicate the critical compositions where the lowest energy phase changes from (1) monoclinic to hexagonal and from (2) hexagonal to cubic.

$0 \leq x \leq 0.5$ with the maximum at $x = 0.25$ where disorder on the octahedral sites is maximum. Due to the more concave shape of the ΔH curve of the c-phase and the generally steeper increasing ΔH curves for $x > 0.5$, a miscibility gap remains up to temperatures of at least 1400 K (1127°C) on the indium-rich side of the phase diagram, where phase separation is expected into the hexagonal and the cubic phase.

3.5 Discussion

3.5.1 Computational results compared to literature

Previous computational work on the phase stability in $(In_xGa_{1-x})_2O_3$ is limited to the reports by Peelaers *et al.* [50] and Maccioni *et al.* [52, 177]. Both works are exclusively based on DFT calculations: Peelaers uses the HSE [178] hybrid functional, Maccioni uses the GGA approximation. The ΔH values calculated by Peelaers for the lowest energy configurations for a few compositions of the monoclinic and cubic bixbyite phases are shown in Fig. 3.20(a). Since Maccioni only presented free energy data at an elevated temperature of 800 K (527°C), we applied an ideal mixing entropy term (see Eq. 2.7) to Peelaers' ΔH data which allowed us to calculate ΔG at 800 K to obtain comparable curves. The free energy curves at a temperature of 800 K (527°C) of monoclinic, cubic bixbyite and hexagonal $(In_xGa_{1-x})_2O_3$, as obtained in these works, are compared to our results in Fig. 3.20(b).

A general observation is that the free energies of all three phases are overestimated in comparison to our findings, for almost the full composition range. This is a consequence

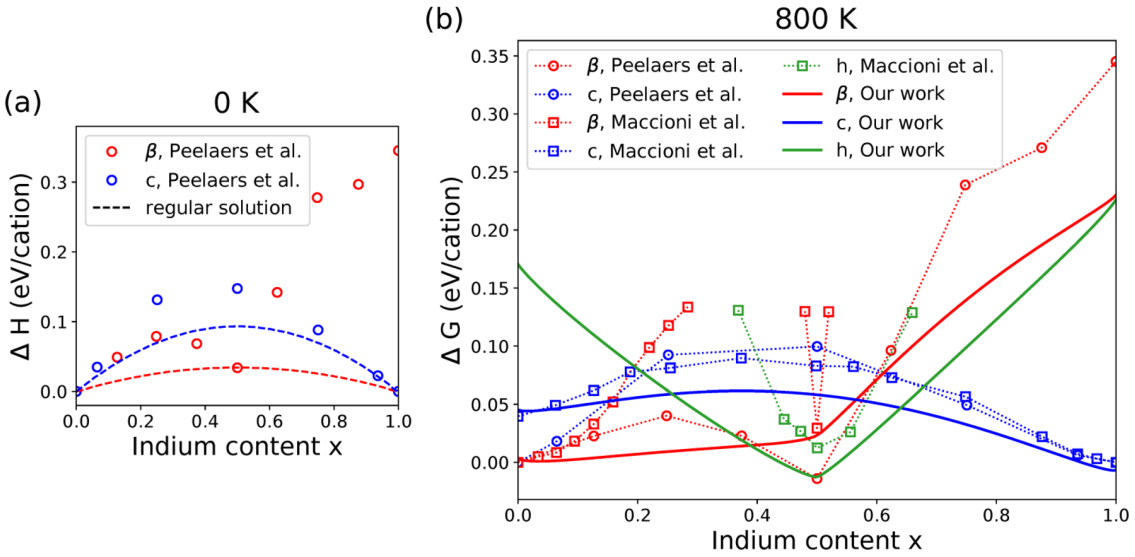

Figure 3.20: (a) ΔH values for the lowest energy configurations of the monoclinic and cubic bixbyite $(In_xGa_{1-x})_2O_3$ phases calculated by Peelaers *et al.* [50]. The parabolas indicate a lower bound for the data within the regular solution model. Adapted from Ref. [50]. (b) Free energies at 800 K (527°C) of monoclinic, cubic bixbyite and hexagonal $(In_xGa_{1-x})_2O_3$, as calculated by Peelaers *et al.* [50] (circles), by Maccioni *et al.* [52] (squares) and in this work (thick lines). The markers, which represent the sampled compositions, are connected by lines as a guide for the eye.

of their DFT approach, which is a rather inefficient method to calculate the energies of the large supercells required for these systems. They have sampled only a limited amount of configurations at each considered composition, which means that their energies form an upper bound for the minimum energy configurations. The smaller supercell sizes used by Peelaers *et al.* might act as an additional source of inaccuracy. In this respect, our cluster expansion approach is much more extensive and efficient and gives a more reliable prediction for the ground-state energies. Especially the ΔG values for the monoclinic phase in the range $x < 0.5$ as calculated by Maccioni *et al.* seem too high, because they probably haven't found the optimized configurations. Nevertheless, both works do mention that they find lowest energy configurations of the β-phase for $x \leq 0.5$ with indium only occupying six-fold coordinated sites, which agrees with our results. Only for the monoclinic phase close to $x = 0.5$, the literature ΔG values are comparable to our values or even lower in the work of Peelaers. This results from the fact that, in their case, the entropy was modeled as that of an ideal mixture, which means ΔS is maximized at $x = 0.5$. We, on the other hand, have set the entropy to zero at $x = 0.5$ after a careful consideration of the energetics of the system and a realization that the ordered configuration at $x = 0.5$ (all In/Ga on six/four-fold sites) is energetically very stable. Displacing gallium for indium on a tetrahedral site costs a large amount of energy, which means other $x = 0.5$ configurations are unprobable at realistic growth temperatures. This more realistic approach for the configurational entropy is an improvement compared to the previous works.

As mentioned before in the introduction, Peelaers' and Maccioni's predictions for the phase stability, as based on the free energy data, lack cogency and in addition are contradictory to each other. Peelaers *et al.* have simply approximated their monoclinic data by the regular solution model which assumes a parabolic ΔH curve (see Eq. 2.2). They

have defined the parabolas for the β- and c-phase in such a way that they form a lower bound for the mixing enthalpy at all sampled configurations, as visible in Fig. 3.20(a). This, however, provides an insufficient description of the data points and completely ignores the underlying physics given by the behavior of their monoclinic ΔH values. By applying an ideal mixing entropy term, only a very approximate lower temperature limit for full miscibility of the monoclinic phase at 812 K (540°C) is provided. Maccioni *et al.* also assume ideal mixing in all three systems and claim that the boundaries of stability (β: $x \leq 0.18$, h: $0.4 \leq x \leq 0.6$, c: $x \geq 0.9$) for each of the phases are independent of temperature, which is counter-intuitive. The entropy term should bring more compositions to a convex behavior for increasing temperatures, slowly reducing the miscibility gaps. Contrary to these conclusions for the stability, which are determined for each phase individually, our model provides a complete description of the stable and metastable ranges, based on the global convex hull of all considered phases. The results that we obtain are intuitive and they match with the prediction of large metastable composition ranges from Holder *et al.* [121] for heterostructural solid solution systems.

3.5.2 Experiment vs. computation: How ordering drives metastable phase formation

As a comparison between the experimental and computational results obtained in this chapter, the experimentally determined compositions from heteroepitaxial single-phase (circles) and phase-separated (diamonds) PLD and MBE samples have been overlaid on the computed phase diagram in Fig. 3.21, as well as the respective indium and gallium solubility limits obtained in pseudohomoepitaxial monoclinic [138] and cubic bixbyite [179] $(In_xGa_{1-x})_2O_3$ by MOVPE and MBE (squares). For the phase separated samples, the mean indium contents of the samples are indicated by the white diamonds, and the local indium contents in the separated phases (which are unknown for the MBE sample) by the connected colored diamonds. Additionally, literature data points (triangles) representing indium and gallium solubility limits, respectively, in monoclinic [48, 54, 61] and cubic [54] $(In_xGa_{1-x})_2O_3$ synthesized by different methods have been added.[2]

A first observation is that almost all experimental compositions exceed the narrow calculated thermodynamic stability ranges, and actually fit better into the calculated metastable windows. PLD, MBE and sol-gel methods are generating $(In_xGa_{1-x})_2O_3$ compounds in the metastable composition range and so extend the solubility limits as expected from thermodynamic equilibrium. Only the allowed indium incorporation in MOVPE grown β-$(In_xGa_{1-x})_2O_3$ of $x = 0.04$ at $T = 825$°C [138] agrees well with the predicted thermodynamic limit. Note that MOVPE is the growth method which operates closest to thermodynamic equilibrium. The powder sintering method by Edwards *et al.* [54] is also considered to deliver materials in thermodynamic equilibrium state, due to the long heating time at 1000°C. Therefore, kinetics should be excluded to play any role in phase formation since atoms by random walk have sufficient time to reach their energetic minimum. Indeed, the Ga solubility limit in the bixbyite powder fits well to the predicted equilibrium limit in our work. The maximum In incorporation of $x = 0.44$ in the monoclinic solid solution obtained in this way, however, strongly exceeds the thermo-

[2] We note that all included experimental data points were not obtained under the exact same oxygen regime, which is another important factor influencing the solubility limit of the occurring phases besides the temperature, but is not incorporated in our calculations.

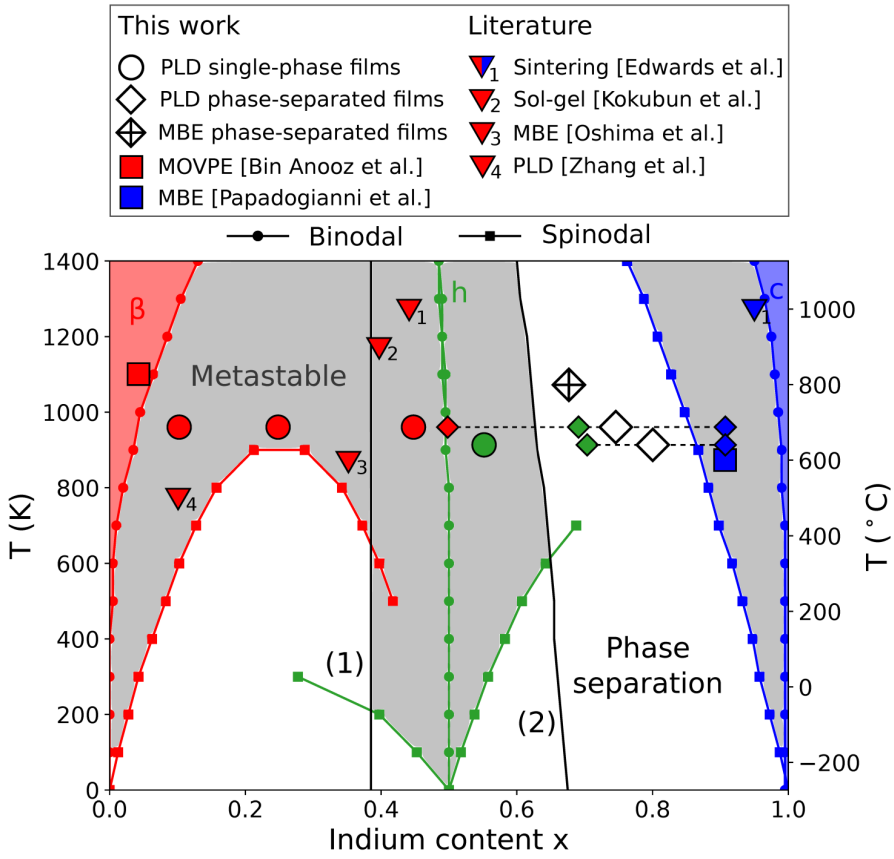

Figure 3.21: The computed phase diagram of $(In_xGa_{1-x})_2O_3$ with experimental data points from PLD and MBE heteroepitaxial films and MOVPE and MBE pseudohomoepitaxial films studied in this work (circles, diamonds and squares [138, 179]) and from other synthesis methods found in literature (triangles [48, 54, 61, 180]) added as symbols. The white diamonds denote the mean compositions of the phase separated films.

dynamic limit and corresponds to a metastable composition according to our calculations. Also in other powder, solution or bulk growth methods (at temperatures higher than 1200°C), rather high solubility limits in β-$(In_xGa_{1-x})_2O_3$ ranging between $x = 0.2 - 0.4$ are found [53, 55–58].

The key point to achieve these metastable compositions is the ability to form the low-energy ordered lattice configurations which the ΔH curves in Fig. 3.15 are comprised of. This is especially important in case of the monoclinic and hexagonal phases where the mixing enthalpy strongly varies with the lattice configuration, as was illustrated in Fig. 3.16. The majority of possible configurations in the β- and h-phase at $x = 0.5$ are approximately 0.2 – 0.3 eV/cation higher in energy than the ground-state configuration, and exceed even the ΔH value for the cubic phase (≈ 0.1 eV/cation). Thus, if ordering would somehow be kinetically forbidden, the β- and h-phase would not be found stable for such a wide composition range. We have evidenced by HAADF-STEM in Fig. 3.9 that the low-energy ordered lattices are forming in the case of PLD growth. This means that, at the growth temperatures employed, there is enough surface diffusion for the atoms to find their energetically preferred site, i.e. indium gets incorporated in its ideal six-fold coordination environment, while gallium mostly occupies four- or five-fold coordinated sites in β- and h-$(In_xGa_{1-x})_2O_3$, respectively. Once these ordered configurations of β- and

h-phase are formed, they are not easily disturbed due to the energy splitting between the ordered and disordered states. This is a very particular property of these multi-coordinated lattices. In the case of zincblende InGaN, which is a singly-coordinated lattice, no such energy gap between ordered and disordered configurations exists and all configurations are distributed within 0.12 eV/cation from each other [181]. For these metastable compounds, small composition fluctuations will be restored and phase separation requires an extra energy barrier to be overcome. Since the energy gain by phase separation given by the distance between the convex hull (black line) and the ΔG curves for concentrations between binodal and spinodal in the free energy plots in Fig. 3.18, is comparatively small, the driving force for phase separation is not sufficient.

Another important point to consider is the influence of kinetics. The basic concepts of phase formation have been developed for metals where diffusion takes place even at room temperature. This is completely different for covalently bonded materials as considered here. Even though surface diffusion is possible during epitaxial growth, bulk diffusion is hampered by the high kinetic barrier to break bonds. Even for the powder sintering approach, it is therefore not evident that the broad stability range of the monoclinic phase obtained after extended heating is the true thermodynamic equilibrium phase as claimed or just a metastable state as indicated by our calculations. The limited possibility for bulk diffusion is probably also the reason we don't see typical spinodal decomposition with composition fluctuations on the nanometer length scale in our films, but rather large domains (> 50 nm) of the separated phases. This suggests that phase separation is mediated by surface diffusion and nucleation. Once a stable nucleus of a different phase has formed, incoming atoms grow on top and adopt the same structure. In that sense, even though the phase separation process is thermodynamically driven, it cannot be realized if it is hampered by kinetic barriers. An additional factor that might play a role in this process is the catalytic effect of the easily oxidizing In atoms on the growth of Ga_2O_3, as observed by Vogt *et al.* [182] in MBE growth. Due to the weaker In-O bond compared to Ga-O, an In-Ga interatomic exchange takes places on the growth surface. For the growth of $(In_xGa_{1-x})_2O_3$, this could imply that indium is incorporated in the current phase of the film up to the allowed limit, and excess indium is left 'floating' on the surface. Once the indium build-up on the surface is too high, phase separated islands form such as seen in MOVPE (see Fig. 3.10), or another phase which allows a higher incorporation of indium starts to grown on top. This would explain the layered phase separation in the PLD films where the phase with the lowest In content is found closest to the substrate and the phase with the highest In content closest to the surface (see Fig. 3.6 & 3.7).

In contrast to the gallium-rich side of the phase diagram, where a miscibility of up to $x \approx 0.63$ is reached by forming metastable compounds, a miscibility gap on the indium-rich side remains up to the highest temperature considered in our calculations of 1400K (= 1127°C). The driving force for phase separation in the composition range $0.63 < x < 0.9$ is significantly stronger, as evidenced in Fig. 3.18 by the steeper ΔG curves with a larger energy separation from the convex hull. The miscibility gap is well reproduced in experiment: PLD samples with a mean composition of $\tilde{x} = 0.75$ and $\tilde{x} = 0.80$, and grown, respectively, at $T = 680$°C and $T = 640$°C, as well as a MBE sample with a global compositions of $\tilde{x} = 0.67$ and grown at $T = 800$°C, present phase separation as expected. In this temperature range, the separated metastable phases according to calculation would be the h-phase with $x \approx 0.63$ and the c-phase with $x \approx 0.87$. The computed indium limit of the cubic phase agrees well to the experimental compositions ($x = 0.91$), both for the

heteroepitaxial PLD layers and the pseudohomoepitaxial MBE layer [179]. The computed indium limit of $x = 0.63$ for the hexagonal phase is exceeded in our PLD films, where we get a maximum incorporation of $x = 0.7$. This could possibly be explained by the defective and grainy structure of the hexagonal phase in experimental films, which could allow for more indium to be incorporated.

4

$(In_xGa_{1-x})_2O_3$ phase formation upon crystallization

In the previous chapter, we have seen that in epitaxial $(In_xGa_{1-x})_2O_3$ films grown at relatively high temperature, the ability of the atoms to diffuse on the growth surface and to form ordered crystal lattices plays an important role on the stability of the phases. Therefore, we asked ourselves the question: How does configurational disorder affect the phase stability? To investigate this experimentally, we deposited amorphous $(In_xGa_{1-x})_2O_3$ films at low temperature, to reach a state with the highest amount of configurational disorder. The films are heated in-situ in the TEM to follow the crystallization and phase evolution of the material as a function of temperature and time. An experimental phase diagram is constructed based on the crystallization data and differences with the phase diagram obtained in the previous chapter are discussed. A model for the crystal phase formation during heating is built based on the atomic-scale kinetics of the observed phase transitions.

4.1 In-situ TEM crystallization of amorphous $(In_xGa_{1-x})_2O_3$

4.1.1 Crystallization data

In the following sections, the phase evolution of amorphous $(In_xGa_{1-x})_2O_3$ films with temperature and time is described based on electron diffraction and HRTEM images. We restrict ourselves to the in-situ vacuum experiments, since it was discussed in the methodology part (Section 2.5) that oxygen atmosphere is not significantly changing the phase formation. Heating rates are varying between 0.2 – 1.0°C/s (except for the fast heating pulse experiment), as summarized in Table 2.2 for each experiment individually, together with other experimental characteristics.

$x \leq 0.22$

Fig. 4.1(a) shows the evolution of the Ga_2O_3 electron diffraction pattern obtained during in-situ annealing of a 100 nm thin amorphous Ga_2O_3 film at relevant temperatures during the crystallization process. For temperatures lower than 470°C, the diffraction pattern

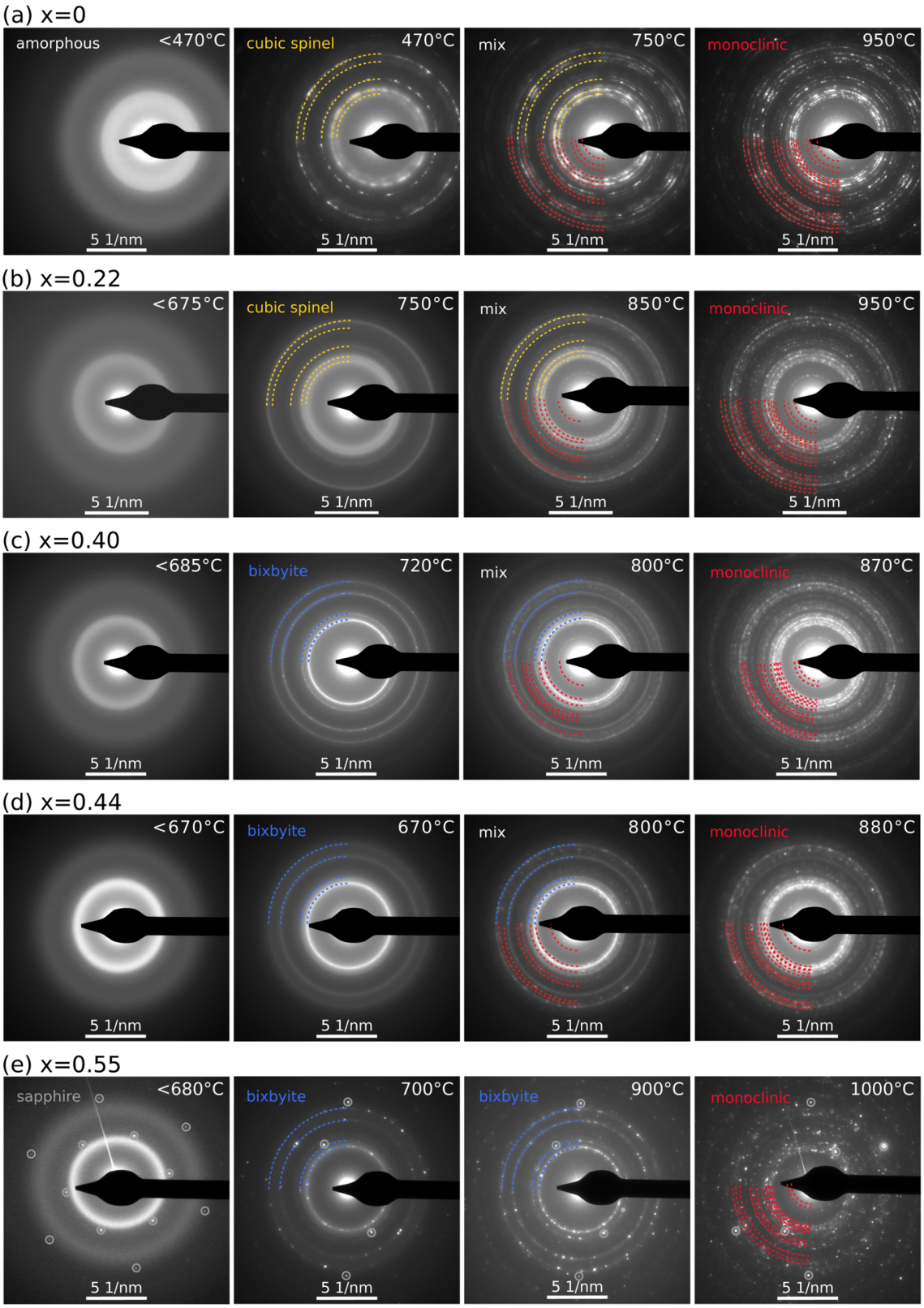

Figure 4.1: Electron diffraction images at relevant temperatures showing the crystallization process of amorphous $(In_xGa_{1-x})_2O_3$ with (a) $x = 0$, (b) $x = 0.22$, (c) $x = 0.40$, (d) $x = 0.44$ and (e) $x = 0.55$. Blue, yellow and red annotations fitted to the Debye-Scherrer rings refer to bixbyite, spinel and monoclinic *hkl* reflections, respectively. The black feature in all images is a beam blanker.

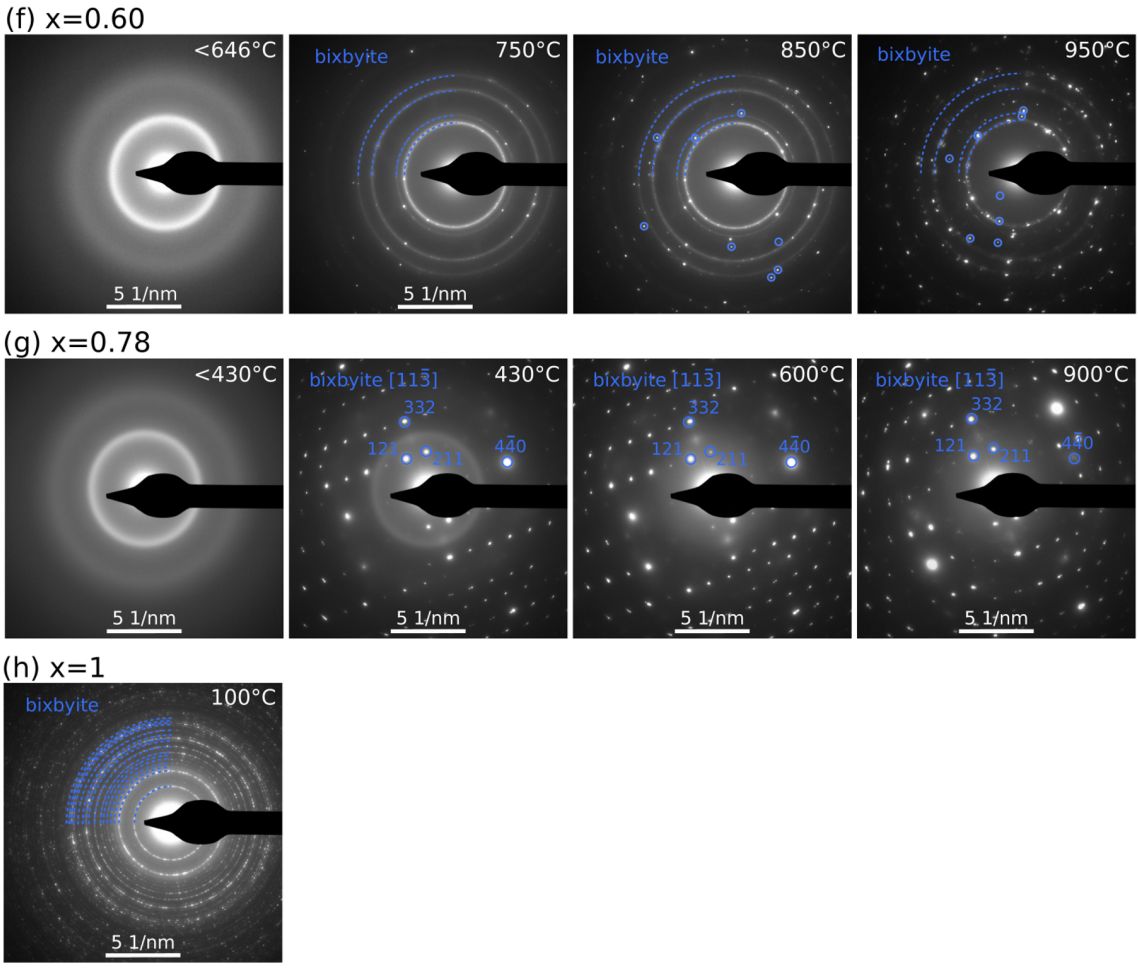

Figure 4.1: (cont.) Electron diffraction images at relevant temperatures showing the crystallization process of amorphous $(In_xGa_{1-x})_2O_3$ with (f) $x = 0.60$, (g) $x = 0.78$ and (h) $x = 1$. Blue, yellow and red annotations fitted to the Debye-Scherrer rings refer to bixbyite, spinel and monoclinic *hkl* reflections, respectively. The black feature in all images is a beam blanker.

shows two broad bands due to the first and second nearest neighbor distribution in the sample, typical for amorphous material. First distinct diffraction spots start to appear at 470°C, marking the onset of crystallization. Keeping the temperature constant at 470°C for two minutes, more and more spots appear and Debye-Scherrer rings form indicating polycrystalline material, as apparent in the second image Fig. 4.1(a). At this point, the amorphous layer is completely crystallized, as shown in the HRTEM image of the sample in Fig. 4.2(a) where lattice fringes can be observed over the full area. The crystal phase is identified from measuring the radii of the Debye-Scherrer rings. The peaks in the radial intensity profile of the diffraction pattern, as plotted in Fig. 4.3(a), agree well with the highest intensity reflections of the powder diffraction data of the cubic spinel phase of γ-Ga_2O_3. The slight discrepancies between the experimental peak positions and the literature values can be explained by the small crystallite sizes and the degree of randomness and/or ordering in the distribution of the vacancies, which might affect the lattice parameter or broaden the peaks. Upon further heating, starting from approximately 500°C, additional diffraction spots and rings are forming hinting to the formation of a new phase. Starting at a temperature of 750°C, a clear fingerprint of

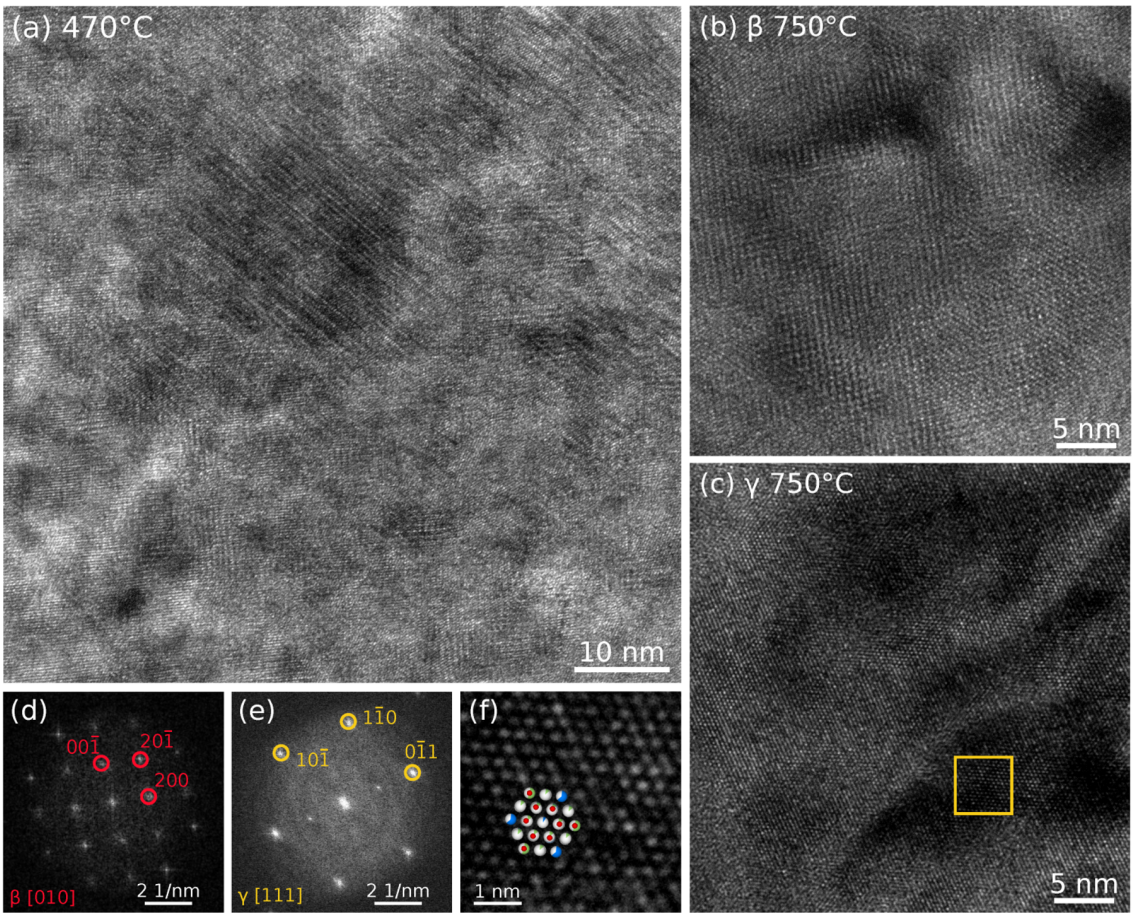

Figure 4.2: (a) HRTEM image of the fully crystallized Ga_2O_3 film at 470°C. (b) and (c) are HRTEM images of a β-Ga_2O_3 grain in [010] projection and a γ-Ga_2O_3 grain in [111] projection, respectively, at an annealing temperature of 750°C, as identified from their fast Fourier transforms (FFT) shown in (d) and (e). The area of the γ-phase grain image indicated by the yellow square is magnified in (f) and the atomic ball structure of γ-Ga_2O_3 in the [111] projection is superimposed.

the β-phase can be recognized in the positions of the Debye-Scherrer rings. A HRTEM investigation of the crystalline grains in the sample kept at 750°C confirms the presence of a mixture of γ- and β-phase. In Fig. 4.2(b) and (c), a β- and γ-phase grain along respective

low order zone axis orientations of [010] and [111] are imaged. The phase and orientation is identified from the symmetry and the reciprocal lattice spacings observed in the fast Fourier transforms of the HRTEM images, shown in 4.2(d) and (e). A high-magnification detail of the image of the γ-phase inside the yellow square reveals the structural pattern of γ-Ga_2O_3 in the [111] projection with an atomic ball model superimposed. Upon further heating to 850°C and 950°C, the rings due to the β-structure become more pronounced and we do not find indications for the presence of γ-phase in our HRTEM images. The radial profile of the diffraction pattern at 950°C is shown in red in Fig. 4.3(b) and the peak positions and their relative intensities fit perfectly to the powder diffraction data of monoclinic β-Ga_2O_3.

Since the amorphous layer was completely crystallized in the γ-phase already at a temperature of 470°C, we conclude that the γ-phase underwent a transition to β-phase. Since the reflections of γ-phase are close in position to those of β-phase, it is hard to

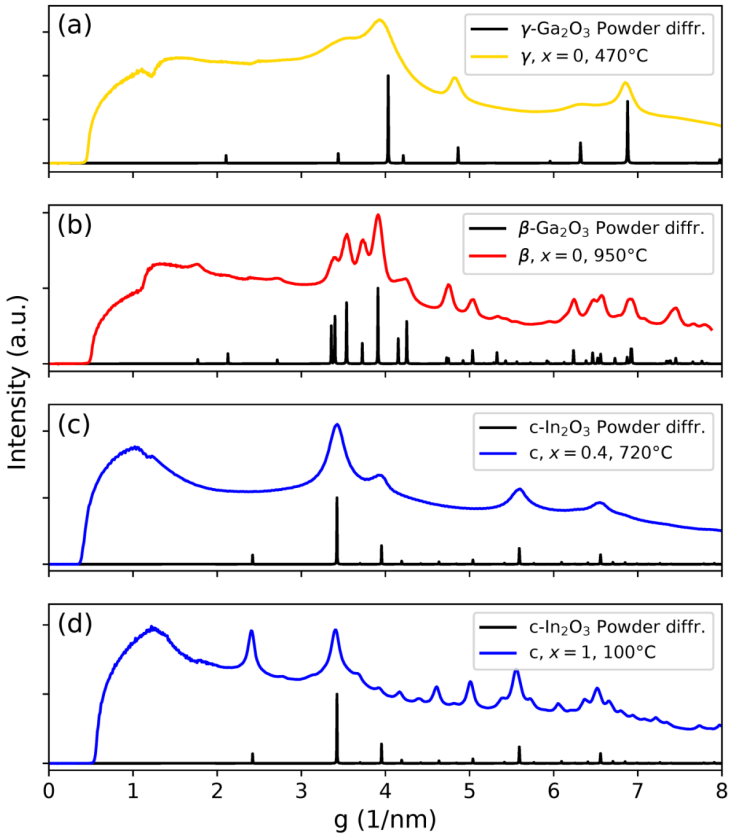

Figure 4.3: Radial intensity profiles of the electron diffraction patterns of the (a) cubic spinel (γ), (b) monoclinic (β) and (c & d) cubic bixbyite polycrystalline phases at the indicated temperatures and compositions. The powder diffraction data of each phase, obtained with VESTA [183], are added as a comparison to literature.

define a distinct transition temperature. Instead, we find that the transition is gradual with a mix of phases for temperatures between ≈ 500°C–800°C. It is clear though that a transition from the high symmetry cubic phase (few reflections) to the low symmetry monoclinic phase (many reflections) takes place. Due to the lack of a crystalline substrate, no preferential direction for the crystallites is imposed and they appear in all possible orientations.

A similar crystallization and phase transition process is observed for the annealing of amorphous $(In_{0.22}Ga_{0.78})_2O_3$, as visualized in Fig. 4.1(b). The material crystallizes in the γ-phase at a temperature of 675°C. Around a temperature of 810°C, new spots start to appear which developed slowly into new rings which correspond to the monoclinic *hkl* lattice reflections. Similar as in Ga_2O_3, a slow transition to the monoclinic phase over a temperature range of ≈ 200°C takes place, with a mix phase around 850°C and, finally, a completed transition at 950°C, as illustrated in the two rightmost images in Fig. 4.1(b).

$0.4 \leq x \leq 0.55$

Three amorphous $(In_xGa_{1-x})_2O_3$ films with indium contents of $x = 0.40$, $x = 0.44$ and $x = 0.55$ present the same phase evolution upon annealing in-situ in vacuum [see Fig. 4.1(c), (d), (e)]. We note that the film with $x = 0.55$ was deposited on a sapphire substrate, in contrast to all other samples which were deposited directly on the amorphous chip

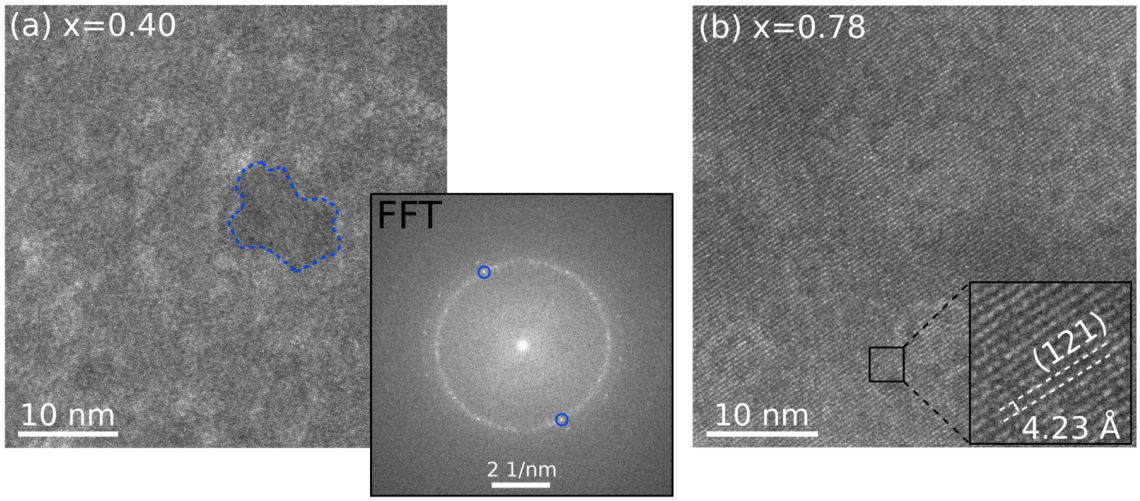

Figure 4.4: (a) HRTEM image of the polycrystalline $(In_{0.40}Ga_{0.60})_2O_3$ film crystallized at 685°C in the cubic bixbyite phase and its fast Fourier transform (FFT). The only clearly visible crystal is indicated by the blue outline and it is responsible for the circled spots in the FFT image. (b) HRTEM image of a single-crystalline area of the $(In_{0.78}Ga_{0.60})_2O_3$ film crystallized at 430°C, with a high magnification detail resolving the (121) planes of the cubic bixbyite phase.

membrane, and therefore diffraction spots from the crystalline sapphire substrate are visible in all diffraction images of that sample in Fig. 4.1(e). In all three films, the crystallization is marked by the appearance of first reflections from the forming crystallites, which happens, respectively, at temperatures of 685°C, 670°C and 680°C for $x = 0.40$, $x = 0.44$ and $x = 0.55$. Keeping the temperature constant at the respective crystallization temperatures, the film crystallizes completely within a few seconds as indicated by the formation of full Debye-Scherrer rings in the diffraction pattern. The radial profile of the diffraction pattern, as imaged in Fig. 4.3(c) for the film with an indium content of $x = 0.40$, is found to match with the powder diffraction data of cubic bixbyite In_2O_3. The four peaks correspond to the (222), (400), (440) and (622) lattice planes, which are the reflections with the highest powder diffraction intensity. In HRTEM images of the crystal phase at the initial crystallization temperature, such as the image in Fig. 4.4(a), lattice fringes are not clearly visible. In this image, only one relatively large grain of approximately 10 nm in diameter can be clearly identified, as indicated by the blue outline. The fast Fourier transform of the image, however, shows a clear Debye-Scherrer ring of the (222) reflection and some extra spots, which proves that the film is completely crystallized, although most grains are too small (< 5 nm) to be distinguished in the HRTEM image. In the films with indium contents of $x = 0.40$ and $x = 0.44$, the bixbyite phase is stable up to approximately 750°C. Around this temperature, additional reflections appear at radial positions that indicate the presence of a new crystal phase. The additional diffraction spots develop into Debye-Scherrer rings upon increasing the temperature, which can be indexed with the *hkl* reflections of the monoclinic lattice of β-Ga_2O_3. At this point, we still have a mixture of phases, as illustrated in the diffraction pattern images in Fig. 4.1(c) and (d) at 800°C. By heating up further, the newly formed rings increase in intensity and a phase transition from the cubic bixbyite to the monoclinic phase takes place close to 835°C and 870°C, respectively, to end up with purely β-phase material. The phase evolution is similar in the film with $x = 0.55$, however, the cubic bixbyite phase is stable up to a

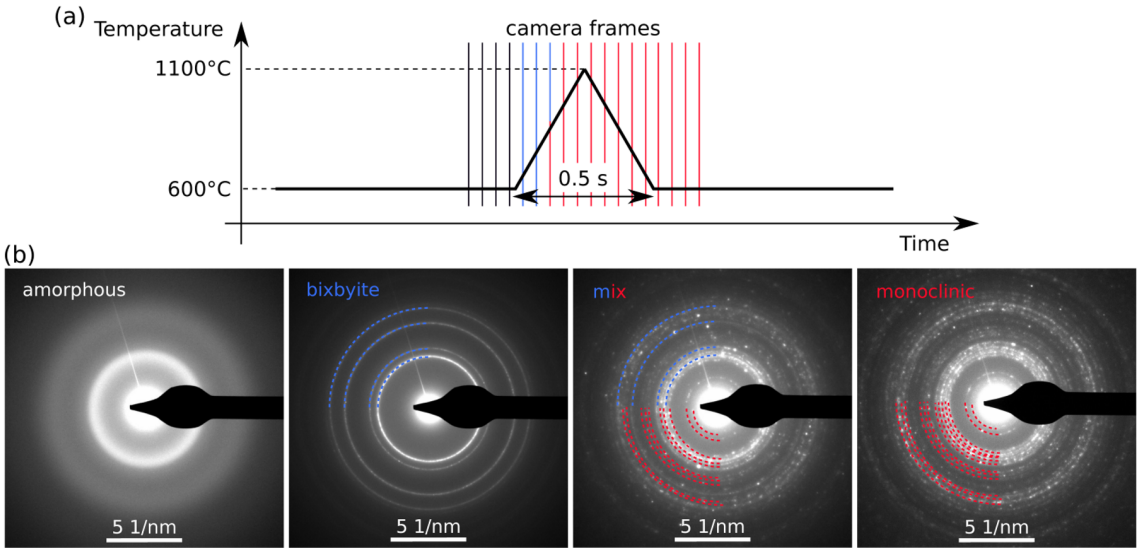

Figure 4.5: (a) Heating pulse applied in-situ in the TEM to an amorphous $(In_{0.40}Ga_{0.60})_2O_3$ film. The camera frames ($\approx$ 20 frames/sec) are indicated by vertical lines and colored according to the phase that was identified in the recorded diffraction pattern. The evolution of that diffraction pattern from amorphous to cubic bixbyite and to monoclinic phase is shown in (b).

temperature of 900°C, as visible in its diffraction pattern at this temperature in Fig. 4.1(e). The presence of full Debye-Scherrer rings in the electron diffraction pattern indicates that the sapphire substrate doesn't impose a preferential orientation for the bixbyite crystals. For temperatures higher than 900°C, the transition to monoclinic phase sets in and at 1000°C, a β-phase fingerprint is clearly identified in the diffraction image.

$x = 0.4$ fast heating pulse

A second sample with an In concentration of $x = 0.4$ was annealed in-situ by applying a short heating pulse to test the effect of heating the sample quickly instead of applying a slow ramp rate of ≤ 1°C/s on the crystallization pathway. The sample was first heated to a starting temperature of 600°C, where it was still amorphous. At this point, a heating pulse 600°C $\rightarrow$ 1100°C $\rightarrow$ 600°C was applied in 0.5 s, as schematically displayed in Fig. 4.5(a). The integration time for the camera was set such that $\sim$ 20 diffraction pattern frames/s were acquired, which corresponds more or less to 1 frame/$\pm$100°C. The same crystallization scheme a $\rightarrow$ c $\rightarrow$ β as in the case of a slow anneal was recorded, as shown in Fig. 4.5(b). Debye-Scherrer rings fitting to the bixbyite phase were captured for 2 frames, i.e. it was stable over a temperature range of $\sim$ 200°C, roughly estimated. In the next frame, a mixture of bixbyite and monoclinic Debye-Scherrer rings were observed, indicating the phase transition to the β-phase has set in. One frame later, the transition is completed and only Debye-Scherrer rings corresponding to the polycrystalline monoclinic phase are visible. After the quick cool down back to 600°C, no significant changes take place in the diffraction pattern and the monoclinic phase remains stable.

$x = 0.6$

Also samples with indium contents higher than $x = 0.6$, crystallize in the cubic bixbyite phase, which remains stable up to the maximum reachable annealing temperature before

Table 4.1: Experimental g-values of the new diffraction spots that appear during annealing of $(In_{0.60}Ga_{0.40})_2O_3$ at temperatures > 850°C [circled in blue in Fig. 4.1(f)], compared to literature g-values of cubic bixbyite In_2O_3.

hkl in c-In_2O_3	g_{exp} (nm^{-1})	$g_{exp}/g(222)_{exp}$	g_{lit} (nm^{-1})	$g_{lit}/g(222)_{lit}$
200	1.96	0.56	1.98	0.58
222	3.47	0.99	3.42	1.00
312	3.75	1.07	3.70	1.08
411	4.23	1.21	4.19	1.22
332	4.78	1.36	4.64	1.35
413	5.20	1.49	5.04	1.47
433	5.85	1.67	5.76	1.68
444	7.00	2.00	6.85	2.00
543	7.20	2.06	6.99	2.04

the sample material starts to degrade, as discussed in Section 2.5.

From the diffraction data of the $(In_xGa_{1-x})_2O_3$ film with an indium content $x = 0.6$, a crystallization temperature of 646°C is determined. Debye-Scherrer rings corresponding to the (222), (400), (440) and (622) lattice reflections of the c-phase form as visible in the diffraction pattern at 750°C in Fig. 4.1(f). Upon further heating, spots at other radial positions start to appear, as visible in the images taken at 850°C and 950°C. These new bright spots appear at the expense of intensity in the Debye-Scherrer rings, which means larger crystals form at the expense of smaller ones. The radial positions, i.e. the g-values, of the spots are summarized in Table 4.1. The ratios of those values with respect to the experimental g-value of the (222) reflection are compared to the same ratios using the literature g-values of c-In_2O_3. By comparing the ratios instead of the absolute values, the differences due to Ga incorporation in the experimental lattice do not matter anymore. All spots fit to a reflection in the bixbyite lattice, suggesting that the c-phase is conserved but larger grains with distinct orientations form that become visible in the diffraction pattern.

$x = 0.78$

Remarkably, for the $(In_xGa_{1-x})_2O_3$ sample with an In content of $x = 0.78$, no Debye-Scherrer rings form upon crystallization at a temperature of 430°C, but the diffraction pattern shown in Fig. 4.1(g) appears abruptly, indicating the formation of one large crystal. Analyzing it, the crystal phase and orientation are found to be cubic bixbyite in the $[11\bar{3}]$ projection. Fig. 4.4(b) shows a HRTEM image right after crystallization in which the (121) lattice planes are visible with a lattice spacing of 4.23Å slightly larger than the literature value for In_2O_3 (= 4.13Å). While gallium incorporation would lead to a decrease in the lattice parameter compared to In_2O_3, it is possible that a high density of lattice defects, such as interstitials and vacancies, are responsible for the expansion of the lattice. Upon changing the position on the sample and imaging through one of the other membrane holes, a different crystal orientation is found. It means the film is not completely single-crystalline but at least large areas in the range of $5-10$ μm are found to have the same orientation. The sample did not fully crystallize immediately, as apparent in the diffraction image at 430°C, where a broad band indicative of amorphous material is still visible. The amorphous areas disappear gradually upon heating such that, finally, around 600°C, the sample is completely crystalline.

$x = 1$

The In_2O_3 film deposited at 100°C is not amorphous but polycrystalline and produces the diffraction pattern shown in Fig. 4.1(h). A comparison of the radial profile with the powder diffraction data of c-In_2O_3, presented in Fig. 4.3(d), gives a good agreement. The highest intensity peaks are again those of the (222), (400), (440) and (622) reflections, which are the only rings that are visible for the other $(In_xGa_{1-x})_2O_3$ polycrystalline bixbyite samples. However, in the pure In_2O_3, multiple additional Debye-Scherrer rings with a lower intensity are observed, which have relative powder diffraction intensities ≤ 0.04 (apart from the first peak at $g = 2.11$ nm^{-1}) compared to the most intense reflection. As cubic bixbyite is already the thermodynamically stable phase of In_2O_3, it is not surprising that it remains stable up to the maximum annealing temperature before sample degradation takes place.

4.1.2 Phase diagram

From the results of all crystallization experiments in vacuum, we construct the phase diagram in Fig. 4.6, where the crystallization pathways discussed above are indicated by the dashed vertical lines and the phase transition temperatures by the diamond symbols. We note here that, since the $\gamma \rightarrow \beta$ and c $\rightarrow \beta$ phase transformations are gradual transitions and thus have no well-defined transition temperature, we used the temperature where the Debye-Scherrer rings of the new phase start to overshadow those of the old phase. For indium contents $x \geq 0.40$, the initial crystallization phase is cubic bixbyite, while for

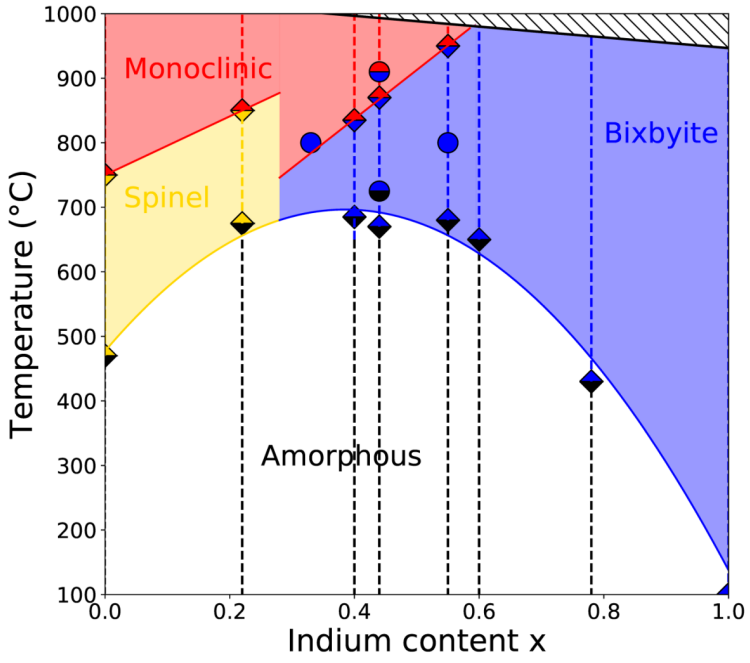

Figure 4.6: Experimental phase diagram for $(In_xGa_{1-x})_2O_3$ obtained from the in-situ TEM annealing of amorphous samples in vacuum. Dashed lines represent the measured crystallization pathways with phase transitions at the diamond symbols. Circular symbols indicate bixbyite solid solutions and transition temperatures obtained by annealing under oxygen atmosphere. In the dashed region (or higher then 1000°C), the sample material started to desorb and decompose.

$x \leq 0.22$, $(In_xGa_{1-x})_2O_3$ crystallizes first in the cubic spinel γ-phase. The crystallization temperature for the spinel phase increases with an increasing indium content in the lattice, while for the bixbyite phase the crystallization temperature increases with an increased gallium content in the lattice. For indium contents $x \geq 0.6$, the cubic bixbyite phase is stable up to the maximum considered temperature, while for compositions $0.4 \leq x \leq 0.55$, it transforms to the monoclinic crystal structure upon annealing. Also, γ-$(In_xGa_{1-x})_2O_3$ undergoes a phase transition to β-$(In_xGa_{1-x})_2O_3$ upon annealing and, for both the c $\rightarrow \beta$ and $\gamma \rightarrow \beta$ transitions, the transition temperatures increase with increasing x. These trends in the phase diagram will be discussed in more detail in Section 4.4. The circular symbols in Fig. 4.6 indicate bixbyite solid solutions and phase transition temperatures obtained by annealing under oxygen atmosphere. The oxygen atmosphere slightly increases the crystallization and phase transition temperatures, as discussed in the methodology Section 2.5, but doesn't further influence the phase formation. It only increases the stability of the current phase/state of the solid solution. From the circular data point at $x = 0.33$ obtained by ex-situ annealing at 800°C, we find that the cubic bixbyite is formed as the primary crystallization phase for indium contents as low as $x = 0.33$.

The $d(222)$ and $d(31\bar{1})$ lattice spacings of bixbyite and monoclinic $(In_xGa_{1-x})_2O_3$, respectively, were extracted from the electron diffraction patterns and plotted as a function of indium content in Fig. 4.7. The monoclinic lattice parameter increases linearly with In content and the bixbyite lattice parameter decreases linearly with increasing Ga content. These trends are both in accordance with Vegard's law, which suggests that indium and gallium are fully incorporated in the respective lattices and no phase separation takes place.

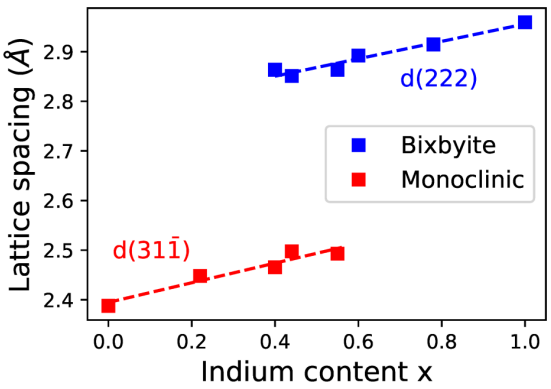

Figure 4.7: TEM electron diffraction determined $d(222)$ and $d(31\bar{1})$ lattice spacings in the bixbyite and monoclinic crystallized phases, respectively, as a function of indium content.

4.2 Effect of configurational entropy on phase stability

Comparing the phase diagram obtained from crystallization experiments with the equilibrium phase diagram calculated in Chapter 3, we find the following striking differences:

- The large miscibility gap that exists on the indium-rich side of the phase diagram in Fig. 3.21 is completely overcome. While the cubic phase was predicted to be stable up to a gallium content of approximately 10% at realistic growth temperatures, which was experimentally confirmed for epitaxially grown layers, we find a significantly extended range of Ga solubility up to 67% ($x \geq 0.33$) in case of crystallization from the amorphous phase.

- The defective spinel phase of γ-Ga_2O_3 is stable for gallium-rich solid solutions up to $x = 0.22$ at low temperatures. The monoclinic phase is only achieved in the high-temperature range between $\approx 750 - 1000$°C.

- The hexagonal phase is completely absent in the phase diagram based on the results of crystallization and annealing experiments.

The only common feature in both phase diagrams is the fact that the monoclinic phase is stable only for indium contents $x \leq 0.5$ approximately.

These findings clearly show that the crystallization of amorphous samples initially does not result in phases that are stable at thermodynamic equilibrium under ambient conditions. The phase diagram of Fig. 3.21, which is based on lowest energy configurations of each phase, describes the ground-state thermodynamics with an entropic contribution that is dependent on the considered temperature. In the experiment described in this chapter, however, the random distribution of indium and gallium atoms in the amorphous phase brings the maximum possible amount of configurational entropy into the system. In other words, we are simulating an extremely-high-temperature solid solution that was cooled down quickly, keeping all atoms fixed in position, such that all possible configurational states are occupied.

To see how this influences the stability of the phases, we have a look on the mixing enthalpy diagram for the β- and c-$(In_xGa_{1-x})_2O_3$ phases as a function of In composition, presented in Fig. 4.8(a). At each composition, the vertical spread in mixing enthalpies (represented by the colored dots) represents the full configurational density of states derived from cluster expansion calculations[1]. Ground-states are indicated in red, and are equivalent to the ΔH values in Fig. 3.15, while the black and blue colored dots correspond to mixing enthalpies of other randomly constructed lattice configurations, i.e. distinct distributions of Ga and In atoms on the different lattice sites. The large energy spread in mixing enthalpies for intermediate compositions of the β-phase follows from the fact that the lattice has two types of coordination sites for the cations and the strong energetic preference of In for the six-fold site. As a consequence, configurations where the majority of In atoms are occupying six-fold positions and the majority of Ga atoms are occupying four-fold positions are relatively low in energy, while in the opposite situation the formation energy is relatively high. The largest energy spread is obtained at $x = 0.5$, where mixing is maximized. For the hexagonal phase, a similar behavior should be expected due to the equal mix of five- and six-fold coordinated cation sites. In contrast, the

[1] Performed by Dr. Christopher Sutton at the Fritz Haber Institute.

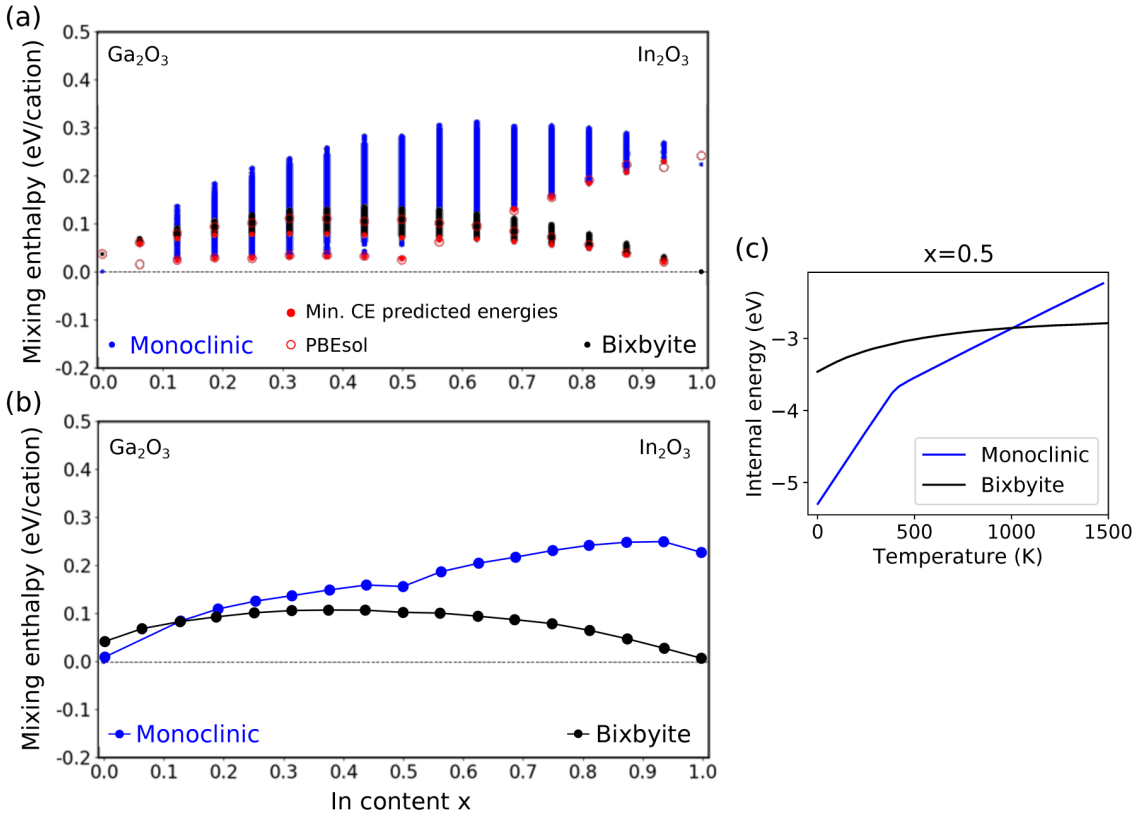

Figure 4.8: (a) CE mixing enthalpies (ΔH) as a function of In content for various configurations of monoclinic and cubic bixbyite $(In_xGa_{1-x})_2O_3$. The lowest energy configurations by CE and recomputed by DFT are indicated by the red filled and empty dots, respectively. (b) Averages of the lowest and highest energy configuration of each phase. (c) Internal energy as a function of temperature for monoclinic and cubic bixbyite $InGaO_3$, i.e. for an In content of $x = 0.5$.

cubic lattice only contains cation sites with six-fold coordination environment. Therefore, the specific distribution of In and Ga atoms does not have such a strong influence on the mixing enthalpy. The spread in the enthalpy results solely from strain contributions due to nearest neighbor interactions, and it is approximately a factor of 3 smaller compared to the β-phase.

Looking solely at the ground-state configurations, β-phase is the lowest energy phase for In concentrations $x \leq 0.61$ and c-phase is the lowest energy phase for $x > 0.61$ (without considering the h-phase). This is a representation of the situation at 0 K. For increasing temperatures, also higher energy configurations have some probability to be occupied. The internal energy[2] is defined to represent the average energy of all occupied lattice configurations of one phase and is plotted as a function of temperature in Fig. 4.8(b) for β- and c-$(In_xGa_{1-x})_2O_3$ with a composition of $x = 0.5$. Because in the monoclinic phase a significant higher number of high energy configurations exist (up to 0.3 eV/cation), while for the cubic phase the mixing enthalpy spread is limited over the range 0.06 – 0.13 eV/cation, the internal energy of the monoclinic solid solution increases more steeply with temperature and keeps on increasing significantly for all considered temperatures. As a result, a cross-over takes place around a temperature of 1000 K (= 727°), where

[2]The internal energy is negative since it is the total energy per atom, not relative to the stable binary phases as in the definition of the mixing enthalpy.

the phase with the lowest internal energy switches from monoclinic to cubic bixbyite. This means that a high-entropy $InGaO_3$ phase, i.e. an effective high-temperature phase, in which all configurational states are occupied, is lower in energy in c-phase than in β-phase. If we approximate the mixing enthalpy of the maximally disordered phases at each composition by the average mixing enthalpy of the lowest and highest energy configurations [Fig. 4.8(b)], we find that the bixbyite phase becomes lower in energy for In compositions in the approximate range $x \geq 0.13$. Only for low In contents, there are not too many unfavorable monoclinic configurations yet and it is still the stable phase. Even though this is a rough estimation, it describes the main effects pretty well and is in good agreement with our experimental phase diagram, where the bixbyite phase is stabilized for $x \geq 0.28$. Additional calculations, which take into account the exact distribution of the different configurations at each composition, are underway to more precisely determine the composition where the transition from monoclinic to cubic bixbyite takes place for high-entropy structures. These results clearly indicate that the multi-coordinated β- and h-phases, which require ordered cation lattices to be stable, are unfavorable as high-entropy solid solutions.

4.3 Phase transitions

The thermodynamic consideration for high-entropy phases described in the previous section, demonstrates how the cubic phase can be stabilized over such a wide composition range in our crystallization experiments. However, to explain the observed phase transitions, a $\rightarrow$ c($\rightarrow \beta$) and a $\rightarrow \gamma \rightarrow \beta$, that are taking place with increasing annealing temperature in more detail, it is important to consider the kinetics of the crystallization and annealing process. First a simplified model for this will be introduced followed by an analysis of the atomic processes during the experimentally observed phase transitions based on crystallographic reasoning. We will identify the spinel phase as a kinetically stabilized disordered state of the monoclinic phase, to explain its formation at low temperatures.

4.3.1 Crystallization kinetics

To illustrate the phase transition processes that happen in our heating experiment, we may start from the simplified scheme plotted in Fig. 4.9. In amorphous $(In_xGa_{1-x})_2O_3$, indium and gallium atoms are randomly distributed, as visualized in Fig. 4.9 by state A. Bond angles and lengths are the result of a local energetic minimum at the nearest neighbor level. No long range order is present and the configurational disorder at this stage is considered maximum. Though the atoms assume a local energetic minimum, it corresponds to a high-energy state at the more global scale. Upon heating, atoms will rearrange their bonds to the neighboring atoms and thus induce long range order, i.e. crystallites will nucleate. In this initial stage of crystallization, atomic movement is limited and the high amount of configurational disorder, i.e. the stochastic distribution of In and Ga atoms, that is trapped in the amorphous phase is conserved. In addition, a high amount of intrinsic lattice defects such as interstitials and vacancies are present. This kinetically stabilized crystalline state of the material is represented in Fig. 4.9 as state B. To reach the final equilibrium state, an extra energy barrier for breaking bonds and diffusion must be overcome. Once the lattice is heated sufficiently, atoms and lattice defects will become mobile and each atom can find

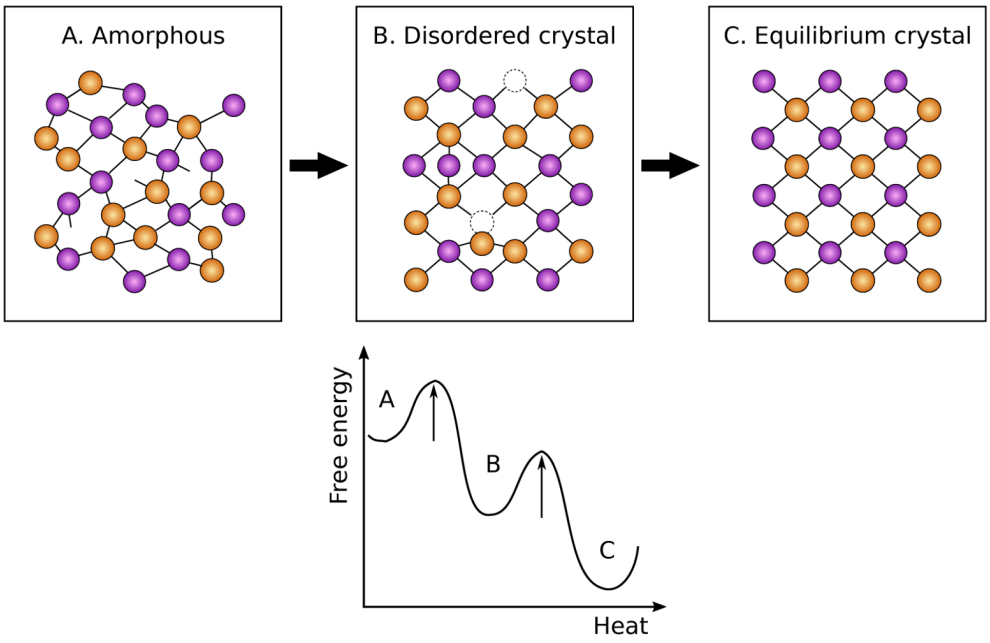

Figure 4.9: Schematic description of the evolution of the atomic structure of an amorphous solid solution A upon heating. Energy barriers for bond rearrangement and atomic diffusion have to be overcome to reach the disordered crystalline state B and eventually the perfect crystalline state C of the solid solution.

its preferred location in the lattice. This results e.g. in an ordered lattice such as the one represented by state C in Fig. 4.9, where the configurational disorder corresponds to that of thermodynamic equilibrium at the given crystallization temperature.

In the following sections, we will demonstrate how the a $\rightarrow$ c($\rightarrow \beta$) and a $\rightarrow \gamma \rightarrow \beta$ phase transitions are governed by similar kinetic considerations.

4.3.2 a $\rightarrow$ c($\rightarrow \beta$) transition in In-rich $(In_xGa_{1-x})_2O_3$

Let us rely on the argument introduced in Fig. 4.9 to explain the a $\rightarrow$ c($\rightarrow \beta$) phase transition observed for $(In_xGa_{1-x})_2O_3$ with indium contents $x \geq 0.33$. During initial crystallization, migration of the atoms is not yet energetically allowed and a crystalline cubic bixbyite solid solution of high configurational disorder is formed. The limited diffusion in the stage where the material still takes on the cubic phase is evident in the evolution of the grain size with temperature, as illustrated by the bright field image series of the sample with In content $x = 0.44$ in Fig. 4.10. Right after crystallization at a temperature of 670°C, the average crystallite size is 7.4 nm. As long as the bixbyite phase is stable, the grains don't really grow in size upon increasing the temperature, as indicated by the data point at 740°C in Fig. 4.10(b). The full layer is crystallized and there is no mobility of the grain boundaries or mobility of atoms in general. However, once the temperature is high enough for diffusion to happen, the transition to monoclinic phase sets in and the grains start to grow with the average grain size increasing at an exponential rate. The lattice transforms to the equilibrium phase and larger grains grow at the expense of smaller grains.

In case of an energetic barrier that needs to be overcome for atoms to move into their equilibrium position, one could imagine that by heating up super quickly, the metastable bixbyite phase could be skipped and the thermodynamically stable monoclinic

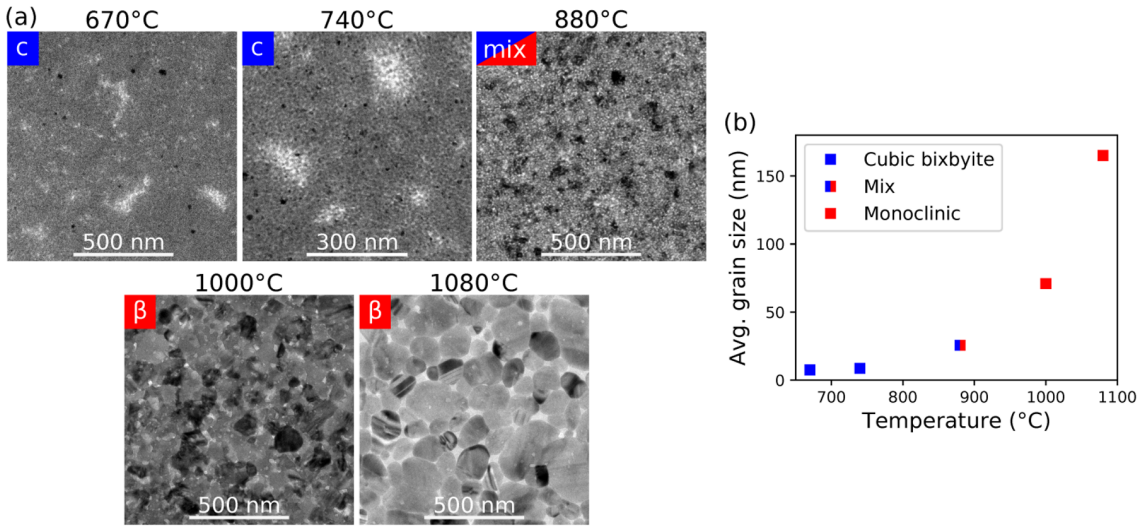

Figure 4.10: (a) Bright field TEM images of the $(In_xGa_{1-x})_2O_3$ sample with In content $x = 0.44$ showing the evolution of the crystallite morphology with temperature during the phase transition from bixbyite to monoclinic phase. (b) Average grain size as a function of temperature.

phase would be reached instantaneously. However, even in the fast heating experiment of the sample with In concentration $x = 0.4$, as described in Fig. 4.5, still the phase transformation from the amorphous to the bixbyite and to the monoclinic phase was resolved in the diffraction pattern. The fact that on such a 'seemingly' short timescale all these different phase formation steps are still taking place can be explained as follows. Atoms are trying to cross the diffusion energy barrier at a rate equal to their vibration frequency, for which typical values are close to 10^{13} Hz (= 1/s). That means we would have to heat up the sample to a sufficient temperature in less then one trillionth of a second, to cross the barrier on the first attempt and not end up in a metastable state. We conclude therefore that it is technically not possible to skip the intermediate bixbyite phase upon crystallization, although it could look like it when the heating pulse time is shorter than the maximum camera frame rate. However, this was not yet the case in the experiment we performed.

4.3.3 a $\rightarrow \gamma \rightarrow \beta$ transition in Ga-rich $(In_xGa_{1-x})_2O_3$

As a main result from the analysis of our electron diffraction series and HRTEM data of the in-situ crystallization experiments, we find that amorphous $(In_xGa_{1-x})_2O_3$ with $x \leq 0.22$ crystallizes completely in the cubic spinel phase of γ-Ga_2O_3. By further increasing the temperature, it undergoes a phase transition to the monoclinic phase, with a mixture of the two phases present over a certain temperature range. An interesting observation from our ex-situ crystallization experiments is that an amorphous Ga_2O_3 film deposited on a c-sapphire substrate and annealed to 600°C to form a $\gamma + \beta$ mixture, shows a preferential orientation of the crystal grains. This is revealed from the electron diffraction patterns of the film shown in Fig. 4.11, which are recorded in two zone axis orientations of the sapphire substrate. The (111) planes of the γ-phase and the $(\bar{2}01)$ planes of the β-phase are parallel to the (0001) planes of the sapphire. The diffraction spots corresponding to those planes are overlapping in the images because of their almost identical spacings [$d(\bar{2}01)\beta$ = 4.70Å and $d(111)\gamma$ = 4.75Å]. The preferred in-plane relations between sapphire and the

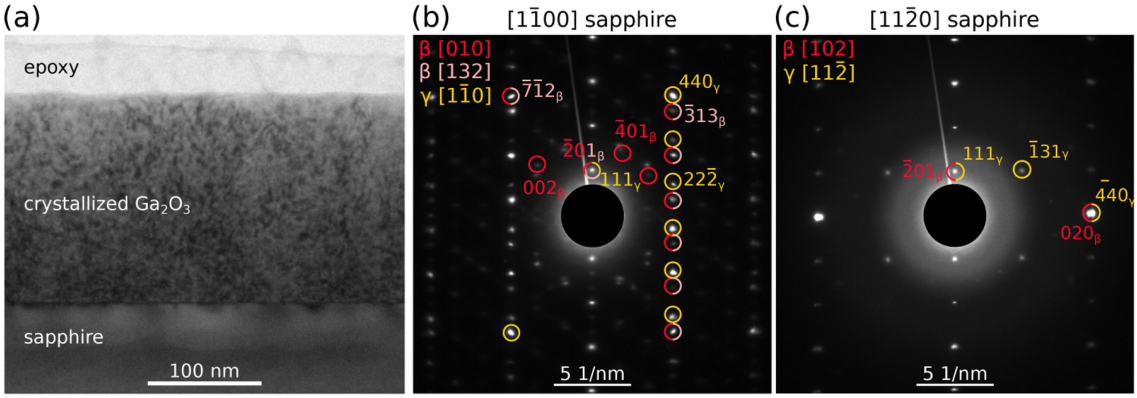

Figure 4.11: (a) Bright field image of a γ+β mixed phase Ga_2O_3 layer on sapphire substrate after annealing to 600°C and (b & c) electron diffraction patterns of the layer taken in the two main zone axis orientations of the sapphire substrate to show the out-of-plane and in-plane epitaxial relationships. Some spots of the different phases/orientations are overlapping and therefore labeled multiple times.

crystallized phases deduced from these patterns are: $[010]_\beta$ and $[132]_\beta \parallel [1\bar{1}0]_\gamma \parallel [1\bar{1}00]_s$ and $[102]_\beta \parallel [11\bar{2}]_\gamma \parallel [11\bar{2}0]_s$, similar as observed in epitaxial growth of β-$(In,Ga)_2O_3$ on c-sapphire, as determined in Chapter 3, and of γ-Ga_2O_3 on c-sapphire, as found in literature [184]. All possible twinned orientations are found as well, i.e. $[0\bar{1}0]_\beta$, $[1\bar{3}2]_\beta$ and $[\bar{1}10]_\gamma$, but those are not labeled in the diffraction pattern for the sake of clarity. Similar diffraction measurements at higher temperatures show that these orientations are conserved during annealing. We conclude that the grains of γ-phase in the $[1\bar{1}0]$ orientation transform to grains of the β-phase in the $[010]$ orientation. From a comparison of the atomic structure of both phases in these orientations, shown in Fig. 4.12(a) and (b), the following similarities in the structural pattern can be recognized:

- Both polymorphs are based on an almost identical face-centered cubic oxygen lattice, which is slightly distorted for the β-polymorph. This is obvious in Fig. 4.12(c), where the same projected volume of the oxygen lattices of both structures are overlaid. Here $(\bar{2}01)_\beta$ and $(111)_\gamma$ are the equivalent upward directions with almost identical spacings, as mentioned earlier.
- Also for the cations, similar positions are occupied in both lattices. This becomes clear when looking at the cations positioned on the edges of the four empty 'tunneling channels' (labeled in black as 1, 2, 3 and 4 in the monoclinic lattice) in Figs. 4.12(a) and (b). In the β-polymorph, all tetrahedral (Th) and octahedral (Oh) Ga positions have full occupation, while in the γ-structure the two inequivalent octahedral and two inequivalent tetrahedral sites all have partial occupation, as illustrated by the partially colored balls in the structural model in Fig. 4.12(b).

To describe the relation between the cation lattices of both structures in more detail, we may define a 'common' lattice that contains the common oxygen sites as well as all possible sites where cations are present in both lattices, as illustrated in Fig. 4.12(d). For that, we have selected the smallest size of a unit cell that contains the common lattice of both symmetries. It contains the four inequivalent tunneling channels in the b-projection of the β-Ga_2O_3 crystal structure defined above. In this projected volume, all cation lattice positions that are present either in the β- or γ-lattice are considered. Some of these sites

Table 4.2: Atomic fractional coordinates of the gallium interstitial positions in the β-Ga_2O_3 unit cell and their transitions to regular β sites, as labeled in the schematic in Fig. 4.12(e).

Interstitial	**Coordination**	**x**	**y**	**z**	**Transitions (see Fig. 4.12(e))**
Ga(I)	Oh	0.5	0.5	0.0	t_1
Ga(II)	Oh	0.5	0.5	0.5	t_2
Ga(III)	Oh	0.34134	0.0	0.169	t_3
Ga(IV)	Th	0.0905	0.5	0.0466	u_1 & v_1
Ga(V)	Th	0.0905	0.5	0.5466	u_1 & v_2
Ga(VI)	Th	0.25	0.5	0.1283	u_1 & v_3
Ga(VII)	Th	0.25	0.0	0.3783	u_4
Ga(VIII)	Th	0.0905	0.0	0.2946	u_5

are common to both lattices and indicated in grey, while others are unique to the spinel lattice and indicated in light blue. As one can see, the 'extra' γ-sites can be identified as interstitials in the four different tunnels of the monoclinic lattice. These sites are visualized individually in Fig. 4.12(e) by light blue atoms for octahedrally coordinated sites and light green atoms for tetrahedrally coordinated sites. The coordinates of these interstitial sites inside the β-Ga_2O_3 unit cell are summarized in Table 4.2. Considering this, we can describe γ-phase as a disordered version of β-phase, where atoms from regular sites on the β-lattice are displaced to interstitial sites leaving a vacancies behind. In both lattices, approximately 22% of the total amount of cation sites in the common lattice are occupied.

In the following, we will undertake the effort to describe the phase transition between the γ- and the β-phase phase as a disorder–order transition and identify possible transitions of individual Ga atoms that underlie that transformation. We will consider next nearest neighbor transitions only, which have travel distances shorter then 2.2Å. All Ga atoms that occupy interstitial positions in the β-phase need to migrate or 'jump' out of the channels into a closeby vacant β-site. The possible paths of those jump processes are indicated in Fig. 4.12(e) by the black and grey arrows. Essentially, three distinct types of transitions can take place:

- Ga atoms located in interstitial octahedral sites of the monoclinic lattice [Ga(I,II,III)] can easily occupy a vacant tetrahedral β-site in a next nearest neighbor position. In these processes, labeled as t_i, three oxygen bonds are broken and three new ones are formed, while three bonds are conserved.

- For the tetrahedrally coordinated interstitials [Ga(IV,V,VI,VII,VIII)], two types of transitions can take place. The Ga interstitials can change their environment to octahedral in the processes labeled as u_i, in which one bond is broken and three new ones are established.

- For the Ga(IV), Ga(V) and Ga(VI) interstitials also a second type of jump is possible to a different vacant tetrahedral position in the processes labeled as v_i. In those, two oxygen bonds are reused while two new ones must be created.

Concluding the above discussion, the spinel phase can be considered as a defective version of the monoclinic phase with high concentrations of quasi-randomly distributed

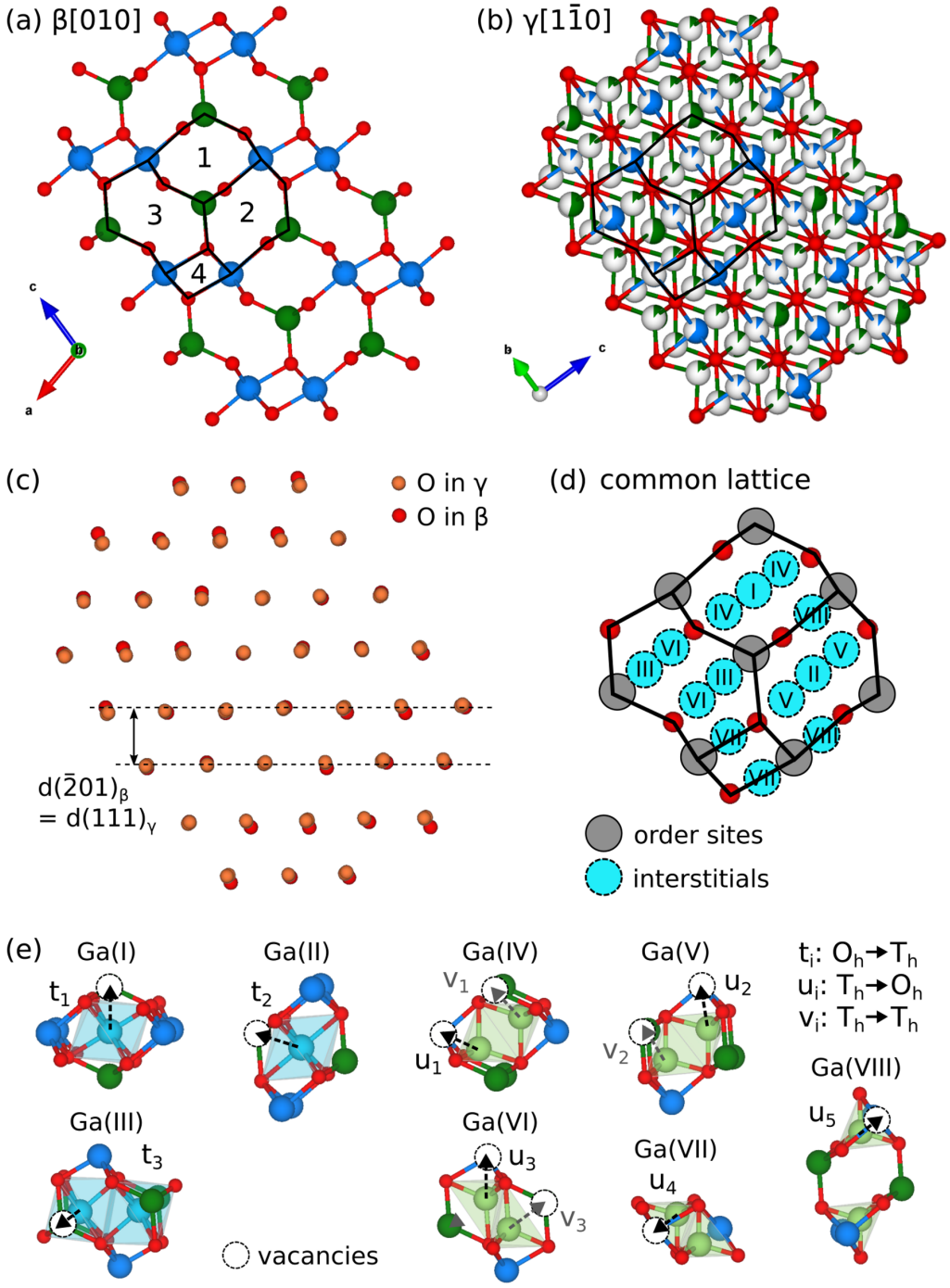

Figure 4.12: Equivalent projected volumes of (a) the β-Ga_2O_3 crystal structure in [010] projection with 4 inequivalent empty tunnels indicated, and (b) the γ-Ga_2O_3 crystal structure in [1$\bar{1}$0] projection with the partial occupation of lattice sites indicated by partly colored balls. In (c), the oxygen lattices of both structures are overlaid. In (d), a common lattice is defined, which contains all possible cation sites in both lattices combined. In (e), the interstitials defined in the different tunnels in (d) are identified as octahedral (blue) and tetrahedral (green) interstitial sites in the β-lattice. The different atomic jumps needed to transition from γ- to β-phase are indicated by arrows and labeled t_i, u_i and v_i.

gallium vacancies and interstitials. Now, looking back at the schematic sketch of Fig. 4.9, a crystallization process in which initially only bonds get rearranged but atoms are not yet allowed to diffuse, results in a highly disordered defective state, characterized by high concentrations of intrinsic defects, rather than in a well-ordered lattice. Thus, the disordered γ-phase forms initially as a kinetically stabilized highly disordered phase and only at higher temperatures, when diffusion is allowed, it transforms to the ordered β-phase. Such a disorder-order transition is a second-order phase transition that happens continuously over time, rather than abruptly, with a continuous transition of the order parameter from 0 to 1. This fits to the continuous phase transition observed experimentally and also to the transition based on atomic migration processes described above. Each of the atomic migration processes defined in Fig. 4.12(e) has its own energy barrier, which also depends on the local structural environment, and therefore will take place or become probable at its own specific temperature. Some of the interstitial positions have already been derived by DFT calculations and are even observed experimentally in Ga_2O_3 bulk crystals. Varley *et al.* [185] demonstrated HAADF-STEM images in which interstitial intensity is observed at positions corresponding to the Ga(I), Ga(II), Ga(IV) and Ga(V) interstitials. They are generally clustering together in regions of sizes of a few nm^2 in projected area. In another work by Kyrtsos *et al.* [186] based on DFT calculations, the Ga(I), Ga(II) and Ga(VI) interstitial sites are found to act as metastable trap states for gallium vacancies. They calculated the energy barriers for the migration paths from the interstitial positions to the nearest neighbor lattice sites, which correspond to the t_1, t_2, u_3 and v_3 transitions that we defined. The energy barriers they find are in the range of 0.6 – 1.4 eV (depending on the charge state), for which temperatures of only 0 – 250°C are needed to activate the process. These barriers are calculated for monoclinic defective lattices with just one gallium vacancy though, and thus the result is not directly comparable to the case of a highly defective γ-structure environment. We have made some attempts in collaboration with Dr. Joel Varley (Lawrence Livermore National Laboratory) to calculate these barriers but due to the large dependency on the local environment in the γ-phase, conventional DFT can not solve the problem. In future work, cluster expansion might therefore be used as a way to more efficiently calculate different configurations of the γ-phase.

4.4 Phase diagram trends in connection to literature

From our experiments, we could define the vacuum crystallization temperature of the binary compounds at 430°C for Ga_2O_3 and lower than 100°C for In_2O_3 since growth at this temperature already produced polycrystalline c-In_2O_3. For indium contents in between, a negative parabolic behavior of the crystallization temperature is found.

An explicit crystallization temperature of Ga_2O_3 based on annealing from the amorphous phase has not yet been reported in literature. There do exist reports on step-wise annealing experiments of amorphous Ga_2O_3, but they started annealing at relatively high temperatures of 500°C [187] and 700°C [188], so no accurate determination of the crystallization temperature was possible. Ga_2O_3 deposition experiments at various temperatures have been done by PLD and magnetron sputtering, which show a transition from amorphous to crystalline β-Ga_2O_3 around deposition temperatures of 350 – 500°C [189–191], which agrees quite well with our crystallization temperature. However, one may doubt the reliability of these literature data, because of the fact that they are based on XRD

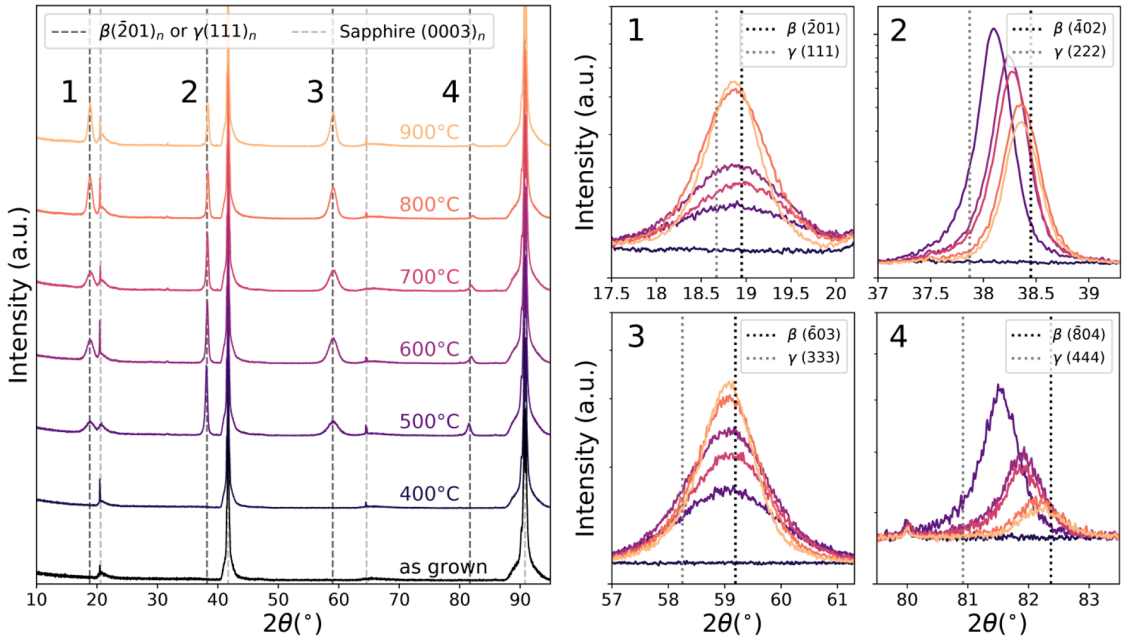

Figure 4.13: XRD $\omega-2\theta$ scans of an as-deposited amorphous Ga_2O_3 thin film on sapphire substrate and at different annealing temperatures (in O_2 atmosphere). The four peaks that appear upon annealing are magnified to highlight their different evolution with temperature. The literature values of the $(111)_\gamma$ and $(\bar{2}01)_\beta$ family of reflections are added as dotted lines.

characterization. One has to bear in mind that crystallites below a critical size may appear amorphous in X-ray studies. From our own experience, we have found that PLD samples grown at room temperature produce Ga_2O_3 films that appear amorphous in XRD measurements, while TEM investigations show that the films are partially crystalline. Additionally, all above-mentioned studies characterize the crystalline Ga_2O_3 as β-phase based on XRD, but neglect the presence of the spinel γ-phase. To distinguish the monoclinic phase from the spinel phase upon XRD characterization is particularly challenging due to the similarity of the two phases, that was displayed in Section 4.3.3. This is shown in Fig. 4.13, based on our own XRD $\omega-2\theta$ scans of a series of annealed Ga_2O_3 films on c-sapphire. The four peaks that appear upon crystallization are typically broad due to the small crystallite sizes and could be associated with either the $(111)_n$ planes of γ-Ga_2O_3 or the $(\bar{2}01)_n$ planes of β-Ga_2O_3. This is illustrated in the magnified images by a comparison to literature 2θ values. Especially in the case of a mixture of the two phases, which is in our in-situ experiments the case starting from annealing temperatures of approximately 500°C, it will be really hard to identify that from XRD. This shows the strength of our in-situ TEM approach, where we are able to distinguish γ- from β-phase and also probe the temperature in a continuous way.

In_2O_3 crystallization temperatures reported in literature based on annealing of amorphously deposited films are 125°C by Moffitt *et al.* [192] (in air) and between 150°C–160°C by Song *et al.* [193]. These values are slightly higher than what we observe, which might again be attributed to the XRD characterization approach, in which the sensitivity to crystallization is lower compared to TEM.

For $x \leq 0.28$ and $x > 0.28$, respectively, incorporation of indium and gallium in the structure increases the thermal stability of amorphous $(In_xGa_{1-x})_2O_3$. The convex

parabolic behavior of the crystallization temperature over the full composition range reflects the contribution of a regular solution mixing enthalpy term, which scales with $x(1-x)$ (see Eq. 2.2). The increase of the a $\rightarrow \gamma$ transition temperature with x can be intuitively explained based on the strong energetic preference of indium for a six-fold coordination environment. Without indium in the amorphous phase, crystallization is relatively easy: all gallium atoms simply make the most straightforward bonds with the neighboring oxygen atoms and a random γ-structure results. With indium atoms substituted in the structure, an extra constraint is added to the crystallization process. To avoid indium being incorporated on six-fold sites, some straightforward bonds might be energetically forbidden, other bonds might have to be formed for which the kinetic barrier might be higher or atomic diffusion might be required. At an indium content of approximately $x = 0.28$, there is too much indium present to avoid it being placed on tetrahedral sites during crystallization and a transition to the bixbyite phase, with only six-fold cation sites, is observed. The increase of the a $\rightarrow$ c transition temperature with $1-x$ has also been observed in a previous study by Moffitt *et al.* [192]. They determined the effective coordination of gallium and indium in the amorphous phase by EXAFS (extended X-ray absorption fine structure) and found that the bonding in a-In_2O_3 is similar to that in c-In_2O_3. Gallium atoms, however, have an effective coordination close to four in the amorphous phase and thus have to change their coordination environment to six-fold upon crystallization into the c-phase, which poses an additional barrier. This work already showed that gallium can be incorporated up to 51%; we increased that range even up to 67%.

The increasing trends of the $\gamma \rightarrow \beta$ and c$\rightarrow \beta$ transition temperatures as a function of indium content can be explained based on a similar coordination environment argument. The more indium that has to find its preferred six-fold coordination site in the monoclinic lattice, the more rearranging is necessary and thus the higher the annealing temperature needed to make that energetically possible. The $\gamma \rightarrow \beta$ transition temperature in pure Ga_2O_3 was determined at 650°C by Roy *et al.* and at 550°C by Playford *et al.* These values are both in the range between our fist observation of monoclinic diffraction spots at 500°C and the formation of a full monoclinic Debye-Scherrer ring pattern at 740°C.

4.5 Chapter summary

Following a series of in-situ TEM annealing experiments of amorphous $(In_xGa_{1-x})_2O_3$ thin films with varying indium contents x, with the objective to crystallize the film and observe the phase evolution as a function of heating temperature, we were able to construct an experimental phase diagram for $(In_xGa_{1-x})_2O_3$ (specific for this type of experiment). We find huge differences in comparison to the equilibrium phase diagram that was calculated in Chapter 3. The bixbyite stability range is hugely extended ($x \geq 0.33$) and the cubic spinel crystal structure appears as a new phase for gallium-rich solid solutions ($x \leq 0.22$). This is the consequence of the combined effect of

1. the maximum possible amount of configurational entropy added to the system by starting from amorphous $(In_xGa_{1-x})_2O_3$, which shifts the relative stability of the phases, and

2. the lack of atomic diffusion for temperatures upon crystallization which doesn't allow the atoms to rearrange themselves in their preferred lattice position, and

definitely doesn't allow the material to phase separate.

Because of these two factors, the multi-coordinated monoclinic and hexagonal phases are strongly disfavored. Upon crystallization, it would be unavoidable that some indium atoms end up in either four- or five-fold sites in the respective lattices and this strongly drives up the formation energy. Although the spinel lattice also has a mix of four- and six-fold coordinated sites (in a ratio 7:4), due to the high density of partially occupied sites and the disordered randomness in the lattice, there is still some freedom for an atom that is fixed in position to chose its coordination environment upon crystallization. Of course, for increasing indium concentrations, it will be harder to avoid indium being forced on tetrahedral sites, and therefore the spinel phase only appears in the gallium-rich region of the phase diagram. At higher indium contents, we see a transition to the cubic bixbyite phase, which only possesses octahedral sites, and where the random occupation of gallium and indium atoms stabilizes this phase energetically. We conclude that phases that can accommodate the high configurational disorder that was trapped in the amorphous matrix are the ones that form upon crystallization. Only at higher annealing temperatures, the atoms have enough energy to overcome the barriers for migration and find their equilibrium position. This results in the phase transition to the monoclinic crystal structure for $0 \leq x \leq 0.55$.

5

The impact of ordering on quantitative HAADF-STEM imaging

As described in Chapter 3, the presence of different types of coordination sites and the energetic preference of indium for a six-fold coordination environment leads to ordered $(In_xGa_{1-x})_2O_3$. Also in other types of materials, ordering phenomena occur and strongly affect their optical, mechanical, electrical and magnetic properties [194–196]. In this chapter, we therefore focus on the impact of ordering on quantitative analysis of HAADF-STEM contrast, specifically in the compositional analysis of (relatively) high-Z solid solutions. We will show how the excitation of the 2*s* Bloch wave state strongly affects the properties of the propagating electron wave function on the crystalline lattice, and thus the scattering to the HAADF detector, with strong impact on the quantification of the contrast.

The Bloch wave and multislice techniques and the simulation parameters used for the HAADF-STEM simulations in this chapter were described in the Sections 2.4.4 and 2.4.5. The supercells of the different lattices are visualized in Appendix A. The results presented in this chapter assume an inner-acceptance angle of the HAADF detector of 35 mrad, however, the findings can be generalized for different scattering angles, as shown in Appendix F. The Bloch wave calculations were performed by Dr. Enzo Rotunno and Dr. Vincenzo Grillo from CNR-NANO in Modena. Partial results of the presented work in this chapter have been published in: C. Wouters *et al.*, Phys. Rev. B 100, 184106 (2019) [197].

5.1 Compositional quantification by Z-contrast STEM

As described earlier in Section 2.4.4 on STEM, combining sample illumination by a convergent STEM electron probe with collection of electrons scattered at relatively high angles (HAADF intensity) provides local Z-contrast. Therefore, this imaging method can be applied to estimate the average atomic number of an unknown sample when measured in combination with a reference material of well-known composition. As such, Rosenauer *et al.* [198] have demonstrated the possibility to determine the Al concentration in $Al_xGa_{1-x}N$ from the measured HAADF-STEM intensity, with GaN as a reference. They

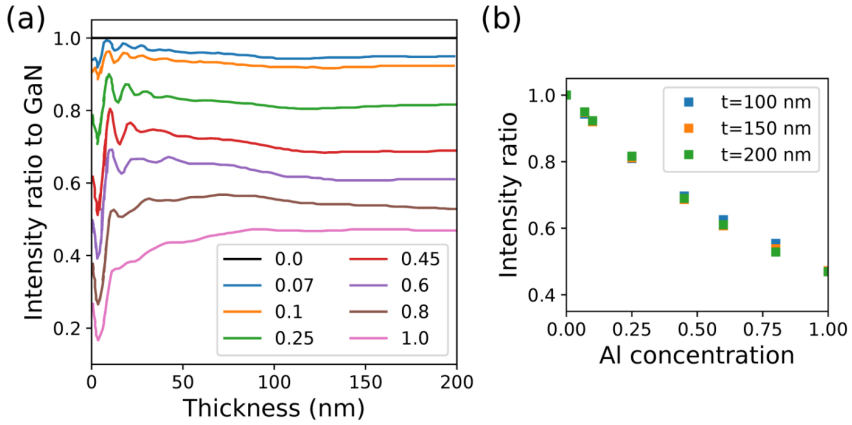

Figure 5.1: (a) Ratios of HAADF intensities simulated for $Al_xGa_{1-x}N$ and GaN with different Al concentrations x between 0 and 1 plotted vs. the specimen thickness. (b) Intensity ratio as a function of Al concentration for different thicknesses. Figure and data taken and adapted from Rosenauer *et al.* [198].

used the frozen phonon approach to simulate the HAADF intensity of wurtzite type $Al_xGa_{1-x}N$ with various x between 0 and 1 as a function of sample thickness, as shown in Fig. 5.1(a), where the outcome is plotted as an intensity ratio/contrast with respect to GaN. The contrast generally decreases as the average Z of the solid solution decreases with an increase of Al content. At thicknesses < 40 nm, the STEM intensity is dominated by channeling behavior of the beam electrons on the atomic columns resulting in an oscillating behavior with thickness. The channeling, which is caused by the beating of the 1*s* Bloch state with the unbound Bloch states, changes periodicity depending on the atomic number of the column and thus on the chemical composition. Therefore, an oscillating behavior with thickness results in the contrast as well. In thicker areas (> 100 nm), a monotonic intensity increase only dependent on the average composition takes place such that a constant contrast is obtained. This thickness regime is ideal for composition quantification since the contrast is independent of thickness, as shown in Fig. 5.1(b).

While Z-contrast STEM provides a reliable method for composition quantification in relatively light solid solutions such as $Al_xGa_{1-x}N$, we will discover in this chapter that the relations shown above do not hold for any material. We show how for solid solutions (i) with an average composition exceeding a specific threshold, and (ii) ordering of different elemental components on specific sublattices, additional effects concerning the beam propagation have to be taken into account to quantify the HAADF contrast that have not been considered in detail before in literature.

5.2 HAADF intensity of $(In_xGa_{1-x})_2O_3$ as a function of composition

Fig 5.2(a) shows results of multislice simulations based on the frozen phonon approach of the [010] projection orientation of the β-lattice of $(In_xGa_{1-x})_2O_3$ for $0 \leq x \leq 0.5$. The HAADF intensities extracted from the simulation are averaged over one unit cell of the monoclinic lattice with indium atoms randomly distributed on all possible cation sites and plotted as intensity ratios with respect to those of Ga_2O_3. The curves are very similar to those of $Al_xGa_{1-x}N$ found in Fig. 5.1(a). First, we find an oscillating contrast at small

thicknesses due to the beating of the 1*s* Bloch states and the strong difference in channeling between Ga_2O_3 and $(In_xGa_{1-x})_2O_3$. Second, once the 1*s* beating has died out at larger thicknesses, the contrast is not oscillating any more and increases monotonously with the amount of indium in the lattice as the average cationic atomic number is increased from $Z = 31$ ($x = 0$) to $Z = 40$ ($x = 0.5$). A more careful look on the curves shows that for thicknesses larger than 100 nm, the contrast is still slightly oscillating and decreases with sample thickness. Thus it does not become constant as shown in the case of $Al_xGa_{1-x}N$ [see Fig. 5.1(a)]. This decrease in contrast is most pronounced for the highest indium concentrations.

We have seen in the previous chapters, both experimentally and as result of the cluster expansion calculations, that indium is not usually randomly distributed in the β-lattice, but rather preferentially incorporated on the octahedrally coordinated lattice sites. Therefore we performed similar simulations for supercells were indium atoms are randomly distributed only on the octahedral cation sites. Since in the [010] projection orientation, i.e. viewed along the beam direction, the cation columns consist either solely of octahedrally coordinated atoms or solely of tetrahedrally coordinated atoms, the former ones will start to get filled with indium atoms, while the latter ones will keep on consisting purely of gallium atoms. In this case, a significantly different behavior of the contrast curves is observed, as can be seen in Fig. 5.2(b). In the channeling regime, the contrast behaves as expected: the 1*s* beating controls the contrast while it still scales with the indium content. For thicknesses higher than 60 nm and indium contents higher than 30 percent, on the other hand, we observe a saturation of the contrast. The intensity ratios decrease with increasing thickness, as observed for the random structure. We performed similar simulations for In incorporated on the tetrahedrally coordinated sites [Fig. 5.2(c)]. A very similar behavior in the contrast curves is found, although the saturating intensity effect is slightly less pronounced. Nevertheless, the intensity for cells with an In content of 40 and 50% is still significantly lower than in the case of random indium distribution on all lattice sites, even though the average atomic number in both unit cells is the same. This suggests the specific sublattice ordering of the cations influences the HAADF intensity. To get more insight in this phenomenon, we performed simulations for off-axis beam illumination, for different crystallographic projections and for different chemical elements on the cation lattice. For an incidence angle of the electron beam 2° off with respect to the [010] zone axis orientation, the effect is less pronounced [Fig. 5.2(d)]. The intensity ratio increases monotonically with increasing In content up to 50%, but we still see a non-linear trend in the contrast up to the maximum considered thickness of 150 nm. For the STEM experiment performed along the [132] orientation of the monoclinic lattice [Fig. 5.2(e)], in which either tetrahedral or octahedral cation columns lie along the beam direction as well but with smaller inter-column distances, we still see the non-linear dependence of the contrast on thickness. In the case where, instead of indium, aluminum ($Z = 13$) is substituted in the β-structure up to compositions of 50% [Fig. 5.2(f)], the behavior of the intensity ratio curves is very similar to those of $Al_xGa_{1-x}N$ with a constant contrast for thicknesses > 100 nm.

From a comparison of all these different cases, we can first of all conclude that the ordering of the two constituent cations on two defined sublattices in a way that pure-element columns form along the beam direction, is strongly affecting the HAADF-STEM intensity. More specifically, for a higher degree of ordering the intensity does not scale anymore with the average atomic number in the sample. Cases (d-f) in Fig. 5.2 indicate

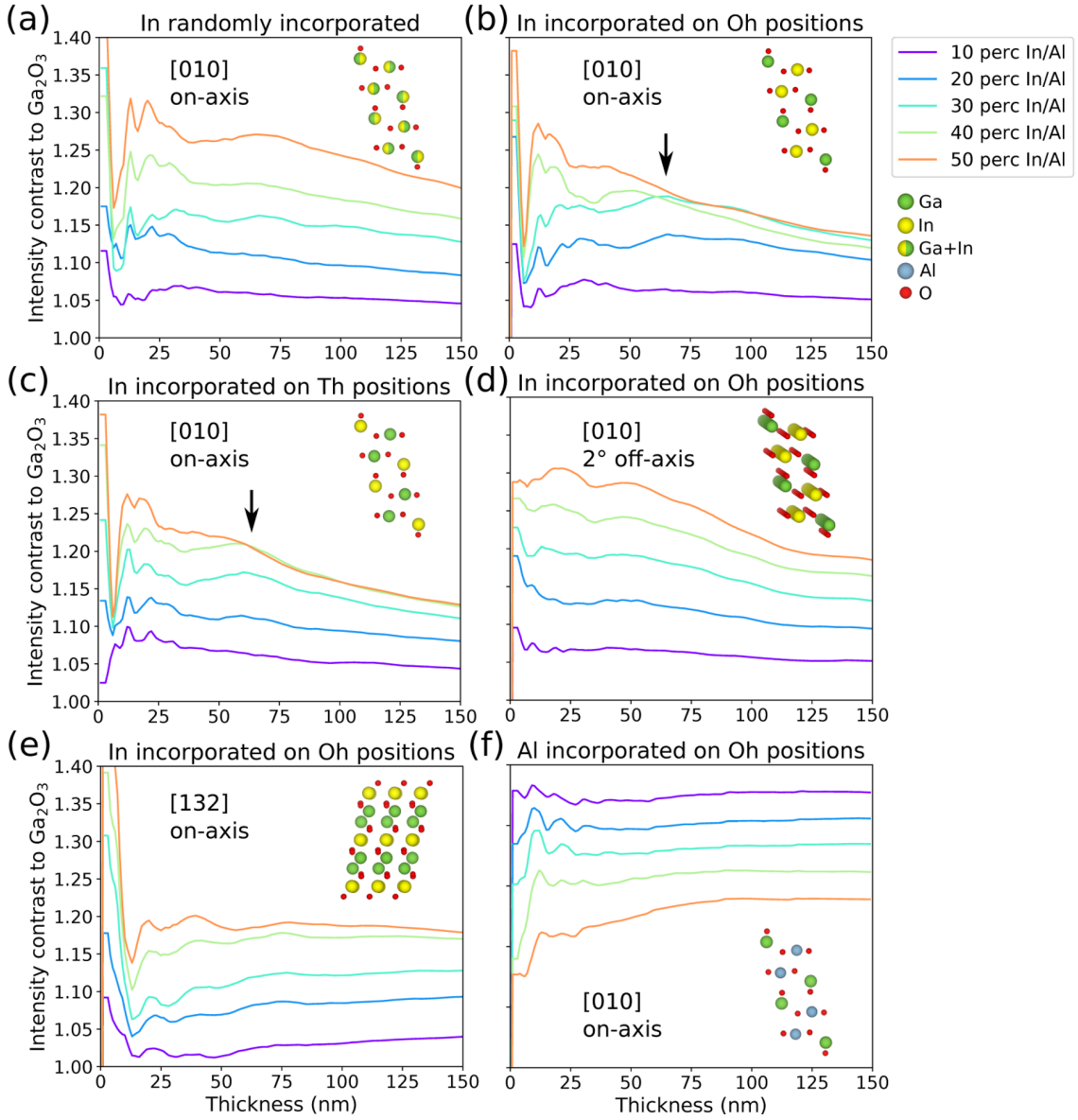

Figure 5.2: Simulated HAADF intensity contrast of (a-e) β-$(In_xGa_{1-x})_2O_3$ and (f) β-$(Al_xGa_{1-x})_2O_3$ for $0 \leq x \leq 0.5$ w.r.t Ga_2O_3 as a function of specimen thickness. (a) Indium randomly incorporated on all cation sites, on-axis [010] projection, (b) indium randomly incorporated on octahedral lattice sites only, on-axis [010] projection, (c) indium randomly incorporated on octahedral lattice sites only, on-axis [010] projection, (d) same as (b) but the incidence angle of the STEM beam is 2° off-axis with respect to the [010] direction, (e) indium randomly incorporated on octahedral lattice sites only, on-axis [132] projection, (f) aluminum randomly incorporated on octahedral lattice sites only, on-axis [010] projection. The projected lattice models for the 50% In/Al cases in each situation are visualized.

that this phenomenon depends on the channeling ability of the electron beam, the atomic column spacing and the relative Z-values of the constituent elements of the solid solution. Especially, since in β-$(Al_xGa_{1-x})_2O_3$, the cation ordering leaves the intensity completely unaffected, we can assume that the beam propagation is qualitatively different for higher Z elements. This phenomenon hampers simple quantitative compositional analysis based on HAADF contrast since (i) the intensity is not uniquely related to a single chemical composition, and (ii) the HAADF contrast depends on thickness which means sample thickness also has to be a known parameter.

5.3 HAADF intensity of ordered vs. disordered lattices

The effect described above, i.e. of a decrease in HAADF intensity with increased order on the cation sublattice, is not unique to monoclinic $(In_xGa_{1-x})_2O_3$. To illustrate this, we compare simulated average HAADF intensities of ordered and disordered solid solutions with different symmetries. In other words, we compare structures with the constituent atoms on a distinct sublattice versus a random distribution of both constituent atoms on all possible lattice sites. $InGaO_3$ [$(In_xGa_{1-x})_2O_3$ with $x = 0.5$], $In_{0.5}Ga_{0.5}N$, $AuCu_3$ and InGa are considered, to show the effect in four different lattice symmetries: monoclinic, wurtzite, cubic fcc and cubic bcc, respectively. In fcc $AuCu_3$, a phase transition from a disordered to an ordered state takes places below a certain transition temperature ($\leq 390°C$), where the Au atoms prefer to be surrounded by Cu atoms as nearest neighbors and they are positioned exclusively on the corners of the face-centered cubic (fcc) unit cell [199]. In contrast to this intrinsic ordering phenomenon, artificial ordering was assumed in the case of $In_{0.5}Ga_{0.5}N$ and the completely artificially constructed bcc InGa lattice. Ordered and disordered supercells with the same mean composition are constructed as described in Section 2.4.5 and the projected unit cell structures perpendicular to the illuminating beam direction are visualized in Fig. 5.3(a-d). The lattice orientations are chosen such that in the ordered structure, the electron beam 'sees' only columns which consist of one type of atom, while in the disordered cell, each cation column consists of a random stoichiometric distribution of the two constituent atoms.

The same trend in the average multislice intensities is observed for all structures: for thicknesses > 40 nm in $InGaO_3$, $In_{0.5}Ga_{0.5}N$ and $AuCu_3$ and > 25 nm in InGa, HAADF intensities of ordered and disordered structures start to diverge, with the disordered lattice always having the higher intensity. The percentage difference between the ordered and disordered intensities at a thickness of 100 nm ranges between 7 – 12.5% for the four systems. This observation is hard to explain intuitively. From the simplified assumption that $I_{\mathrm{HAADF}} \sim Z^{1.7}$ [200, 201], we would expect that each disordered $Ga_{0.5}In_{0.5}$ column produces an intensity of $\left(\frac{(31+49)}{2}\right)^2 = 1600$, while each ordered Ga and In column produce an intensity of 31^2 and 49^2, respectively, which gives an average of 1681. This would mean that the ordered lattice results in a slightly higher intensity, but exactly the opposite is observed.

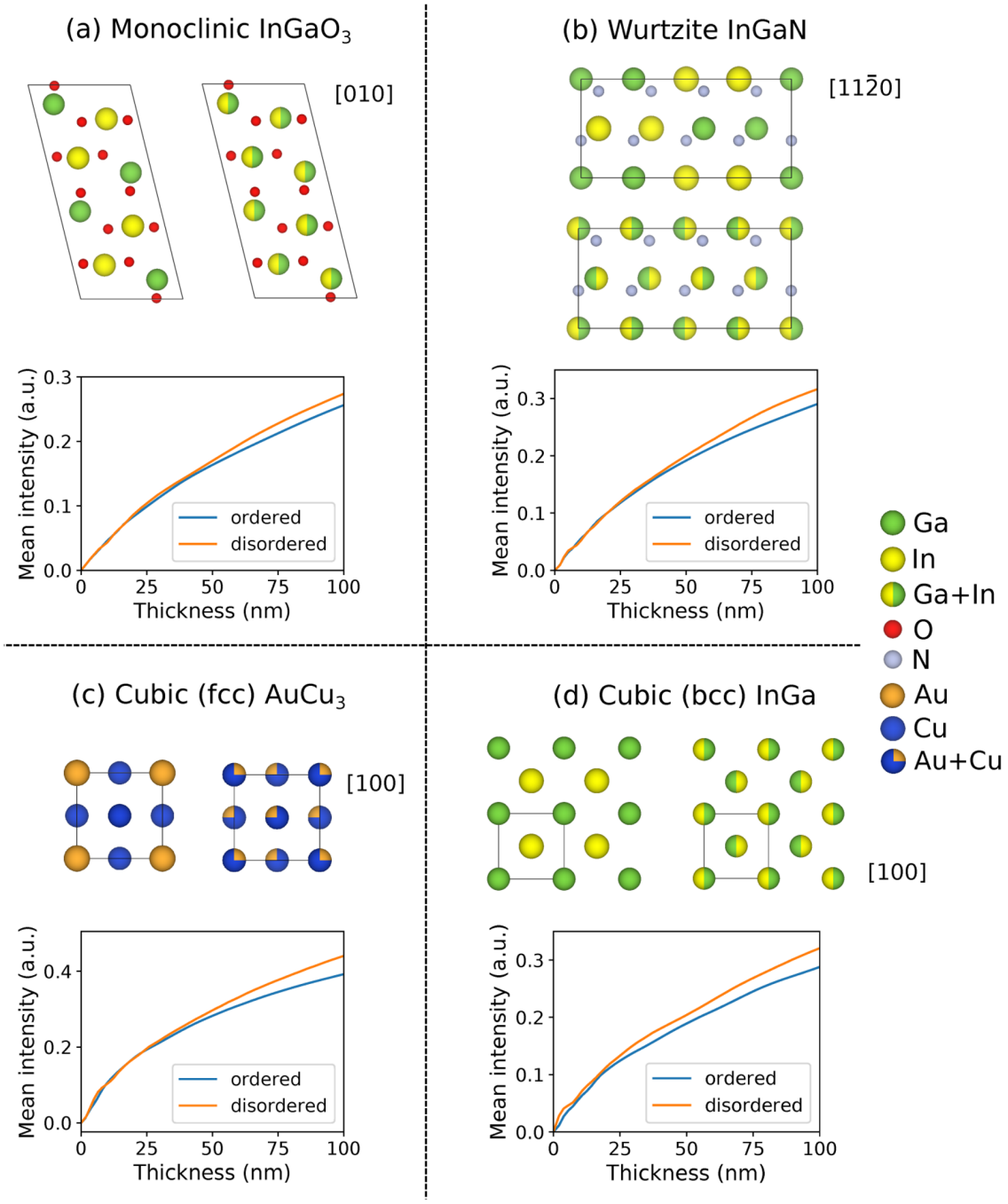

Figure 5.3: Ball models of the unit cells, projected perpendicular to the beam direction, of ordered and disordered monoclinic $InGaO_3$, wurtzite InGaN, face-centered cubic $AuCu_3$ and body-centered cubic InGa lattices. Balls represent atomic columns going in the page, and they are either single-element in the ordered structures or mixed in the disordered structures. The average HAADF-STEM intensity of an ordered vs. disordered unit cell of each structure is plotted as a function of thickness.

5.4 Excitation of 2*s* Bloch wave state and its consequences

To get insight into the effect of ordering on STEM-HAADF contrast, we investigate how the electron wave function of the beam is interacting with a single atomic column as dependent on the atomic number of the element(s) that the column is comprised of and as dependent on thickness. To this end, we apply Bloch wave calculations, of which the main principles have been described in Section 2.4.4.

5.4.1 2*s* state excitation

To demonstrate the effect of increasing Z values on the propagating electron wave, results of Bloch wave and multislice simulations of a convergent STEM electron probe propagating on Ga ($Z = 31$), Zr ($Z = 40$) and In ($Z = 49$) atomic columns are shown in Fig. 5.4. In the left panel, the Bloch wave excitation amplitude as a function of transverse energy (E_T) is compared for the three cases. The transverse energy [159, 202] of the jth Bloch wave was defined in Eq. 2.42 as the difference between the z component of the electron wave kinetic energy in the sample and in the vacuum and is thus proportional to the square of the wave vector k_z^j along the propagation direction ($E_T \sim k_z^{j2} - k_{i,z}^2$). Bound or localized Bloch states have a positive E_T and form sharp lines in the energy spectrum, while unbound or dispersive states have a negative E_T and are contained in the excitation energy continuum at lower energies. The amount of bound states and their transverse energy depends on the depth of the potential of the atomic column. For the gallium column, only the 1*s* state is bound by the potential of the column. As the average atomic number of the column increases, the potential becomes larger and more eigenstates will start to get confined. For the zirconium and especially the indium column, the potential is deep enough to confine also the 2*p* and 2*s* states, and they get separated from the unbound continuum in the energy spectrum. We also see that the transverse energy of the bound states increases drastically for heavier atoms due to a stronger localization. We note that the 2*s* states of the Zr and heavier columns have negative E_T values that are very close to 0, as reported in Table 5.1. This means that these states spread out over a very long distance and for the purpose of this discussion we can safely assume them to be bound states.

The plots on the right in Fig. 5.4 result from multislice calculations and show a cut through the electron wave function intensity ($= |\psi|^2$) as a function of sample thickness (on abscissas) and spatial coordinate (on ordinates) for Ga, Zr and In columns. The electron probe is placed exactly at the center of the atomic column. Due to beating between the bound (B) and the continuum of unbound states (UB), oscillations in the wave function

Table 5.1: Bloch wave properties of a STEM electron probe propagating on different types of atomic columns.

	Ga	Zr	In	$Ga_{0.5}In_{0.5}$
1*s* E_T (Å^{-2})	28.5	45.7	83.2	62.8
2*s* E_T (Å^{-2})	-	-3.8	-1	-2.8
Unbound states (UB) $< E_T >$ (Å^{-2})	-8	-11	-11	-11
1*s*+UB beating wavelength (nm)	10.8	7.2	4.3	5.5
2*s*+UB beating wavelength (nm)	-	56.5	40.6	50.2

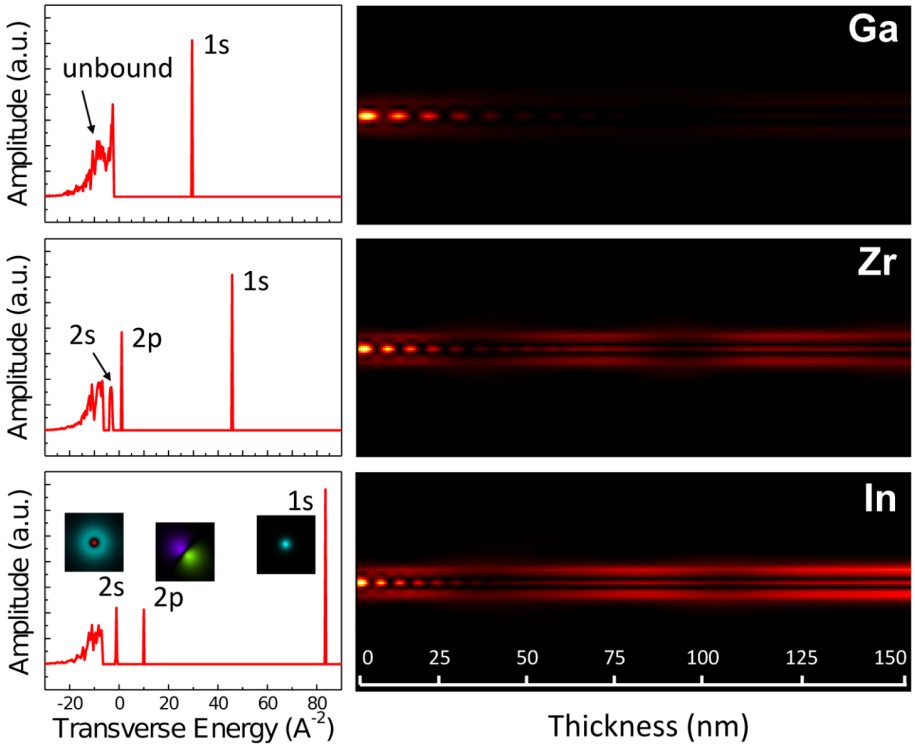

Figure 5.4: Left: Bloch wave excitation spectrum as a function of transverse energy (E_T) for a STEM electron probe propagating on Ga ($Z = 31$), Zr ($Z = 40$) and In ($Z = 49$) atomic columns. Right: Multislice simulation showing a cut through the electron wave function intensity as a function of thickness. The lateral dimension of the images (y-axis) is 1.5 nm and they contain 5 atomic columns each.

amplitude along the propagation direction arise with a frequency equal to $f = |k_z^{\mathrm{B}} - k_z^{\mathrm{UB}}|$. For the continuum of unbound states, the wave vector is determined by the median of the distribution. Beating of the 1*s* state with the unbound states produces the short wavelength wave function oscillation at small thicknesses in each of the three cases. For Zr and In columns, the excited 2*s* states produce a similar beating oscillation, of longer wavelength because the unbound and 2*s* states are closer together in energy. Apart from the amplitude oscillation centered on the column, the 2*s* state is also characterized by a second radially symmetric wave function amplitude maximum at a distance of approximately 0.9 Å from the column center, where the oscillation is also visible. The values reported in Table 5.1, which are obtained from the Bloch wave calculations, show that the beating wavelength decreases with increasing atomic number, due to a stronger confinement. This agrees with the trend observed in the electron wave functions (Fig. 5.4 right), where the extinction length of the 1*s* oscillation is clearly decreasing with increasing Z. As described by the Bloch wave model of Rotunno *et al.* [159], the amplitude of the beating oscillations is damped due to a dephasing of the continuum of unbound states. The damping factor responsible for this was calculated according to [159] in the case of an In column and plotted as a function of thickness in Fig. 5.5. After having traveled a certain thickness, the unbound states start to rephase again and a second local maximum in the damping profile is reached around a thickness of 90 nm. The same damping profile applies for 1*s* and 2*s* oscillations, and the rephasing thus causes also the reappearance of the 1*s* wave function oscillation with reduced intensity at higher thickness, as seen in Fig. 5.4. The

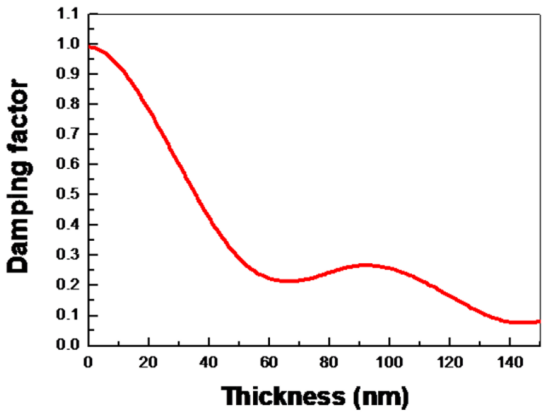

Figure 5.5: Damping factor of the beating oscillations for a STEM probe propagating on an In column as a function of sample thickness calculated according to the Bloch wave model in Ref. [159].

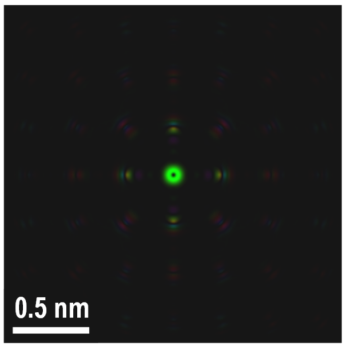

Figure 5.6: Complex representation of the p-state of the STEM electron probe propagating on an In column. The intensity is the modulus squared of the wave function and the color represents the phase.

additional effect of anomalous absorption[1] of 1s states, however, further attenuates the 1s oscillation and therefore it dies out quicker than the 2s state oscillation.

An interesting side note we want to make here addresses the excitation of the 2p states for heavier columns. In contrast to their lack of cylindrical symmetry, they can still be excited by a cylindrically symmetric probe. Since the STEM simulations are performed by repeating a Bloch wave calculation for every incidence direction in the illumination cone, a slightly different set of Bloch states is excited for each possible incident direction and the final STEM 'superstate' is the superposition of these single-electron states. The p-superstate has been calculated, as illustrated in Fig. 5.6, and turns out to have 4-fold rotational symmetry around the atomic column on which the STEM probe is located. Most of the intensity of the p-type superstate is located around neighboring columns, while a node is present above the central atomic column. We can generally say that p superstates have no/negligible intensity directly along atomic columns, neither on the central one nor on neighboring atomic columns, in any crystal system. Therefore they will produce only a negligible contribution to the HAADF intensity. However, p-states will contribute to the

[1] Electron waves that travel on the atomic columns (such as 1s) undergo a larger absorption than electron waves where part of the amplitude is located between atomic columns (such as 2s or 2p). This phenomenon is termed 'anomalous absorption' and its main cause is thermal diffuse scattering of the electrons.

depth dependent evolution of the total wave function.

5.4.2 Implications for quantitative HAADF imaging

From the Bloch wave results, it is clear that beyond a threshold Z value, $2s$ Bloch states are excited in the propagating electron wave function. This threshold lies close to $Z \approx 40$, although we emphasize that this threshold value depends on a variety of parameters such as the spacing between the atoms and the initial beam characteristics. In contrast to the $2p$ state, the $2s$ oscillation keeps the electron wave function amplitude strongly focused on the center of the atomic column and we can thus expect it to affect scattering to the HAADF detector. Therefore, let us now investigate how the excitation of the bound $2s$ Bloch wave state is influencing the HAADF intensity as a function of sample thickness.

Multislice STEM simulations are performed for two series of isolated atomic columns with increasing average atomic number to study the effect of the onset of the bound $2s$ eigenstate. In the first series, the columns consist of one type of element with Z increasing from 22 to 49. In the second series, we start from a pure Ga column and increase the mean atomic number of the column by randomly replacing Ga by In with composition ratios ranging from 0 : 1. The on-column intensity output recorded by the simulated HAADF detector is plotted as a function of sample thickness in Fig. 5.7(a) and (b). For both series, the small intensity oscillations at low thicknesses (< 40 nm) are caused by the $1s$-unbound wave function oscillation.

For larger thicknesses, a strong change in the behavior of the intensity can be observed once the average atomic number along the column exceeds a certain threshold. For the low Z columns, the intensity keeps on increasing at a more or less constant rate with increasing thickness. This is because after dechanneling of the $1s$ state, the electron wave is largely spread out and it simply 'feels' the average atomic number of the specimen. For the high Z columns, a more step-like increase in intensity takes place. This sudden increase can be attributed to the excitation of the bound $2s$ Bloch wave state which keeps the electron wave channeled on the column. The threshold value for its excitation can be refined to $Z \approx 38$ for the specific atomic spacing of 3Å considered here. The onset of this feature takes places at a thickness of around 40 – 60 nm, which coincides approximately with the second beating period of the $2s$-UB interaction (see Table 5.1). This interaction

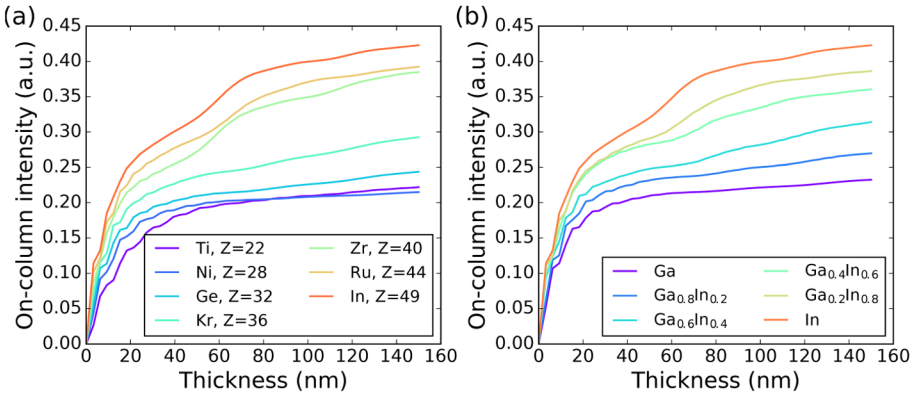

Figure 5.7: Simulated on-column HAADF-STEM intensity of isolated atomic columns for (a) columns containing a single type of element with $22 < Z < 49$ and (b) columns containing a mix of Ga and In atoms in different composition ratios in a random configuration with $31 < Z_{\text{avg}} < 49$.

causes long-wavelength intensity oscillations to persist more strongly as the average atomic number of the column increases. The shortening of the beating wavelength with increasing atomic number is reflected in the shifting of the onset of the 2*s* intensity increase to lower thicknesses for higher average Z. The fact that the same general trend is observed in both the single-atom type series and the increasing composition series consisting of a mix of two elements indicates that the onset of confinement of the 2*s* state is mostly determined by the average atomic density along the column. However, just like the 1*s* oscillation, we expect that the 2*s* oscillation causes some dependency of the HAADF intensity on the local distribution of atomic number density along the depth of the column. When more heavy atoms are located at the depth were the 2*s* wave function oscillation amplitude has its maximum, a stronger scattering and thus a stronger HAADF intensity increase can be expected.

Since high Z columns are strongly affected by the 2*s* Bloch wave state excitation, let us now see what the implications are for the compositional analysis based on HAADF-STEM intensity in high Z solid solutions. As illustrated for $Al_xGa_{1-x}N$ in Section 5.1, the composition of a crystal is typically quantified in a region where the HAADF intensity ratio with respect to the reference material becomes independent of the sample thickness and knowledge of the exact thickness of the specimen is not necessary for comparing the experimental image to the simulation. In Fig. 5.8, we compare similar intensity ratios in randomly configured monoclinic $(Ga_xAl_{1-x})_2O_3$ and $(In_xGa_{1-x})_2O_3$ in the [010] projection orientation. In the case of $(Ga_xAl_{1-x})_2O_3$, the intensity ratio of $(Ga_{0.5}Al_{0.5})_2O_3$ and Ga_2O_3 to Al_2O_3 becomes constant for thicknesses above approximately 100 nm. However, for $(In_xGa_{1-x})_2O_3$, the intensity ratio does not get constant beyond a given thickness. Instead, after the channeling oscillations, the contrast doesn't saturate at a constant value, but strong contrast oscillations remain present even at large thicknesses due to the long-wavelength 2*s* oscillations present for high-Z materials. This effect is especially visible in the derivatives of the contrast curves, where an oscillatory behavior is clearly observed up to almost 200 nm. In the contrast curves, the visibility of the 2*s* oscillations is obscured by a second effect, which is the steady decrease of the contrast at thicknesses > 100 nm. The reason for this effect is not entirely clear yet. Due to these behaviors, composition quantification in such heavier systems is not straightforward anymore since the specimen thickness has to be determined precisely.

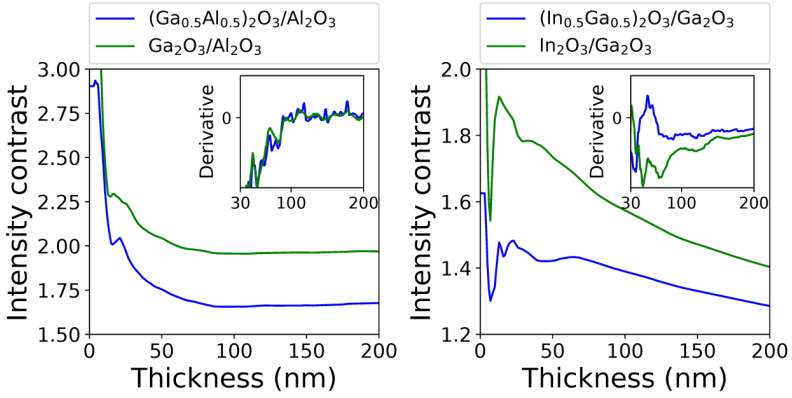

Figure 5.8: $(Ga_xAl_{1-x})_2O_3$/ Al_2O_3 and $(In_xGa_{1-x})_2O_3$/ Ga_2O_3 intensity ratios for $x = 0.5$ and $x = 1$ plotted as a function of specimen thickness, with the derivatives of the curves added as subplots.

5.4.3 Ordered vs. disordered solid solutions revisited

Having evidenced the effect of the excitation of 2*s* states for high-*Z* atomic columns on the HAADF intensity, we can, as a next step, try to explain the difference in HAADF intensity for ordered and disordered structures introduced in Sections 5.2 and 5.3. To this end, we consider two simplified two-column atomic structures, one consisting of a pure In and a pure Ga column and one consisting of two randomly configured $Ga_{0.5}In_{0.5}$ columns, with inter-column and intra-column atomic spacings of 3Å, as visualized schematically in Fig. 5.9(a). The total HAADF intensities of both configurations are compared in Fig. 5.9(b), and their difference is plotted as well. In Fig. 5.9(c), the intensity difference between the simulated STEM images of the ordered and disordered structures are evaluated at the different thicknesses indicated by the arrows in (b).

In the low thickness regime, which is dominated by 1*s* channeling, the intensities of both structures are still as good as equal. The positive and negative differences on the left and right column, respectively, are strongly centered on the columns and cancel each other out. For thicknesses larger than 25 nm, the set of randomly configured columns consistently produces the higher intensity, which means the differences on each column are not canceling out anymore. In this thickness regime, the 1*s* state starts to dechannel of the column and does not contribute to the HAADF intensity anymore. It is the 2*s* wave function oscillation that starts to dominate. This is evident in the difference images in Fig. 5.9(c), where the negative difference between the Ga and $Ga_{0.5}In_{0.5}$ columns spreads out in a much wider area around the column center than the positive difference between the In and $Ga_{0.5}In_{0.5}$ columns for thicknesses $\geq$ 25 nm. This can be understood as follows: for the pure Ga column, the 2*s* state is not contributing, while for the mixed $Ga_{0.5}In_{0.5}$ ($Z_{avg} = 40$) columns and the pure In column it is (see Table 5.1). Since the 2*s* state, with its second radially symmetric wave function maximum, is much wider than the 1*s* state, the difference of non-excitation versus excitation is visible in a wider area around the atomic column. For beam positions up to $\approx$ 1Å from the column center, electrons are channeled on the column and more strongly scattered. The intensity bump around a thickness of $\approx 50-60$ nm that was attributed to the 2*s* excitation, as demonstrated for isolated In and $Ga_{0.5}In_{0.5}$ columns (see Fig. 5.7), is also visible here. Since in the disordered structure both columns produce this bump while in the ordered structure only the In column does, the intensity difference builds up the strongest around that thickness.

Let us transfer these results to the complete lattice structures considered in Fig. 5.3. In the case of bcc InGa, the ordered and disordered lattices can be considered as a combination of multiple two-column structures, as the ones considered above, with a slightly smaller inter-column spacing of 2.47Å. The total lattice intensity can therefore be approximated as the sum of multiple two-column structure intensities and the same intensity difference as a function of thickness is expected. This is indeed observed in the simple cubic InGa structure: the higher contrast of the disordered lattice has a step-like increase at approximately 25 nm, with a second step close to 60 nm. A similar explanation accounts for the $InGaO_3$, $In_{0.5}Ga_{0.5}N$ and $AuCu_3$ structures due to the mixture of one low *Z* (i.e. no 2*s* excitation) and one high *Z* (i.e. 2*s* excitation) element. This means that in the ordered lattice, the 2*s* state is excited for only half of the cation columns (or $1/4^{th}$ in $AuCu_3$), while in the disordered lattice, the 2*s* state is excited for all cation columns, and therefore produces the higher HAADF intensity.

This simple approach gives a sound explanation for the intensity difference between

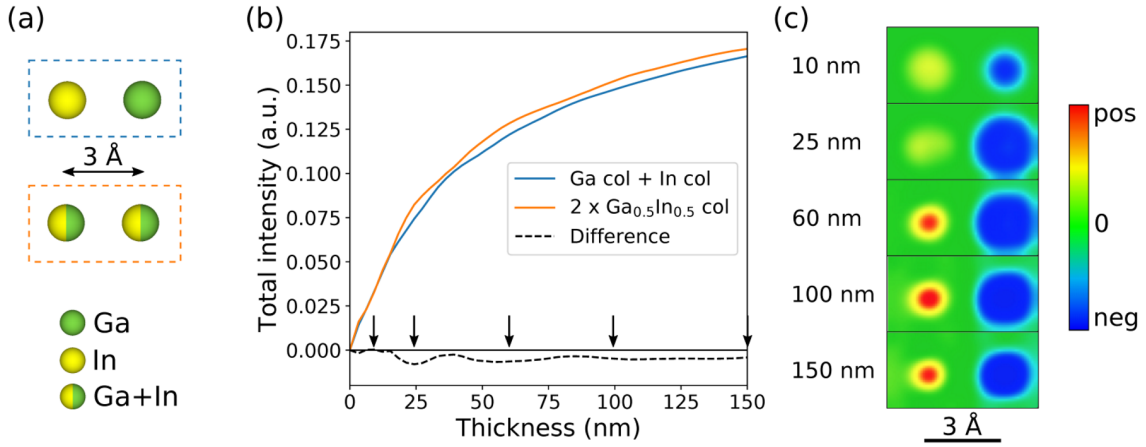

Figure 5.9: (a) Schematic representation of the projected In + Ga (ordered) and $Ga_{0.5}In_{0.5}$ + $Ga_{0.5}In_{0.5}$ (disordered) two-column structures. (b) Comparison of the total HAADF intensity as a function of thickness of the two structures described in (a) and their difference. (c) The intensity difference between the simulated STEM images of the ordered and disordered structures evaluated at different thicknesses.

ordered and disordered configurations of many different lattices. However, in reality, for the more complicated crystal symmetries or stoichiometries, more factors, like cross-correlation between neighboring columns and the exact symmetry of the lattice, are additionally influencing the wave function propagation through the crystal. This is illustrated in the case of monoclinic $InGaO_3$ in Fig. 5.10. It shows the simulated HAADF-STEM images for ordered and disordered cells at a thickness of 60 nm and the evolution of the intensity difference (ordered minus disordered) as a function of thickness. As a reminder, in the ordered lattice indium is only incorporated on the octahedral lattice sites, such that the blue balls indicate pure In columns and the green balls pure Ga columns, compared to mixed $Ga_{0.5}In_{0.5}$ columns in the disordered lattice. For small thicknesses, the difference is again located on the centers of the cation columns, due to the dominating 1*s* states. At larger thicknesses, the positive difference between the In and $Ga_{0.5}In_{0.5}$ columns stays mostly centered on the cation column, while the negative difference between the Ga and $Ga_{0.5}In_{0.5}$ columns spreads out more into the surroundings of the cation column. Around a thickness of 30 nm, the negative difference is located in the empty-space vicinity of the cation column, while starting from a thickness of 60 nm, the negative difference mainly sits on the neighboring oxygen columns, indicated by the red rectangles in Fig. 5.10. This intensity difference is not directly caused by the oxygen column, since they are too light to produce significant high-angle scattering. Rather, when the neighboring cation column is a $Ga_{0.5}In_{0.5}$ column for which the 2*s* state is excited, the strong attraction channels the electrons from the oxygen column onto the cation column resulting in a strongly enhanced scattering to the HAADF detector. This is not the case when the neighboring column is a pure Ga column, for which the 2*s* state is not excited. In contrast, there is no strong intensity difference on the oxygen columns that are neighbor to the octahedral cation columns, since in both lattices the neighboring cation column (either In or $Ga_{0.5}In_{0.5}$) is heavy enough to attract the electrons.

As a consequence of this order-disorder intensity difference, composition quantification becomes challenging when the ordering in the solid solution system under study is unknown. However, when the composition and thickness of the sample is known, this

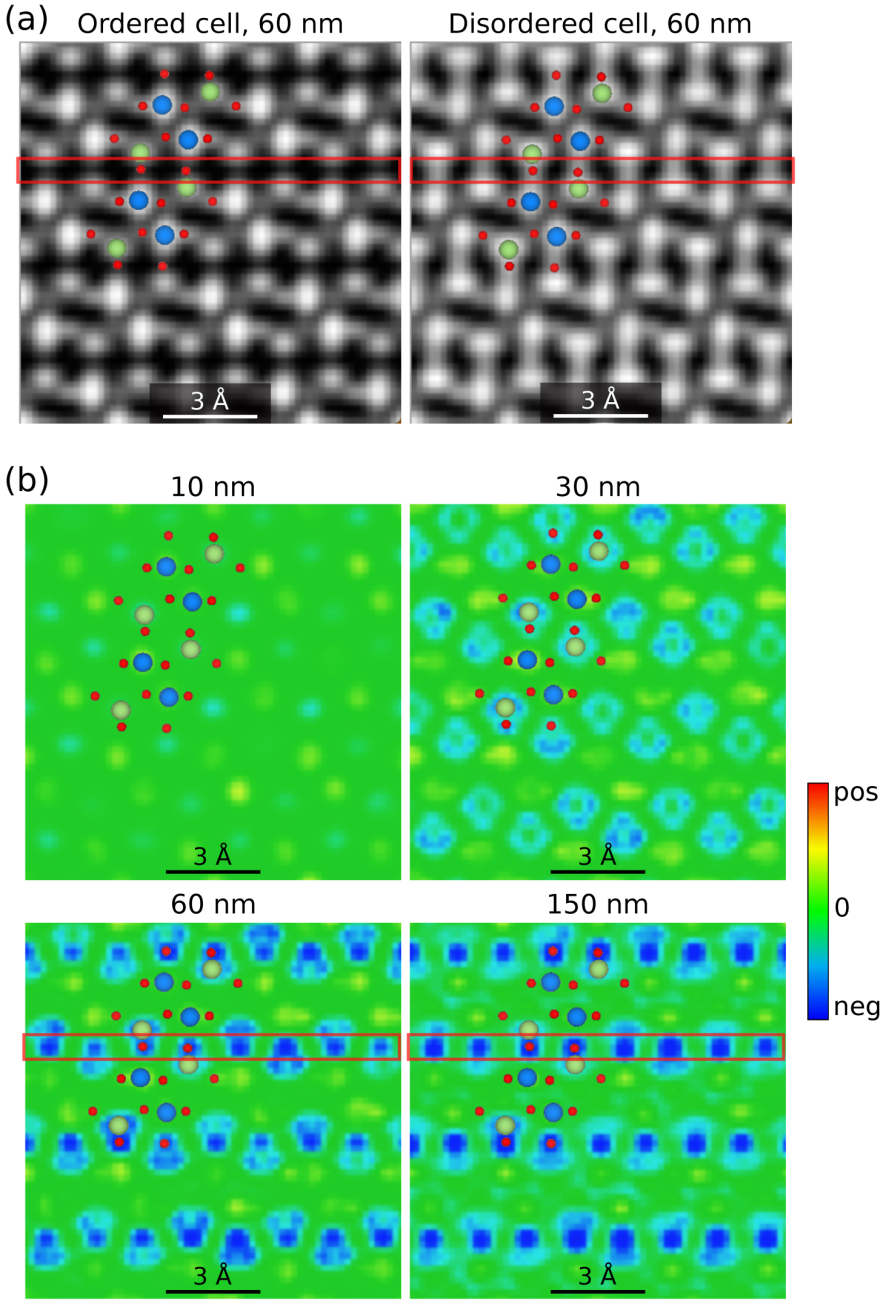

Figure 5.10: (a) Simulated HAADF-STEM images of ordered (In only on octahedral sites) and disordered $InGaO_3$ lattices with a thickness of 60 nm. (b) The intensity difference between the simulated STEM images of the ordered and disordered structures evaluated at different thicknesses. In all images the β-Ga_2O_3 model structure is overlaid to match the intensity maxima to specific atomic columns. The biggest difference in intensity for thicknesses $\geq$ 60 nm can be seen in the row of oxygen columns indicated by the red rectangles.

phenomenon could possibly be exploited to quantify its order parameter. The dependency of the HAADF intensity on the ordering in the system could be used to estimate the amount of order in materials by comparing experimental STEM-HAADF images to simulations. To see if this holds, additional supercells were created for $InGaO_3$, $In_{0.5}Ga_{0.5}N$ and $AuCu_3$ structures with varying degree of order. To describe the amount of order, we introduce a long-range order parameter S, as defined by Cowley *et al.* [203], which quantifies the number of atoms that are occupying their 'correct' position in the lattice. $S = 0$ means a completely random distribution of atoms; $S = 1$ means a perfectly ordered crystal. HAADF intensities are determined at a thickness of 100 nm and their dependency to S is shown in Fig. 5.11. For $InGaO_3$ and $In_{0.5}Ga_{0.5}N$, a monotonic decrease in intensity is found as the order parameter increases. In the case of $AuCu_3$, the intensity increases slightly as some small amount of order is introduced, but for $S > 0.5$ a significant and monotonic decrease of intensity is observed. A parabolic curve gives a good fit to all data sets.

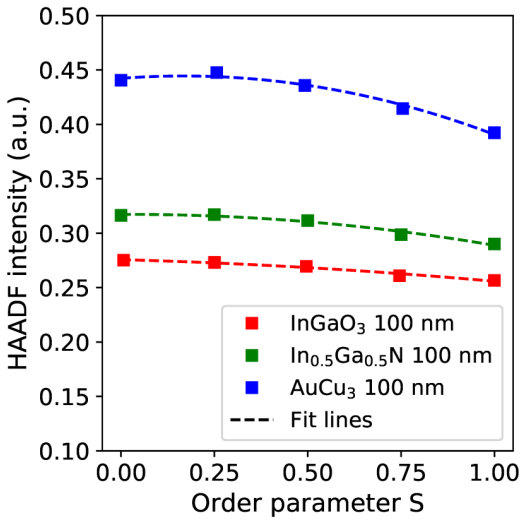

Figure 5.11: Simulated HAADF-STEM intensity at a thickness of 100 nm as a function of order parameter for $InGaO_3$, $In_{0.5}Ga_{0.5}N$ and $AuCu_3$ with parabolic fit lines to the data.

5.5 Chapter summary

In this last chapter, the importance and the consequences of the excitation of the bound $2s$ Bloch wave eigenstate in a STEM electron probe propagating on an atomic column, which comes into play above a certain atomic number threshold, was illustrated. Just like the $1s$ excitation, it produces an oscillation – in this case of longer wavelength – of the electron wave function due to the beating with the unbound Bloch wave states. Since this $2s$ oscillation keeps the beam focused on the atom column, it strongly affects scattering to the HAADF detector, which is reflected by an oscillating behavior of the HAADF-STEM intensity which persists up to thicknesses larger than 100 nm. As a result, intensity contrast in heavy solid solutions is strongly modulated up to large thicknesses which hampers composition quantification. A second important consequence that is especially important in connection to the work presented in this thesis, relates to solid solutions that consist of a mixture of elements of relatively low and high Z. When the

constituent atoms of the mixture are ordered on distinct sublattices and imaged in a zone axis direction such that all columns consist of the same atom, the average HAADF intensity is systematically lower than when the structure is disordered, starting from thicknesses larger than approximately 50 nm. In $(In_xGa_{1-x})_2O_3$, imaged in the [010] projection, where ordering is induced by the preference of indium for the six-fold lattice sites, the decrease in HAADF intensity upon ordering destroys a clear relation between HAADF intensity and composition. Apart from this challenging compositional quantification by Z-contrast in heavy solid solutions, it was also shown how the dependency of the STEM-HAADF intensity on the order parameter provides a method to estimate the degree of long-range order in these types of systems.

6

Conclusion

In this work, we investigated the phase formation in $(In_xGa_{1-x})_2O_3$. We applied established TEM characterization techniques and developed novel approaches to follow the crystallization of amorphous solid solutions in-situ in the TEM. Based on our experimental results and theory data obtained from cluster expansion, we developed a phase diagram for this system. The studied samples cover the whole compositional range ($0 \leq x \leq 1$) and are either epitaxially grown on native or foreign substrates by pulsed laser deposition, molecular beam epitaxy and metal organic vapor phase epitaxy or deposited amorphously by molecular beam epitaxy. Our studies yield the following main results.

Order drives thermodynamic equilibrium phase diagram

Because of the variety of phases and the diversity of the coordination environment of the cations in the group-III oxides, standard assumptions on solid solution mixing can not be applied and an improved methodology for constructing the phase diagram is required. First of all, this is evident in the mixing enthalpy of the ground-state lattice configurations as a function of In concentration. While the c-phase, with only six-fold coordinated cation sites, behaves as a regular solution, the mixing enthalpy of the multi-coordinated monoclinic and hexagonal phases is determined by the energetically preferred coordination environments of indium and gallium. Relatively low monoclinic mixing enthalpies are observed for $x \leq 0.5$, where indium can be incorporated in the six-fold coordinated cation sites. Additionally, at $x = 0.5$, both the β- and h-structures exhibit exceptional stability because all indium and gallium atoms can be accommodated in their preferred lattice position and a long-range ordered lattice results. For PLD growth close to 650°C, the formation of such ordered β- and h-lattices is evidenced experimentally by STEM, while in the c-phase, cations are distributed stochastically on the cation sublattice. These observations drive us to modify the general assumption of ideal mixing in solid solutions for considering the configurational entropy in the case of the monoclinic and hexagonal phase. According to calculations by cluster expansion, the maximally ordered configurations of the β- and h-phase at $x = 0.5$ are energetically strongly separated from the disordered configurations, such that it is justified to assume the entropy approximates zero. For other concentrations mixing is assumed only on coordination-specific sites. Based on these considerations, we were able to construct the full temperature dependent

equilibrium phase diagram of $(In_xGa_{1-x})_2O_3$. It improves current available literature where the only existing phase diagram is that from Edwards *et al.* [54], which is based on a sintered powder approach and covers only a limited temperature range. In addition, our efficient cluster expansion approach forms an improvement to current DFT-based literature works [50, 52], which fail to explain experimentally observed solubility limits. In our phase diagram, very narrow thermodynamic stability ranges for each phase are found, while large metastable composition ranges exist, especially for the monoclinic phase because of its flat ΔH curve in the range $x \leq 0.5$. An excellent agreement with experiment is found, where these metastable ordered compounds can be achieved due to the mobility of the atoms on the growth surface in epitaxy: the β-phase is found metastable for $x \leq 0.5$, the h-phase for $0.55 \leq x \leq 0.70$ and the c-phase for $x \geq 0.91$, while a miscibility gap remains for $0.7 < x < 0.91$ at all realistic growth temperatures. These metastable compounds are further stabilized after growth due to limited bulk diffusion in these covalently bonded materials, which inhibits phase separation. In view of applications, the achievement of metastable compounds far outside the predicted thermodynamic equilibrium solubility limits is very promising.

Configurational entropy shifts stability

While ordered lattice configurations determine the ground-state thermodynamics of the $(In_xGa_{1-x})_2O_3$ system, the stability of the phases shifts for high-configurational-entropy solid solutions. In this case, the energy distribution of the full configurational density of states of each phase has to be taken into account to evaluate their relative stability. Crystallization from the amorphous phase has been shown to offer a way to kinetically stabilize such effective high-temperature phases. Due to limited atomic mobility in a certain temperature range above the crystallization temperature, the configurational disorder present in the amorphous phase is conserved upon crystallization and phase separation is inhibited. Because energetically highly unfavorable configurations in the β- and h-phase are present in cases where In occupies unfavorable four- or five-fold cation sites, these phases become energetically unfavorable. Instead, the bixbyite phase, for which the mixing enthalpy is much less dependent on the distribution of Ga and In atoms due to its solely six-fold coordinated lattice, is stabilized for the huge composition range $x \geq 0.33$. The miscibility gap that exists in the In-rich part of the phase diagram under ambient conditions ($0.7 < x < 0.9$) is completely overcome. As another consequence of the high configurational entropy in the amorphous phase, the initial phase formed upon crystallization is characterized by a high concentration of intrinsic atomic defects such as interstitials and vacancies. This leads to the formation of spinel γ-$(In_xGa_{1-x})_2O_3$ for In concentrations $x \leq 0.22$. We showed how its defective spinel lattice can be described as a disordered monoclinic lattice. Both phases are assigned a common lattice and the phase transition is described by exchange of cations from regular lattice sites to interstitial sites in the monoclinic lattice leaving vacancies behind and vice versa. When annealed at higher temperatures, cation vacancies become mobile and they can rearrange into their equilibrium configuration, which results in the observed $\gamma \rightarrow \beta$ transition.

Our results demonstrate that solid-state crystallization of an amorphous film deposited on a crystalline lattice could be an approach to expand solubility limits of In-rich solid solutions, where the metastable solubility under thermodynamic equilibrium is limited to values as low as 9%. Moreover, it could be a way to synthesize undiscovered metastable

polymorphs by the described kinetic stabilization mechanism.

Effect of order on quantitative analysis of HAADF-STEM contrast

While Z-contrast STEM provides a reliable method for composition quantification in relatively light solid solutions such as $Al_xGa_{1-x}N$, we demonstrated that channeling may pose strong limitations to this method for materials with high atomic number. The general assumption that HAADF-STEM contrast is dominated by the 1s excited states in the propagating beam and governed by channeling oscillations at small thicknesses and a monotonic intensity increase at larger thicknesses dependent on the average atomic number of the sample, doesn't hold anymore. Our multislice and Bloch wave simulations showed that for materials with an average composition exceeding a specific threshold ($Z_{avg} \gtrsim 38$), the HAADF contrast is significantly modulated starting from a thickness of 40 nm. This observation is attributed to the 2s Bloch state excitation for beam propagation on heavy columns which produces a wave function oscillation of longer wavelength than the 1s oscillation, that is reflected in the HAADF intensity. Another important consequence of the 2s excitation, which connects to the rest of this work, is that ordered and disordered lattices produce a different intensity, which provides a way to estimate the degree of order in solid solutions like $(In_xGa_{1-x})_2O_3$.

Acknowledgements

Working on my doctorate for the past four years and the adventure of moving to Germany has been an enriching experience, both professionally and personally. All the people that have contributed to my work and supported my journey, deserve a special thank you.

First of all, I would like to thank my supervisor Dr. Martin Albrecht, for his welcoming and appreciative attitude, his guidance throughout all the steps of the PhD and all the interesting scientific discussions. His passion for science and all the projects he is involved in really brought along a motivating and supporting atmosphere. I am very grateful for my time at the IKZ, especially due to the company of my current and former colleagues from the electron microscopy group, who have provided a very enjoyable working atmosphere: thanks to Dr. Houari Amari, Leonardo Cancellara, Dr. Mariia Anikeeva, Martina Zupancic, Musbah Nofal, Dr. Robert Schewski, Thilo Remmele, Dr. Tobias Schulz, Dr. Toni Markurt and Valeria Bonito-Oliva. A special thank you goes out to Toni for familiarizing me with the TEM instrument, your scientific input and just everything I have learned from you, Robert for teaching me your personally developed tricks for TEM sample preparation, and Thilo for all the technical help at the TEM.

An important part of this work was constructed through collaborations with theory groups. Many thanks to Dr. Christopher Sutton, Dr. Luca Ghiringhelli and Prof. Dr. Matthias Scheffler from the Fritz Haber Institute in Berlin for performing the CE and DFT calculations and your input from theory side into the topic. Also Dr. Enzo Rotunno and Dr. Vincenzo Grillo from CNR-NANO in Modena deserve gratitude for their Bloch wave calculations, which provided useful insights in our STEM simulation studies.

I want to acknowledge the people who were responsible for growing the samples that I studied and the complementary characterization they performed and shared with me. Thanks to Dr. Oliver Bierwagen, Dr. Piero Mazzolini, Alexandra Papadogianni and Dr. Patrick Vogt from the Paul-Drüde-Institut in Berlin for the growth of MBE samples and the development of the in-situ sample deposition method. Thanks to Dr. Holger von Wenckstern and Anna Hassa from the Universität Leipzig for the growth of PLD samples. Thank you to my colleagues from IKZ, Dr. Saud Bin Anooz for the growth of MOVPE samples, and Albert Kwasniewski for XRD characterization of my samples.

I am thankful for the willingness of Prof. Dr. Christoph Koch, Prof. Dr. Thomas Schröder and Prof. Dr. Sandra Van Aert to read and review this thesis. In that regard, I also want to thank again Martin for your useful comments and proofreading of this work.

I want to acknowledge GraFOx, the Leibniz Gemeinschaft and the Forschungverbund Berlin for the funding to make this project possible and for providing a network of stimulating collaborations which lead to many fruitful discussions. Thanks for all the well-organized GraFOx meetings and the ability to participate in conferences and summer schools to develop professional skills. I am thankful to Prof. Dr. Thomas Schröder, our director at IKZ, for trusting in my work and giving me the necessary time and financial support to finish my PhD in an optimal way.

Natuurlijk wil ik ook de mensen bedanken die het dichtst bij mij staan, te beginnen met mijn familie. Bedankt aan mijn ouders om me altijd te hebben gesteund in mijn

keuzes en mijn studies, ook al was het niet bij de deur, en de thuis die nog altijd even warm aanvoelt bij elk bezoek. Lennaert, Roseline en Sebastiaan, bedankt dat ik ondanks mijn afwezigheid altijd terecht kan bij jullie voor eender wat. Ook bedankt aan de familie Ceulemans, jullie warme steun werd hard geapprecieerd. Naar familiebezoekjes werd telkens heel hard uitgekeken!

Laurine en Rodric, wat waren jullie enorm belangrijk als 'partners' in dit Duitsland avontuur. Bedankt om samen zo veel ervaringen te delen, die ik voor altijd zal koesteren. Thank you Momo & Daniel, Markus & Sarah, Taylor & Peter, for the support, the friendship and for bearing through two lockdowns together.

Ruben, samen begonnen we aan dit avontuur in Berlijn en samen ronden we het af, wat een ongelofelijke belevenis waren de voorbije vier jaar met jou. Ik kan je niet genoeg bedanken voor je eeuwige steun, motivatie en liefde, die me hebben geholpen tot dit eindresultaat te komen. Bedankt om er altijd voor me te zijn!

Bibliography

[1] W. Shockley. Circuit Element Utilizing Semiconductor Material. U.S. Patent 2269347, 25 September 1951.

[2] H. Krömer. Theory of a Wide-Gap Emitter for Transistors. *Proc. IRE* **45**, 1535, doi:10.1109/JRPROC.1957.278348 (1957).

[3] Z. I. Alferov and R. F. Kazarinov. Semiconductor laser with electric pumping. Inventor's Certificate No. 181737 [in Russian], Application No. 950840, priority as of March 30, 1963.

[4] Z. I. Alferov, V. M. Andreev, V. I. Korolkov, E. L. Portnoi and D. N. Tretyako. Coherent radiation of epitaxial heterojunction structures in AlAs-GaAs system. *Sov. Phys. Semicond. - USSR* **2**, 1289 (1969).

[5] Z. I. Alferov. The double heterostructure: Concept and its applications in physics, electronics and technology. *Rev. Mod. Phys.* **73**, 767, doi:10.1142/S0217979202010233 (2001).

[6] K. V. Klitzing, G. Dorda and M. Pepper. New method for high-accuracy determination of the fine-structure constant based on quantized hall resistance. *Phys. Rev. Lett.* **45**, 494, doi:10.1103/PhysRevLett.45.494 (1980).

[7] S. Fujita. Wide-bandgap semiconductor materials: For their full bloom. *Jpn. J. Appl. Phys.* **54**, 030101, doi:10.7567/JJAP.54.030101 (2015).

[8] D. Klimm. Electronic materials with a wide band gap: Recent developments. *IUCrJ* **1**, 281, doi:10.1107/S2052252514017229 (2014).

[9] B. F. Levine, K. K. Choi, C. G. Bethea, J. Walker and R. J. Malik. New 10 μm infrared detector using intersubband absorption in resonant tunneling GaAlAs superlattices. *Appl. Phys. Lett.* **50**, 1092, doi:10.1063/1.97928 (1987).

[10] I. Schnitzer, E. Yablonovitch, C. Caneau and T. J. Gmitter. Ultrahigh spontaneous emission quantum efficiency, 99.7% internally and 72% externally, from AlGaAs/GaAs/AlGaAs double heterostructures. *Appl. Phys. lett.* **62**, 131, doi:10.1063/1.109348 (1993).

[11] M. L. Lee, E. A. Fitzgerald, M. T. Bulsara, M. T. Currie and A. Lochtefeld. Strained Si, SiGe, and Ge channels for high-mobility metal-oxide- semiconductor field-effect transistors. *J. Appl. Phys.* **97**, 011101, doi:10.1063/1.1819976 (2005).

[12] S. Nakamura, M. Senoh and T. Mukai. P-GaN/N-InGaN/N-GaN double-heterostructure blue-light-emitting diodes. *Jpn. J. Appl. Phys.* **32**, L8, doi:10.1143/JJAP.32.L8 (1993).

[13] S. Nakamura *et al.* InGaN-Based Multi-Quantum-Well-Structure Laser Diodes. *Jpn. J. Appl. Phys.* **35**, L74, doi:10.1143/JJAP.35.L74 (1996).

[14] T. K. Gachovska and J. L. Hudgins. 5 - SiC and GaN Power Semiconductor Devices. In M. H. Rashid (ed.) *Power Electronics Handbook (Fourth Edition)*, 95 – 155, doi:https://doi.org/10.1016/B978-0-12-811407-0.00005-2 (Butterworth-Heinemann, 2018).

[15] I. H. Ho and G. B. Stringfellow. Solid phase immiscibility in GaInN. *Appl. Phys. Lett.* **69**, 2701, doi:10.1063/1.117683 (1996).

[16] R. Mohamad, A. Béré, J. Chen and P. Ruterana. Investigation of strain effects on phase diagrams in the ternary nitride alloys (InAlN, AlGaN, InGaN). *Phys. Stat. Sol. A* **214**, 1600752, doi:10.1002/pssa.201600752 (2017).

[17] K. Irmscher *et al.* On the nature and temperature dependence of the fundamental band gap of In_2O_3. *Phys. Stat. Sol. A* **211**, 54, doi:10.1002/pssa.201330184 (2014).

[18] H. H. Tippins. Optical absorption and photoconductivity in the band edge of β-Ga_2O_3. *Phys. Rev.* **140**, A316, doi:10.1103/PhysRev.140.A316 (1965).

[19] M. Orita, H. Ohta, M. Hirano and H. Hosono. Deep-ultraviolet transparent conductive β-Ga_2O_3 thin films. *Appl. Phys. Lett.* **77**, 4166, doi:10.1063/1.1330559 (2000).

[20] H. He *et al.* First-principles study of the structural, electronic, and optical properties of Ga_2O_3 in its monoclinic and hexagonal phases. *Phys. Rev. B* **74**, 195123, doi:10.1103/PhysRevB.74.195123 (2006).

[21] S. Fujita and K. Kaneko. Epitaxial growth of corundum-structured wide band gap III-oxide semiconductor thin films. *J. Cryst. Growth* **401**, 588, doi:10.1016/j.jcrysgro.2014.02.032 (2014).

[22] P. Thompson, D. Cox and J. Hastings. Rietveld refinement of Debye-Scherrer synchrotron X-ray data from Al_2O_3. *J. Appl. Cryst.* **20**, 79, doi:10.1107/S0021889887087090 (1987).

[23] J. Ahman, G. Svensson and J. Albertsson. A Reinvestigation of β-Gallium Oxide. *Acta Cryst.* **C52**, 1336, doi:10.1107/S0108270195016404 (1996).

[24] M. Marezio. Refinement of the crystal structure of In_2O_3 at two wavelengths. *Acta Cryst.* **20**, 723, doi:10.1107/s0365110x66001749 (1966).

[25] R. Roy, V. G. Hill and E. F. Osborn. Polymorphism of Ga_2O_3 and the System Ga_2O_3-H_2O. *J. Am. Chem. Soc.* **74**, 719, doi:10.1021/ja01123a039 (1952).

[26] H. Y. Playford, A. C. Hannon, E. R. Barney and R. I. Walton. Structures of uncharacterised polymorphs of gallium oxide from total neutron diffraction. *Chem. Eur. J.* **19**, 2803, doi:10.1002/chem.201203359 (2013).

[27] M. B. Maccioni, F. Ricci and V. Fiorentini. Structure and gap of low-x $(Ga_{1-x}In_x)_2O_3$ alloys. *J. Physics: Conf. Ser.* **566**, 012016, doi:10.1088/1742-6596/566/1/012016 (2014).

[28] R. L. Weiher and R. P. Ley. Optical properties of indium oxide. *J. Appl. Phys.* **37**, 299, doi:10.1063/1.1707830 (1966).

[29] H. Müller. Electrical and Optical Properties of Sputtered In_2O_3 Films. *Phys. Stat. Sol. B* **27**, 723, doi:10.1002/pssb.19680270229 (1968).

[30] G. Rupprecht. Untersuchungen der elektrischen und lichtelektrischen Leitfähigkeit dünner Indiumoxydschichten. *Z. Physik* **139**, 504, doi:10.1007/BF01374559 (1954).

[31] O. Bierwagen. Indium oxide - A transparent, wide-band gap semiconductor for (opto)electronic applications. *Semicond. Sci. Technol.* **30**, 024001, doi:10.1088/0268-1242/30/2/024001 (2015).

[32] R. Groth. Untersuchungen an halbleitenden Indiumoxydschichten. *Phys. Stat. Sol. B* **14**, 69, doi:10.1002/pssb.19660140104 (1966).

[33] G. S. Chae. Modified transparent conducting oxide for flat panel displays only. *Jpn. J. Appl. Phys.* **40**, 1282, doi:10.1143/jjap.40.1282 (2001).

[34] A. Porch, D. V. Morgan, R. M. Perks, M. O. Jones and P. P. Edwards. Transparent current spreading layers for optoelectronic devices. *J. Appl. Phys.* **96**, 4211, doi:10.1063/1.1786674 (2004).

[35] A. N. Tiwari *et al.* CdTe solar cell in a novel configuration. *Prog. Photovolt.* **12**, 33, doi:10.1002/pip.525 (2004).

[36] Z. Galazka. β-Ga_2O_3 for wide-bandgap electronics and optoelectronics. *Semicond. Sci. Technol.* **33**, 113001, doi:10.1088/1361-6641/aadf78 (2018).

[37] Z. Galazka *et al.* On the bulk β-Ga_2O_3 single crystals grown by the Czochralski method. *J. Cryst. Growth* **404**, 184, doi:10.1016/j.jcrysgro.2014.07.021 (2014).

[38] Z. Galazka *et al.* Scaling-Up of Bulk β-Ga_2O_3 Single Crystals by the Czochralski Method. *ECS J. Solid State Sci. Technol.* **6**, Q3007, doi:10.1149/2.0021702jss (2017).

[39] M. Higashiwaki, K. Sasaki, A. Kuramata, T. Masui and S. Yamakoshi. Gallium oxide (Ga_2O_3) metal-semiconductor field-effect transistors on single-crystal β-Ga_2O_3 (010) substrates. *Appl. Phys. Lett.* **100**, 013504, doi:10.1063/1.3674287 (2012).

[40] M. H. Wong, K. Sasaki, A. Kuramata, S. Yamakoshi and M. Higashiwaki. Electron channel mobility in silicon-doped Ga_2O_3 MOSFETs with a resistive buffer layer. *Jpn. J. Appl. Phys.* **55**, 1202B9, doi:10.7567/JJAP.55.1202B9 (2016).

[41] A. J. Green *et al.* 3.8-MV/cm Breakdown Strength of MOVPE-Grown Sn-Doped β-Ga_2O_3 MOSFETs. *IEEE Electron Device Lett.* **37**, 902, doi:10.1109/LED.2016.2568139 (2016).

[42] N. A. Moser *et al.* High pulsed current density β-Ga_2O_3 MOSFETs verified by an analytical model corrected for interface charge. *Appl. Phys. Lett.* **110**, 143505, doi:10.1063/1.4979789 (2017).

[43] K. Irmscher, Z. Galazka, M. Pietsch, R. Uecker and R. Fornari. Electrical properties of β-Ga_2O_3 single crystals grown by the Czochralski method. *J. Appl. Phys.* **110**, 063720, doi:10.1063/1.3642962 (2011).

[44] K. Sasaki, M. Higashiwaki, A. Kuramata, T. Masui and S. Yamakoshi. MBE grown Ga_2O_3 and its power device applications. *J. Cryst. Growth* **378**, 591, doi:10.1016/j.jcrysgro.2013.02.015 (2013).

[45] M. Higashiwaki, H. Murakami, Y. Kumagai and A. Kuramata. Current status of Ga_2O_3 power devices. *Jpn. J. Appl. Phys.* **55**, 1202A1, doi:10.7567/JJAP.55.1202A1 (2016).

[46] K. Konishi *et al.* 1-kV vertical Ga_2O_3 field-plated Schottky barrier diodes. *Appl. Phys. Lett.* **110**, 103506, doi:10.1063/1.4977857 (2017).

[47] R. Suzuki, S. Nakagomi, Y. Kokubun, N. Arai and S. Ohira. Enhancement of responsivity in solar-blind β-Ga_2O_3 photodiodes with a Au Schottky contact fabricated on single crystal substrates by annealing. *Appl. Phys. Lett.* **94**, 222102, doi:10.1063/1.3147197 (2009).

[48] Y. Kokubun, T. Abe and S. Nakagomi. Sol-gel prepared $(Ga_{1-x}In_x)_2O_3$ thin films for solar-blind ultraviolet photodetectors. *Phys. Stat. Sol. A* **207**, 1741, doi:10.1002/pssa.200983712 (2010).

[49] H. von Wenckstern *et al.* Structural and optical properties of $(In,Ga)_2O_3$ thin films and characteristics of Schottky contacts thereon. *Semicond. Sci. Technol.* **30**, 024005, doi:10.1088/0268-1242/30/2/024005 (2015).

[50] H. Peelaers, D. Steiauf, J. B. Varley, A. Janotti and C. G. Van De Walle. $(In_xGa_{1-x})_2O_3$ alloys for transparent electronics. *Phys. Rev. B* **92**, 085206, doi:10.1103/PhysRevB.92.085206 (2015).

[51] R. Wakabayashi *et al.* Band alignment at β-$(Al_xGa_{1-x})_2O_3$/β-Ga_2O_3 (100) interface fabricated by pulsed-laser deposition. *Appl. Phys. Lett.* **112**, 232103, doi:10.1063/1.5027005 (2018).

[52] M. B. Maccioni and V. Fiorentini. Phase diagram and polarization of stable phases of $(Ga_{1-x}In_x)_2O_3$. *Appl. Phys. Express* **9**, 041102, doi:10.7567/APEX.9.041102 (2016).

[53] R. Shannon and C. Prewitt. Synthesis and structure of phases in the In_2O_3-Ga_2O_3 system. *J. Inorg. Nucl. Chem.* **30**, 1389, doi:10.1016/0022-1902(68)80277-5 (1968).

[54] D. D. Edwards, P. E. Folkins and T. O. Mason. Phase Equilibria in the Ga_2O_3-In_2O_3 System. *J. Am. Ceram. Soc.* **80**, 253, doi:10.1111/j.1151-2916.1997.tb02820.x (1997).

[55] V. Vasyltsiv, Y. Rym and Y. Zakharko. Optical absorption and photoconductivity at the band edge of β-$Ga_{2-x}In_xO_3$. *Phys. Stat. Sol. B* **195**, 653, doi:10.1002/pssb.2221950232 (1996).

[56] A. Kudo and I. Mikami. Photocatalytic activities and photophysical properties of $Ga_{2-x}In_xO_3$ solid solution. *J. Chem. Soc.* **94**, 2929, doi:10.1039/a805563g (1998).

[57] L. Binet, G. Gauthier, C. Vigreux and D. Gourier. Electron magnetic resonance and optical properties of $Ga_{2-2x}In_{2x}O_3$ solid solutions. *J. Phys. Chem. Solids* **60**, 1755, doi:10.1016/S0022-3697(99)00021-9 (1999).

[58] C. Vigreux, L. Binet, D. Gourier and B. Piriou. Formation by laser impact of conducting β-Ga_2O_3-In_2O_3 solid solutions with composition gradients. *J. Solid State Chem.* **157**, 94, doi:10.1006/jssc.2000.9043 (2001).

[59] H. Von Wenckstern *et al.* Continuous composition spread using pulsed-laser deposition with a single segmented target. *CrystEngComm* **15**, 10020, doi:10.1039/c3ce41327f (2013).

[60] C. Kranert *et al.* Lattice parameters and Raman-active phonon modes of $(In_xGa_{1-x})_2O_3$ for $x < 0.4$. *J. Appl. Phys.* **116**, 013505, doi:10.1063/1.4915627 (2014).

[61] T. Oshima and S. Fujita. Properties of Ga_2O_3-based $(In_xGa_{1-x})_2O_3$ alloy thin films grown by molecular beam epitaxy. *Phys. Stat. Sol. C* **5**, 3113, doi:10.1002/pssc.200779297 (2008).

[62] A. Wang *et al.* Growth, microstructure, charge transport, and transparency of random polycrystalline and heteroepitaxial metalorganic chemical vapor deposition-derived gallium-indium-oxide thin films. *J. Mater. Res.* **17**, 3155, doi:10.1557/JMR.2002.0456 (2002).

[63] Z. Galazka *et al.* Czochralski growth and characterization of β-Ga_2O_3 single crystals. *Cryst. Res. Technol.* **45**, 1229, doi:10.1002/crat.201000341 (2010).

[64] H. W. Kim and N. H. Kim. Growth of gallium oxide thin films on silicon by the metal organic chemical vapor deposition method. *Mater. Sci. Eng. B* **110**, 34, doi:10.1016/j.mseb.2004.01.012 (2004).

[65] C. Y. Huang, R. H. Horng, D. S. Wuu, L. W. Tu and H. S. Kao. Thermal annealing effect on material characterizations of β-Ga_2O_3 epilayer grown by metal organic chemical vapor deposition. *Appl. Phys. Lett.* **102**, 011119, doi:10.1063/1.4773247 (2013).

[66] G. Wagner *et al.* Homoepitaxial growth of β-Ga_2O_3 layers by metal-organic vapor phase epitaxy. *Phys. Stat. Sol. A* **211**, 27, doi:10.1002/pssa.201330092 (2014).

[67] D. Gogova *et al.* Structural properties of Si-doped β-Ga_2O_3 layers grown by MOVPE. *J. Cryst. Growth* **401**, 665, doi:10.1016/j.jcrysgro.2013.11.056 (2014).

[68] Y. Oshima, E. G. Víllora and K. Shimamura. Quasi-heteroepitaxial growth of β-Ga_2O_3 on off-angled sapphire (0001) substrates by halide vapor phase epitaxy. *J. Cryst. Growth* **410**, 53, doi:10.1016/j.jcrysgro.2014.10.038 (2015).

[69] K. Nomura *et al.* Thermodynamic study of β-Ga_2O_3 growth by halide vapor phase epitaxy. *J. Cryst. Growth* **405**, 19, doi:10.1016/j.jcrysgro.2014.06.051 (2014).

[70] G. A. Battiston, R. Gerbasi, M. Porchia, R. Bertoncello and F. Caccavale. Chemical vapour deposition and characterization of gallium oxide thin films. *Thin Solid Films* **279**, 115–118, doi:10.1016/0040-6090(95)08161-5 (1996).

[71] S. Rafique *et al.* Homoepitaxial growth of β-Ga_2O_3 thin films by low pressure chemical vapor deposition. *Appl. Phys. Lett.* **108**, 182105, doi:10.1063/1.4948944 (2016).

[72] E. G. Víllora, K. Shimamura, K. Kitamura and K. Aoki. Rf-plasma-assisted molecular-beam epitaxy of β-Ga_2O_3. *Appl. Phys. Lett.* **88**, 031105, doi:10.1063/1.2164407 (2006).

[73] P. Vogt and O. Bierwagen. Reaction kinetics and growth window for plasma-assisted molecular beam epitaxy of Ga_2O_3 : Incorporation of Ga vs. Ga_2O desorption. *Appl. Phys. Lett.* **108**, 072101, doi:10.1063/1.4942002 (2016).

[74] T. Oshima, T. Okuno and S. Fujita. Ga_2O_3 thin film growth on c-plane sapphire substrates by molecular beam epitaxy for deep-ultraviolet photodetectors. *Jpn. J. Appl. Phys.* **46**, 7217, doi:10.1143/JJAP.46.7217 (2007).

[75] M. Orita, H. Hiramatsu, H. Ohta, M. Hirano and H. Hosono. Preparation of highly conductive, deep ultraviolet transparent β-Ga_2O_3 thin film at low deposition temperatures. *Thin Solid Films* **411**, 134–139, doi:10.1016/S0040-6090(02)00202-X (2002).

[76] K. Matsuzaki *et al.* Growth, structure and carrier transport properties of Ga_2O_3 epitaxial film examined for transparent field-effect transistor. *Thin Solid Films* **496**, 37, doi:10.1016/j.tsf.2005.08.187 (2006).

[77] S. Müller, H. Von Wenckstern, D. Splith, F. Schmidt and M. Grundmann. Control of the conductivity of Si-doped β-Ga_2O_3 thin films via growth temperature and pressure. *Phys. Stat. Sol. A* **211**, 34, doi:10.1002/pssa.201330025 (2014).

[78] R. Wakabayashi *et al.* Oxygen-radical-assisted pulsed-laser deposition of β-Ga_2O_3 and β-$(Al_xGa_{1-x})_2O_3$ films. *J. Cryst. Growth* **424**, 77, doi:10.1016/j.jcrysgro.2015.05.005 (2015).

[79] M. V. Abrashev, N. D. Todorov and J. Geshev. Raman spectra of R_2O_3 (R - Rare earth) sesquioxides with C-type bixbyite crystal structure: A comparative study. *J. Appl. Phys.* **116**, doi:10.1063/1.4894775 (2014).

[80] Y. Repelin, C. Proust, E. Husson and J. M. Beny. Vibrational spectroscopy of the C-form of yttrium sesquioxide. *J. Solid State Chem.* **118**, 163, doi:10.1006/jssc.1995.1326 (1995).

[81] N. D. Todorov *et al.* Raman spectroscopy and lattice dynamical calculations of Sc_2O_3 single crystals. *Phys. Rev. B* **87**, 104301, doi:10.1103/PhysRevB.87.104301 (2013).

[82] E. Tarsa, J. English and J. Speck. Pulsed laser deposition of oriented In_2O_3 on (001) InAs, MgO, and yttria-stabilized zirconia. *Appl. Phys. Lett.* **62**, 2332, doi:10.1063/1.109408 (1993).

[83] N. Taga *et al.* Deposition of heteroepitaxial In_2O_3 thin films by molecular beam epitaxy. *Jpn. J. Appl. Phys.* **37**, 6524, doi:10.1143/jjap.37.6524 (1998).

[84] Z. Galazka, R. Uecker and R. Fornari. A novel crystal growth technique from the melt: Levitation-Assisted Self-Seeding Crystal Growth Method. *J. Cryst. Growth* **388**, 61, doi:10.1016/j.jcrysgro.2013.11.049 (2014).

[85] B. Cockayne, M. Chesswas and D. B. Gasson. Single-crystal growth of sapphire. *J. Mater. Sci.* **2**, 7, doi:10.1007/BF00550046 (1967).

[86] H. LaBelle and A. Mlavsky. Growth of Sapphire Filaments from the Melt. *Nature* **216**, 574, doi:10.1038/216574b0 (1967).

[87] A. Horowitz *et al.* The growth of dome-shaped sapphire crystals by the gradient solidification method (GSM). *J. Cryst. Growth* **128**, 824, doi:10.1016/S0022-0248(07)80052-2 (1993).

[88] A. Nehari *et al.* Ti-doped sapphire (Al_2O_3) single crystals grown by the Kyropoulos technique and optical characterizations. *Cryst. Growth Des.* **11**, 445, doi:10.1021/cg101190q (2011).

[89] M. Epifani and P. Siciliano. Ambient pressure synthesis of corundum type In_2O_3. *J. Am. Chem. Soc.* **126**, 4078, doi:10.1021/ja0318075 (2004).

[90] D. Liu *et al.* High-pressure X-ray diffraction and Raman spectra study of indium oxide. *J. Appl. Phys.* **104**, 083506, doi:10.1063/1.2999369 (2008).

[91] M. F. Bekheet *et al.* Orthorhombic In_2O_3: A metastable polymorph of indium sesquioxide. *Angew. Chem. Int. Ed.* **52**, 6531, doi:10.1002/anie.201300644 (2013).

[92] H. Yusa, T. Tsuchiya, J. Tsuchiya, N. Sata and Y. Ohishi. α-Gd_2S_3-type structure in In_2O_3: Experiments and theoretical confirmation of a high-pressure polymorph in sesquioxide. *Phys. Rev. B* **78**, 092107, doi:10.1103/PhysRevB.78.092107 (2008).

[93] G. Busca. The surface of transitional aluminas: A critical review. *Catal. Today* **226**, 2, doi:10.1016/j.cattod.2013.08.003 (2014).

[94] L. Samain *et al.* Structural analysis of highly porous γ-Al_2O_3. *J. Solid State Chem.* **217**, 1, doi:10.1016/j.jssc.2014.05.004 (2014).

[95] N. Lindulf, M. Halvarsson, H. Nordén and S. Vuorinen. Microstructural investigation of the κ-$Al_2O_3 \rightarrow \alpha$-$Al_2O_3$ transformation in multilayer coatings of chemically vapour deposited κ-Al_2O_3. *Thin Solid Films* **253**, 311, doi:10.1016/0040-6090(94)90340-9 (1994).

[96] Z. Cheng, M. Hanke, P. Vogt, O. Bierwagen and A. Trampert. Phase formation and strain relaxation of Ga_2O_3 on c-plane and a-plane sapphire substrates as studied by synchrotron-based X-ray diffraction. *Appl. Phys. Lett.* **111**, 162104, doi:10.1063/1.4998804 (2017).

[97] R. Schewski *et al.* Epitaxial stabilization of pseudomorphic α-Ga_2O_3 on sapphire (0001). *Appl. Phys. Express* **8**, 011101, doi:10.7567/APEX.8.011101 (2015).

[98] H. Nishinaka, D. Tahara, S. Morimoto and M. Yoshimoto. Epitaxial growth of α-Ga_2O_3 thin films on a-, m-, and r-plane sapphire substrates by mist chemical vapor deposition using α-Fe_2O_3 buffer layers. *Mater. Lett.* **205**, 28, doi:10.1016/j.matlet.2017.06.003 (2017).

[99] D. Y. Guo *et al.* Epitaxial growth and solar-blind photoelectric properties of corundum-structured α-Ga_2O_3 thin films. *Mater. Lett.* **164**, 364, doi:10.1016/j.matlet.2015.11.001 (2015).

[100] S. D. Lee, K. Akaiwa and S. Fujita. Thermal stability of single crystalline alpha gallium oxide films on sapphire substrates. *Phys. Stat. Sol. C* **10**, 1592, doi:10.1002/pssc.201300259 (2013).

[101] D. Machon, P. F. McMillan, B. Xu and J. Dong. High-pressure study of the β-to-α transition in Ga_2O_3. *Phys. Rev. B* **73**, 094125, doi:10.1103/PhysRevB.73.094125 (2006).

[102] R. S. Zhou and R. L. Snyder. Structures and transformation mechanisms of the η, γ and θ transition aluminas. *Acta Cryst.* **B47**, 617, doi:10.1107/S0108768191002719 (1991).

[103] H. Y. Playford *et al.* Characterization of structural disorder in γ-Ga_2O_3. *J. Phys. Chem. C* **118**, 16188, doi:10.1021/jp5033806 (2014).

[104] M. Zinkevich *et al.* Microstructural and thermodynamic study of γ-Ga_2O_3. *Z. Met.* **95**, 756, doi:10.3139/146.018018 (2004).

[105] S. W. Kim, S. Iwamoto and M. Inoue. Solvothermal oxidation of gallium metal. *Ceram. Int.* **35**, 1603, doi:10.1016/j.ceramint.2008.09.005 (2009).

[106] T. Oshima, T. Nakazono, A. Mukai and A. Ohtomo. Epitaxial growth of γ-Ga_2O_3 films by mist chemical vapor deposition. *J. Cryst. Growth* **359**, 60, doi:10.1016/j.jcrysgro.2012.08.025 (2012).

[107] H. Hayashi, R. Huang, F. Oba, T. Hirayama and I. Tanaka. Epitaxial growth of Mn-doped γ-Ga_2O_3 on spinel substrate. *J. Mater. Res.* **26**, 578, doi:10.1557/jmr.2010.32 (2011).

[108] F. Boschi *et al.* Hetero-epitaxy of ϵ-Ga_2O_3 layers by MOCVD and ALD. *J. Cryst. Growth* **443**, 25, doi:10.1016/j.jcrysgro.2016.03.013 (2016).

[109] Y. Yao *et al.* Growth and characterization of α-, β-, and ϵ-phases of Ga_2O_3 using MOCVD and HVPE techniques. *Mater. Res. Lett.* **6**, 268, doi:10.1080/21663831.2018.1443978 (2018).

[110] I. Cora *et al.* The real structure of ϵ-Ga_2O_3 and its relation to κ-phase. *CrystEngComm* **19**, 1509, doi:10.1039/C7CE00123A (2017).

[111] M. Kneiß *et al.* Tin-assisted heteroepitaxial PLD-growth of κ-Ga_2O_3 thin films with high crystalline quality. *APL Mater.* **7**, doi:10.1063/1.5054378 (2019).

[112] R. Fornari *et al.* Thermal stability of ϵ-Ga_2O_3 polymorph. *Acta Mater.* **140**, 411, doi:10.1016/j.actamat.2017.08.062 (2017).

[113] S. H. Wei and S. B. Zhang. Structure stability and carrier localization in CdX (X = S, Se, Te) semiconductors. *Phys. Rev. B* **62**, 6944, doi:10.1103/PhysRevB.62.6944 (2000).

[114] F. P. Sabino, L. N. De Oliveira and J. L. F. Da Silva. Role of atomic radius and d-states hybridization in the stability of the crystal structure of M_2O_3 (M=Al, Ga, In) oxides. *Phys. Rev. B* **90**, 155206, doi:10.1103/PhysRevB.90.155206 (2014).

[115] J. Ma and S.-H. Wei. Origin of the structural diversity of M_2O_3 (M=Al, Ga, In). *Comput. Mater. Sci.* **104**, 35, doi:10.1016/j.commatsci.2015.03.017 (2015).

[116] F. Hanic, M. Hartmanová, G. G. Knab, A. A. Urusovskaya and K. S. Bagdasarov. Real structure of undoped Y_2O_3 single crystals. *Acta Cryst.* **B40**, 76, doi:10.1107/S0108768184001774 (1984).

[117] M. Marezio and J. P. Remeika. Bond lengths in the α-Ga_2O_3 structure and the high-pressure phase of $Ga_{2-x}Fe_xO_3$. *J. Chem. Phys.* **46**, 1862, doi:10.1063/1.1840945 (1967).

[118] S. Geller. Crystal Structure of β-Ga_2O_3. *J. Chem. Phys.* **33**, 676, doi:10.1063/1.3642962 (1960).

[119] C. Wouters *et al.* Investigating the ranges of (meta)stable phase formation in $(In_xGa_{1-x})_2O_3$: Impact of the cation coordination. *Phys. Rev. Mater.* **4**, 125001, doi:10.1103/PhysRevMaterials.4.125001 (2020).

[120] J. H. Hildebrand. Solubility. XII. Regular solutions. *J. Am. Chem. Soc.* **51**, 66, doi:10.1021/ja01376a009 (1929).

[121] A. M. Holder *et al.* Novel phase diagram behavior and materials design in heterostructural semiconductor alloys. *Sci. Adv.* **3**, e1700270, doi:10.1126/sciadv.1700270 (2017).

[122] W. Kohn, A. D. Becke and R. G. Parr. Density functional theory of electronic structure. *J. Phys. Chem.* **100**, 12974, doi:10.1021/jp960669l (1996).

[123] V. Blum *et al.* Ab initio molecular simulations with numeric atom-centered orbitals. *Comput. Phys. Commun.* **180**, 2175, doi:10.1016/j.cpc.2009.06.022 (2009).

[124] A. H. Larsen *et al.* The atomic simulation environment-a Python library for working with atoms. *J. Physics: Condens. Matter* **29**, 273002, doi:10.1088/1361-648X/aa680e (2017).

[125] J. P. Perdew, K. Burke and M. Ernzerhof. Generalized gradient approximation made simple. *Phys. Rev. Lett.* **77**, 3865, doi:10.1103/PhysRevLett.77.3865 (1996).

[126] J. P. Perdew *et al.* Restoring the density-gradient expansion for exchange in solids and surfaces. *Phys. Rev. Lett.* **100**, 136406, doi:10.1103/PhysRevLett.100.136406 (2008).

[127] Bergerhoff, G. and Brown, I.D. in "Crystallographic Databases", F.H. Allen et al. (Hrsg.), Chester, International Union of Crystallography, (1987).

[128] Y. C. Eldar and G. Kutyniok. *Compressed sensing: Theory and applications* (Cambridge University Press, 2009).

[129] Q. Wu, B. He, T. Song, J. Gao and S. Shi. Cluster expansion method and its application in computational materials science. *Comput. Mater. Sci.* **125**, 243, doi:10.1016/j.commatsci.2016.08.034 (2016).

[130] M. D. Santia, N. Tandon and J. D. Albrecht. Effects of strain on the optical and thermodynamic properties of β-Ga_2O_3. *Solid State Commun.* **297**, 1, doi:10.1016/j.ssc.2019.04.012 (2019).

[131] Z. Guo *et al.* Anisotropic thermal conductivity in single crystal β-gallium oxide. *Appl. Phys. Lett.* **106**, 111909, doi:10.1063/1.4916078 (2015).

[132] N. Preissler, O. Bierwagen, A. T. Ramu and J. S. Speck. Electrical transport, electrothermal transport, and effective electron mass in single-crystalline In_2O_3 films. *Phys. Rev. B* **88**, 085305, doi:10.1103/PhysRevB.88.085305 (2013).

[133] B. Fultz. Vibrational thermodynamics of materials. *Prog. Mater. Sci.* **55**, 247, doi:10.1016/j.pmatsci.2009.05.002 (2010).

[134] M. Baldini *et al.* Semiconducting Sn-doped β-Ga_2O_3 homoepitaxial layers grown by metal organic vapour-phase epitaxy. *J. Mater. Sci.* **51**, 3650, doi:10.1007/s10853-015-9693-6 (2016).

[135] R. Schewski *et al.* Evolution of planar defects during homoepitaxial growth of β-Ga_2O_3 layers on (100) substrates — A quantitative model. *J. Appl. Phys.* **120**, 225308, doi:10.1063/1.4971957 (2016).

[136] R. Schewski *et al.* Step-flow growth in homoepitaxy of β-Ga_2O_3 (100) - The influence of the miscut direction and faceting. *APL Mater.* **7**, 022515, doi:10.1063/1.5054943 (2019).

[137] S. Bin Anooz *et al.* Step flow growth of β-$_2O_3$ thin films on vicinal (100) β-Ga_2O_3 substrates grown by MOVPE. *Appl. Phys. Lett.* **116**, 182106, doi:10.1063/5.0005403 (2020).

[138] S. Bin Anooz *et al.* Indium incorporation in homoepitaxial β-Ga_2O_3 thin films grown by metal organic vapor phase epitaxy. *J. Appl. Phys.* **125**, 195702, doi:10.1063/1.5090213 (2019).

[139] D. B. Williams and C. B. Carter. *Transmission Electron Microscopy* (Plenum Press, New York, 1996).

[140] B. Fultz and J. M. Howe. *Transmission Electron Microscopy and Diffractometry of Materials* (Springer, Berlin Heidelberg, 2013).

[141] H. Bethge and J. Heydenreich. *Electron Microscopy in Solid State Physics* (Elsevier, Amsterdam, 1987).

[142] S. J. Pennycook and P. D. Nellist. *Scanning Transmission Electron Microscopy: Imaging and Analysis* (Springer, New York, 2011).

[143] L. de Broglie. Waves and Quanta. *Nature* **112**, 540, doi:10.1038/112540a0 (1923).

[144] O. Scherzer. The theoretical resolution limit of the electron microscope. *J. Appl. Phys.* **20**, 20, doi:10.1063/1.1698233 (1949).

[145] H. Lichte. Optimum Focus for Taking Electron Holograms. *Ultramicroscopy* **38**, 13, doi:10.1016/0304-3991(91)90105-F (1991).

[146] O. Scherzer. Uber einige Fehler von Elektronenlinsen. *Z. Physik* **101**, 593, doi:10.1007/BF01349606 (1936).

[147] H. Rose. Outline of a spherically corrected semiplanatic medium-voltage transmission electron-microscope. *Optik* **85**, 19 (1990).

[148] H. Rose. Correction of aberrations, a promising means for improving the spatial and energy resolution of energy-filtering electron microscopes. *Ultramicroscopy* **56**, 11, doi:10.1016/0304-3991(94)90142-2 (1994).

[149] C. L. Jia, M. Lentzen and K. Urban. High-resolution transmission electron microscopy using negative spherical aberration. *Microsc. Microanal.* **10**, 174, doi:10.1017/S1431927604040425 (2004).

[150] A. Howie. Image Contrast And Localized Signal Selection Techniques. *J. Microsc.* **117**, 11, doi:10.1111/j.1365-2818.1979.tb00228.x (1979).

[151] C. R. Hall and P. B. Hirsch. Effect of thermal diffuse scattering on propagation of high energy electrons through crystals. *Proc. Royal Soc. A* **286**, 158, doi:10.1098/rspa.1965.0136 (1965).

[152] L. M. Peng. Electron atomic scattering factors and scattering potentials of crystals. *Micron* **30**, 625, doi:10.1016/S0968-4328(99)00033-5 (1999).

[153] P. D. Nellist. Scanning Transmission Electron Microscopy. In P. W. Hawkes and J. C. H. Spence (eds.) *Springer Handbook of Microscopy* (Springer, Cham, 2019).

[154] P. D. Nellist and S. J. Pennycook. Incoherent imaging using dynamically scattered coherent electrons. *Ultramicroscopy* **78**, 111, doi:10.1016/S0304-3991(99)00017-0 (1999).

[155] A. Howie. Diffraction channelling of fast electrons and positrons in crystals. *Philos. Mag.* **14**, 223, doi:10.1080/14786436608219008 (1966).

[156] Z. L. Wang. Dislocation contrast in high-angle hollow-cone dark-field TEM. *Ultramicroscopy* **53**, 73, doi:10.1016/0304-3991(94)90106-6 (1994).

[157] V. Grillo *et al.* Strain, composition and disorder in ADF imaging of semiconductors. *J. Physics: Conf. Ser.* **326**, 012006, doi:10.1088/1742-6596/326/1/012006 (2011).

[158] B. F. Buxton, J. E. Loveluck and J. W. Steeds. Bloch waves and their corresponding atomic and molecular orbitals in high energy electron diffraction. *Philos. Mag. A* **38**, 259, doi:10.1080/01418617808239233 (1978).

[159] E. Rotunno *et al.* Electron-Beam Shaping in the Transmission Electron Microscope: Control of Electron-Beam Propagation Along Atomic Columns. *Phys. Rev. Appl.* **11**, 044072, doi:10.1103/PhysRevApplied.11.044072 (2019).

[160] A. J. F. Metherell. Diffraction of Electrons by Perfect Crystals. In U. Valdrè and E. Ruedl (eds.) *Electron Microscopy in Materials Science II* (CEC, Brussels, 1975).

[161] J. M. Cowley and A. F. Moodie. The scattering of electrons by atoms and crystals. I. A new theoretical approach. *Acta Cryst.* **10**, 609, doi:10.1107/s0365110x57002194 (1957).

[162] E. J. Kirkland, R. F. Loane and J. Silcox. Simulation of Annular Dark Field STEM Images Using a Modified Multislice Method. *Ultramicroscopy* **23**, 77, doi:10.1016/0304-3991(87)90229-4 (1987).

[163] R. F. Loane, P. Xu and J. Silcox. Thermal vibrations in convergent-beam electron diffraction. *Acta Cryst.* **A47**, 267, doi:10.1107/S0108767391000375 (1991).

[164] C. Kranert *et al.* Lattice parameters and Raman-active phonon modes of β-$(Al_xGa_{1-x})_2O_3$. *J. Appl. Phys.* **117**, 125703, doi:10.1063/1.4915627 (2015).

[165] R. D. Ramsier and J. T. Yates. Electron-stimulated desorption: Principles and applications. *Surf. Sci. Reports* **12**, 243, doi:10.1016/0167-5729(91)90013-N (1991).

[166] S. Sepulveda-Guzman *et al.* In situ formation of bismuth nanoparticles through electron-beam irradiation in a transmission electron microscope. *Nanotechnology* **18**, 335604, doi:10.1088/0957-4484/18/33/335604 (2007).

[167] Z. Dang *et al.* In Situ Transmission Electron Microscopy Study of Electron Beam-Induced Transformations in Colloidal Cesium Lead Halide Perovskite Nanocrystals. *ACS Nano* **11**, 2124, doi:10.1021/acsnano.6b08324 (2017).

[168] P. Vogt and O. Bierwagen. Kinetics versus thermodynamics of the metal incorporation in molecular beam epitaxy of $(In_xGa_{1-x})_2O_3$. *APL Mater.* **4**, 086112, doi:10.1063/1.4961513 (2016).

[169] G. Cliff and G. W. Lorimer. The quantitative analysis of thin films. *J. Microsc.* **103**, 203, doi:10.1111/j.1365-2818.1975.tb03895.x (1975).

[170] Y. Lv *et al.* Characterization of β-Ga_2O_3 thin films on sapphire (0001) using metal-organic chemical vapor deposition technique. *Vacuum* **86**, 1850, doi:10.1016/j.vacuum.2012.04.019 (2012).

[171] M. Kracht *et al.* Tin-Assisted Synthesis of ϵ-Ga_2O_3 by Molecular Beam Epitaxy. *Phys. Rev. Appl.* **8**, 054002, doi:10.1103/PhysRevApplied.8.054002 (2017).

[172] M. Kneiß *et al.* Epitaxial stabilization of single phase κ-$(In_xGa_{1-x})_2O_3$ thin films up to $x = 0.28$ on c-sapphire and κ-Ga_2O_3 (001) templates by tin-assisted VCCS-PLD. *APL Mater.* **7**, 101102, doi:10.1063/1.5120578 (2019).

[173] O. Bierwagen and J. S. Speck. Nucleation of islands and continuous high-quality In_2O_3(001) films during plasma-assisted molecular beam epitaxy on Y-stabilized ZrO_2(001). *J. Appl. Phys.* **107**, 113519, doi:10.1063/1.3415539 (2010).

[174] O. Bierwagen, J. Rombach and J. S. Speck. Faceting control by the stoichiometry influence on the surface free energy of low-index bcc-In_2O_3 surfaces. *J. Physics: Condens. Matter* **28**, 224006, doi:10.1088/0953-8984/28/22/224006 (2016).

[175] I. O. Mayboroda *et al.* Growth of AlGaN under the conditions of significant gallium evaporation: Phase separation and enhanced lateral growth. *J. Appl. Phys.* **122**, 105305, doi:10.1063/1.5002070 (2017).

[176] R. Hoppe. Effective coordination numbers (ECoN) and mean fictive ionic radii (MEFIR). *Z. Kristallogr.* **150**, 23, doi:10.1524/zkri.1979.150.14.23 (1979).

[177] M. B. Maccioni, F. Ricci and V. Fiorentini. Properties of $(Ga_{1-x}In_x)_2O_3$ over the whole x range. *J. Phys. Condens. Matter* **28**, 224001, doi:10.1088/0953-8984/28/22/224001 (2016).

[178] J. Heyd, G. E. Scuseria and M. Ernzerhof. Erratum: Hybrid functionals based on a screened Coulomb potential [J. Chem. Phys. 118, 8207 (2003)]. *J. Chem. Phys.* **124**, 219906, doi:10.1063/1.2204597 (2006).

[179] A. Papadogianni, T. Nagata, C. Wouters, M. Albrecht and O. Bierwagen. Structural and electronic transport properties of single-crystalline $(In_{1-x}Ga_x)_2O_3$ thin films in the bixbyite phase end. Not published yet.

[180] F. Zhang, K. Saito, T. Tanaka, M. Nishio and Q. Guo. Wide bandgap engineering of $(GaIn)_2O_3$ films. *Solid State Commun.* **186**, 28, doi:10.1016/j.ssc.2014.01.024 (2014).

[181] J. Z. Liu and A. Zunger. Thermodynamic states and phase diagrams for bulk-incoherent, bulk-coherent, and epitaxially-coherent semiconductor alloys: Application to cubic (Ga,In)N. *Phys. Rev. B* **77**, 205201, doi:10.1103/PhysRevB.77.205201 (2008).

[182] P. Vogt, O. Brandt, H. Riechert, J. Lähnemann and O. Bierwagen. Metal-Exchange Catalysis in the Growth of Sesquioxides: Towards Heterostructures of Transparent Oxide Semiconductors. *Phys. Rev. Lett.* **119**, 196001, doi:10.1103/PhysRevLett.119.196001 (2017).

[183] K. Momma and F. Izumi. VESTA 3 for three-dimension visualization of crystal, volumetric and morphology data. *J. Appl. Crystallogr.* **44**, 1272, doi:10.1107/S0021889811038970 (2011).

[184] R. Huang, H. Hayashi, F. Oba and I. Tanaka. Microstructure of Mn-doped γ-Ga_2O_3 epitaxial film on sapphire (0001) with room temperature ferromagnetism. *J. Appl. Phys.* **101**, 063526, doi:10.1063/1.2713349 (2007).

[185] J. B. Varley, H. Peelaers, A. Janotti and C. G. Van De Walle. Hydrogenated cation vacancies in semiconducting oxides. *J. Phys. Condens. Matter* **23**, 334212, doi:10.1088/0953-8984/23/33/334212 (2011).

[186] A. Kyrtsos, M. Matsubara and E. Bellotti. Migration mechanisms and diffusion barriers of vacancies in Ga_2O_3. *Phys. Rev. B* **95**, 245202, doi:10.1103/PhysRevB.95.245202 (2017).

[187] S. Jiao *et al.* The Structural and Photoelectrical Properties of Gallium Oxide Thin Film Grown by Radio Frequency Magnetron Sputtering. *ECS J. Solid State Sci. Technol.* **8**, Q3086, doi:10.1149/2.0161907jss (2019).

[188] H. Altuntas, I. Donmez, C. Ozgit-Akgun and N. Biyikli. Effect of postdeposition annealing on the electrical properties of β-Ga_2O_3 thin films grown on p-Si by plasma-enhanced atomic layer deposition. *J. Vac. Sci. Technol. A* **32**, 041504, doi:10.1116/1.4875935 (2014).

[189] S. S. Kumar *et al.* Structure, Morphology, and Optical Properties of Amorphous and Nanocrystalline Gallium Oxide Thin Films. *J. Phys. Chem. C* **117**, 4194, doi:10.1021/jp311300e (2013).

[190] F. Zhang, H. Li, Y. T. Cui, G. L. Li and Q. Guo. Evolution of optical properties and band structure from amorphous to crystalline Ga_2O_3 films. *AIP Adv.* **8**, 045112, doi:10.1063/1.5021867 (2018).

[191] J. Wu *et al.* Temperature-Dependent Crystallization of Ga_2O_3 for Ultraviolet Photodetectors. *J. Electron. Mater.* **49**, 4581, doi:10.1007/s11664-019-07924-x (2020).

[192] S. L. Moffitt *et al.* Probing the Unique Role of Gallium in Amorphous Oxide Semiconductors through Structure–Property Relationships. *Adv. Electron. Mater.* **3**, 1, doi:10.1002/aelm.201700189 (2017).

[193] P. K. Song, H. Akao, M. Kamei, Y. Shigesato and I. Yasui. Preparation and crystallization of tin-doped and undoped amorphous indium oxide films deposited by sputtering. *Jpn. J. Appl. Phys.* **38**, 5224, doi:10.1143/jjap.38.5224 (1999).

[194] J. B. Cohen. A brief review of the properties of ordered alloys. *J. Mater. Sci.* **4**, 1012, doi:10.1007/BF00555319 (1969).

[195] F. Millange, V. Caignaert, B. Domengès, B. Raveau and E. Suard. Order-Disorder Phenomena in New $LaBaMn_2O_{6-x}$ CMR Perovskites. Crystal and Magnetic Structure. *Chem. Mater.* **10**, 1974, doi:10.1021/cm980130v (1998).

[196] A. J. Hauser *et al.* Unlocking the potential of half-metallic Sr_2FeMoO_6 films through controlled stoichiometry and double-perovskite ordering. *Phys. Rev. B* **83**, 014407, doi:10.1103/PhysRevB.83.014407 (2011).

[197] C. Wouters, T. Markurt, M. Albrecht, E. Rotunno and V. Grillo. Influence of 2s Bloch wave state excitations on quantitative HAADF STEM imaging. *Phys. Rev. B* **100**, 184106, doi:10.1103/PhysRevB.100.184106 (2019).

[198] A. Rosenauer *et al.* Measurement of specimen thickness and composition in $Al_xGa_{1-x}N$ / GaN using high-angle annular dark field images. *Ultramicroscopy* **109**, 1171, doi:10.1016/j.ultramic.2009.05.003 (2009).

[199] T. Claeson and J. B. Boyce. Order-disorder transformation in Au-Cu alloys studied by extended x-ray-absorption fine structure. *Phys. Rev. B* **29**, 1551, doi:10.1103/PhysRevB.29.1551 (1984).

[200] R. Brydson. *Aberration-corrected Analytical Transmission Electron Microscopy* (RMS-Wiley, Chichester, West Sussex, U.K., 2011).

[201] Z. W. Wang *et al.* Quantitative Z-contrast imaging in the scanning transmission electron microscope with size-selected clusters. *Phys. Rev. B* **84**, 073408, doi:10.1103/PhysRevB.84.073408 (2011).

[202] P. Geuens and D. Van Dyck. The S-state model: A work horse for HRTEM. *Ultramicroscopy* **93**, 179, doi:10.1016/S0304-3991(02)00276-0 (2002).

[203] J. M. Cowley. An approximate theory of order in alloys. *Phys. Rev.* **77**, 669, doi:10.1103/PhysRev.77.669 (1950).

[204] R. D. Shannon and C. T. Prewitt. Effective ionic radii in oxides and fluorides. *Acta Cryst.* **B25**, 925, doi:10.1107/s0567740869003220 (1969).

A

Supercells for STEM multislice simulations

The Vesta [183] structures of the supercells of [010] and [132] projected monoclinic $InGaO_3$, [11$\bar{2}$0] projected wurtzite $In_{0.5}Ga_{0.5}N$, [100] projected fcc $AuCu_3$ and [100] projected bcc InGa lattices and single-column and two-column structures used for the HAADF-STEM simulations of Chapter 5 are visualized below (Figs. A.1-A.6). Periodic boundary conditions in the x, y and z directions are ensured. All cell dimensions and an indication of the STEM scanning area are added onto the figures. For each of the disordered lattice supercells, a random configuration with the indicated thickness along the projection (z) direction was constructed and repeated multiple times to reach the final thickness. The validity of this approach is demonstrated for $InGaO_3$ in Fig. A.7. Using a 30 nm thick (approximated) random configuration and repeating it five times along the beam direction produces the same multislice simulation results as using a 150 nm thick random configuration, and thus no periodicity effects are introduced in this way. For the disordered supercells, we want to clarify that the stick-and-ball structures only represents the configuration of the first atomic slice of the structure (second, third, etc., slices have different configurations), while for the ordered structure every slice looks the same.

For the [010] monoclinic $(In_xGa_{1-x})_2O_3$ and $(Al_xGa_{1-x})_2O_3$ simulations with different x concentrations, the same structure for the supercell was used as the one in Fig. A.1, with an adaptation of the lattice parameters according to the linear relations found by Kranert *et al.* in Refs. [60] and [164]. The β-angle was not changed for simplicity. The supercell size corresponds to six unit cells in the c-direction (x), three unit cells in the a-direction (y) and 500 unit cells in the b-direction (z), which results in the supercell dimensions summarized in Table A.1.

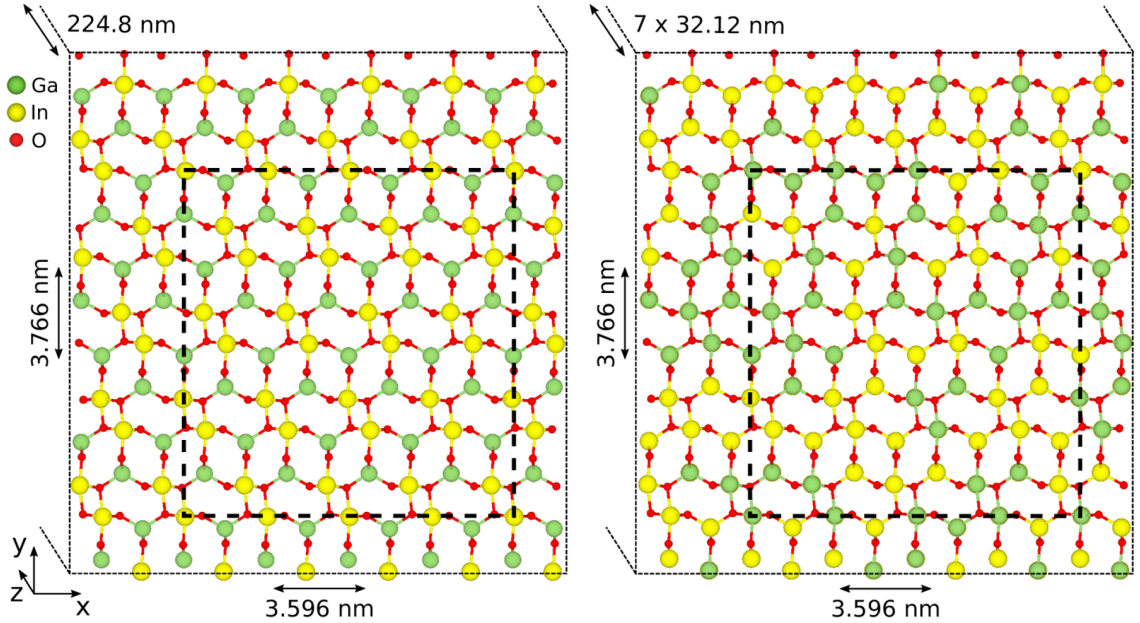

Figure A.1: [010] projected ordered and disordered monoclinic $InGaO_3$ [i.e. $(In_{0.5}Ga_{0.5})_2O_3$] supercells and the full supercell dimensions. For the disordered supercell, a random configuration of 32.12 nm thickness was constructed and repeated seven times in the z direction. The STEM scanning area is indicated by the black dashed rectangle.

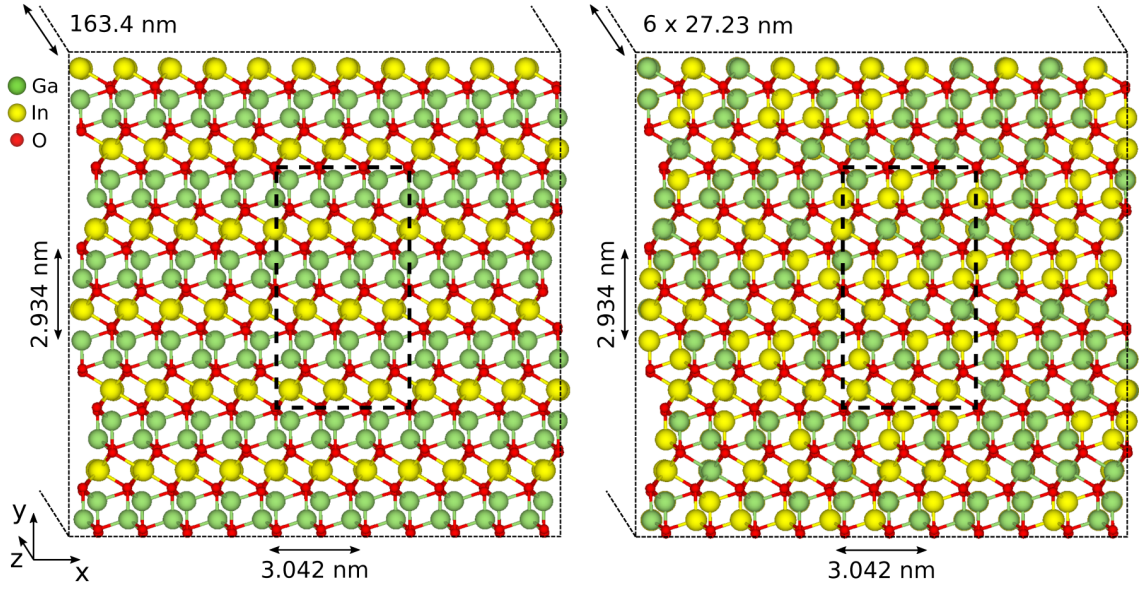

Figure A.2: [132] projected ordered and disordered monoclinic $InGaO_3$ supercells and the full supercell dimensions. For the disordered supercell, a random configuration of 27.23 nm thickness was constructed and this one was repeated six times in the z direction to reach the final thickness of 163.4 nm. The STEM scanning area is indicated by the black dashed rectangle.

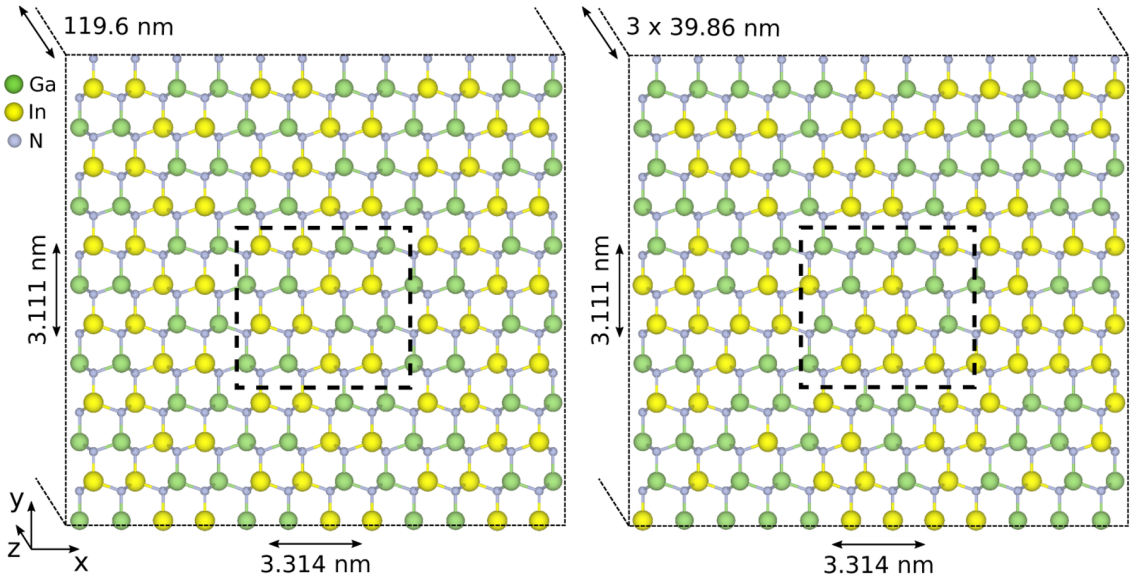

Figure A.3: [11$\bar{2}$0] projected ordered and disordered wurtzite $In_{0.5}Ga_{0.5}N$ supercells and the full supercell dimensions. For the disordered supercell, a random configuration of 39.86 nm thickness was constructed and repeated three times in the z direction. The STEM scanning area is indicated by the black dashed rectangle.

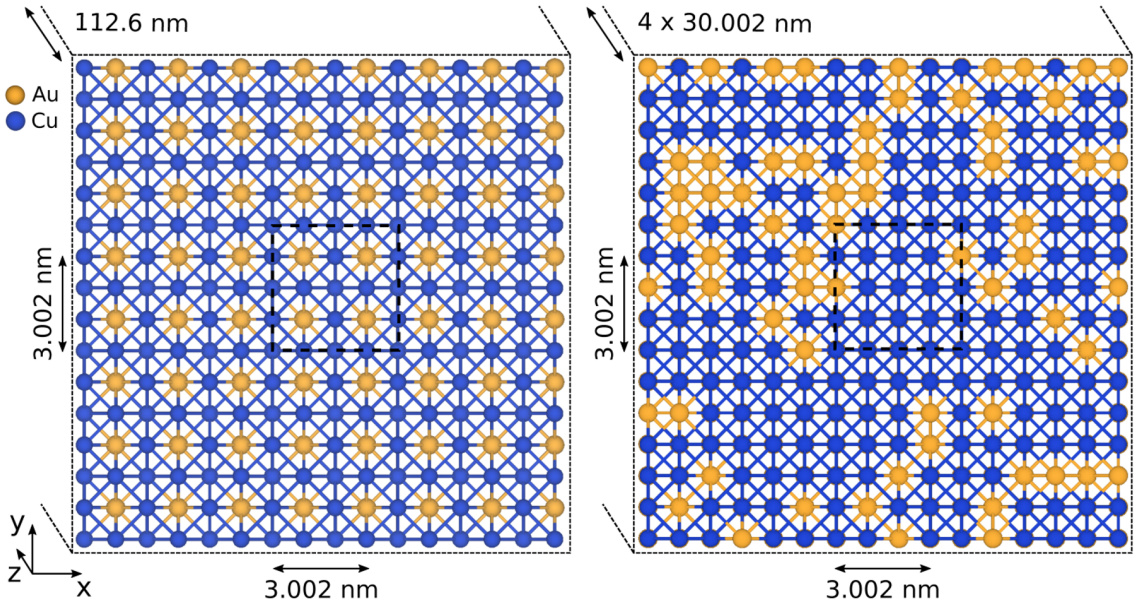

Figure A.4: [100] projected ordered and disordered cubic $AuCu_3$ supercells and the full supercell dimensions. For the disordered supercell, a random configuration of 30.002 nm thickness was constructed and repeated four times in the z direction. The STEM scanning area is indicated by the black dashed rectangle.

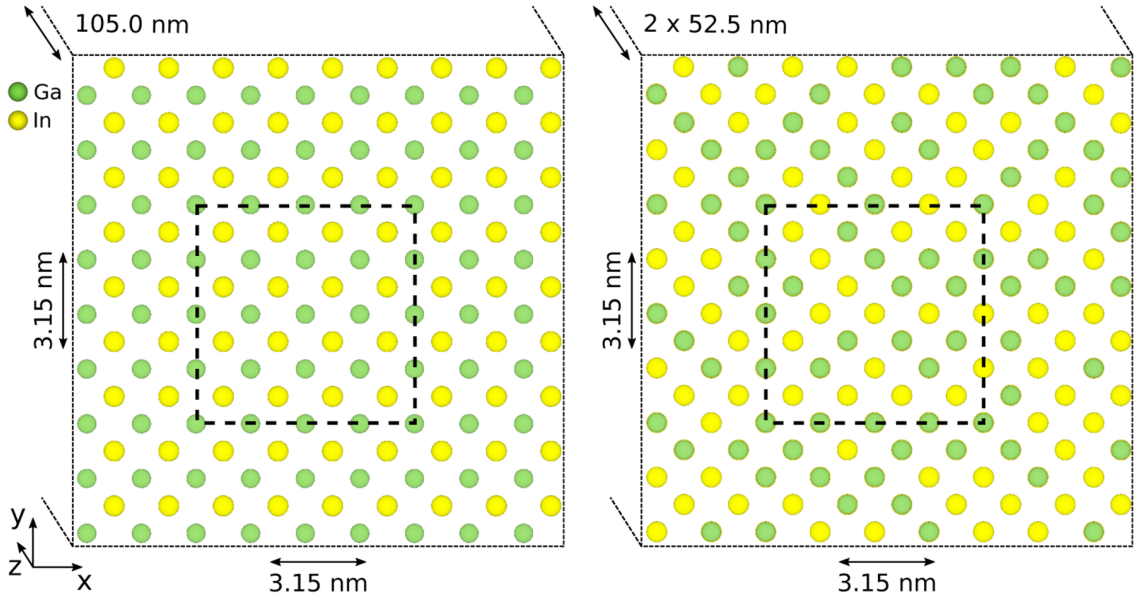

Figure A.5: [100] projected ordered and disordered cubic InGa supercells and the full supercell dimensions. For the disordered supercell, a random configuration of 52.50 nm thickness was constructed and repeated two times in the z direction. The STEM scanning area is indicated by the black dashed rectangle. No bonds are defined here since this is a non-existing artificial structure.

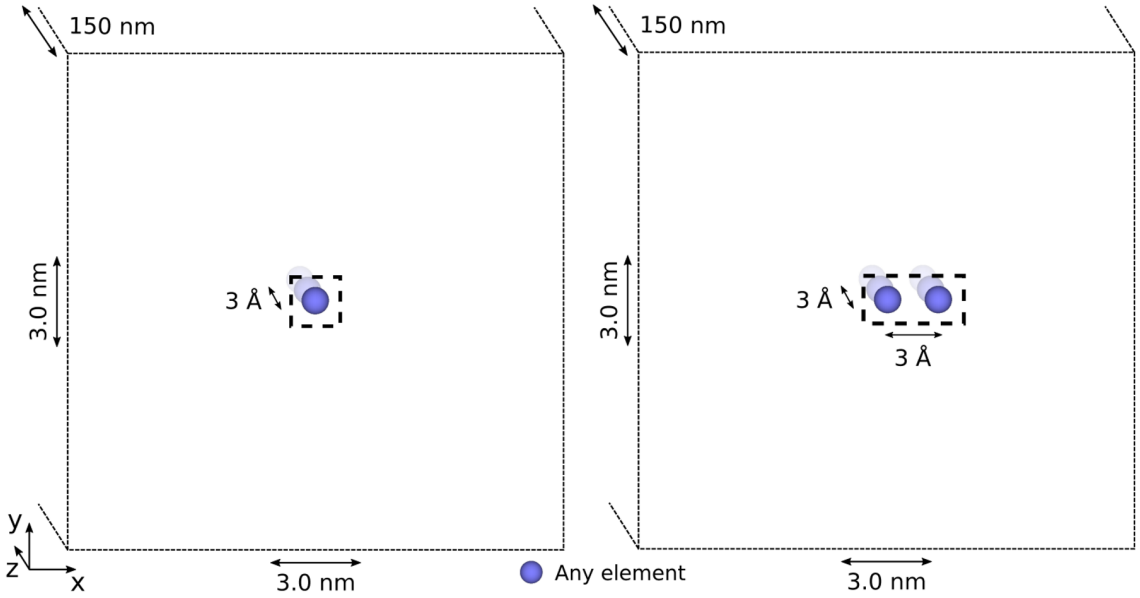

Figure A.6: Single-column and two-column supercells with the full supercell dimensions. For disordered columns, a random configuration with the full thickness of 150 nm was constructed. The STEM scanning area is indicated by the black dashed rectangle.

Table A.1: Dimensions of the $(In_xGa_{1-x})_2O_3$ and $(Al_xGa_{1-x})_2O_3$ supercells for different x.

	x (nm)	y (nm)	z (nm)
$(In_{0.5}Ga_{0.5})_2O_3$	3.596	3.766	160.60
$(In_{0.4}Ga_{0.6})_2O_3$	3.572	3.725	158.85
$(In_{0.3}Ga_{0.7})_2O_3$	3.549	3.683	157.10
$(In_{0.2}Ga_{0.8})_2O_3$	3.526	3.642	155.35
$(In_{0.1}Ga_{0.9})_2O_3$	3.502	3.600	153.60
Ga_2O_3	3.479	3.558	151.85
$(Al_{0.1}Ga_{0.9})_2O_3$	3.476	3.545	151.35
$(Al_{0.2}Ga_{0.8})_2O_3$	3.466	3.532	150.70
$(Al_{0.3}Ga_{0.7})_2O_3$	3.455	3.520	150.05
$(Al_{0.4}Ga_{0.6})_2O_3$	3.445	3.508	149.40
$(Al_{0.5}Ga_{0.5})_2O_3$	3.435	3.496	148.75

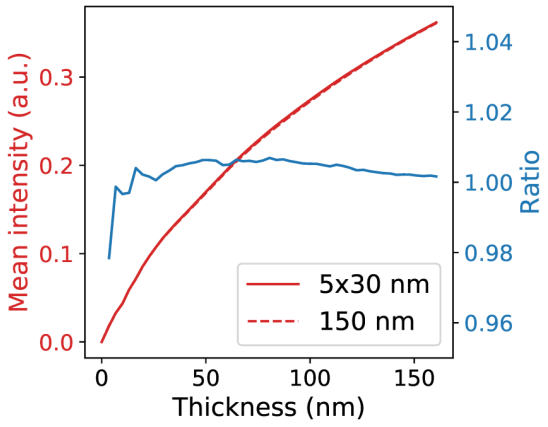

Figure A.7: Unit cell averaged simulated HAADF intensity as a function of thickness of a disordered [010] $InGaO_3$ lattice, comparing the use of a randomly configured supercell with a thickness of 30 nm repeated five times along the beam direction and a randomly configured supercell with a thickness of 150 nm. The ratio of the two curves is also plotted to show how minimal the difference is.

B

SEM-EDXS measurements before and after annealing

Fig. B.1 shows the SEM-EDXS spectra of our as-deposited amorphous $(In_xGa_{1-x})_2O_3$ films and after annealing in-situ and ex-situ. The O, Ga and In peaks are produced by the sample, while the Al peak is caused by the aluminum sample holder to which the sample is attached in the SEM and the Si peak in (a) and (b) comes from the SiC and SiN membranes on the heating chip. For the samples in (a), which were heated in-situ to a final temperature above 1000°C (exact T_{max} summarized in Table 2.2), the In/Ga peak ratio decreases for most samples after annealing. In addition, the relative height of the Si peak compared to other peaks generally increases. This indicates a thinning of the sample film (more beam electrons reach the underlying SiC and SiN membrane) and a stronger desorption of In compared to Ga for annealing to $T \geq 1000$°C, as described in the main text in Section 2.5.3. Only the film with indium content of $x = 0.55$, which was deposited on sapphire and prepared as a wedge-shaped in-situ lamella, preserved its composition upon heating to 1050°C. For a second film with $x_i = 0.44$, the annealing experiment was repeated and stopped at a lower temperature of 800°C. In that case, the composition of the film is still unaffected, as shown in Fig. B.1(b). Two $(In_xGa_{1-x})_2O_3$ films with $x = 0.33$ and $x = 0.55$ on sapphire were annealed ex-situ in an oven at a temperature of 800°C for 30 minutes. Spectra of these samples before and after annealing, as added in Fig. B.1(d), show that also in those cases the composition of the film was conserved.

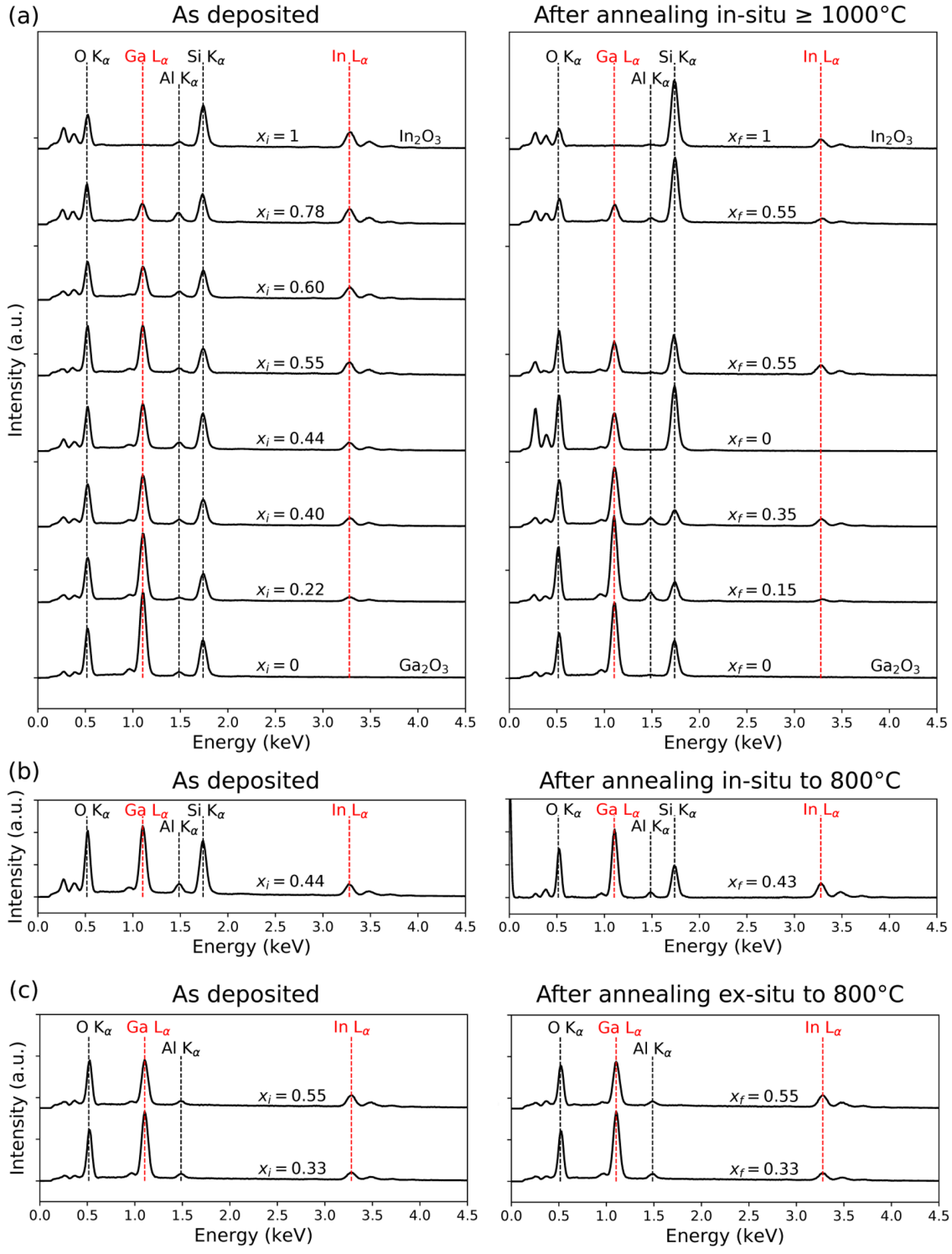

Figure B.1: SEM-EDXS spectra of as-deposited $(In_xGa_{1-x})_2O_3$ films and after annealing (a) in-situ to T_{max}, which is ≥ 1000°C, (b) in-situ to 800°C, and (c) ex-situ to 800°C. The In/Ga ratio x is quantified for each spectrum. All spectra were obtained with an electron beam of 7 keV, except the spectra in image (b) on the right which was obtained at 8 kV.

C

Sample degradation during in-situ TEM heating

We provide here evidence for the sample degradation that takes place during the in-situ heating of $(In_xGa_{1-x})_2O_3$ in the TEM, for temperatures exceeding approximately 1000°C. In the diffraction pattern, typically a change in behavior is observed when the temperature exceeds ~ 1000°C. Existing spots are quickly disappearing and new ones are appearing such that the clear Debye-Scherrer rings disappear and what seems like a random distribution of diffraction spots forms, as shown in Fig. C.1. This is probably the result of decomposition on the one hand, and desorption of the sample material from the chip on the other hand. As shown in the main text, indium is desorbing more strongly in this process than gallium and the average composition of the sample starts to change. In Fig. C.2 is illustrated how this degradation process is accelerated under high-magnification imaging with the 300 kV electron beam. A HRTEM image series recorded over 35 seconds of a Ga_2O_3 film under exposure of the electron beam and heated at 1000° is shown. The sample material is disappearing and reducing in thickness and the underlying membrane is becoming more visible. The movement of the boundary between the membrane and the sample is indicated by the red arrow.

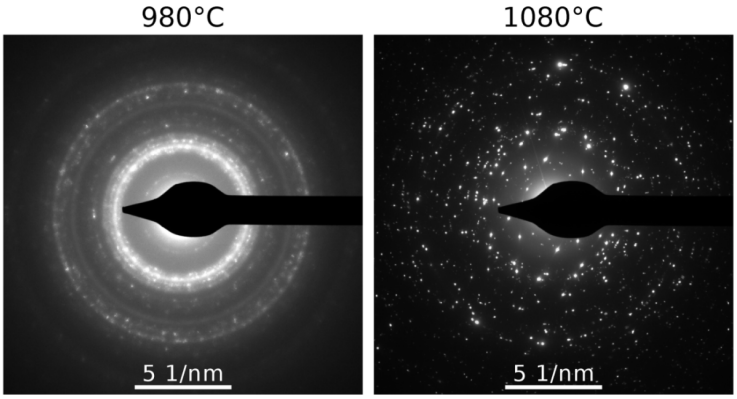

Figure C.1: Electron diffraction images of the $(In_xGa_{1-x})_2O_3$ film with initial indium content $x_i = 0.44$ in-situ annealed to 980°C and 1080°C.

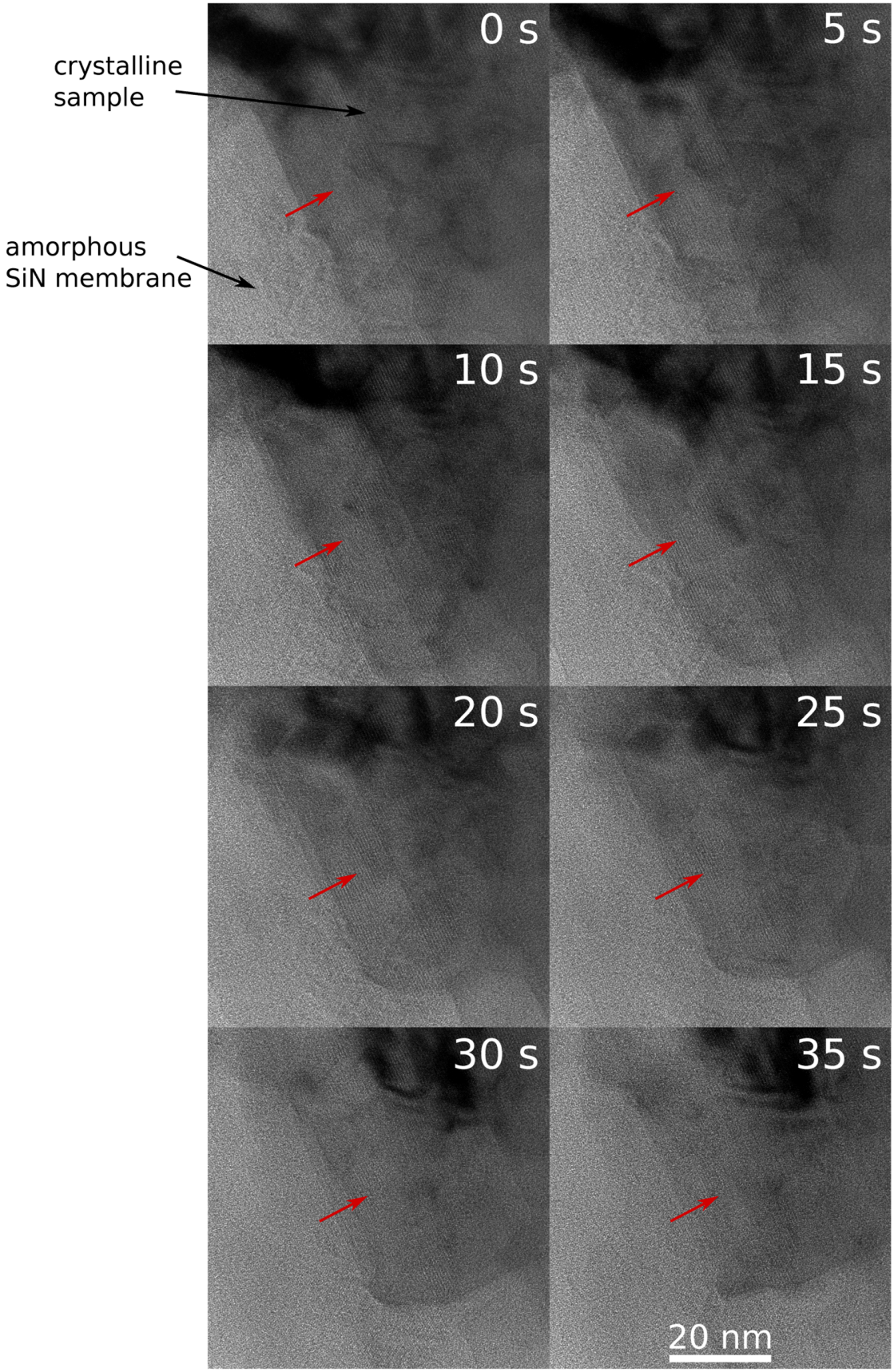

Figure C.2: HRTEM image series at a constant temperature of 1000°C of the crystallized Ga_2O_3 sample on the amorphous SiN membrane. The movement of the boundary between the membrane and the sample is indicated by the red arrow. The same scale bar applies to all images.

D

Epitaxial relations of the polymorphs to sapphire

Fig. D.1 describes the geometrical epitaxial relationships between the different $(In_xGa_{1-x})_2O_3$ phases observed in heteroepitaxial films and the sapphire substrate. The unit cells are projected along the growth direction, which is perpendicular to the planes mentioned at the top of the figure. The c-, h- and γ-phase all have in-plane six-fold rotational symmetry, just like the hexagonal sapphire substrate. The β-phase lacks this property, which results in the growth of 60° rotational $(In_xGa_{1-x})_2O_3$ grains, as illustrated in Fig. 3.3 in the main text.

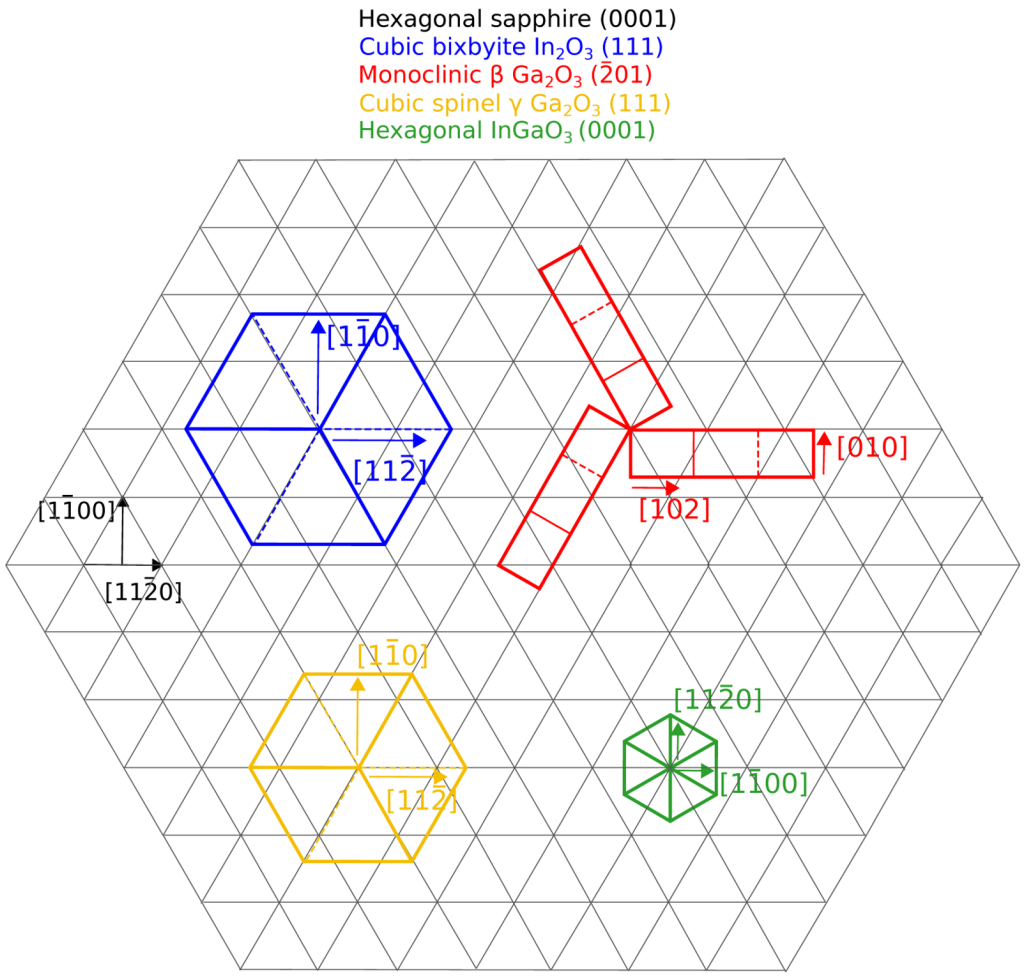

Figure D.1: Geometrical epitaxial relationships between the different $(In_xGa_{1-x})_2O_3$ phases observed in heteroepitaxial films and the sapphire substrate projected along the growth direction.

E

Calculation of the effective coordination number

The calculation of the effective coordination number (ECN) in the CE generated lattice configurations is based on the paper of R. Hoppe [176]. The nearest-neighbor distances between an atom h and its nearest neighbors of atom type i in the crystal lattice are called $d(h \rightarrow i)_j$. These distances are classified by increasing length such that $d(h \rightarrow i)_1$ is the shortest of all. First of all, a fictive ionic radius (FIR) is defined by multiplying the atomic bond distance by the ratio $R(h)/[R(h) + R(i)]$

$$\mathrm{FIR}(h \rightarrow i)_j = d(h \rightarrow i)_j \frac{R(h)}{R(h) + R(i)}, \tag{E.1}$$

where $R(h)$ and $R(i)$ are the ionic radii of atoms h and i, respectively. Values for the ionic radii are found in Shannon and Prewitt [204]. For each atom h, as many FIRs are defined as there are different nearest neighbor distances. Therefore, we can also define a weighted mean fictive ionic radius MEFIR, as follows:

$$\mathrm{MEFIR}(h \rightarrow i) = \frac{\sum_i \sum_j \mathrm{FIR}(h \rightarrow i)_j n(h \rightarrow i)_j \exp\left[1 - \left(\frac{\mathrm{FIR}(h \rightarrow i)_j}{\mathrm{FIR}(h \rightarrow i)_1}\right)^6\right]}{\sum_i \sum_j n(h \rightarrow i)_j \exp\left[1 - \left(\frac{\mathrm{FIR}(h \rightarrow i)_j}{\mathrm{FIR}(h \rightarrow i)_1}\right)^6\right]}. \tag{E.2}$$

It sums over all atom types i and all different distances j, which appear with a multiplicity $n(h \rightarrow i)_j$, and adds for each term a weight that is inversely proportional to the FIR distance. The weight is 1 for the closest neighbors ($j = 1$) and becomes smaller than 1 for increasing $j > 1$. With these two quantities defined, the ECN can be calculated by

$$\mathrm{ECN}(h \rightarrow i) = \sum_i \sum_j n(h \rightarrow i)_j \exp\left[1 - \left(\frac{\mathrm{FIR}(h \rightarrow i)_j}{\mathrm{MEFIR}(h)}\right)^6\right]. \tag{E.3}$$

The exponential term adds a weight to the summation of the nearest neighbors that is inversely proportional to their respective distance from atom h. For terms with FIR < MEFIR, the weight will be larger than 1, while for terms with FIR > MEFIR, the weight

will be smaller than 1.

In our case, for each Ga and In atom in the lattice, the nearest neighbor O atoms are considered to calculate the ECN. For example, if an In atom has six nearest O neighbors at equivalent distances, only one $d(h \rightarrow i)_j$ exists which has multiplicity $n = 6$. Then it follows that FIR(In $\rightarrow$ O) = MEFIR(In$\rightarrow$ O) and ECN = 6. In the case that one of the six nearest neighbors has a slightly longer bond distance, the term corresponding to that bond in Eq. E.3 will get a weight smaller than 1. Consequently, 5 < ECN < 6, depending on how large the elongation of the bond distance is compared with the other five bond distances.

F

HAADF-STEM simulations for different camera lengths

All the HAADF-STEM simulation results presented in Chapter 5 are done for an inner-acceptance angle of the annular HAADF detector of 35 mrad. In here, we show that the results can be generalized for different scattering angles by considering two other inner-acceptance angles of 54 and 89 mrad, which is equivalent to changing the camera length. On increasing the minimum scattering angle (i.e. shortening the camera length), the total intensity is lowered, but the same trends, although less pronounced, in the most relevant plots can still be observed, as shown below in Figs. F.1-F.3.

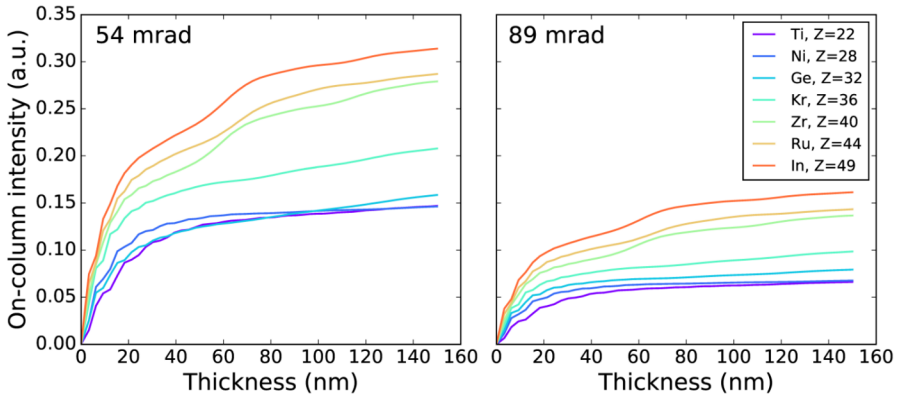

Figure F.1: Simulated on-column HAADF-STEM intensity of isolated atomic columns containing a single type of element with $22 < Z < 49$ for two different inner-acceptance angles of the annular detector.

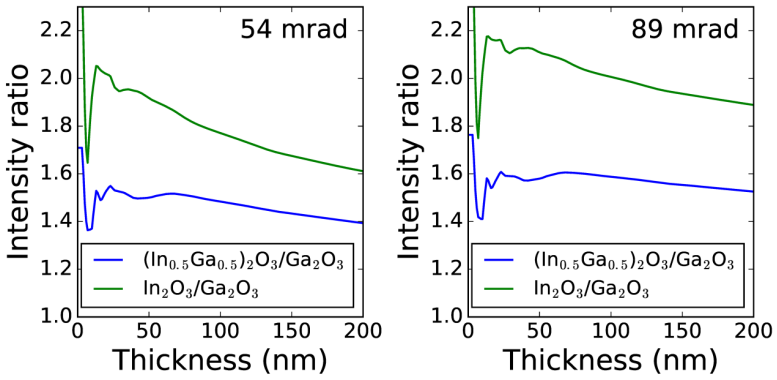

Figure F.2: $(In_xGa_{1-x})_2O_3$/ Ga_2O_3 intensity ratios for $x = 0.5$ and $x = 1$ plotted as a function of specimen thickness for two different inner-acceptance angles of the annular detector.

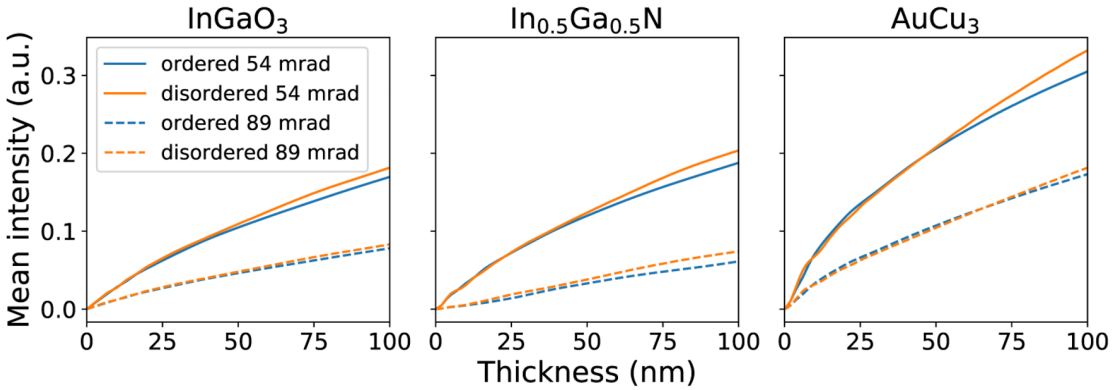

Figure F.3: Average HAADF-STEM intensity as a function of thickness of an ordered vs. disordered unit cell of $InGaO_3$, $In_{0.5}Ga_{0.5}N$ and $AuCu_3$, for two different inner-acceptance angles of the annular detector.

Publications and contributions

Publications (ordered by date of publication):

1. P. Mazzolini, P. Vogt, R. Schewski, C. Wouters, M. Albrecht, and O. Bierwagen. Faceting and metal-exchange catalysis in (010) β-Ga_2O_3 thin films homoepitaxially grown by plasma-assisted molecular beam epitaxy. APL Materials **7**, 022511 (2019).

2. R. Schewski, K. Lion, A. Fiedler, C. Wouters, A. Popp, S. V. Levchenko, T. Schulz, M. Schmidbauer, S. Bin Anooz, R. Grüneberg, Z. Galazka, G. Wagner, K. Irmscher, M. Scheffler, C. Draxl, and M. Albrecht. Step-flow growth in homoepitaxy of β-Ga_2O_3 (100) — The influence of the miscut direction and faceting. APL Materials **7**, 022515 (2019).

3. S. Bin Anooz, A. Popp, R. Grüneberg, C. Wouters, A. Fiedler, M. Ramsteiner, D. Klimm, K. Irmscher, R. Schewski, M. Schmidbauer, M. Albrecht, Z. Galazka, and G. Wagner. Indium incorporation in homoepitaxial β-Ga_2O_3 thin films grown by metal organic vapor phase epitaxy. Journal of Applied Physics **125**, 195702 (2019).

4. **C. Wouters**, T. Markurt, E. Rotunno, V. Grillo, and M. Albrecht. Influence of 2*s* Bloch wave state excitations on quantitative HAADF STEM imaging. Physical Review B **100**, 184106 (2019).

5. P. Mazzolini, A. Falkenstein, C. Wouters, R. Schewski, T. Markurt, Z. Galazka, M. Martin, M. Albrecht, and O. Bierwagen. Substrate-orientation dependence of β-Ga_2O_3 (100), (010), (001), and ($\bar{2}$01) homoepitaxy by indium-mediated metal-exchange catalyzed molecular beam epitaxy (MEXCAT-MBE). APL Materials **8**, 011107 (2020).

6. S. Bin Anooz, R. Grüneberg, C. Wouters, R. Schewski, M. Albrecht, A. Fiedler, K. Irmscher, Z. Galazka, W. Miller, G. Wagner, J. Schwarzkopf, and A. Popp. Step flow growth of β-Ga_2O_3 thin films on vicinal (100) β-Ga_2O_3 substrates grown by MOVPE. Applied Physics Letters **116**, 182106 (2020).

7. **C. Wouters**, R. Schewski, and M. Albrecht. Comment on "Phase transformation in MOCVD growth of $(Al_xGa_{1-x})_2O_3$ thin films" [APL Mater. 8, 031104 (2020)]. APL Materials **8**, 089101 (2020).

8. A. Hassa, C. Wouters, M. Kneiß, D. Splith, C. Sturm, H. von Wenckstern, M. Albrecht, M. Lorenz, and M. Grundmann. Control of phase formation of $(Al_xGa_{1-x})_2O_3$ thin films on c-plane Al_2O_3. Journal of Physics D: Applied Physics **53**, 485105 (2020).

9. S. Bin Anooz, R. Grüneberg, T. Chou, A. Fiedler, K. Irmscher, C. Wouters, R. Schewski, M. Albrecht, Z. Galazka, W. Miller, J. Schwarzkopf and A. Popp. Impact of chamber pressure and Si-doping on the surface morphology and electrical properties of homoepitaxial (100) β-Ga_2O_3 thin films grown by MOVPE. Journal of Physics D: Applied Physics **54**, 034003 (2020).

10. **C. Wouters**, C. Sutton, L. M. Ghiringhelli, T. Markurt, R. Schewski, A. Hassa, H. von Wenckstern, M. Grundmann, M. Scheffler, M. Albrecht. Investigating the ranges of (meta)stable phase formation in $(In_xGa_{1-x})_2O_3$: Impact of the cation coordination. Physical Review Materials **4**, 125001 (2020).

Conference contributions (ordered by date of presentation):

1. C. Wouters, T. Markurt, C. Sutton, P. Vogt, O. Bierwagen, H. Von Wenckstern, and M. Albrecht. "Miscibillity and phase formation in $(In_xGa_{1-x})_2O_3$" Transparent Conductive Oxides (TCO), Leipzig, Germany (2017). [poster presentation]

2. C. Wouters, T. Markurt, C. Sutton, P. Vogt, O. Bierwagen, H. Von Wenckstern, and M. Albrecht. "Investigating phase formation in $(In_xGa_{1-x})_2O_3$ by in-situ TEM crystallization" In-situ TEM workshop, KIT Karlsruhe, Germany (2018). [poster presentation]

3. C. Wouters, T. Markurt, C. Sutton, P. Vogt, O. Bierwagen, H. Von Wenckstern, and M. Albrecht. "Exploring phase stability in $(In_xGa_{1-x})_2O_3$ by TEM, Compound Semiconductor Week (CSW), Boston, USA (2018). [poster presentation]

4. C. Wouters, T. Markurt, C. Sutton, P. Vogt, O. Bierwagen, H. Von Wenckstern, and M. Albrecht. "Exploring phase stability in $(In_xGa_{1-x})_2O_3$ by TEM investigations" European Materials Research Society Fall Meeting, Warsaw, Poland (2018). [oral presentation]

5. C. Wouters, T. Markurt, C. Sutton, P. Mazzolini, P. Vogt, O. Bierwagen, L. Ghiringhelli, M. Scheffler, and M. Albrecht. "In-situ transmission electron microscopy annealing for crystallization and phase stability studies in the Ga_2O_3-In_2O_3 System" Microscopy of Semiconducting Materials (MSM), Cambridge, UK (2019). [oral presentation]

6. C. Wouters, T. Markurt, E. Rotunno, V. Grillo and M. Albrecht, "Influence of $2s$ Bloch wave state excitation on STEM-HAADF intensity and how it affects analysis in ordered alloy structures" Microscopy of Semiconducting Materials (MSM), Cambridge, UK (2019). [poster presentation]

7. C. Wouters, T. Markurt, C. Sutton, P. Mazzolini, P. Vogt, O. Bierwagen, L. Ghiringhelli, M. Scheffler, and M. Albrecht. "In-situ transmission electron microscopy annealing for crystallization and phase stability studies in the Ga_2O_3-In_2O_3 System" Microscopy and Microanalysis (MnM), Portland, USA (2019). [poster presentation]

Declaration of independent work

I declare that I have completed the thesis independently using only the aids and tools specified. I have not applied for a doctor's degree in the doctoral subject elsewhere and do not hold a corresponding doctor's degree. I have taken due note of the Faculty of Mathematics and Natural Sciences PhD Regulations, published in the Official Gazette of Humboldt-Universität zu Berlin no. 42/2018 on 11/07/2018.

Berlin, December 15, 2020

Charlotte Wouters